UC Santa Barbara

UC Santa Barbara Electronic Theses and Dissertations

Title

Engineering Magnetic and Topological Properties in Epitaxial Heusler Compounds

Permalink

https://escholarship.org/uc/item/64r9q8qs

Author

Brown-Heft, Tobias Levi

Publication Date

2018

Peer reviewed|Thesis/dissertation

eScholarship.org Powered by the California Digital Library
University of California

University of California
Santa Barbara

Engineering Magnetic and Topological Properties in Epitaxial Heusler Compounds

A dissertation submitted in partial satisfaction
of the requirements for the degree

Doctor of Philosophy
in
Materials

by

Tobias Levi Brown-Heft

Committee in charge:

Professor Chris J. Palmstrøm, Chair
Professor Ram Seshadri
Professor Stephen D. Wilson
Professor Ania C. Bleszynski Jayich

September 2018

The Dissertation of Tobias Levi Brown-Heft is approved.

Professor Ram Seshadri

Professor Stephen D. Wilson

Professor Ania C. Bleszynski Jayich

Professor Chris J. Palmstrøm, Committee Chair

September 2018

Engineering Magnetic and Topological Properties in Epitaxial Heusler Compounds

Copyright © 2018

by

Tobias Levi Brown-Heft

Acknowledgements

Placing my name alone beneath the title of this dissertation felt somewhat strange because it could not have been completed without the combined efforts of a vast number of individuals. So to begin, I want to say a general thank you to all the people who gave me advice and information, everyone who maintains and organizes facilities and equipment that I used, all the students I interacted with, and all of my friends and family. I couldn't have done this without you, and I am in your debt.

First, I would like to thank my advisor, Professor Chris Palmstrøm. His patience, curiosity, unwavering commitment to excellence, and knack for scientific storytelling has been inspiring. His attention to detail and knowledge of common pitfalls when designing experiments and interpreting results has made him a formidable scientist and a fantastic advisor. I also thank my doctoral committee. Professor Ania Blesyinski-Jayich, Professor Stephen Wilson, and Professor Ram Seshadri have always had helpful comments and suggestions about underlying physics, new experiments to try, techniques for publishing, and ways to maintain reasonable goals and keep projects grounded and moving forward.

None of the experimental work I have done could have been completed without the efforts of the Palmstrøm group members, past and present: Alex (Yu Hao), Amanda, Anthony, Aranya, Asbjørn, Bo (Borzoyeh), Daniel, Elizabeth, Elliot, Hadass, Jason, Jay (John), Javad, Joon Sue, Luca, Michael, Michelle, Mihir, Mitchell, Nate, Rachel, Ryan, Sahil, Sean, Shouvik, Sukgeun, and Tony. The development of experimental methods, equipment maintenance, a broad knowledge base when designing new experiments, sheer muscle, emotional support, and camaraderie are the gifts you all have given me daily. AdditionalIy, I have to thank Tony for the times we shared brewing beer and lifting weights.

I am indebted to the staff of the nanofabrication facility, the Materials Research

Lab X-ray diffraction lab, the physics machine shop, and the Arizona State University Goldwater Materials Science Facility. Their skill, professionalism, and speed have made it possible to obtain the scientific results presented here and interpret them correctly. In particular, I thank Guy Patterson for his patience and guidance each time I came to machine a difficult part, especially when I broke his tools in the process. I also thank Barry Wilkens and Mark Mangus for their knowledge and vigilant maintenance of the Rutherford backscattering spectrometry accelerator. Their willingness to work around my non-standard requests and occasional rush jobs is commendable.

I emphatically thank the members of Intel's Components Research division that took interest in my projects and maintained a collaboration with us. My work has benefitted immeasurably from their perspective and experience. I am honored to accept their offer to join their team after my graduation.

Next, I must acknowledge the friendships I have forged in Santa Barbara. It has been a privilege to share the graduate school experience with such a talented, intelligent, conscientious, and wonderful group of scientists and non-scientists. In particular, I thank my fellow Acetones Quartet members, Garth Ratliff, Chris Freeze, and Thomas Cristiani. It has been joy to make music with you these past few years. I also thank my housemates Daniel Becerra, John Kaminsky, Ryan Need, Chris Freeze, Anirudh Natarajan, David Hwang, Chris Zollner, and Elliot Young for bringing additional balance to my life via board games, Halo nights, BBQs, road trips, and general shenanigans.

Finally, I'd like to thank my family. My parents Heidi and Wallace provided a safe and stable home and a down-to-earth perspective on life, as well as thousands of pieces of great advice that I probably should have listened to more. I am incredibly thankful for my brothers, Jacob and Isaac. We have traveled through this life together, sometimes scratching and biting, and emerged as an unstoppable team. I know that when we stand together, our futures will all be bright.

Curriculum Vitæ

Tobias Levi Brown-Heft

EDUCATION

2018 — Doctorate of Philosophy in Materials Science, University of California at Santa Barbara, Santa Barbara, CA 93106. GPA 3.86/4.00. Advisor: Christopher J. Palmstrøm

2013 — Bachelor of Science with major in Physics and minor in Organic Chemistry. University of Oregon, Eugene, OR, 97402. GPA: 3.85/4.00, *summa cum laude*, Dean's List [Fall 2011 - June 2013]

2011 — Associate of Science, Oregon Transfer Degree, Lane Community College, Eugene, OR, 97405. GPA: 4.11/4.00, President's List [Fall 2009 - Winter 2011]

ACADEMIC EXPERIENCE

08/2013 - 09/2018 — Graduate Research Assistant, Full Time. Materials Department, University of California at Santa Barbara. Chris J. Palmstrøm, Advisor, molecular beam epitaxy lab, cjpalm@ucsb.edu

02/2016 - 07/2016 — Graduate Student Mentor, Palmstrøm Group. Amanda Andreasson, Master's Degree Exchange Student, Lund University, Sweden. Provide and direct a Master's student project. Growth of Mn_3Ge/STO (001) by MBE.

06/2015 - 08/2015 — Graduate Student Mentor, REU. Elizabeth Lee, Undergraduate Researcher, Harvey Mudd University, Claremont, CA. Wendy Ibsen, Director, Center for Science and Engineering Partnerships, ibsen@cnsi.ucsb.edu

12/2014 - 03/2015 — Teaching Assistant, Materials 101. Materials Department, UCSB. James S. Speck, Professor, speck@mrl.ucsb.edu. Lead discussion section. Develop course materials including homework and exams.

12/2014 - 03/2015 — Course Instructor, *From Atoms to iPhones*. School for Scientific Thought, Center for Science and Engineering Partnerships, UCSB. Wendy Ibsen, Director, Center for Science and Engineering Partnerships, ibsen@cnsi.ucsb.edu. Create physics demonstrations and

lecture series for high school outreach program.

06/2010 - 08/2013 Undergraduate Researcher. Physics Department, University of Oregon, Eugene, OR. Daniel A. Steck, Principle Investigator, atom optics lab, dan@steck.us. Assemble and troubleshoot ultra-stable laser equipment.

09/2010 - 06/2011 Math and Science Tutor. Math Resource Center, Lane Community College, Eugene, OR. Robert Thompson, MRC Director, 1-541-463-5399. College Reading and Learning Association Tutor Certification, January 2011

PUBLICATIONS

2018 **T. L. Brown-Heft**, A. P. McFadden, J. A. Logan, C. Guillemard, P. Le Févre, F. Bertran, S. Andrieu, C. J. Palmstrøm. "Epitaxial Heusler superlattice Co_2MnAl/Fe_2MnAl with perpendicular magnetic anisotropy and termination-dependent half-metallicity,"Phys. Rev. Materials 2, 034402 (2018).

2018 S. D. Harrington, A. D. Rice, **T. L. Brown-Heft**, B. Bonef, A. Sharan, A. P. McFadden, J. A. Logan, M. Pendharkar, M. M. Feldman, O. Mercan, A. G. Petukhov, A. Janotti, L. Colakerol Arslan, and C. J. Palmstrøm. "Growth, electrical, structural, and magnetic properties of half-Heusler $Co_2Ti_{1-x}Fe_xSb$." Phys. Rev. Materials 2, 014406 (2018).

2017 A. P. McFadden, **T. L. Brown-Heft**, D. Pennachio, N. S. Wilson, J. A. Logan, C. J. Palmstrøm. "Oxygen migration in epitaxial $CoFe/MgO/Co_2MnSi$ magnetic tunnel junctions," J. Appl. Phys. 122, (2017).

2017 A. P. McFadden, N. S. Wilson, **T. L. Brown-Heft**, D. Pennachio, M. Pendharkar, J. A. Logan, C. J. Palmstrøm, "Interface Formation of Epitaxial $MgO/Co_2MnSi(001)$ Structures: Elemental Segregation and Oxygen Migration." J. Magn. Magn. Mater. 444, 383-389 (2017).

2017 J. A. Logan, **T. L. Brown-Heft**, S. D. Harrington, N. S. Wilson, A. P. McFadden, A. D. Rice, M. Pendharkar, and C. J. Palmstrøm, "Growth, structural, and magnetic properties of single-crystal full-Heusler Co_2TiGe thin films," J. Appl. Phys., vol. 121, no. 21, p.

213903, (2017).

2012 E. C. Cook, P. J. Martin, **T. L. Brown-Heft**, J. C. Garman, and D. A. Steck, "High passive-stability diode-laser design for use in atomic-physics experiments," Review of Scientific Instruments, vol. 83, no. 4, (2012).

PRESENTATIONS

01/2018 **T. L. Brown-Heft**, A. P. McFadden, J. A. Logan, C. Guillemard, P. Le Févre, F. Bertran, S. Andrieu, C. J. Palmstrøm, "Surface Termination Layer Dependence in Heusler Superlattices." Contributed talk and poster session presented at Conference on the Physics and Chemistry of Surfaces and Interfaces, 14 - 18 January 2018, Kailua-Kona, HI.

10/2017 **T. L. Brown-Heft**, A. P. McFadden, J. A. Logan, C. Guillemard, P. Le Févre, F. Bertran, S. Andrieu, C. J. Palmstrøm, "High Spin Polarization and Perpendicular Magnetic Anisotropy in Single-Crystal Full-Heusler Co_2MnAl/Fe_2MnAl Superlattice." Contributed talk presented at the American Vacuum Society 64th Symposium, 29 October - 3 November 2017, Tampa, FL.

09/2017 **T. L. Brown-Heft**, A. P. McFadden, J. A. Logan, C. Guillemard, P. Le Févre, F. Bertran, S. Andrieu, C. J. Palmstrøm, "High Spin Polarization and Perpendicular Magnetic Anisotropy in Single Crystal Heusler Superlattice." Contributed paper, talk, and poster session presented at Semiconductor Research Corporation TECHCON, 10 - 12 September 2017, Austin, TX.

01/2017 **T. L. Brown-Heft**, A. P. McFadden, J. A. Logan, C. J. Palmstrøm, "Epitaxial Heusler Superlattices with Perpendicular Magnetization." Contributed talk and poster session presented at: Conference on the Physics and Chemistry of Surfaces and Interfaces, 15 - 19 January 2017, Santa Fe, NM.

03/2016 **T. L. Brown-Heft**, E. Lee, M. Pendharkar, C. J. Palmstrøm, "Lower than predicted interface anisotropy of Fe/MgO(001) can be compensated with a Pt cap." Contributed talk presented at: American Physical Society March Meeting, 14 - 18 March 2016, Baltimore, MD.

01/2016 **T. L. Brown-Heft**, E. Lee, M. Pendharkar, C. J. Palmstrøm. "Influence of Cap Layers on Perpendicular Magnetic Anisotropy of Ultra-thin Fe/MgO(001) Films." Contributed talk and poster session presented at: Conference on the Physics and Chemistry of Surfaces and Interfaces, 17 - 22 January 2016, Palm Springs, CA.

08/2012 **T. L. Brown-Heft**, P. J. Martin., E. C. Cook, D. A. Steck. "Progress Toward a Strontium Magneto-Optical Trap," Scholarships for Oregon Scientists, August 2012. Poster session.

2010 **T. L. Brown-Heft**, P. J. Martin, E. C. Cook, D. A. Steck. "Measurement of the Casimir-Polder Force," Undergraduate catalytic outreach and research experiences, 2010. Poster and presentation.

FELLOWSHIPS

2015 National Science Foundation Graduate Research Fellowship Program, Honorable Mention. Awarded enhanced access to supercomputing resources at a national facility.

09/2011 - 06/2013 Scholarships for Oregon Scientists (SOS). University of Oregon, Christine Butler, Director, 1-541-346-6199. $10k/year scholarship with paid summer undergraduate research provision.

06/2010 - 09/2011 Undergraduate Catalytic Outreach and Research Experiences (UCORE). University of Oregon, Jodi Myers, Director, 1-541-346-4787. Similar to REU. Outreach component during the 2010-11 school year. Returned in a minor leadership capacity during summer 2011.

Abstract

Engineering Magnetic and Topological Properties in Epitaxial Heusler Compounds

by

Tobias Levi Brown-Heft

Commercially viable spintronic devices require magnetic contacts with high electrical conductivity, high spin polarization, low Gilbert damping, and perpendicular magnetic anisotropy. The contact must also be amenable to thin film growth techniques to allow device scalability. Until now, this combination of properties had yet to be obtained in a single material. The exquisite control over crystal growth conditions and elemental composition imparted by molecular beam epitaxy can be leveraged to tune magnetic and electronic material properties closer to the ideal set desired by device researchers.

Ferromagnetic metals composed of elements with low atomic weight are commonly used for spintronics, but the industry standard CoFeB does not possess high spin polarization, and its perpendicular magnetic anisotropy depends on film thickness, limiting its versatility. On the other hand, Heusler compounds are a class of over 1000 ternary intermetallic materials with highly variable magnetic and electronic properties. The Heusler compound Co_2MnSi is well known as a half-metal with 100% spin polarization at the Fermi level, making it an ideal source of spin-polarized current. However, Co_2MnSi does not possess perpendicular magnetic anisotropy.

In this work, the magnetic anisotropy of Heusler compounds is engineered by breaking their cubic crystal symmetry. This can be accomplished by growing tetragonal crystal structures with the unique axis aligned out-of-plane, or by engineering superlattices composed of alternating layers of dissimilar Heusler compounds. In both cases, the resulting perpendicular magnetic anisotropy does not depend on film thickness, making the ma-

terials attractive for a broad range of spintronic device applications. Additionally, the Heusler compound superlattices studied here are composed of Co_2MnAl and Fe_2MnAl, which combine their electronic structures to produce 95% spin polarization as measured by spin-resolved photoemission spectroscopy. This combines two important magnetic properties never before seen in a single material system. The growth, structural, electronic and magnetic properties of the engineered films will be presented.

Finally, Co_2TiGe is explored as a candidate of an exotic class of topological materials known as Weyl semimetals. These systems possess a unique band structure that arises due to broken time-reversal symmetry resulting from the internal magnetization. Electrons with energy and momentum near so-called Weyl points have zero effective mass and a discrete chiral charge, making them analogous to the elusive Weyl fermion. The signatures of Weyl semimetallicity in Co_2TiGe are probed using magnetotransport and synchrotron-based angle-resolved photoemission spectroscopy.

Contents

Chapter 1

Introduction

Dirac revealed spins,

Nearest neighbors interact,

Ferromagnetism.

Magnetic materials have been employed to store information in audio, video, and computer applications for over a century. The ability to easily write and rewrite information onto magnetic materials continues to make them essential building blocks for modern information technology [1]. Each recording application has specific material requirements, and these become more difficult to satisfy as data density increases and the methods used to read and write the data become more exotic. Invented in 1878, published in 1888, and finally constructed in 1898, the telegraphone was first magnetic audio recorder and required nothing more than a spool of fine steel wire as the recording medium [2]. In contrast, magnetic tunnel junctions are spintronic devices that can store a single bit of data in magnetic particles only a few tens of nanometers in diameter [3]. Arrays of magnetic tunnel junctions form magnetic random access memory, which is energy efficient, can be written and read quickly, and stores data for at least years. To improve the properties of magnetic tunnel junctions to the point where they are competitive with established

data storage solutions, the properties of their magnetic constituents must be tuned and optimized [4, 5].

Spintronics is a rapidly developing field of research in which the intrinsic spin of the electron is exploited to perform logic operations or carry signals [1]. The spin degree of freedom is a vector quantity independent of the scalar charge, and for this reason spintronic devices have the potential to outperform traditional charge-based devices both in operational complexity and energy efficiency. Quantum operations on spins can produce much richer output than the traditional zeros and ones of transistor-based logic [6]. Power losses arise from moving charge through an electric potential, but spin-based signals or electronic states topologically protected from scattering can exist without dissipative losses [7]. These qualities make spintronics attractive to the information technology industry. Spintronic devices require a source of spin-polarized electrons on which to operate. Spin polarization is an imbalance in the number of spin up and spin down electrons at the conduction energy, or Fermi level. The most practical method of obtaining spin polarized current is through the use of electrical contacts composed of ferromagnetic metals [8]. Traditionally, elemental ferromagnets or simple alloys such as Fe or CoFe have been used, but these have severe limitations due to their low spin polarization, in-plane magnetization, and low magnetocrystalline anisotropy. More recently, Heusler compounds have become the material of choice for spintronic contacts because of their high degree of tunability of electronic, magnetic, and structural properties [4]. In addition to being a source of spin-polarized electrons, the internal field generated by ferromagnets leads to the breaking of time-reversal symmetry. In certain ferromagnetic Heusler compounds, this can give rise to new topological states of matter that are only just beginning to be explored [9, 10].

1.1 Heusler compounds

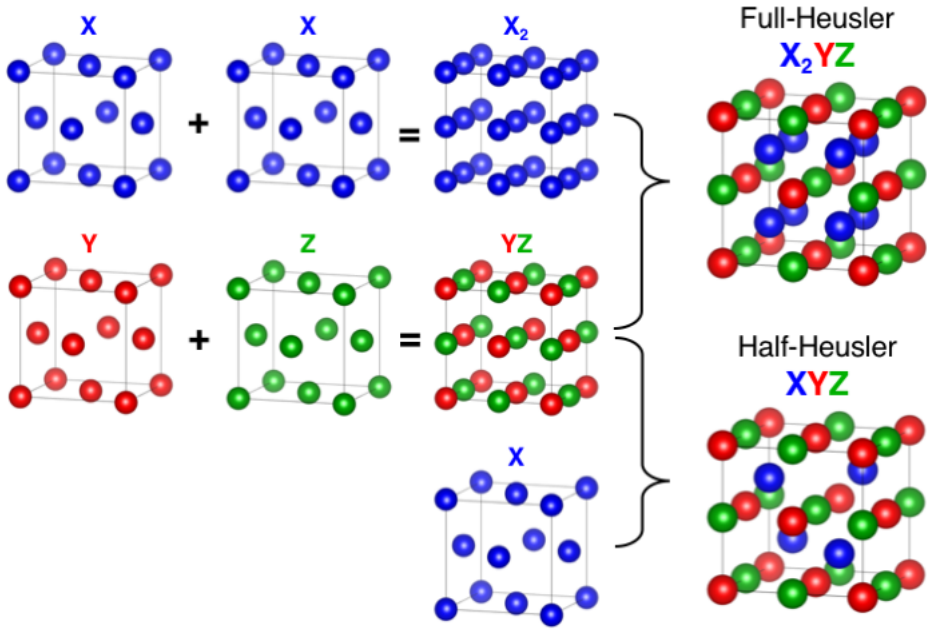

Figure 1.1: The full-Heusler $L2_1$ crystal structure can be thought of as four interpenetrating face-centered cubic crystals. Alternatively, it can be viewed as a combination of a rocksalt YZ structure and simple cubic X_2 structure. The half-Heusler $C1_b$ crystal structure also has a rocksalt YZ sublattice, but only one face-centered cubic X sublattice.

Heusler compounds are a vast family of over 1000 materials [4, 11]. They have cubic crystal symmetry, and appear in two main varieties. First, full-Heuslers have chemical formula X_2YZ and have $L2_1$ crystal structure, where the Y and Z elements form a rocksalt lattice that is stuffed with X atoms in each of the 8 tetrahedral sites, as shown in Fig. 1.1. Second, half-Heusler compounds have chemical formula XYZ and have $C1_b$ crystal structure, where the Y and Z elements form the same rocksalt structure, but only half of the tetrahedral sites are stuffed with a face-centered cubic sublattice of X atoms. X and Y are typically d- or f-block elements and Z is typically an sp element, as shown in Fig. 1.2. Heusler compounds exhibit many different properties depending on the choice of atoms in the formula unit [4]. These properties range from shape-memory

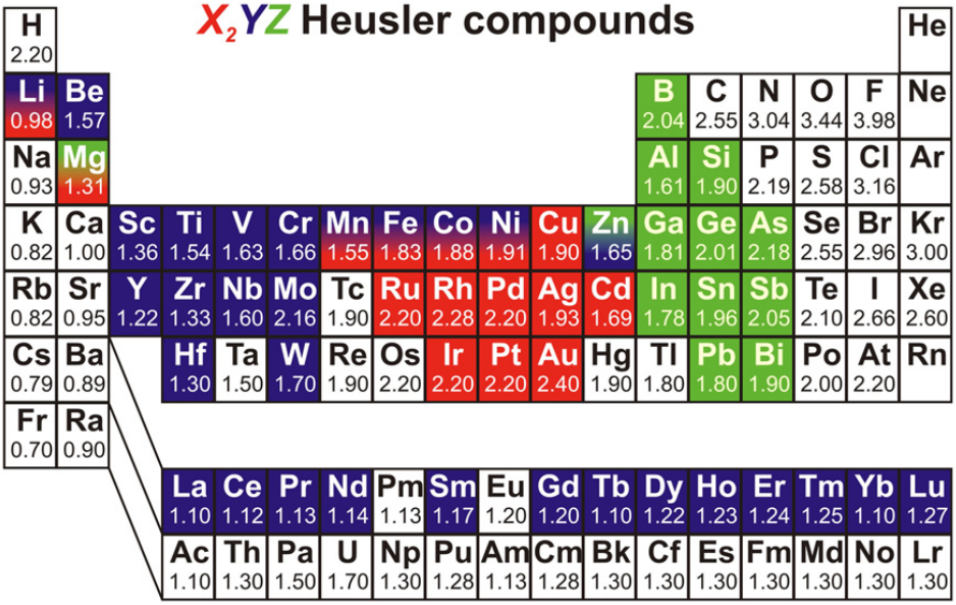

Figure 1.2: Heusler compounds can be formed by combinations of atoms from a significant fraction of the periodic table. Each compound has unique properties, but many have properties in common based on the number of valence electrons in a formula unit. Image reprinted from [4] with permission.

(Ni_2MnGa [12]), thermoelectric (ZrNiSn [13]), metallic (Ni_2TiSn [14]), semiconducting (CoTiSb [15]), ferromagnetic (Fe_2MnAl [16]), half-metallic (Co_2MnSi [17]), ferrimagnetic (Mn_2MnGe [18]), superconducting (Pd_2ZrAl [19]), topologically insulating (PtLuSb [20]), and Weyl semimetallic (Co_2TiGe [21]) varieties. A few of these properties are summarized schematically in Fig. 1.3.

The varied electronic properties of Heusler compounds are interesting, but become quite exciting due to their compatibility with traditional III-V substrates such as GaAs and InP [15]. Heusler varieties composed of lighter elements, such as Co_2MnSi, are well lattice matched to GaAs and can be grown with minimal interfacial reactions, even without the use of diffusion barrier layers [22]. On the other hand, Heusler compounds with slightly larger lattice parameters can be grown on ternary III-V materials with compositions that give nearly perfect lattice match. Even those Heusler compounds that contain elements such as Ti that would readily react with III-V materials can be

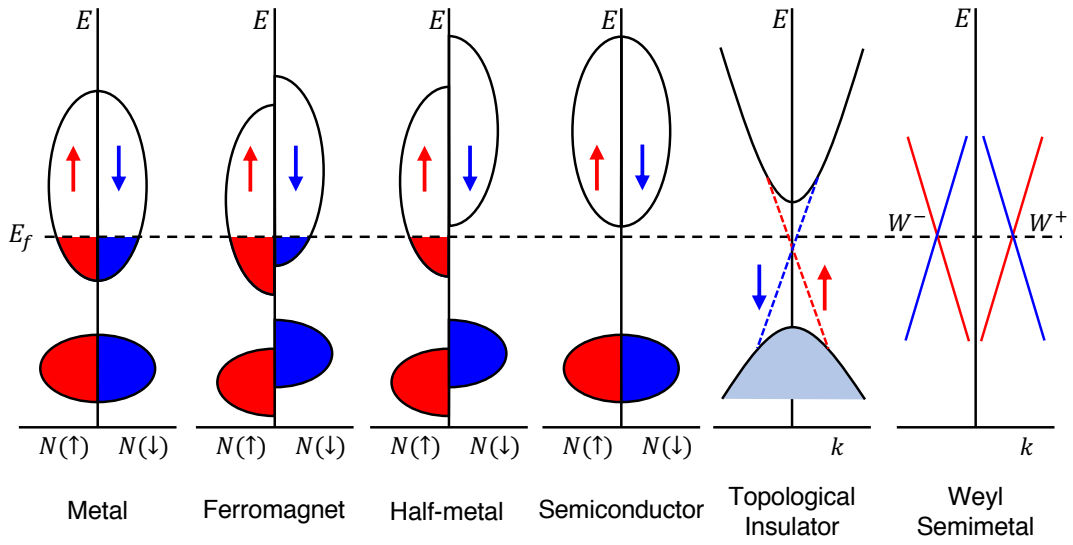

Figure 1.3: Heusler compounds exhibit a wide variety of electronic and magnetic properties depending on their valence electron count and average atomic mass.

stabilized against interface reactions through the use of a rare earth/group V interlayer such as GdAs [21]. This ability to combine Heusler compounds and their multitudinous attributes with traditional semiconductor growth techniques gives them the potential for integration into technologically relevant, scalable device structures, such as those used in sensors, transistors, and data storage media [1, 4]. Finally, Heusler compounds with differing properties have the potential of forming exotic and useful interfaces with one another, while maintaining similar lattice parameter and crystal structure throughout the heterojunction [11].

1.2 Magnetic ordering in condensed matter

Diamagnets are materials that develop a magnetic moment in the opposite direction of an applied field, which causes them to be repelled from the field. In the Bohr model of the atom, this arises from a change in angular momentum of electrons orbiting the nucleus. This would result in an opposing magnetic field generated by the net electron current

induced in each orbit, not unlike that described by Lenz's Law for charge current-derived magnetic fields. The quantum description of diamagnetism gives an identical magnitude of the effect, but is explained by small perturbations of the probability distributions of electron orbitals closer or further from the nucleus, depending on orbital momentum [23]. Thus, all materials exhibit weak diamagnetism, and those with no other magnetic contributions are called diamagnets.

The early semiclassical particle theories failed to account for ferromagnetism because it is a direct result of the intrinsic spin of the electron [23, 24]. Spin was proposed in 1925 by G. Uhlenbeck and S. Goudsmit and subsequently canonized in the Dirac equation in 1928 [25]. Atoms possess a magnetic moment proportional to the number of unpaired spins in their valence electron orbitals, as determined by Hund's rule for relatively light elements. When these elements comprise a solid, the valence orbitals of neighboring atoms overlap with one another to produce bonds. The energy of the bond is modified by the interactions between unpaired spins. In the Heisenberg model, this interaction is called the exchange energy, which can be written in greatly simplified terms as $E_{ex} = -J\boldsymbol{S_1} \cdot \boldsymbol{S_2}$, where $\boldsymbol{S_1}$ and $\boldsymbol{S_2}$ are the net spin vectors of unpaired electrons on the first and second atoms [23]. The exchange constant J can be positive or negative, and its value depends on an enormous number of factors including the energy level and atomic shell in which the electrons reside (s, p, d, f), the crystal structure and specific crystal site of each atom, and corrections due to Einstein's theory of relativity, which increase for elements with large nuclear charge. Determining the value of J requires quantum mechanical simulations that calculate the orbital overlap integral, accounting for spin-orbit coupling [26].

Once J is known for the various atomic pairs in a given material, the behavior of the net unpaired spins on each atom can be approximated as a single magnetic moment that prefers to align parallel or anti-parallel to neighboring atomic moments. Magnetic sys-

tems always try to minimize their energy. For $J < 0$, the net spins of neighboring atoms will align to be anti-parallel such that $\boldsymbol{S_1} \cdot \boldsymbol{S_2} < 0$, minimizing the exchange energy. In other words, a material with negative J for all magnetic bonds will be antiferromagnetic [23]. As a result, the field produced by the spins cancel out and there is no external magnetic field, and the material only seems to have a diamagnetic response in weak magnetic fields. However, the spin texture is still present on a microscopic scale, and strong magnetic fields can induce spin canting effects and spin-flop transitions. On the other hand, materials with bonds that all have $J > 0$ will tend to give $\boldsymbol{S_1} \cdot \boldsymbol{S_2} > 0$ such that the net spins are parallel, giving a ferromagnet which produces an external field and is strongly attracted to an applied field [23]. In addition, the overall magnetization direction of ferromagnets can be switched by applying a reversing magnetic field of sufficient strength. The field required to switch a ferromagnet is known as the coercive field.

Antiferromagnets and ferromagnets possess a magnetic ordering phase transition temperature, below which they exhibit their respective magnetic properties. The transition occurs at the Néel temperature for antiferromagnets, and the Curie temperature for ferromagnets. Above the transition temperatures, most antiferromagnets and ferromagnets become paramagnetic. Paramagnets possess unpaired spins but these are all completely randomized to maximize entropy. An applied field can skew the distribution of spin orientations such that they are weakly attracted by the field, but this induced internal field vanishes entirely when the applied field is removed [23, 24].

Finally, ferrimagnetism results from a combination of ferromagnetic and antiferromagnetic interactions. These materials have two or more magnetic sublattices, but the net magnetic moment of each sublattice is not equal and opposite as it is in antiferromagnets. As a result, ferrimagnets possess a net moment and produce an external field, and their magnetization can be attracted or switched by an applied magnetic field [23]. However, the energy required to simultaneously switch both magnetic sublattices is

fairly large, so ferrimagnets typically have a coercive field that is much higher than that of ferromagnets [27].

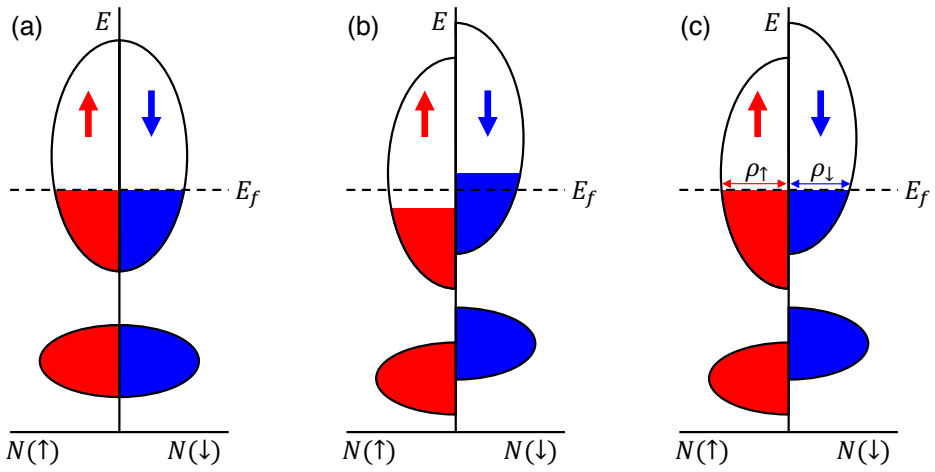

Figure 1.4: Spin-dependent density of states for (a) a normal metal, (b) a metal perturbed by the exchange interaction and (c) an itinerant ferromagnet. The total magnetization can be found by determining the imbalance in the number of spin up and spin down electrons. The density of states for majority and minority spins near the Fermi level are shown as $\rho_\uparrow$ and $\rho_\downarrow$.

Prior to 1903, it was assumed that all ferromagnetic materials contained the ferromagnetic elements Fe, Co, Ni, or Gd. In that year, Friedrich Heusler discovered a Cu_2MnSn alloy that possessed slightly higher magnetization than that of Ni metal. Magnetism in so-called Heusler compounds and other metallic ferromagnets is now understood to arise from itinerant ferromagnetism [28, 29, 30]. In itinerant magnets, the localized moment approximation breaks down because the unpaired electrons are mobile and exist in a dispersive energy band created by the periodic crystal potential. The electronic band structure including magnetic interactions must be calculated from first principles using density functional theory. By incorporating the exchange energy, the spin-dependent density of states of the ferromagnet can be found as shown schematically in Fig. 1.4.

Due to the exchange interaction, the energy of electrons in the minority band increases relative to those in the majority band. The electrons in the minority band can then lose

energy by undergoing a spin flip transition and relaxing into the majority band. The number of electrons that make this transition depends on the energy difference between minority and majority electron bands, and the density of states near the Fermi level. The magnetization of itinerant ferromagnets is then directly proportional to the total majority spin excess determined by integrating the two spin channels of the density of states [30]. Finally, while the overall magnetization in itinerant ferromagnets is produced by delocalized unpaired electrons, it is possible to calculate the average magnetic moment near a particular atomic site. This leads us back to a form of the localized moment approximation, but it is important to remember that the spins that comprise this local moment are, themselves, delocalized [31].

1.3 The Slater-Pauling curve

The ferromagnetic full-Heusler compounds of interest in this work follow an exceedingly simple relationship between the number of valence electrons and the net magnetization of the X_2YZ formula unit. This relationship is known as the Slater-Pauling curve and is given as

$$m = |N_V - 24|, \tag{1.1}$$

where m is the total moment in Bohr magnetons ($\mu_B = 9.274 \times 10^{-21}$ emu), and N_V is the sum of the valence electrons. The Slater-Pauling curve is an extension of Hund's rule [23, 32, 33], taken as the average number of unpaired electrons contributed by each atom,

$$m = |\langle N_V \rangle - 6| = |N_V - 6N_a|, \tag{1.2}$$

where $N_a = 4$ is the number of atoms in an ideal full-Heusler formula unit.

The expected saturation magnetization of a Heusler compound is found by normaliz-

ing m by the volume per formula unit. There are four X_2YZ formula units per unit cell, and a unit cell has volume of a^3. Thus, the saturation magnetization is expected to be

$$M_S = \frac{4m\mu_B}{a^3} \tag{1.3}$$

1.4 Spin polarization

Spintronic devices require a source of spin-polarized electrons on which to operate [1]. The most practical method of obtaining spin polarized current is through the use of ferromagnetic contacts [8]. As discussed above, ferromagnets possess an imbalance in the total number of electrons in the spin up and spin down states. The total spin imbalance is related to the bulk saturation magnetization of the ferromagnet. However, for electronic devices we are concerned almost exclusively with the small group of mobile electrons near the Fermi level. The spin polarization of a material is defined as

$$P = \frac{\rho_\uparrow - \rho_\downarrow}{\rho_\uparrow + \rho_\downarrow}, \tag{1.4}$$

where $\rho_\uparrow$ and $\rho_\downarrow$ are the density of states of majority and minority spins at the Fermi level, respectively, as shown schematically in Fig. 1.4. Electrons conducting through a ferromagnet will adopt the spin polarization of the bulk material, resulting in a spin-polarized current that can be used in magnetic tunnel junctions or injected into a semiconductor for other spintronic applications [34].

Half-metallic Heusler compounds such as Co_2MnSi behave like a metal for the majority spin channel, but an insulator or semiconductor in the minority spin channel [35, 36]. The complete imbalance of the density of states in the vicinity of the Fermi level results in 100% spin polarization, as shown schematically in Fig. 1.3.

1.5 Magnetic anisotropy

The energy of a free electron does not depend on the direction of its spin due to spherical symmetry. However, in a solid the electron energy is modified by its local environment, causing the spin to prefer to lie in one direction or another [23]. This gives rise to magnetic anisotropy, of which there are three types: shape, magnetocrystalline, and interface anisotropy.

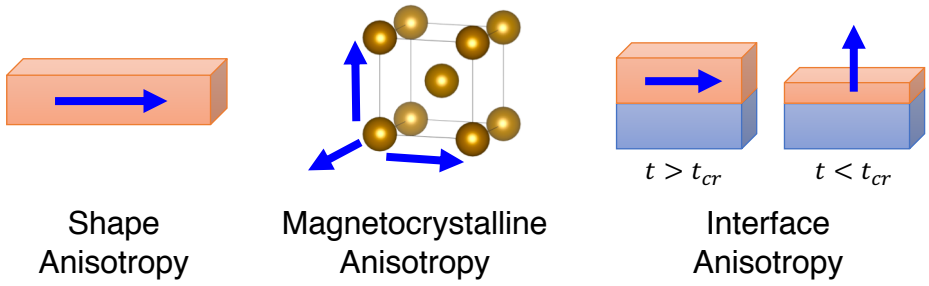

Figure 1.5: Types of magnetic anisotropy. Magnetization (blue arrow) prefers the long axis of a ferromagnet with some shape other than a perfect sphere. Magnetization prefers principle crystallographic directions. Modified magnetocrystalline anisotropy near interfaces can influence magnetization for films thinner than some critical thickness t_{cr}. These anisotropies are all in competition with one another.

Shape anisotropy is a consequence of the dipolar field produced by individual spins and can be considered as a completely classical effect [37]. Dipoles prefer to align themselves in the longest possible chain. A sphere would then have no shape anisotropy. However, an arbitrarily-shaped sample prefers magnetization in the general direction of the longest axis. Thin films have two extended axes and one highly constricted axis in the growth direction. This geometry produces anisotropy that strongly prefers in-plane magnetization by means of the extremely high energy penalty $E_{shape} = 2\pi M_S^2 \cos^2\theta$, where M_S is the magnetization per unit volume and θ is the polar angle between the magnetization direction and surface normal. This and all other magnetic equations in this dissertation are given in *cgs* units.

Magnetocrystalline anisotropy is a consequence of spin-orbit coupling [24]. In a crystal, the unpaired electrons are in orbitals that form bonds with nearest neighbor atoms, creating a lattice. Spin-orbit coupling causes the spins to have a preferred orientation within the orbital. This, in turn, produces a minimum in the electron energy when all the spins in the lattice are aligned with an axis of high crystal symmetry. The directions of minimum and maximum energy are known as magnetic easy and hard axes, respectively. Generally, *ab initio* methods are required to predict the preferred orientation of the spins in a given crystal structure composed of a given set of elements. On the other hand, an educated guess can be made based on trends in simple ferromagnets. For example, body centered cubic Fe prefers magnetizations along the <100> directions, while face centered cubic Ni prefers the <111> directions [23]. Non-cubic crystal structures typically have magnetizations that lie along the unique axis. Hexagonal close packed Co prefers <0001> magnetization, and tetragonal Mn_3Ge prefers <001> magnetization directions (along the c axis where $a = a < c$) [18]. However, these orientations can change depending on the specific compound, and are actually based on the value of anisotropy constants that must either be measured experimentally or calculated with density functional theory. For a spherical ferromagnetic particle with cubic crystal symmetry the total magnetic energy can be written

$$E(\boldsymbol{M}, T) = K_0 + K_1(T)(\alpha_1\alpha_2 + \alpha_2\alpha_3 + \alpha_3\alpha_1) + K_2(T)\alpha_1\alpha_2\alpha_3, \tag{1.5}$$

where $K_i(T)$ are the temperature-dependent anisotropy constants resulting from the series expansion in direction cosines, given as $\alpha_i = \{\cos\phi\sin\theta, \sin\phi\sin\theta, \cos\theta\}$. Here, ϕ and θ are the azimuthal and polar angles of the magnetization vector $\boldsymbol{M}$ with respect to the [100] and [001] directions, respectively. The temperature dependence of the anisotropy constants is related to the orbital angular momentum of electrons contributing

to magnetism [38]. K_1 is the most important anisotropy constant for most cubic ferromagnets, and taking $K_2 = 0$ means that $K_1 > 0$ corresponds to magnetic easy axes along <100>, while $K_1 < 0$ corresponds to easy axes along <111>. Equation (1.5) is valid

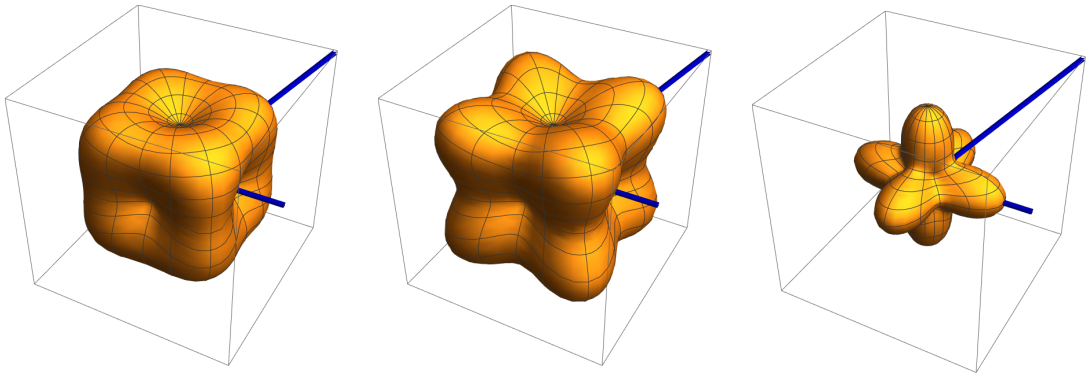

Figure 1.6: Plots of magnetic energy density according to equation (1.5) for the given values of anisotropy constants. The blue lines are along the [100] and [111] directions.

only for cubic crystals; other types of crystal symmetry have different series expansions in direction cosines, though some of these these can be approximated by wrapping them into an effective out-of-plane anisotropy constant as shown in the following section.

The final type of magnetic anisotropy is interface or surface anisotropy, which is a special type of magnetocrystalline anisotropy [39]. Chemical bonding at the interface of two dissimilar materials can result in rehybridization of the orbitals responsible for producing easy axes. For example, the $3d$ orbitals of Fe normally bond with one another along the shortest interatomic distance. This is in the [111] direction for bcc Fe, which results in orbitals with d_{xy}, d_{xz}, d_{yz} hybridization. When the Fe is grown on magnesium oxide (MgO), the d orbitals of Fe at the interface rehybridize to form a bond with the $2p$ orbitals of the rocksalt MgO lattice, which is aligned normal to the interface. This produces orbitals with d_{z^2} and $d_{x^2-y^2}$ character, which have vastly different spin-orbit coupling, and therefore different magnetic easy axes [40]. When the film is sufficiently

thin such that the interface magnetocrystalline anisotropy is the dominant energy term, the whole film can undergo a spin reorientation transition to adopt the easy axis of the interface. In the case of Fe grown on MgO (001), this happens to be in the out-of-plane direction. This is exciting because the anisotropy is strong enough to overcome the significant shape anisotropy, resulting in perpendicular magnetic anisotropy. This is also the method exploited by the industry standard spintronic material CoFeB [41].

1.6 Perpendicular magnetic anisotropy

Magnetic anisotropy plays an important role in the design of spintronic devices. Perpendicular magnetic anisotropy (PMA) is preferred for devices such as magnetic tunnel junctions because the energy barrier between magnetization states can be very high, and this allows enhanced device scalability suitable for magnetic random access memory applications [42]. The energy barrier between magnetization states gives stability against thermal fluctuations that tend to randomly switch the ferromagnet between its easy axes. This barrier is the minimum energy required to rotate the magnetization vector away from its current stable local minimum into any other stable local minimum. Cubic magnetocrystalline anisotropy energy is typically small. For example, Fe has $K_1 = 4.8 \times 10^5$ erg/cm^3 [24]. The energy barrier is given as $E_B = K_{eff}V$, where V is the volume of the magnetic particle and K_{eff} is the anisotropy constant involved in the most energetically favorable coherent domain rotation [43, 42]. For cubic ferromagnets with no other anisotropy contributions, $K_{eff} = K_1$. For an iron particle in a technologically relevant device 20 nm in diameter and 5 nm in thickness, the energy barrier would be $E_B = 7.5 \times 10^{-13}$ erg, while the thermal energy at room temperature is $k_BT = 4.1 \times 10^{-14}$ erg. This provides a thermal energy protection factor of only $E_B/k_BT = 18$. For a magnetic particle to remain stable to thermal fluctuations for 10

years, this barrier factor must be greater than 60 [44, 43, 45]. Thus, scalable spintronic devices require magnets with much higher anisotropy constants. One way to achieve this is by utilizing materials with extremely high PMA, which can be on the order of 10^7 erg/cm^3 [18].

For the purposes of examining PMA, equation (1.5) can be modified by separating the in-plane and out-of-plane anisotropy terms, and adding in the contributions from shape and interface anisotropy. The model is then written

$$E(\boldsymbol{H}, \boldsymbol{M}) \approx K_{eff}^{//}(\phi) \sin^2\theta - K_{eff}^{\perp} \cos^2\theta - \mu_0 \boldsymbol{H} \cdot \boldsymbol{M}, \tag{1.6}$$

where $K_{eff}^{//}(\phi)$ is the effective in-plane anisotropy, $K_{eff}^{\perp}$ is the effective out-of-plane anisotropy, and $\mu_0 \boldsymbol{H}$ is the applied magnetic field. For ferromagnets with four-fold in-plane anisotropy, $K_{eff}^{//}(\phi) = K_1 \sin^2(2\phi)$, which produces in-plane easy axes along [100] for $K_1 > 0$. The $K_{eff}^{\perp}$ term can be broken down into the three main anisotropy types [37, 46]:

$$K_{eff}^{\perp} = K_{MCA}^{\perp} + K_s/t_{film} - 2\pi M_S^2, \tag{1.7}$$

where $K_{MCA}^{\perp}$ is the out-of-plane magnetocrystalline anisotropy, K_i/t_{film} is the interface anisotropy that scales with the thickness of the film, and $2\pi M_S^2$ is the thin film shape anisotropy, again given in *cgs* units. The Zeeman energy term ($\mu_0 \boldsymbol{H} \cdot \boldsymbol{M}$) that appears in the presence of a magnetic field applies a torque on the magnetization vector. Inclusion of the Zeeman term upgrades the simple description of magnetic energy to a Stoner-Wohlfarth model [47, 48], which can be used to simulate the behavior of a single-domain ferromagnet under the influence of an applied field, as shown in Fig. 1.7. For further details about Stoner-Wohlfarth models, please refer to [49] for an accessible resource. Equation (1.6) will be used throughout the following chapters to explain the behavior of

ferromagnetic thin films grown by molecular beam epitaxy. Note that this approximation allows incorporation of tetragonal crystal systems provided the unique axis is aligned out-of-plane, because equation (1.6) is itself tetragonally symmetric about the z axis. These tetragonal contributions are wrapped up into the $K^{\perp}_{MCA}$ term.

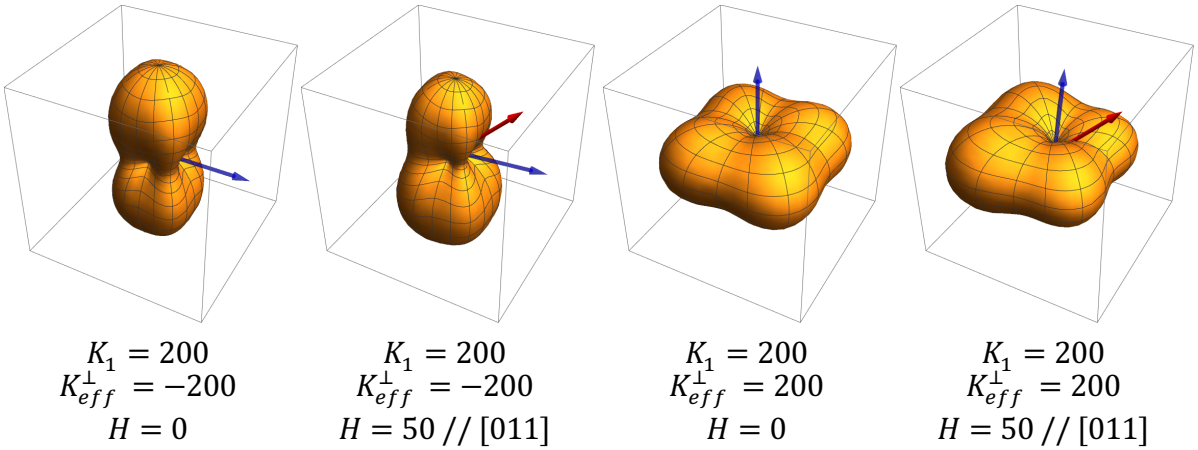

Figure 1.7: Plots of magnetic energy density for the given values of anisotropy constants according to equation (1.6). The blue and red arrows are the magnetization and applied field directions, respectively. Note that the magnetization direction is stable to perturbations in either the in-plane or out-of-plane directions depending on the sign of $K^{\perp}_{eff}$. Although, canted magnetizations can occur when $K^{\perp}_{eff}$ is close to zero.

By taking advantage of the competition of anisotropy terms in $K^{\perp}_{eff}$, we can tune a ferromagnet to be more or less perpendicular through the application of broken symmetry. This can be done by using interfaces with high K_s, tetragonal ferromagnets, and magnetic superlattices. The exploration of these systems dominates the following chapters of this dissertation.

1.7 Magnetic tunnel junctions

Magnetic tunnel junctions (MTJs) are among the simplest of spintronic devices. In an MTJ, an insulating tunnel barrier separates two ferromagnetic layers, as illustrated in

Fig. 1.8. Each ferromagnet has a certain spin polarization (P) and magnetization ($\boldsymbol{M}$) that can change directions under the influence of an applied field ($\boldsymbol{H}$) or other perturbing torque [50]. The tunnel barrier is 1–2 nm thick, which is sufficiently thin that electrons can quantum tunnel from one ferromagnetic layer to the other. This allows a net charge current to flow across the tunnel barrier in response to an applied voltage. When the magnetization vectors of the two ferromagnetic layers are aligned parallel to one another, the electrical resistance across the junction is low. Conversely, when the magnetizations are anti-parallel, the resistance across the junction is high. The dependence on relative magnetization arises because the tunneling conductance across the barrier depends on the number of spin-dependent states that are filled in the cathode, and empty in the anode. When magnetization reverses, so too does the density of states at the Fermi level. The tunneling current in each spin channel can be written as [51, 52]

$$I_{\uparrow} \propto \int_{-\infty}^{+\infty} |M|^2 [f(E - eV) - f(E)] \rho_{1,\uparrow}(E - eV) \rho_{2,\uparrow}(E) dE, \tag{1.8}$$

$$I_{\downarrow} \propto \int_{-\infty}^{+\infty} |M|^2 [f(E - eV) - f(E)] \rho_{1,\downarrow}(E - eV) \rho_{2,\downarrow}(E) dE, \tag{1.9}$$

where $|M|$ is a tunneling matrix element not to be confused with magnetization, E is the electron energy, V is the applied voltage, e is the fundamental charge, and ρ_1 and ρ_2 are the spin-dependent density of states of the first and second ferromagnetic layers. The function f is the Fermi-Dirac distribution

$$f(E) = \frac{1}{1 + \exp[(E - E_F)/k_B T]}, \tag{1.10}$$

where E_F is the Fermi energy, k_B is the Boltzmann constant, and T is the temperature of the MTJ. The total current through the tunnel barrier is simply written as $I_{tot} = I_{\uparrow} + I_{\downarrow}$.

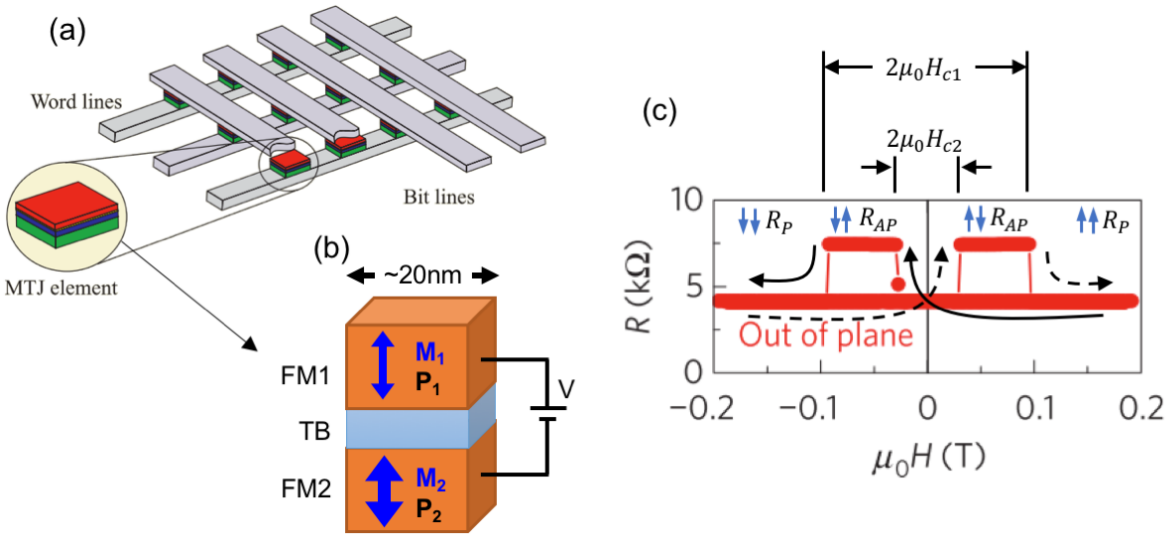

Figure 1.8: (a) Magnetic random access memory in a simple cross-point architecture. (b) Magnetic tunnel junction composed of two ferromagnets (FM1, FM2) and a tunnel barrier layer (TB). Each ferromagnet has its own magnetization ($\boldsymbol{M}$) and spin polarization (P). (c) Resistance of a magnetic tunnel junction vs. out-of-plane field. Forward and backward scans are guided by the dashed and solid black lines, respectively. Anti-parallel alignment of $\boldsymbol{M_1}$ and $\boldsymbol{M_2}$ results in higher resistance, and occurs in field ranges between the two coercive field values $\mu_0 H_{c1}$ and $\mu_0 H_{c2}$. Figure (a) reprinted from [3] under Fair Use (Section 107 of the U.S. Copyright Act), and (c) reprinted with permission from [42].

When the MTJ is in the parallel state, $\rho_{1,\uparrow}$ and $\rho_{2,\uparrow}$ are both large, while $\rho_{1,\downarrow}$ and $\rho_{2,\downarrow}$ are both small. In this case, $I_\downarrow \ll I_\uparrow$, but $I_\uparrow$ is quite large overall, so the total resistance across the device is low. On the other hand, in the anti-parallel MTJ state, $\rho_{1,\uparrow}$ is large but $\rho_{2,\uparrow}$ is small, while $\rho_{1,\downarrow}$ is small and $\rho_{2,\downarrow}$ is large. This configuration gives $I_\uparrow \approx I_\downarrow$, but both of them are quite small, resulting in a high resistance across the device.

Technologically relevant MTJs are designed such that one of the layers has fixed magnetization through the use of a pinning layer [3]. However, in basic MTJ research a pinning layer is often not used, and the two ferromagnetic layers are instead designed to have different coercive fields (H_c) [42]. When an external field is applied, the layer with lower coercive field switches direction first such that the two magnetizations are anti-parallel. This results in a high resistance across the device as shown in Fig. 1.8.

In terms of information storage, the relative magnetization state of the two ferromagnetic layers is the recorded bit, which can be read out by measuring the resistance of the MTJ. The relative difference in resistance between parallel and anti-parallel magnetization states is the figure of merit for these devices, and is called the tunnel magnetoresistance ratio (TMR), given as

$$TMR = \frac{\Delta R}{R} = \frac{R_{AP} - R_P}{R_P}, \tag{1.11}$$

where R_P and R_{AP} are the resistance of the MTJ in the parallel and anti-parallel states.

In a practical device, TMR should be large so that MTJ states can be easily distinguished. One of the major objectives of MTJ research is to maximize TMR by choosing and optimizing ferromagnetic materials with suitable electronic properties. Thus, it is important to understand the origin of TMR in terms of the electronic density of states of their ferromagnetic contacts. In 1975, M. Julliere was able to show that [53]

$$TMR = \frac{2P_1P_2}{1 - P_1P_2}, \tag{1.12}$$

where P_1 and P_2 are the spin polarizations of the two ferromagnetic layers. This can be proven with simple algebra after simplifying equations (1.8) and (1.9) by assuming low temperature, constant density of states in the vicinity of the Fermi level, constant matrix element $|M|$, and that spins are conserved during tunneling. Combining this with the definitions (1.4) and (1.11) results in the Julliere equation (1.12).

Equation (1.12) shows that MTJ contacts with high spin polarization should give high TMR. For this reason a great deal of effort is being invested in the integration of half-metals into MTJs [54, 11, 1]. Half-metals are expected to produce MTJs with extremely high TMR of over 1000% [55]. However, so far, MTJs with half-metallic contacts have not

overtaken those using industry-standard CoFeB contacts, which can have experimental TMR as high as 604% at $300K$ and 1144% at $5K$ [41].

Fundamentally, this is because the tunneling process involves many factors not considered by the Julliere equation. These complicating factors include interface growth technique [56, 17], interface oxidation state [40, 57], interface contamination [58], interface electronic resonance states [59], interface termination layer [60], interface composition [22, 54, 61], and spin-filtering effects in the tunnel barrier [62], just to name a few. For these reasons, care must be taken to properly analyze and understand the growth mechanics, chemistry, and crystal quality at MTJ interfaces.

Magnetic tunnel junctions composed of Ta/CoFeB/MgO/CoFeB/Ta layers are able to out-compete MTJs composed of half-metallic Heusler compounds because of the unique way in which the CoFeB/MgO interface forms. CoFeB films are typically produced by sputtering. The resulting films are amorphous due to the large molar fraction of boron (around 20%), which acts as an interstitial impurity [63]. The amorphous CoFeB is extremely smooth, and allows the formation of perfectly planar CoFeB and MgO tunnel barrier layers. After growth, the entire MTJ structure is annealed to 300–600 °C [41]. Annealing first causes the MgO layer to preferentially crystallize with (001) orientation out-of-plane. Then, boron begins to diffuse into the Ta spacer layers, which act as a sponge for the small boron atoms [64, 65]. The decreasing boron content allows the CoFe to slowly crystallize, using the MgO as a template for nucleation and growth [66], resulting in a perfectly crystalline, abrupt interface with low dislocation density and high chemical purity. The high uniformity of the layers is compatible with industrial-scale development [43].

The Ta/CoFeB/MgO system seems nearly perfect for making MTJs, and is already being used to produce commercially viable magnetic random access memory [67]. MTJs have also been used commercially for over a decade as the magnetic field sensor in hard

disk drive read heads [68]. However, the method used to read and write a bit stored in MTJs is power inefficient, and magnetic random access memory remains prohibitively expensive as a direct replacement for most computer memory applications. A summary of data storage cost efficiency for several consumer-grade memory types is shown in Table 1.1. For these reasons, research continues to study novel magnetic and tunnel barrier materials, as well as energy efficient methods to switch the ferromagnetic layers in MTJs.

Memory Type	Capacity	Cost ($)	Mbit/$
Hard Disk Drive	3 Tbyte	150.80	167000
Solid State Drive	1 Tbyte	374.66	22000
NAND Flash	32 Gbit	43.85	747
Dynamic RAM	8 Gbit	23.72	345
Static RAM	72 Mbit	81.23	0.886
Magnetic RAM	16 Mbit	44.17	0.362

Table 1.1: List of common consumer-grade computer memory types including magnetic hard disks, solid state drives, Flash memory, and several types of random access memory (RAM). The data storage cost efficiency is shown in units of Mbit/$. Data sourced from Mouser Electronics [69].

1.8 Electrical switching of ferromagnetic layers

For research purposes, testing the TMR of MTJs requires only an applied magnetic field to be swept across a single device. This strategy doesn't work when attempting to individually address a single MTJ in an array of billions of them, because an applied field cannot be localized above a single MTJ without a complex and expensive system of moving parts. Instead, solid state solutions are required. The three main techniques being developed to write MTJs are spin transfer torque (STT), spin-orbit torque (SOT), and magnetoelastic switching.

STT is currently the industry standard technique for electrical switching of magneti-

zation [67]. STT requires one of the ferromagnetic layers to be free to change direction, and the other to have magnetization pinned in a determined direction by an antiferromagnetic pinning layer [70]. The two ferromagnets are called the free layer and pinned layer, respectively. When a large voltage is applied across the MTJ, enormous current densities develop in the range of 10^6–10^7 amps/cm^2 [42]. This is so high that spin imbalances develop in the free layer. The pinned layer can be considered to have constant density of spin up and spin down electrons because it has constrained magnetization. As shown in Fig. 1.9, an MTJ in the anti-parallel state can be switched to the parallel state by applying a negative voltage to the pinned layer. This causes spin up electrons tunneling from the pinned layer to overwhelm the spin down electrons in the free layer, causing the net magnetization to rotate toward the parallel state. Conversely, an MTJ in the parallel state can be switched to the anti-parallel state by applying a negative voltage to the free layer. Because the magnetization of the pinned layer is constrained, spin up electrons preferentially tunnel into the pinned layer, leaving behind excess spin down electrons in the free layer. The excess spin down electrons rotate the net magnetization of the free layer toward the anti-parallel state. This is a highly simplified description of the process, and a more rigorous treatment can be found in [71]. Unfortunately, STT dissipates a large amount of power due to the high current densities required. For this reason, research is moving toward alternatives to this technology, such as SOT and magnetoelastic switching.

SOT is a technique that utilizes a heavy transition metal layer such as W or Pt adjacent to the perpendicularly magnetized ferromagnet to be switched. Due to the spin-Hall effect and interfacial Rashba effect, an in-plane charge current in the heavy metal layer produces a spin current in the out-of-plane direction. These spins accumulate at the heavy metal/ferromagnet interface, which applies a torque on the magnetization of the ferromagnet [72, 73]. Since the current transport is in the low-resistance heavy

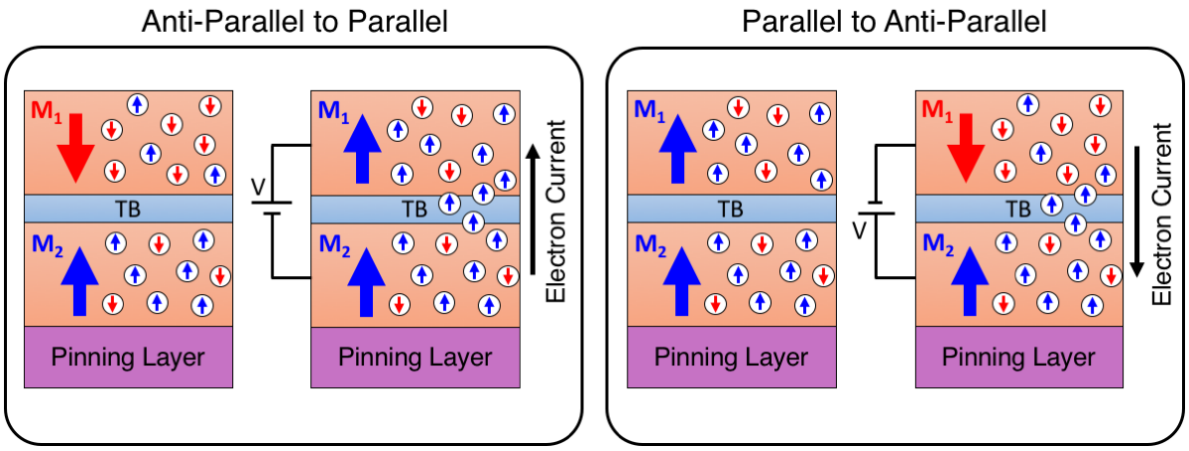

Figure 1.9: Anatomy of spin transfer torque. The free layer (top ferromagnet) changes its magnetization direction in response to spin accumulation due to an imbalance in tunneling current.

metal layer, high dissipative losses are avoided despite the large current densities of $\sim 10^7$ amps/cm^2 [73].

Magnetoresistive switching would require even less power to switch a magnetic layer. The ferromagnetic contact of a magnetic tunnel junction would be grown on a piezoelectric or ferroelectric substrate [74]. When a voltage is applied across the substrate, it expands and contracts due to the piezoelectric effect. This strain is transferred to the ferromagnetic layer, where it triggers a change in the magnetocrystalline anisotropy due to magnetostriction. In this way, the ferromagnetic layer could be switched using only precisely timed voltage pulses applied to a capacitor-like structure [75]. The associated currents would be tiny, and for technologically relevant devices the dissipation would be in the range of several attojoules (10^{-18} J = 6.2 eV) per bit writing operation [76]. For this reason, there is a strong motivation for exploring magnetic materials with strong perpendicular magnetic anisotropy that can be deposited epitaxially on ferroelectric materials such as $BaTiO_3$ and $BiFeO_3$, which will be discussed in Chapter 4.

1.9 Weyl semimetals

Chapter 6 of this dissertation addresses a completely different area of research involving a special type of ferromagnet. Time-reversal symmetry breaking Weyl semimetals are a novel class of topological materials. Their unique band structure produces chiral band crossings known as Weyl nodes. Electrons with energy and momentum near the Weyl nodes exhibit behavior reminiscent of massless, chiral Weyl fermions. The following section, while lengthy, contains important details about the underlying physics, experimental detection, and previous work on Weyl semimetals. This field is quite new, and no high quality reviews exist that give a comprehensive view of the properties of Weyl semimetals, especially the time-reversal symmetry breaking variety of interest here. This information is summarized below to expedite future studies into this exciting class of materials.

1.9.1 Weyl physics and topology in condensed matter

In 1928, Paul Dirac delivered a complete quantum description of electrons and other spin-1/2 particles known as fermions. One year later, Hermann Weyl published his work that attempted to reconcile the effects of gravitation in Dirac's theory [77]. One result of Weyl's work was a quantum description of massless fermions. As a consequence of their lack of mass, Weyl fermions were predicted to have invariant chirality, which is a quantum property distinct from spin [78]. An unconstrained, massive Dirac particle Ψ can be described as a combination of two chiral components $\Psi = \Psi_L + \Psi_R$, where Ψ_L and Ψ_R are the left-hand and right-hand chiral wavefunctions. Chiral projection operators L and R can be defined such that $L\Psi = \Psi_L$ and $R\Psi = \Psi_R$. The two chiralities are orthogonal, as shown by the relation $R\Psi_L = L\Psi_R = 0$. The overall chirality of a Dirac fermion can be measured, in principle, however chirality is not invariant under

Lorentz transformations. That is, the chirality of electrons and other massive fermions depends on reference frame. On the other hand, a massless Weyl fermion has a simplified wavefunction described only by either Ψ_L or Ψ_R, and has conserved chirality, even under Lorentz transformation [78].

Weyl fermions have been sought in high energy physics experiments since their prediction. Neutrinos were initially thought to be Weyl fermions since they have no charge and, for many years, their vanishingly small masses were indistinguishable from zero. Recent measurements indicate that neutrinos do have finite mass [79], ruling them out as Weyl fermions. Particles with zero charge can also be explained with a different subset of Dirac fermions known as Majorana fermions. Majorana particles are their own antiparticle and must have zero charge, but they retain a finite mass term and are therefore a more accurate description of neutrinos [78].

Despite the lack of experimental verification of free Weyl fermions, it has been predicted that electrons in certain condensed matter systems can behave as if they were Weyl fermions, providing an analogue through which to study Weyl physics [80]. Materials exhibiting this type of behavior are known as Weyl semimetals and are an example of a topologically non-trivial three-dimensional (3D) system. The prediction of Weyl semimetals follows other predictions of novel and useful physical phenomena arising from non-trivial topology of electronic band structure, which led to the 2016 Nobel Prize in Physics being awarded to David Thouless, Duncan Haldane and Michael Kosterlitz for their work on topological classifications of matter.

Topology has long been known to have a strong effect in two dimensional (2D) systems, where it gives rise to otherwise physically impossible phase transitions, such as those involved in the fractional quantum Hall effect [81]. Over the last decade there has been an intense search for examples of 3D materials that exhibit topological properties. For example, a topological insulator is a material that is insulating in the bulk, but is

conductive on the surface. This effect arises in materials with a set of electronic bands that are inverted across the energy gap as compared to a normal insulator, usually due to a high degree of spin orbit coupling. At the interface between a topological insulator and a normal insulator or vacuum, the inverted bands must continuously disperse toward the non-inverted band structure. This produces protected surface states that *must* exist due to band topology. These topological surface states (TSS) cannot be destroyed by poor interface quality since they are a consequence of the bulk band topology; defects would merely shift the position of the interface between topologically trivial and non-trivial regions [82]. Furthermore, TSS have exciting properties such as spin-momentum locking and massless transport protected from backscattering, which makes them potentially useful as sources of 100% spin-polarized electrons [83]. This has broad applications in the field of spintronics. There is evidence that TSS provide extremely high spin-orbit torque on ferromagnets adjacent to topological insulators, which could enable fast, energy efficient switching of magnetic tunnel junction free layers [84]. Bi_2Se_3 is currently the prototype for this class of materials because of its relatively large bulk band gap and clear TSS that have been observed in angle-resolved photoemission spectroscopy (ARPES) [85]. The half-Heusler PtLuSb has also recently been shown to possess spin-momentum locked TSS [20].

Weyl semimetals are similar to topological insulators in that the important behavior of electrons arises from non-trivial electronic band topology. However, instead of a bulk band gap with topologically protected 2D surface states, the primary interest in Weyl semimetals lies in the behavior of electrons near Weyl nodes that exist in 3D reciprocal space, within the bulk of the material. Weyl nodes appear in the first Brillouin zone and are produced by accidental degeneracy, or the crossing of two dissimilar electronic bands. Due to crystal symmetry, Weyl nodes always appear in pairs with exactly opposite crystal momentum, as shown in Fig. 1.10. Close to the Weyl node, the bands disperse

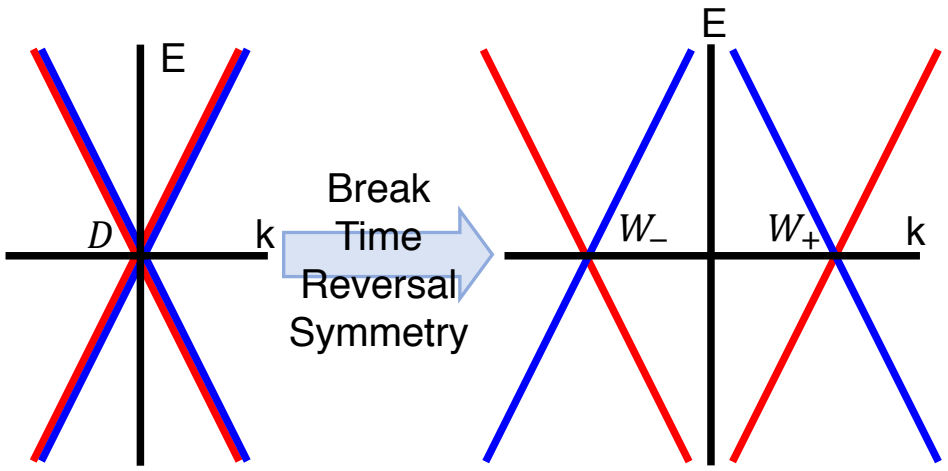

Figure 1.10: Energy dispersion diagrams for (left) Dirac semimetals and (right) Weyl semimetals. Electrons at either D or W points are massless, but those at W points possess chirality (+/−) that can modify conductivity in strong magnetic fields. Dirac points with degenerate bands can be separated into a pair of Weyl nodes upon application of a magnetic field that breaks time-reversal symmetry.

roughly linearly, reminiscent of Dirac points in materials such as graphene [86]. Due to the linearly dispersing bands, electrons with momenta near Weyl nodes have a vanishing effective mass $m^* \approx 0$, and can thus be described by the simplified Weyl equation that governs massless particles. In addition, the dissimilarity of the bands comprising Weyl nodes gives rise to definable chirality that is not present in Dirac points due to band degeneracy. Pairs of Weyl nodes always have opposite chirality, and the only way to destroy this intrinsic topological character is to reduce the k-space separation of the Weyl pair until they are fully degenerate. In fact, Dirac points can be viewed as the product of the annihilation of two Weyl nodes when their separation in reciprocal space tends toward zero. Conversely, Dirac points can be separated into two Weyl nodes by breaking inversion or time-reversal symmetry, for example by applying a strong magnetic field [87].

The intrinsic chirality of Weyl nodes manifests itself as a defect in the Berry curvature of Weyl semimetals. Berry curvature ($\boldsymbol{\Omega_k}$) is a property of crystalline solids that

have either broken inversion symmetry, broken time-reversal symmetry, or both. The effects of Berry curvature are analogous to a magnetic field that acts on electrons in momentum space ($\boldsymbol{k}$), curving any changes in electron momenta according to the cross product $\dot{\boldsymbol{r}} \propto \dot{\boldsymbol{k}} \times \boldsymbol{\Omega_k}$. This can be viewed as the reciprocal-space analogue of the Lorentz force which can be written as $\dot{\boldsymbol{k}} \propto \dot{\boldsymbol{r}} \times \boldsymbol{B}$. Broken symmetry is essential because inversion symmetry implies that $\boldsymbol{\Omega_k} = -\boldsymbol{\Omega_{-k}}$, while time-reversal symmetry implies that $\boldsymbol{\Omega_k} = \boldsymbol{\Omega_{-k}}$. If both types of symmetry are present, then $\boldsymbol{\Omega_k} = -\boldsymbol{\Omega_k}$, and therefore $\boldsymbol{\Omega_k}$ must be zero everywhere [88]. For this reason, Weyl semimetals are separated into two types: inversion symmetry breaking (type I) and time-reversal symmetry breaking (type II). Type II Weyl semimetals break time-reversal symmetry because they are magnetic materials, and therefore manage to fall into the general theme of this thesis.

Berry curvature is normally a non-divergent and well-behaved function. However, singularities appear in the Berry curvature at Weyl nodes. Performing an integral of the Berry curvature flux through a closed surface in reciprocal space will result in an integer,

$$C = \frac{1}{2\pi\hbar} \oint d\boldsymbol{S} \cdot \boldsymbol{\Omega_k} = 0, \pm 1, \pm 2, ... \tag{1.13}$$

Here, C is the chirality of the Weyl node by virtue of the Stokes theorem, also known as the Chern number [89, 88]. A Chern number of zero indicates that a band crossing is topologically trivial, while non-zero Chern number indicates the presence of a topologically non-trivial band crossing known as a Weyl node. Pairs of Weyl nodes have exactly opposite crystal momentum and always have opposite chirality, and in this context this means that they behave either as a source or sink of Berry curvature. Since Berry curvature is analogous to a magnetic field, Weyl nodes can be viewed as magnetic monopoles in reciprocal space as shown in Fig. 1.11.

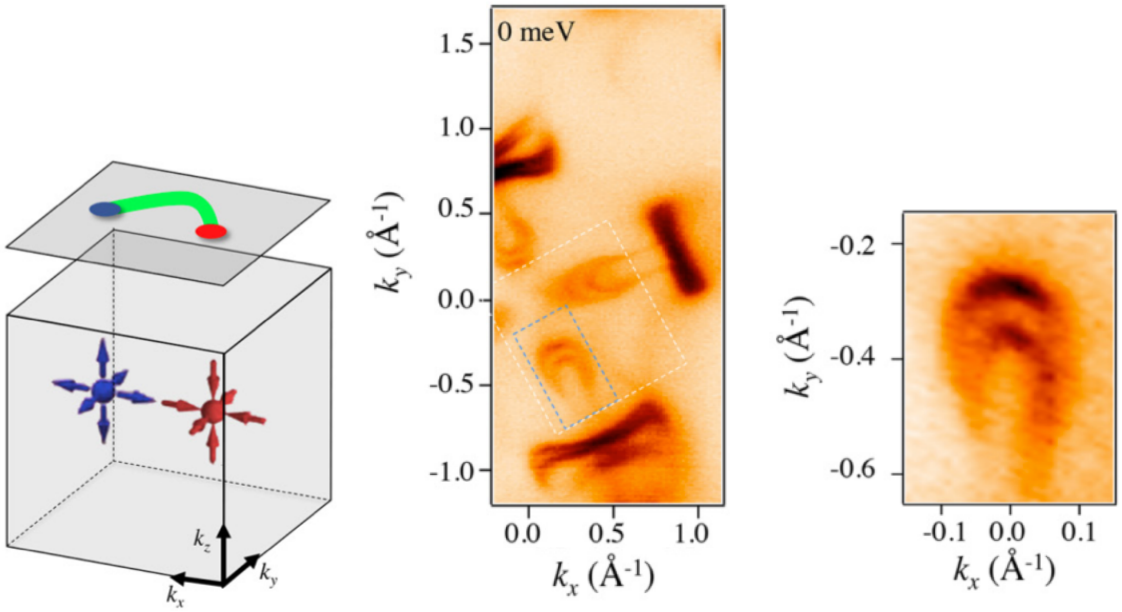

Figure 1.11: (Left) Weyl semimetals possess Weyl nodes that behave like magnetic monopoles in momentum space. The Weyl nodes produce a surface state known as a Fermi arc at the boundary between the Weyl material and a topologically trivial material that are protected by the discrete chirality of the Weyl nodes. (Center) Fermi arcs at the surface of TaAs as measured by ARPES. The arcs terminate at the surface projection of the Weyl nodes. (Right) zoom in of the Fermi arc enclosed by the blue dashed line in the center image. Images reprinted from Ref [90] with permission.

1.9.2 Detection of Weyl Semimetallicty

In addition to being a source/sink of Berry curvature and massless electron transport in the bulk, the topological nature of Weyl nodes also stabilizes and protects gapless TSS on the boundary surface of bulk samples. These manifest as Fermi arcs as seen in ARPES, for example in certain pyrochlore irridates as well as in TaAs [89, 90]. Pairs of Weyl nodes of opposite chirality are connected by a chiral edge state, and the projection of this state into the surface Brillouin zone gives an arc of electron density that terminates at the surface projection of the two Weyl nodes as shown in Fig. 1.11 [89].

In the early theoretical work done on Weyl semimetals it was proposed that a phenomenon known as the Adler-Bell-Jackiw anomaly, or chiral anomaly, would be the *de*

facto signature of the presence of Weyl fermions [88, 91, 92]. The chiral anomaly is a valley charge pumping mechanism that arises from the high Berry curvature near Weyl nodes and manifests as an increase in conductivity when a large magnetic field is applied parallel to the current-generating electric field [87]. When $\boldsymbol{E}//\boldsymbol{B}$, the increase in conductivity referred to as the chiral conductance is given as,

$$\sigma_{zz} = \frac{e^2}{4\pi^2\hbar c}\frac{\upsilon}{c}\frac{(eB\upsilon)^2}{\mu^2}\tau, \tag{1.14}$$

where υ is the Fermi velocity, B is the magnetic field, τ is the intervalley scattering time, and $\mu = E_{Weyl} - E_F$ is the energy difference between the Weyl point and the Fermi level. From an experimental perspective, a few key details stand out of equation (1.14). First, it scales with B^2, a dependency that can be incorporated into fitting models to determine the effective contribution of σ_{zz} [87]. Second, the chiral conductance decreases quickly as the Fermi level moves away from the Weyl point. Intuitively this makes sense because conduction electrons far from the Weyl node will not be significantly affected by the associated discontinuity in Berry curvature. However, this complicates detection of Weyl nodes in materials with significant μ, or in materials with Fermi levels that are not well established, such as those only recently predicted with density functional theory techniques that tend to have large Fermi level errors.

Detecting the chiral anomaly entails measuring the resistance of a Hall bar as a function of applied field in a longitudinal geometry where the applied magnetic and electric fields are parallel, $\mathbf{B}//\mathbf{E}$, or, equivalently, $\mathbf{H}//\mathbf{I}$. The chiral anomaly should then appear as a increase in conductivity (decrease in resistance) at high fields. Magnetoresistance is defined as $\mathrm{MR} = (V_{xxH} - V_{xx0})/V_{xx0}$, so a decrease in resistance at high field as compared to that at zero field gives a negative value of MR. This so-called negative longitudinal magnetoresistance (NLMR) has been measured in several proposed inversion symmetry

breaking Weyl semimetal systems, most notably in TaAs [93].

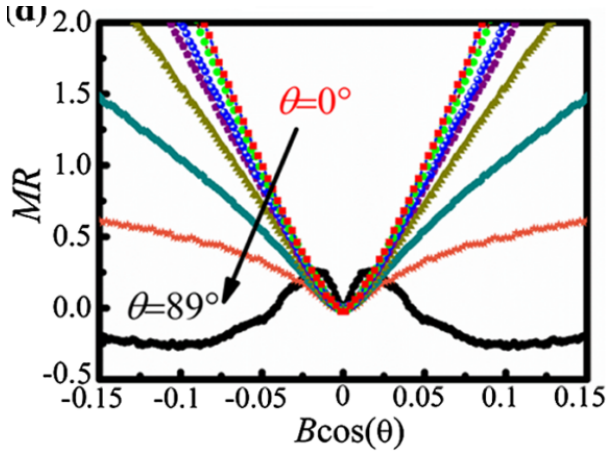

Figure 1.12: Negative longitudinal magnetoresistance of -30% in TaAs is argued to arise from the chiral anomaly when $E//B$. Image reprinted from Ref [93] under the Creative Commons Attribution 3.0 License.

However, more recently there has been skepticism that the NLMR is a valid metric for detecting the chiral anomaly. NLMR can also be produced through a process known as current jetting, where the resistance of a material with sufficient electron mobility becomes highly anisotropic in large fields due to the orbital effect [94]. This results in an inhomogeneous current distribution within the sample, which can give a false reading of negative MR. Compensated semimetals are known to have the highest degree of current jetting, and many of these compounds such as TaAs, NbAs, TaP, and NbP are being studied intensely as potential Weyl semimetals. Indeed, TaP has been shown to exhibit NLMR even when it behaves as a normal semimetal. While TaP does have Weyl nodes, the chirality is not well defined for samples that have a Fermi level sufficiently lower than the node energy. This low Fermi energy results in nodes of opposite chirality contained within a single Fermi surface, which is expected to eliminate the chiral conductance [95]. Instead, the NLMR was found to depend on the sample geometry, leading Arnold *et al.* to conclude that current jetting, and not the chiral anomaly, was responsible. Despite all this, NLMR remains an important, albeit not incontrovertible, piece of evidence in the

search for Weyl semimetallicity in new material systems.

So far, most work on Weyl semimetals has focused on inversion symmetry breaking (type I) varieties such as TaAs. The ease with which these can be synthesized as large, nearly perfect single crystals lends itself to techniques such as magnetic torque [95], de Haas-van Alphen [95], Shubnikov-de Haas [95, 93, 86], and ARPES measurements [90, 96, 97, 98, 86]. These techniques all compliment one another to build up a picture of what the band structure and Fermi surface looks like, how electrons move through the sample in response to electric and magnetic fields, and what surface states appear at the interface between the the sample and vacuum. Unfortunately, the number of Weyl nodes in inversion symmetry breaking Weyl semimetals is large due the very lack of symmetry that produces them. For example, TaAs has 12 pairs of Weyl nodes enclosed in "banana-shaped" Fermi surfaces due to its $I4_1md$ space group symmetry, which greatly complicates transport measurements [93]. On the other hand, time-reversal symmetry breaking (type II) Weyl semimetals have an axis of rotational symmetry about the magnetization direction, which, in several cases, collapses the number of Weyl nodes down to a single pair at a given binding energy, potentially providing an ideal system in which to study Weyl physics [97, 9, 10]. This should simplify the analysis of magnetotransport and ARPES measurements, and is one of the main motivations for seeking new systems exhibiting this second type of symmetry breaking.

1.10 Overview of this Dissertation

This dissertation outlines efforts to develop novel, physically interesting and technologically useful ferromagnetic properties in a range of metallic material systems. It provides the background knowledge to understand the physics of these properties on both atomic and macroscopic scales, and discusses how to harness these principles to

engineer magnetic materials with desired properties. It also documents the engineering challenges commonly encountered in the growth, fabrication, and characterization of metallic ferromagnets, and provides some solutions to these issues.

Chapter 2 discusses the capabilities and infrastructure involved in molecular beam epitaxy. The tools and techniques utilized to calibrate the growths and characterize the resulting samples are also detailed.

Chapter 3 discusses the growth and characterization of ultra-thin layers of Fe deposited on MgO (001) substrates. This is a relatively simple system and provides a stepping stone for understanding the more exotic magnetic materials in the following chapters.

Chapter 4 discusses the hard ferrimagnet Mn_3Ge, which can be used to achieve perpendicular magnetic anisotropy when an appropriate substrate is used to pin the unique axis of the tetragonal $D0_{22}$ crystal structure out-of-plane. This material could be used as a pinning layer for softer magnetic materials.

Chapter 5 discusses highly engineered Heusler compound superlattices composed of alternating layers of Co_2MnAl and Fe_2MnAl. These superlattices exhibit both perpendicular magnetic anisotropy and half-metallicity, although so far these properties are individually optimized under different conditions.

Chapter 6 discusses the proposed time-reversal symmetry breaking Weyl semimetal Co_2TiGe. The stoichiometric material is probed for the signatures of exotic Weyl fermion-like electronic conduction and topological surface states, however none are found due to the large separation between the Fermi energy and Weyl points. The possibility of tuning the Fermi energy closer to the Weyl points using a $Co_{2-x}Ni_xTiGe$ alloy is then explored.

Chapter 7 summarizes the dissertation and proposes future work to optimize the properties of the developed materials, and combine them into device structures.

1.11 Permissions and Attributions

The content of Chapter 3 is the result of a collaboration with Mihir Pendharkar[1] and Elizabeth Lee[2].

The content of Chapter 4 is the result of a collaboration with Anthony P. McFadden[1], Amanda Andreasson[3], Nikita Gaur[4], and Ramamoorthy Ramesh[4].

The content of Chapter 5 is the result of a collaboration with John A. Logan[5], Anthony P. McFadden[1], Charles Guillemard[6,7], Patrick Le Fèvre[7], François Bertran[7], and Stéphane Andrieu[6], and has previously appeared in Physical Review Materials [16]. It is reproduced here with permission from the American Physical Society.

The content of Chapter 6 is the result of a collaboration with John A. Logan[5], Sean Harrington[5], Shouvik Chatterjee[1], Yu Hao Chang[5], Hadass Inbar[5], and Elliot Young[5].

Affiliations

1. Department of Electrical and Computer Engineering, University of California, Santa Barbara, California, USA
2. Engineering Department, Harvey Mudd College, Claremont, California, USA
3. Department of Physics, Lund University, Lund, Sweden
4. Department of Materials Science and Engineering, University of California, Berkeley, California, USA
5. Materials Department, University of California, Santa Barbara, California, USA
6. Institut Jean-Lamour, UMR 7198, CNRS, Université Lorraine, Nancy, France
7. Synchrotron SOLEIL, L'Orme des Merisiers, Saint-Aubin, BP 48, F-91192 Gif sur Yvette, France

Chapter 2

Growth and Characterization Techniques

2.1 Interconnected ultra-high vacuum growth and characterization system

The ferromagnetic samples studied in this dissertation were prepared using molecular beam epitaxy (MBE) facilities at the University of California Santa Barbara in the Chris Palmstrøm Lab. The lab consists of numerous ultra-high vacuum (UHV) interconnected growth and characterization modules, as shown in Fig. 2.1. These facilities include six MBE chambers, several independent electron beam (e-beam) evaporators and effusion cell stations for metal and oxide deposition, X-ray photoemission spectroscopy (XPS), magneto-optic Kerr effect (MOKE) magnetometry, and scanning tunneling microscopy. Combined, the available tools allow the growth of complex materials and layered structures, and allows the surface, electronic, and chemical characterization of pristine films. Reactive species in the atmosphere, namely water and oxygen, rapidly degrade the sur-

face quality of films. Maintaining UHV conditions in all the sample transfer chambers allows transfer and analysis of pristine films, without introducing the degrading effects of air.

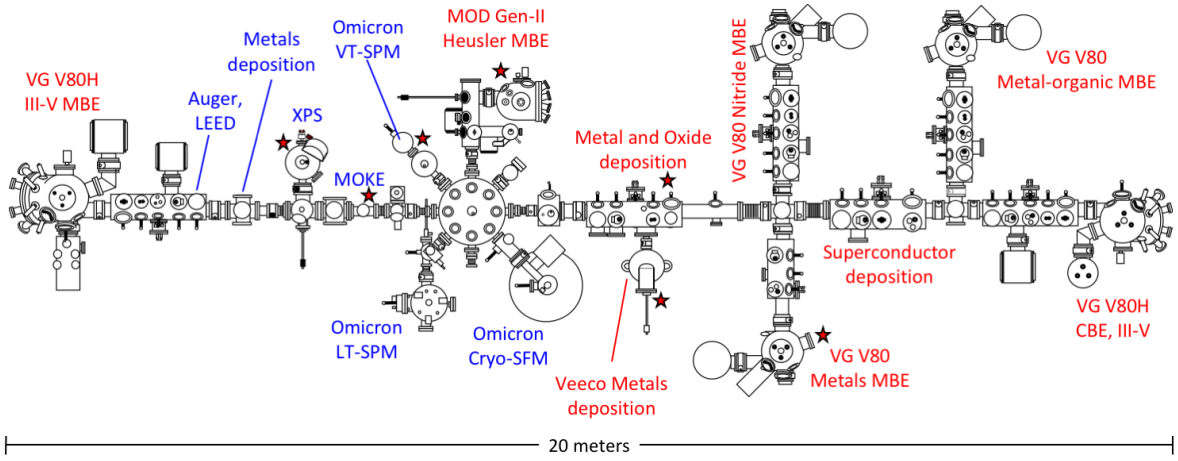

Figure 2.1: Ultra-high vacuum interconnected molecular beam epitaxy and surfaces characterization suite in the Chris Palmstrøm Lab at University of California Santa Barbara.

Each module has unique capabilities and limitations, some of which will be described below. The focus on ferromagnetic materials in this work has, thankfully, limited the number of chambers and techniques required for the studies outlined in the following chapters. Of the systems shown in the figure above, this work primarily utilized the systems labeled with a red star.

2.2 Molecular beam epitaxy

MBE is a technique that provides exquisite control of crystal growth conditions. It is used to produce uniform thin films with high crystal quality and chemical purity. These individual films can be layered on top of one another to produce abrupt interfaces, forming heterostructures that perform specific electronic tasks. Epitaxy is a growth regime where single-crystal substrates are used as a template for the growth of single-crystal thin films.

To achieve conditions favorable for epitaxy, MBE utilizes UHV conditions, feedback-controlled substrate temperature, effusion cells containing high-purity elemental source material, and low growth rates.

UHV refers to pressures lower than 10^{-9} Torr, though MBE strives to achieve chamber base pressures in the 10^{-11} Torr range. The mean free path of a gas molecule in UHV conditions ranges from a few to several tens of kilometers. Since the MBE chamber itself is on the order of a meter in length, gas species can be considered ballistic and non-interacting. To reach these pressures, an MBE growth chamber is first pumped out using an oil-free roughing pump such as a scroll or diaphragm pump, which can reach pressures of 10^{-3} Torr. Once a pressure of lower than 10^{-2} Torr is obtained, a turbopump can be activated and used to reach pressures as low as 10^{-9} Torr. Ion pumps can be activated safely at 10^{-7} Torr, while cryo-pumps can be activated at slightly higher pressures, and can both reach extremely low pressures. Titanium sublimation pumps can be activated at fairly high pressures, but the thin layer of Ti will quickly react, whereas at lower pressures the Ti will continue to getter reactive species for a long time. Finally, to achieve the lowest pressures possible, a cryoshield filled with liquid nitrogen is used to adsorb any residual gases with boiling point higher than 77 K, such as water and hydrocarbons. The cryoshield also serves to maintain the chamber walls at a low temperature to prevent outgassing.

The total pressure of an MBE chamber is the sum of the partial pressures of individual gas species. Of these species, the primary cause for concern is the presence of water and oxygen molecules. Water adsorbs to the chamber walls and must be removed by baking the chamber from 150–200 °C for several days while actively pumping. Any remaining oxygen is usually a sign of a leak in one of the chamber seals, so after the bake the chamber should be checked for any minute leaks using a residual gas analyzer to detect He gas sprayed at the seals between chamber components. Any residual water, oxygen,

and other reactive species are removed readily by ion pumps and titanium sublimation pumps. Low partial pressure of reactive species is essential for MBE to maintain the desired crystal structure and chemical purity of thin films.

The substrate temperature is maintained using a proportional-integral-differential (PID) feedback controller. The controller reads the temperature of a thermocouple mounted near the substrate and applies current to a resistive heater to correct for any deviations from the setpoint. It is important to note that the thermocouple, heater, and substrate are thermally coupled to one another only by infrared radiation. UHV does not allow efficient heat transfer via convection, and thermal conduction is usually small due to the geometry of the sample manipulator. Since the thermocouple is not in direct contact with the substrate, the true substrate temperature is not the value measured by the thermocouple. Temperature deviations are commonly 50–100 °Cor more depending on the placement of thermocouple and the emissivity of the sample block and manipulator. Deviations worsen as temperature increases. Despite this, the true temperature of the substrate is consistent and stable, and generally tracks with the thermocouple value. The deviation can be corrected somewhat by observing phase transitions that are known to occur at specific temperatures. A common calibration point is to use the desorption of an arsenic capping layer from a surface, which occurs at 350 °C. Additionally, a pyrometer can be used for substrates with well-established infrared emissivity values.

MBE utilizes effusion cells with crucibles containing high-purity source material, which are each heated and stabilized with a PID temperature controller similar to that used for the substrate heater. The crucible is typically made of pyrolytic boron nitride, beryllium oxide, tantalum, or some other chemically inert, refractory material. The source material typically has purity of 4N (four nines pure, or 99.99% pure) or 5N for transition metals, but can be 7N or higher for materials like Ga and As used in III-V semiconductor growth. The effusion cell heats the source material until the vapor pressure

above the material is significant, usually in the range of 10^{-7}–10^{-6} Torr. The evaporated material effuses from the crucible and travels ballistically through UHV in a molecular beam with a certain atomic flux, usually in the range of $10^{14} - 10^{15}$ atoms/cm^{2}min.

When the molecular beam reaches the substrate, the atoms adsorb to the surface and become adatoms. These adatoms have some surface diffusion constant that allows them to be fairly mobile. They diffuse across the surface until they encounter the lowest energy position, and are then incorporated into the growing epitaxial crystal. The low vapor pressure of the effused material gives a low growth rate of $1 - 2$ Å/min for the epitaxial thin films considered here, providing plenty of time for the adatoms to incorporate. The drawback of low growth rates is the influence of contamination via the background pressure of the growth chamber. Exposed surfaces are constantly bombarded with residual gases such as H_2 and N_2, and most of these are harmless. However, water or oxygen molecules will readily react with the desirable adatoms. A useful unit to remember is the Langmuir (L), which is a unit of dose that produces 1 monoatomic layer of material, and has the conversion factor $1L = 10^{-6}$ Torr $\cdot$ s. In other words, if the partial pressure of oxygen is 10^{-8} Torr, the surface will be fully covered in oxygen in 100 seconds. The Langmuir is a rough approximation based on kinetic particle theory and the ideal gas law, and a more accurate surface dose can be determined by going back to a more general mathematical treatment. The flux of a given ambient gas species is given by [99]

$$J_N = P\sqrt{\frac{1}{2\pi k_B T m}}, \tag{2.1}$$

where P is the partial pressure of the molecular species, k_B is the Boltzmann constant, T is the ambient temperature, and m is the mass of the molecular species. For $T = 300K$,

pressure in units of Torr, and mass in units of amu, the flux of a given species is

$$J_N = 1.216 \times 10^{23} \frac{P/torr}{\sqrt{M/amu}} \frac{1}{\text{cm}^2 \text{ min}}, \tag{2.2}$$

In MBE, although the partial pressures of oxygen and water should each be less than 10^{-12} Torr, a low growth rate of 1 Å/min would thus allow incorporation of a significant amount of contamination, around $10^{17} - 10^{18}/\text{cm}^3$, assuming a contaminant sticking coefficient equal to one.

When an adatom is deposited on the substrate surface, it has some probability of either adhering or desorbing. This probability is known as the sticking coefficient. Some elements, such as As and Sb, have a sticking coefficient much less than one, depending on substrate temperature, which can be used to create a growth window. A growth window is a range of parameter space where nearly perfect epitaxy is maintained despite large deviations from ideal conditions in several parameters. For example, stoichiometric GaAs is grown by setting the As flux as much as 50 times higher than that of Ga, while the substrate temperature is elevated to reduce the As sticking coefficient. Arsenic that is bonded to Ga will not desorb, while free As adatoms desorb readily. In this way, Ga becomes the limiting reagent and a perfect stoichiometric crystal is grown. Unfortunately, for the materials studied in this dissertation, the sticking coefficient can be considered to be equal to unity. Transition metals nearly always stick and react with whatever is present on a surface, so no self-limiting growth window exists. Instead, the fluxes of each effusion cell must be painstakingly and precisely calibrated, and set to temperatures that produce a stoichiometric flux.

2.2.1 Calibration of atomic flux in MBE

The vapor pressure of an effusion cell follows an Arrhennius relationship, reflecting the thermally activated nature of evaporation, which is given as

$$\Phi(T) = \Phi_0 \exp(-E_a/k_B T), \tag{2.3}$$

where $\Phi(T)$ is the atomic flux at the substrate position in units of atoms/cm^{2}min, Φ_0 is a geometric constant that accounts for the effusion cell placement relative to the sample, E_a is the thermal activation barrier for an evaporating atom of a given species, and $k_B T$ is the thermal energy available within the effusion cell.

Calibration of effusion cells can be aided with the use of a retractable ionization gauge placed in the path of the molecular beam. Referred to as flux gauges in this application, they detect the beam-equivalent pressure of the effusion cell flux. Ionization gauges have a filament that is heated by applying a current. The hot filament boils off electrons in UHV, and these are accelerated toward a metallic, cylindrical grid held at +160 V. Most of the electrons pass through the grid and bombard and ionize any gas atoms present within the cylinder. The positively charged atoms are then attracted to a collector wire held at -24 V. The collector current responds to incident atomic flux in an approximately linear fashion given by

$$I_C = \alpha \Phi(T) + \beta, \tag{2.4}$$

where I_C is the collector current, and α and β are fitting parameters unique to each molecule. These fitting parameters also include geometric factors such as the distance and angular placement of the effusion cell. Calibration of both the effusion cell temperature and flux gauge collector current is essential to maintain control over the stoichiometry of samples. This calibration is done by growing a series of samples, each with a different

effusion cell temperature. The cell temperature and flux gauge reading are recorded, along with the total growth time for the calibration sample. The samples are then sent to the Ion Beam Analysis of Materials facility in the Eyring Materials Center at Arizona State University, where Rutherford backscattering spectrometry (RBS) measurements are performed. RBS is able to measure the total areal atomic density of a thin film in units of atoms/cm^2, and is also able to separate multiple elements deposited on a single sample into individual elemental peaks. The area under an elemental peak is proportional to the areal density of that species on the sample surface. Once the areal density of the elements are quantified, the true flux on the sample can be found by dividing the RBS-derived atomic density by the growth time. The natural logarithm of the flux is then plotted against 1/T to obtain the fit to the modified Arrhennius equation

$$\ln(\Phi(T)) = A + B/T, \tag{2.5}$$

where A and B are fit parameters determined by linear regression to the true flux measured using RBS. The flux gauge fit parameters α and β are determined using a direct linear fit of Φ vs. I_C, as shown in Fig. 2.2.

For a description of best practices for fitting RBS peaks in the Genplot RUMP software, see Appendix C. Once the fit parameters are known, the effusion cell temperatures can be set to an arbitrary temperature to obtain an approximate flux corresponding to the best fit to the Arrhennius equation. However, geometric factors in an MBE chamber change slowly over time. The primary reasons for this are changes in the shape of the source charge in the effusion cell crucible, and material building up on the lip of the crucible. These geometric changes are reflected in the Arrhennius calibration term A, but the temperature-dependent term B is usually found to change very little between independent calibrations. The use of a properly calibrated flux gauge allows real-time

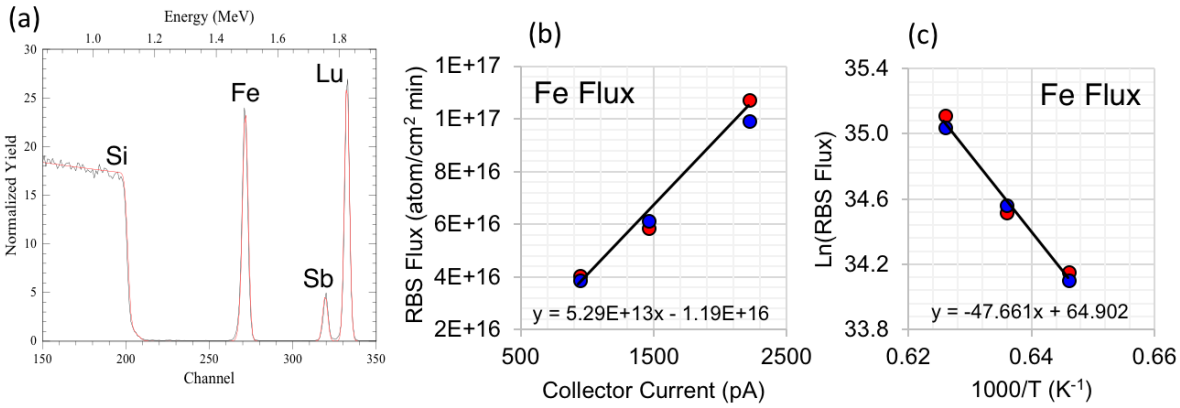

Figure 2.2: (a) Raw RBS data for an Sb/Lu/Fe/Si (001) sample. The total areal atomic density of each element is proportional to the area under the corresponding peaks. (b) Flux determined from RBS vs. flux gauge collector current, with fitting parameters α and β. (c) RBS flux shown on an Arrhennius plot, with fitting parameters A and B. The red and blue circles are data taken at $\theta = 8°$ and $\theta = 60°$, respectively.

correction of these geometric variations that frequently occur between growth runs. Often this correction is performed iteratively by adjusting the cell temperature by a small amount, and measuring the flux again. This can be a time-consuming process, especially for the ternary and quaternary Heusler compounds studied here.

The efficiency of the effusion cell correction and stabilization process can be increased dramatically by combining the two RBS calibration methods into a single correction term. The following procedure assumes that the flux gauge measures the effusion cell flux accurately and precisely. We begin by noting that, given perfect calibration data, we could combine equations (2.4) and (2.5) to give

$$\frac{I_C - \beta}{\alpha} = \Phi(T) \approx \exp(A + B/T). \tag{2.6}$$

Of course, this is not strictly true, but it is very close and requires only a small correction.

To determine this correction, first rewrite the right-hand side of equation (2.6):

$$\Phi(T) = \exp(A + B/T) \tag{2.7}$$

Then, take the first-order series expansion centered on the initial cell temperature T_i:

$$\Phi_1(T_f) = \Phi(T_i)\left[1 - \frac{B}{T_i^2}(T_f - T_i)\right] \tag{2.8}$$

Here, $\Phi_1(T_f)$ is the first-order approximation of the flux at T_f, based on the slope of the Arrhennius equation at T_i, as shown in Fig. 2.3. Note that the geometric calibration factor A does not appear explicitly in the expansion. This equation can be used to find the required change in cell temperature based on the target flux (Φ_f) desired by the MBE operator and the present flux (Φ_i) measured by the flux gauge. Substituting the initial and final flux gauge readings into the first-order equation above gives

$$\Phi_f = \Phi_i\left[1 - \frac{B}{T_i^2}(T_f - T_i)\right] \tag{2.9}$$

The present flux Φ_i is known from the flux gauge, T_i is the temperature value of the thermocouple for which flux was measured, the target flux value is determined by the MBE operator, and B is known from RBS calibrations. Therefore, T_f is the cell temperature that should give the target flux Φ_f. Solving for T_f gives

$$T_f = \frac{T_i^2}{B}\left(1 - \frac{\Phi_f}{\Phi_i}\right) + T_i, \tag{2.10}$$

which is the first-order correction to the effusion cell temperature based on the flux gauge reading and the known slope of the Arrhennius relationship for the element in question. Application of this correction rapidly approaches the desired flux within a

cycle or two. Alternatively, a second order expansion of equation (2.7) can be used, which typically gives the correct effusion cell temperature immediately, even for large temperature corrections. The second-order Arrhennius expansion is

$$\Phi_2(T_f) = \Phi_f = \Phi_i\left[1 - \frac{B}{T_i^2}(T_f - T_i) + \frac{B(B+2T_i)}{2T_i^4}(T_f - T_i)^2\right] \tag{2.11}$$

Solving this for the target temperature T_f gives

$$T_f = \frac{T_i}{B(B+2T_i)}\left[B^2 + 3BT_i + T_i\sqrt{-\frac{B}{\Phi_i}}\sqrt{B(\Phi_i - 2\Phi_f) + 4T_i(\Phi_i - \Phi_f)}\right] \tag{2.12}$$

which is the second-order correction to the effusion cell temperature based on the current flux gauge reading and the slope of the Arrhennius equation. The accuracy of this result can be inferred by looking at how closely $\Phi_2(T)$ follows $\Phi(T)$ over a wide temperature range in Fig. 2.3.

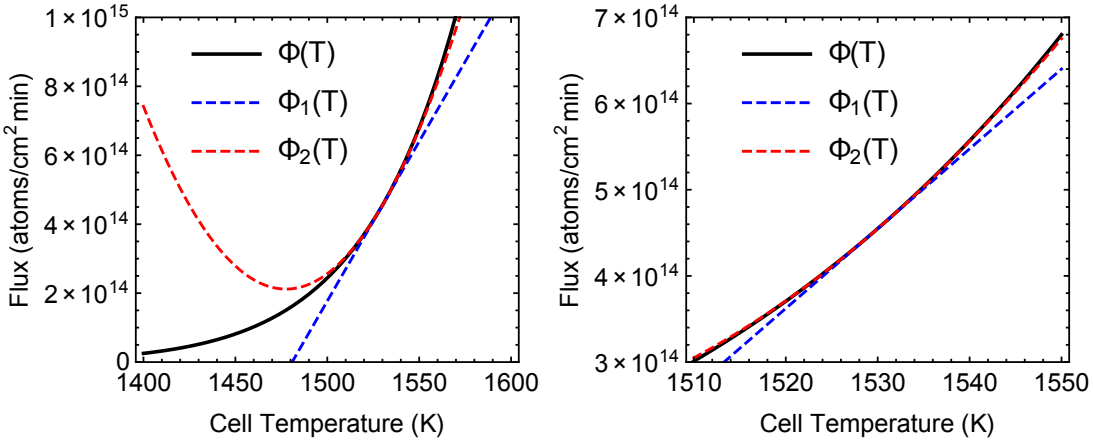

Figure 2.3: Flux of an Fe effusion cell vs. cell temperature. $\Phi(T)$ is the Arrhennius equation, while $\Phi_1(T)$ and $\Phi_2(T)$ are the first- and second-order series expansions of $\Phi(T)$ centered on $T_i = 1530K$. Note that the range of temperatures with low error is about 10K wide for $\Phi_1(T)$, while $\Phi_2(T)$ is valid over a much wider temperature window.

2.3 Magneto-optic Kerr effect

An *in-situ* Magneto-optic Kerr effect (MOKE) magnetometer was developed for the work done in Chapter 3 due to the versatility and vacuum-compatibility of the technique [100]. The Kerr effect refers to the change in polarization of light when it reflects from a magnetized surface. The four-component dielectric tensor of the surface determines the absorption and reflection of light depending on its angle of incidence and polarization [101]. The values of the tensor components depend on the magnetization vector of the sample surface. As an applied magnetic field is swept across the sample, the magnetization vector moves in response, causing the reflected light to experience a rotation in its linear polarization angle. This rotation can be detected as a change in intensity after passing through a polarizing filter placed in the path of the reflected beam. The benefit of MOKE magnetometry is that it can be performed on samples without removing them from the UHV system. Capping layers that are normally used to protect the sample surface can modify the magnetic properties of thin films, which will be discussed in Chapter 3.

The MOKE magnetometer schematically shown in Fig. 2.4 consists of a HeNe laser operating at 633 nm wavelength, several steering mirrors, an initial linear polarizer (LP) to fully polarize the light after the steering mirror reflections, a half-wave plate (HWP) to reorient the beam to either S or P polarization, a pair of transparent UHV windows, a sample stage in UHV, a second analyzing linear polarizer, and finally a pair of balanced silicon photodetectors (DET). The analyzer is set to 5° to optimize the signal-to-noise ratio [102, 103]. S and P polarization refers to light that has its electric field component aligned transverse to the plane of reflection or within the plane of reflection, respectively. The sample stage is mounted on a transfer arm that allows the sample to be positioned at any azimuthal angle, and at either the in-plane vector magnet or out-of-plane solenoid

field positions. The sample stage has no active heating or cooling, and is thus limited to room temperature measurements.

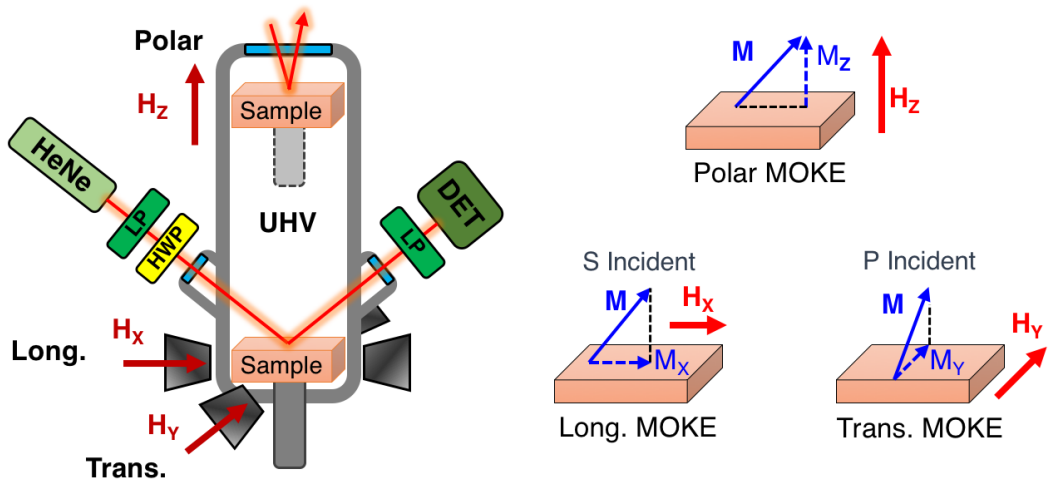

Figure 2.4: Schematic of the *in-situ* magneto-optic Kerr effect magnetometer, and a diagram of the magnetization components probed in each of the three primary MOKE modes.

The MOKE is capable of operating in the transverse, longitudinal, and polar geometries. For excellent, rigorous descriptions of the physics and geometry of MOKE magnetometers see [104, 100, 105, 101, 103]. Let the projection of the reflected beam onto the sample surface be the x direction, and the sample normal be the z direction. The y direction is in the sample plane, orthogonal to both x and z. In longitudinal MOKE, S polarized light is reflected from the sample at a glancing angle while a magnetic field is applied along the x direction, which measures the component of magnetization parallel to x. In transverse MOKE, P polarized light is reflected from the sample at a glancing angle while a magnetic field is applied along the y direction, which measures the component of magnetization parallel to y. In polar MOKE, either S or P polarized light is reflected from the sample at near-normal incidence while a magnetic field is applied along the z direction, which measures the component of magnetization parallel to z. The in-plane vector magnet for longitudinal and transverse MOKE is capable of reaching fields of

5000 Oe, while polar MOKE utilizes a water-cooled air-core solenoid with a maximum field intensity of 800 Oe. Sweeping the applied field in these three orthogonal directions allows full characterization of the easy and hard axis hysteretic behavior of magnetic thin films.

In addition to these three primary MOKE geometries, the vector magnet allows application of the rotational MOKE technique [106]. Instead of sweeping the applied field at a constant angle, the MOKE response is recorded at a constant field intensity while the applied field direction is rotated about the z axis. The applied field is set much larger than the coercive field of the sample so hysteretic effects are completely eliminated. In this configuration, the anisotropy-related magnetic torques within the sample can be probed. When the applied field angle is in the vicinity of an easy axis, the magnetization is attracted to the energy minimum in the easy direction, which displaces it away from the applied field. Conversely, as the applied field approaches a hard axis, the magnetization vector is repelled from the hard axis, again resulting in a slight displacement. These displacements can be analyzed and compared against the expected behavior according to an in-plane Stoner-Wohlfarth model to obtain the values of anisotropy constants, which cannot be obtained from the three primary MOKE modes.

The MOKE chamber is connected to the UHV system using welded bellows sections, and is thereby mostly isolated from vibrations produced by pumps and other equipment. The HeNe laser is placed sufficiently far from the electromagnets that any Zeeman-related wavelength shifts are minimized. The minimum number of steering mirrors is used to reduce scattering of the beam, and all source optics are mounted to a single stage. Any remaining noise is greatly reduced through the use of an optical chopper and lock-in amplifier. One remaining noise source is thermal drift over time scales of ~ 10 min. This issue can be minimized by quickly collecting data only in applied field ranges of interest. Any remaining drift is small and a linear correction may be subtracted from the collected

MOKE hysteresis loops. A Quantum Design MPMS XL SQUID magnetometer was used to confirm the accuracy of the *in-situ* MOKE. A direct comparison of the two techniques for a MgO/Fe/MgO sample can be seen in Fig. 2.5.

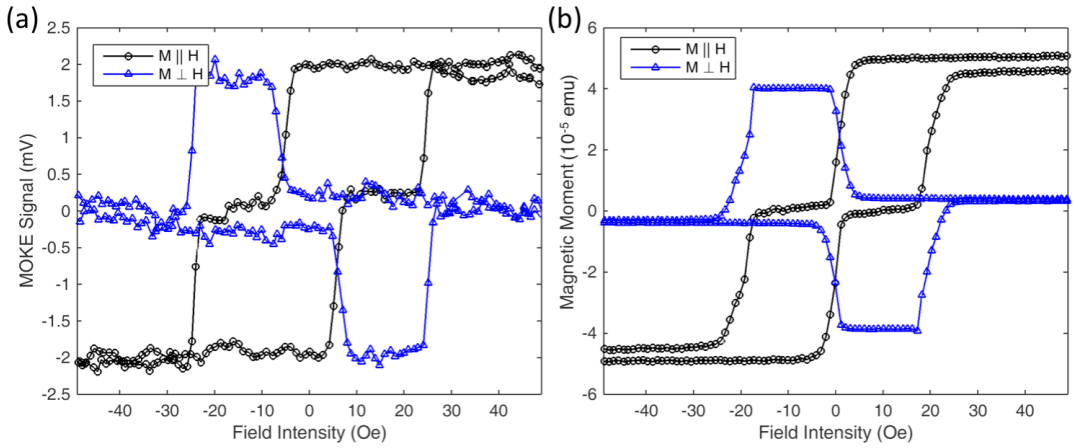

Figure 2.5: (a) MOKE data for a 14-Å-thick Fe film deposited on MgO (001). The black curve is taken in transverse MOKE mode, while the blue curve was taken in longitudinal MOKE mode, but with the field applied in the transverse direction. (b) SQUID data for the same sample, measuring the same components of magnetization.

2.4 SQUID Magnetometry

A superconducting quantum interference device (SQUID) magnetometer is used to measure the total magnetization of a sample as a function of applied field and temperature. A SQUID loop consists of two Josephson junctions connected by a loop of superconducting wire, which is able to detect individual magnetic flux quanta passing through the loop. The SQUID loop is so sensitive that it must be shielded from external electromagnetic interference and separated from the sample detection loop through a low-pass isolation transformer. The sample detection coils, transformer, signal coil, and SQUID loop are all made of superconducting wire. A schematic of the SQUID loop circuit is shown in Fig. 2.6.

As a magnetized sample is moved through the detector array, the changing magnetic field induces a persistent current in the array wiring. This signal is passed through the isolation transformer to the signal loop, which then transmits the signal to the SQUID loop. The voltage of the SQUID loop is then plotted against the sample position. The resulting plot has a known, characteristic curve due to the shape and spacing of the detector array. By fitting the theory to this curve, the total moment of the sample can be determined.

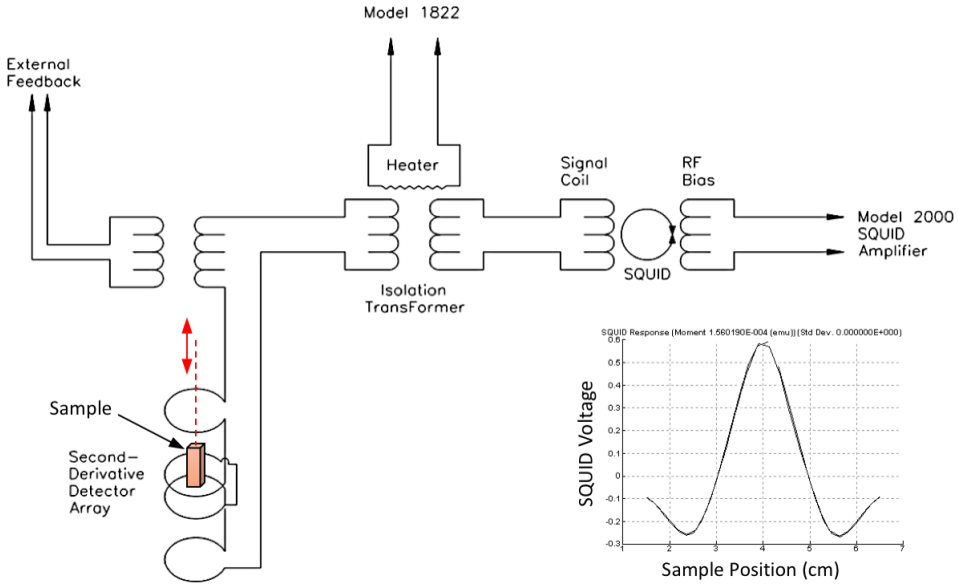

Figure 2.6: Schematic of a SQUID magnetometer showing magnetization detector array, isolation electronics, SQUID loop, and resulting SQUID voltage vs. sample position data for a Co_2TiGe thin film. Figure adapted from Quantum Design MPMS XL Hardware Manual.

Hysteresis curves can be measured by adjusting the applied field, which is provided by a 7 T superconducting solenoid magnet surrounding the detector array. The field must be static when measuring the sample because changing the field induces a large persistent current in the detector array. Each time the field is changed and stabilized, a heater within the isolation transformer heats the wiring above the superconducting phase transition, which eliminates the persistent current via ohmic heating in the normal

wire region. The heater then switches off and the wire becomes superconducting again, allowing another SQUID measurement.

When a magnetic thin film is measured in a SQUID magnetometer, the total magnetization includes the properties of the film, the substrate, and any bulk contaminants in the substrate or on the sample surface. Each of these contributes its own diamagnetic response, plus any paramagnetic or ferromagnetic response. Iron oxide is magnetic and is one of the primary components of dust in the air. Samples, tools, and sample mounting supplies left exposed to air can easily become covered with ferromagnetic contaminants. Since the properties of contaminants are not well known, it is best to avoid them entirely by maintaining a clean and organized workspace around the SQUID. This is absolutely essential when measuring ultra-thin films such as those discussed in Chapter 3 of this dissertation.

The ferromagnetic films studied here, while strongly magnetized, have minuscule volumes compared to the substrates. Since all materials exhibit diamagnetism, a nominally non-magnetic substrate will produce a large diamagnetic background that is superimposed onto the ferromagnetic response of the film. To obtain the magnetic properties of the film, subtraction of the diamagnetic background is required. This is fairly easy for most hysteresis loops. Data should be collected for at least several thousand Oe on either side of the magnetic saturation field value of the film. These data should lie on a straight line with negative slope. Fitting a line to this tail of the hysteresis curve, and then subtracting the slope obtained from the entire data set, eliminates the diamagnetic background.

Unfortunately, this simple technique doesn't always work. For example, MgO (001) substrates are diamagnetic at temperatures above 10 K, but below this temperature they become weakly paramagnetic. The saturation field of the paramagnetism is on the order of 7 T, so a true diamagnetic tail cannot be obtained with the SQUID. Instead,

the paramagnetism should also be subtracted. The total magnetization in the high-field region of a hysteresis curve, away from the ferromagnetic behavior of the film, can be written

$$M_{tot}(H) = M_f \cdot \text{sign}(H) + \chi_d H + M_p \cdot L(\alpha H) \tag{2.13}$$

where M_f is the saturation magnetization of the film, χ_d is the total diamagnetic susceptibility, and M_p is the saturation magnetization of the paramagnetic background. The sign(x) function approximates the ferromagnetic switch of the film, and $L(x)$ is the Langevin function that describes the field behavior of paramagnets [23],

$$L(x) = \coth(x) - \frac{1}{x} \tag{2.14}$$

The fitting parameter α determines the horizontal scale of the Langevin function, and can be used to estimate the ratio of magnetic energy to thermal energy for spins in the paramagnet [23]. Thus, this protocol requires a four parameter fit, but gives highly accurate results, as can be seen in Fig. 2.7.

2.5 Magnetic Anisotropy Analysis

The magnetization of a given sample points in the direction of the global minimum of the total magnetic energy density including the Zeeman term. Magnetic anisotropy energy can be represented as a closed surface in three dimensions, as discussed in Section 1.5. The overall shape of the energy surface is determined by crystal symmetry and the shape anisotropy of the ferromagnetic particle. See equation (1.6) for a representative Stoner-Wohlfarth model. The anisotropy constants themselves are most rigorously quantified using dynamic techniques such as ferromagnetic resonance [107]. Static techniques such as SQUID can also be used to quantify magnetic anisotropy. However, the

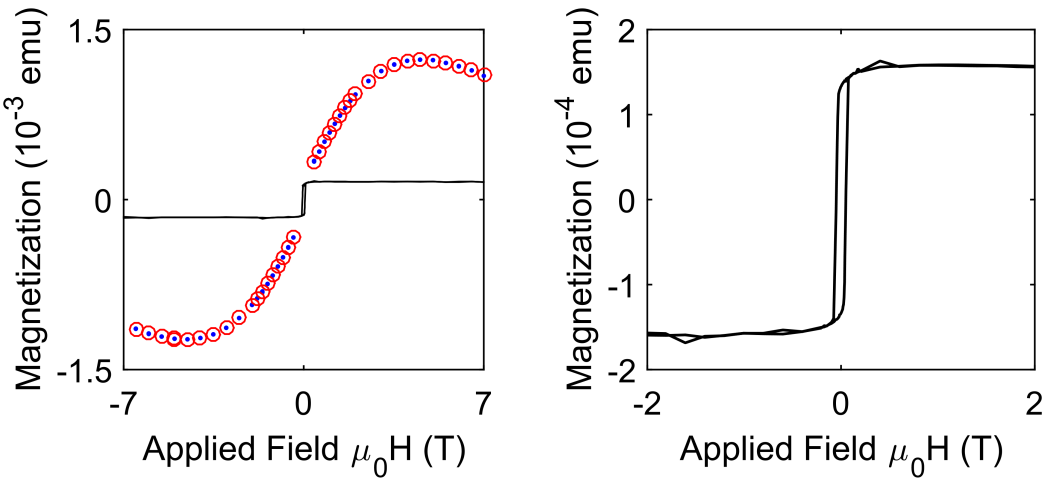

Figure 2.7: SQUID data for a Co_2TiGe/MgO (001) sample at $T = 5$ K. (Left) Raw data (blue dots) taken at the high field tails is used to fit (red circles) equation (2.13). The fitted function with $M_f = 0$ is then subtracted from the entire data set, giving the ferromagnetic contribution of the film (black line). (Right) Zoom-in of the corrected data.

important caveat is that SQUID can only determine the *difference* in anisotropy energy between two directions. Therefore, SQUID is particularly useful for quantifying $K_{eff}^{\perp}$, the effective perpendicular anisotropy constant with respect to some in-plane direction. The method presented here can also be found in Ref. [37].

Generally, the sample magnetization vector $\boldsymbol{M}$ is a complicated hysteretic function of the applied field vector $\boldsymbol{H}$, written as $\boldsymbol{M} = \boldsymbol{M}(\boldsymbol{H})$. In SQUID, the orientation of a sample is constant while the magnitude of the applied field $|\boldsymbol{H}| = H$ is varied. Let the orientation of the field with respect to the sample be the unit vector $\hat{\boldsymbol{r}}_1$. Then, $\boldsymbol{M} = \boldsymbol{M}(H\hat{\boldsymbol{r}}_1)$. Furthermore, SQUID only measures the magnitude of the magnetization vector projected along the same applied field direction, $M_1 = \hat{\boldsymbol{r}}_1 \cdot \boldsymbol{M}(H\hat{\boldsymbol{r}}_1)$. By changing the orientation ($\hat{\boldsymbol{r}}_1$, $\hat{\boldsymbol{r}}_2$, ...) of the sample between measurements, one can obtain dissimilar magnetization curves (M_1, M_2, ...), the shapes of which depend on the magnetic anisotropy of the sample. The difference in magnetic anisotropy energy between two sample orientations can be found by taking the difference between the hysteresis curves

and integrating with respect to applied field [37],

$$\Delta E = E_2 - E_1 = \mu_0 \int_0^\infty [M_2(H\hat{\boldsymbol{r}}_2) - M_1(H\hat{\boldsymbol{r}}_1)]dH \tag{2.15}$$

Of course, as stated above, this technique is typically used to determine $K_{eff}^{\perp}$. In this case, $\hat{\boldsymbol{r}}_2$ is the out-of-plane direction, which is [001] for (001) oriented samples. The direction $\hat{\boldsymbol{r}}_1$ is that of the easiest in-plane axis, which is along [110] for most Heusler compounds.

Raw SQUID data requires some additional processing before it can be analyzed using this technique. First, SQUID measures different saturation magnetization (M_S) values for the same sample in different orientations. This is caused by the inductive coupling of the sample and detection loop changing depending on sample orientation. For this reason, it is necessary to choose one of the M_S values and normalize the other data set to it. Typically, M_S values are much more consistent between measurements for in-plane than for out-of-plane sample orientations, so the in-plane value is chosen. Second, the SQUID data is unevenly spaced and must be interpolated to produce a regularly spaced array that can be easily processed by numerical methods. Third, the forward and backward SQUID scans must be averaged together to eliminate hysteresis. Fourth, SQUID data does not extend out to infinite field, so field must be varied at least to the point of magnetic saturation. Taken together, these modifications give

$$K_{eff}^{\perp} = \mu_0 M_{S,[110]} \int_0^{H_{sat}} [m_{[001]}(H\hat{\boldsymbol{r}}_{[001]}) - m_{[110]}(H\hat{\boldsymbol{r}}_{[110]})]dH, \tag{2.16}$$

where $m = M(H)/M_S$ is the normalized hysteresis loop. The result of this analysis can be seen in Fig. 2.8 for two samples, one with an in-plane easy axis and one with an out-of-plane easy axis.

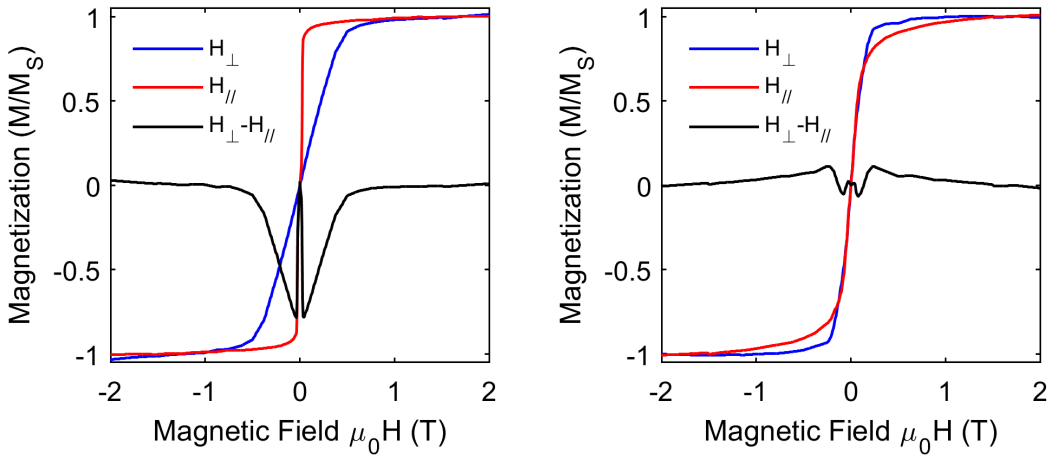

Figure 2.8: Perpendicular magnetic anisotropy analysis for (left) an in-plane magnetized sample and (right) weakly out-of-plane magnetized sample.

2.6 X-ray photoemission spectroscopy

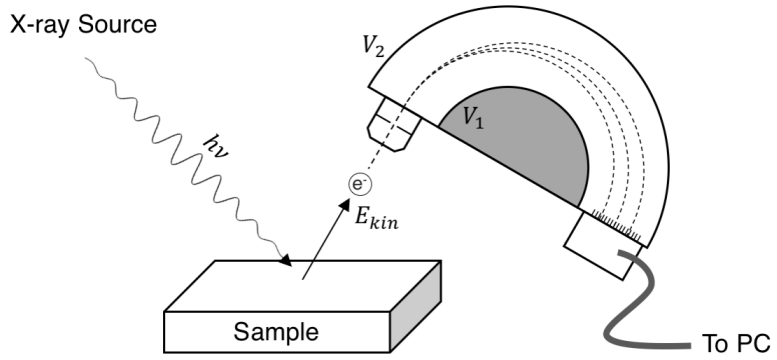

Figure 2.9: Schematic of an X-ray photoemission spectrometer with cylindrical analyzer.

XPS is a surface-sensitive chemical analysis technique based on the photoelectric effect. When an X-ray photon with energy $h\nu$ encounters an atom at the surface of a material, a core level electron has some probability of becoming excited into the free electron kinetic energy continuum. The kinetic energy of the emitted photoelectrons is the difference between $h\nu$ of the X-ray and the characteristic energy of the orbital from which the electron came. Electrons that exit the surface of the sample also incur an energy penalty to overcome the material work function, ϕ. The kinetic energy of a

photoelectron is then written

$$E_{kin} = h\nu - E_{bind} - \phi. \tag{2.17}$$

The kinetic energy of the photoelectrons can be quantified using an electron analyzer, which consists of two concentric cylinders held at different voltages. The radially aligned electric field exerts a force that curves the trajectories of the electrons passing through the space between the cylinder surfaces. High energy electrons are curved by the analyzer voltage less than low energy electrons, which splits the beam into an energy-resolved spectrum. By sweeping the analyzer voltages and measuring the number of electrons that arrive at an array of detectors at the far side of the analyzer, the electron energy spectrum can be reconstructed. Once the electron kinetic energies are known, the original electron binding energies can be back-calculated as

$$E_{bind} = h\nu - E_{kin} - \phi. \tag{2.18}$$

Since core level electrons are mostly shielded from the external chemical environment, the energy of electrons residing in them does not change much. Thus, core level peaks in XPS spectra are unique to each element and can be used to determine the chemical composition of a sample surface. Additionally, orbitals closer in energy to the valence band do experience slight changes in energy that depend on the chemical bonding of the atom. This chemical energy shift can be leveraged to determine the chemical bonding environment of an atom. For example, the Fe 2p orbital has lower binding energy for an Fe–Fe bond, and higher binding energy for an Fe–O bond.

Finally, XPS is a surface sensitive technique. While X-rays can penetrate sample surfaces for several hundred microns, electrons have a short inelastic mean free path in

solids, on the order of several nanometers [108]. The probability of an electron escaping a surface decreases exponentially with distance of the source atom from the surface. This makes XPS sensitive primarily to the surface chemistry, making it an ideal tool for detecting surface contamination and chemical bonding at interfaces beneath ultra-thin films.

The XPS module used in this work was in the UHV interconnected Palmstrøm Lab, allowing analysis of freshly-grown, pristine surfaces. It utilizes an Al $K_{\alpha 1}$ X-ray source with Ge monochromator, giving $h\nu = 1487$ eV with linewidth of around 0.8 eV.

2.7 High resolution X-ray diffraction

High resolution X-ray diffraction (XRD) is used to measure the crystalline properties of solids. Since XRD was used heavily for the work presented in this dissertation, a few key details of the theory are given here, but this cannot substitute for a proper course on XRD. See [109] for a good resource. A sample to be measured is affixed to a goniometer, and an X-ray source is directed onto the sample. The goniometer carefully varies the angles between the source, sample, and an X-ray detector, while recording the number of diffracted X-rays entering the detector. At certain sets of angles, a diffraction condition is satisfied and the sample emits a beam of X-rays into the detector, which produces a peak in a plot of count rate vs. angle. By analyzing the angles at which the sample diffracts, the lattice parameter can be found. The linewidth of the peak can be used to judge the crystal quality via the Scherrer equation [110]. The presence or absence of certain peaks can be used to determine the type of crystal present, or whether a film grown by MBE consists of a single crystal phase or multiple reaction phases. These are only a few of the pieces of information that can be gleaned from XRD. However, solid foundational knowledge is required to select the proper scan conditions and analyze the

results.

In this work, a diffractometer with monochromated Cu $K_{\alpha 1}$ X-rays with wavelength $\lambda = 1.540598$ Å is used. The X-rays are directed onto a sample, where the light waves are scattered by interactions with the electrons that surround each atomic position. Each scattering point produces a spherical wave of X-ray light. However, in a crystal where the atomic positions are periodic, the spherical waves from the ensemble of scattering points either constructively or destructively interfere depending on the wavelength and angle of the incident wavevector relative to the crystal lattice. In three dimensions, the crystal lattice can be viewed as a set of atomic planes that are defined by Miller indices (hkl). For example, the (001) plane of a cubic crystal is oriented with its normal vector in the [001] direction, and has interplanar spacing of a, the lattice constant. An arbitrary (hkl) plane faces the $[hkl]$ direction and has an interplanar spacing of

$$d_{hkl} = \frac{a}{\sqrt{h^2 + k^2 + l^2}}. \tag{2.19}$$

These planes diffract X-rays according to Bragg's law

$$\lambda = 2d_{hkl} \sin\theta, \tag{2.20}$$

where θ is the angle between the (hkl) plane and the incident beam. This definition is useful when analyzing the $(00l)$ plane of a (001) oriented crystal, but becomes unwieldy otherwise because it does not intuitively describe the angles native to the XRD goniometer. To simplify the explanation of diffraction for arbitrary (hkl), it is useful to define reciprocal space, which is a mathematical construct that serves to help visualize systems of planes and angles. For cubic systems, the point in reciprocal space with position $(h/a, k/a, l/a)$ corresponds to the (hkl) plane in real space. Each reciprocal space

point can be given as a vector $\boldsymbol{G}_{hkl}$. The incident beam of X-rays can be represented in reciprocal space by a wavevector with magnitude $k = 2\pi/\lambda$, and angle the same as that in real space. Using this construct, Bragg's law becomes

$$\boldsymbol{G}_{hkl} = \boldsymbol{k}_D - \boldsymbol{k}_S, \tag{2.21}$$

where $\boldsymbol{k}_S$ and $\boldsymbol{k}_D$ are the wavevectors of the source and diffracted beams. Diffraction occurs when the difference between the incident and diffracted wavevectors is equal to a vector for a reciprocal space point.

To make this easier to digest, it is useful to consider the Ewald sphere construction, which can be seen schematically in Fig. 2.10. Here, the $Q_\perp$ axis represents the direction normal to the nominal crystallographic orientation plane of the sample, while $Q_{//}$ is orthogonal to the former axis and lies in the scattering plane. For a perfectly aligned crystal with no miscut, $Q_\perp$ and $Q_{//}$ are normal and in-plane to the sample surface. When representing a single scattering plane such as this, the Ewald sphere becomes a circle with radius of k_S, shown in blue. The center of the circle represents the X-ray source, out at great distance. The red line represents the incident wavevector $\boldsymbol{k}_S$. The circle is drawn such that the origin of reciprocal space is on the edge of the circle, and the entire circle can rotate freely about the origin.

It is critical to always remember that the most important angle in scattering physics is 2θ. Indeed, the angle between $\boldsymbol{k}_S$ and $\boldsymbol{k}_D$ is defined as 2θ, and everything else is built around, and aligned to, that definition. The angle between the $Q_{//}$ axis and $\boldsymbol{k}_S$ is the angle ω. The angles ω and 2θ are the two principle goniometer axes with the highest resolution and precision. When performing on-axis scans along $Q_\perp$ where only $(00l)$ peaks are measured, $\omega = 2\theta/2$. However, when performing off-axis scans of arbitrary (hkl) peaks, this is not generally true. Thus, it is useful to define an offset angle such

that $offset = \omega - 2\theta/2$, the geometry of which can be seen in Fig. 2.10.

As ω is varied, the Ewald sphere rotates about the origin of reciprocal space, and intersects with various (hkl) points. Each of these intersections represents a satisfied diffraction condition. However, most of the intersections that occur are not in the scattering plane shown, but rather in some off-axis direction. Almost none of these stray diffraction events can be detected because the XRD detector has a small aperture that only detects diffracted beams that pass into it.

To restrict our view to only those diffraction conditions that are relevant to high resolution XRD, it is useful to place a second Ewald sphere on the plot of reciprocal space, which represents the diffracted beam and the detector. The line connecting the origin to the center of the second sphere is $\boldsymbol{k}_D$. The center of the circle represents the detector out at large distance. When ω is such that the source Ewald sphere intersects a reciprocal space point, and θ is such that the detector Ewald sphere intersects the same reciprocal space point simultaneously, the detector will be struck with diffracted X-rays. Using this construction, the angles ω and 2θ can be determined with simple trigonometry for any accessible (hkl) desired.

While performing XRD, it is common to utilize a coupled $\omega/2\theta$ scan, where $\dot{\omega} = \dot{\theta}$. It is helpful to keep in mind that this scan condition produces a straight line in reciprocal space that passes through the origin, no matter what starting values are used for ω and 2θ. The scanning line will be rotated away from $Q_\perp$ by the $offset$ angle. When performing an on-axis symmetric scan as shown in Fig. 2.10(a), this line is able to pass through all accessible $(00l)$ points. Similarly, when performing a coupled scan through the (111) point, the scan will also capture the (222) and (333) points.

Finally, it must be stated that the intensity of a Bragg reflection depends on the structure factor of the specific crystal being measured. Systematic absences of diffraction peaks can be used to determine the space group symmetry, and thus the type of crystal

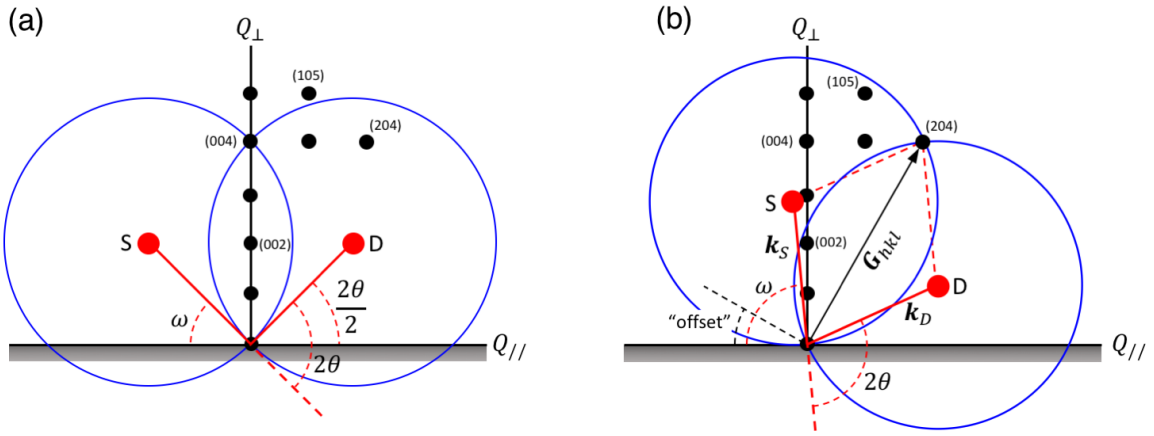

Figure 2.10: Ewald sphere construction of reciprocal space for a (001) oriented cubic crystal showing the diffraction condition for (a) an on-axis symmetric scan accessing the (004) Bragg reflection, and (b) an off-axis asymmetric scan accessing the (204) Bragg reflection. S and D refer to the X-ray source and detector.

system. Additionally, the ratio of peak areas can be used to infer the atomic basis or degree of chemical ordering within a crystal. For example, perfect Heusler crystals possess a weak (111) Bragg reflection, while disordered Heusler crystals do not, which is explained in further detail in Chapters 5 and 6. The structure factors used in this work were calculated using the VESTA software package. Certain important peak intensities were confirmed manually by determining the relativistic X-ray scattering form factor (f) of select elements [111], obtaining the structure factor (σ) via Fourier transform of the crystallographic basis, and then calculating the resulting scattering intensity (I) using the formulae [112]

$$\sigma = \sum_n \exp[2\pi i(\boldsymbol{r}_n \cdot \boldsymbol{G}_{hkl})] \tag{2.22}$$

$$F = \sum_m \sigma_m f_m \tag{2.23}$$

$$I = F^* F \left(\frac{d_{hkl}}{a}\right)^3 \frac{1}{\sin(2\theta)}, \tag{2.24}$$

where the sums are over the n basis atoms per m elemental species in the unit cell, F is a complex number representing the scattering amplitude, $(d_{hkl}/a)^3$ is the number of scattering planes per volume, and $1/\sin(2\theta)$ is the Lorentz factor to correct for the constant angular velocity of the goniometer during data collection. It is notable that no polarization factor, nor multiplicity factors are used in modeling high-resolution XRD scattering intensities. The four-bounce monochromator fully polarizes the incident X-rays, so there is no unpolarized component to preferentially scatter from the sample. Multiplicity is used only in power diffraction to correct for the probability of scattering from randomly oriented planes of a given type in a crystal system.

2.8 Reciprocal space mapping

Reciprocal space mapping (RSM) is a type of XRD that measures a two-dimensional slice of reciprocal space in the scattering plane. It can be used to measure the exact position, size and shape of reciprocal space points. It is particularly useful for measuring strain in thin films deposited on single crystal substrates. See [112] for a good resource. Collection of RSMs is performed using an automated diffractometer routine that measures the diffracted intensity at an array of points corresponding to values of 2θ and ω. While this is normally done in triple-axis mode, where an analyzing diffraction crystal is placed on the detector for greater angular resolution, this process can be vastly accelerated through the use of a CCD line detector. This map is them converted into invariant space (reciprocal space) using the following equations [113]:

$$Q_{\perp} = \frac{1}{\lambda}[\sin(\omega) + \sin(2\theta - \omega)] \tag{2.25}$$

$$Q_{//} = \frac{1}{\lambda}[\cos(\omega) - \cos(2\theta - \omega)] \tag{2.26}$$

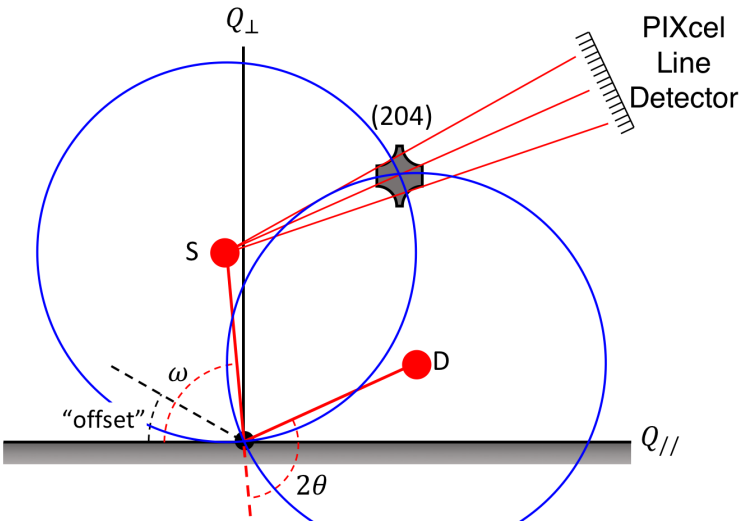

Figure 2.11: Ewald sphere construction of RSM collection. A reciprocal space point has some shape and size that corresponds to crystal imperfections and strain. The finite size produces a diffracted beam with some angular divergence, which can be detected by an analyzer crystal, or by a CCD line detector.

Reciprocal space points have finite width because they represent the spacing between imperfect crystal planes [114]. When the source Ewald sphere intersects this blob-like feature it produces diffracted light at a range of angles corresponding to the entire surface of intersection. An analyzer crystal on the detector can be used to scan 2θ across this divergent beam to determine the scattering intensity across the intersection surface. To build up a 2D image of the reciprocal space point, this must be done for a range of ω values, which is a time-consuming process. Alternatively, a CCD line detector such as a Panalytical PIXcel detector provides hundreds of individual detectors along a 2.5° range on the 2θ axis, which improves data collection time. The trade-off is a large detector streak in the resulting data, corresponding to the Fourier transform of an individual CCD pixel convolved with the Bragg peak. This artifact is not significant for most of the reciprocal space points measured in this work.

Once the angle map has been converted into reciprocal space, the RSM can be analyzed by fitting two-dimensional Gaussian functions to the peaks. The fit returns the

position of the center of the measured (hkl) peak in reciprocal space, $(q_{//}, q_{\perp})$, as well as the standard deviation of the peak $(\sigma_{//}, \sigma_{\perp})$. The primary interest in this work is a direct measurement of biaxial film strain. For nominally cubic crystals, biaxial strain results in tetragonal distortion, where the out-of-plane lattice parameter differs from the two in-plane lattice parameters. For this simplified case, the in-plane and out-of-plane lattice parameters can be calculated as

$$a = \frac{\sqrt{h^2 + k^2}}{q_{//}}; \qquad \sigma_a = a\frac{\sigma_{//}}{q_{//}} \tag{2.27}$$

$$c = \frac{l}{q_{\perp}}; \qquad \sigma_c = c\frac{\sigma_{\perp}}{q_{\perp}}, \tag{2.28}$$

where σ_a and σ_c are the standard deviation of the in-plane and out-of-plane lattice parameters, respectively. Note that the in-plane lattice parameter a can only be determined by measuring off-axis reciprocal space points collected in asymmetric geometry, where $q_{//} \neq 0$. These relations are valid only for systems with cubic or tetragonal symmetry without out-of-plane tilt. In other words, for films with Film [001] // Substrate [001]. New relations must be derived for other applications.

2.9 Magnetotransport

Electrical measurements can be used to determine the resistivity, carrier type (electron or hole), carrier concentration, carrier mobility, and the types of carrier scattering mechanisms present in a sample [23]. The favored technique for performing magnetotransport measurements is Hall bar analysis. A Hall bar is a thin, uniform rectangular prism of the sample material with length l along the x direction, width w along the y direction, and thickness t along the z direction, as shown in Fig. 2.12. Note that the voltage probes have finite width and the length l is measured from center-to-center of

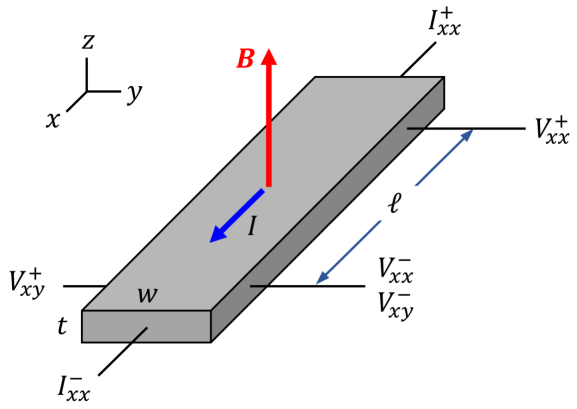

Figure 2.12: Schematic of a standard Hall bar.

the longitudinal Hall bar contacts. Current I_{xx} is applied along x, while the longitudinal voltage V_{xx} and transverse voltage V_{xy} are measured. The positive and negative terminals of V_{xy} are selected based on the assumption of conventional current consisting of positively charged carriers. In that case, the Lorentz force on the carriers is

$$\boldsymbol{F}_L = +e\boldsymbol{v} \times \boldsymbol{B}, \tag{2.29}$$

where $\boldsymbol{v} = v\hat{\boldsymbol{x}}$ is the velocity of the carriers and $\boldsymbol{B} = B\hat{\boldsymbol{z}}$ is the magnetic inductance in the sample. The cross product then yields $\boldsymbol{F}_L = -F_L\hat{\boldsymbol{y}}$, which bends the positive conventional current towards the $-\hat{\boldsymbol{y}}$ direction for a positive applied field. This produces a positive voltage on the $-\hat{\boldsymbol{y}}$ side of the Hall bar as indicated in Fig. 2.12. Conversely, for negatively charged electrons, a negative voltage develops on the $-\hat{\boldsymbol{y}}$ side of the Hall bar. Maintaining use of the conventional probe position therefore allows determination of the sign of the charge carriers, with positive and negative readings corresponding to holes and electrons, respectively.

The total resistance of a Hall bar is given by Ohm's law,

$$R_{xx} = \frac{V_{xx}}{I_{xx}}. \tag{2.30}$$

In the absence of accurate values of film thickness, it is often useful to define the sheet resistance of the film as

$$R_{sheet} = R_{xx}\frac{w}{l} = \frac{V_{xx}}{I_{xx}}\frac{w}{l}. \tag{2.31}$$

The resistivity of the film, which is intrinsic to the material and independent from the shape or size of the Hall bar, is given by

$$\rho_{xx} = R_{sheet} \cdot t = \frac{V_{xx}}{I_{xx}}\frac{w}{l}t. \tag{2.32}$$

Likewise, the Hall voltage V_{xy} can be normalized by the applied current to give Hall resistance

$$R_{xy} = \frac{V_{xy}}{I_{xx}}, \tag{2.33}$$

and then multiplied by the film thickness to obtain the Hall resistivity

$$\rho_{xy} = R_{xy} \cdot t = \frac{V_{xy}}{I_{xx}}t, \tag{2.34}$$

However, note that the Hall resistivity does not contain l or w, since the Hall voltage does not depend on the lateral dimensions of the Hall bar, but rather only on the film thickness.

In addition to the ordinary Hall effect (OHE) described above, samples that possess a net magnetization $\boldsymbol{M}$ also exhibit the anomalous Hall effect (AHE) [115]. This produces an anomalous Hall voltage proportional to the out-of-plane component of the

magnetization, $M_z = \boldsymbol{M} \cdot \hat{\boldsymbol{z}}$. The total Hall voltage can then be written

$$R_{xy}(B, M_z) = R_H B + R_{AH} \frac{M_z}{M_S}, \tag{2.35}$$

where R_H is the Hall resistance in units of Ω/T, R_{AH} is the anomalous Hall resistance in units of Ω, and M_S is the saturation magnetization of the sample.

As mentioned above, the OHE can be used to determine the carrier concentration and mobility of a sample. Here, we assume a simple, single charge-carrier model. The Hall resistance R_H can be found by fitting a line to the high-field region of V_{xy} far from any AHE contributions and extracting the slope, dV_{xy}/dB, as shown in Fig 2.13. This

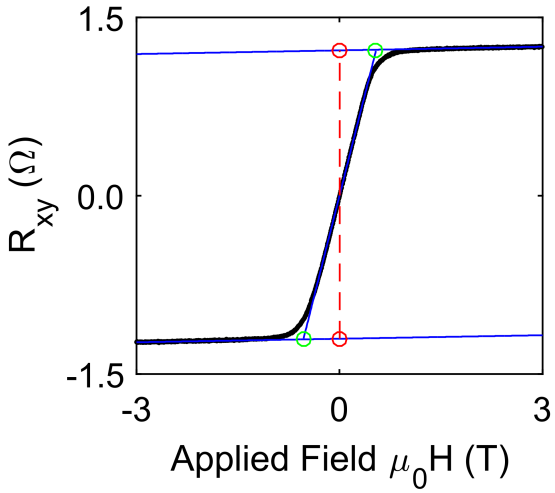

Figure 2.13: Hall resistance for a 20-nm-thick Co_2TiGe film at $T = 10$ K (black line). Three linear fits (blue lines) to the high field regions and the low field region are required to separate the OHE from the AHE. R_H is proportional to the slope of the high field region, while R_{AH} is half of the total height of the red dashed line. The saturation field is also extracted and shown as green circles.

slope is then normalized by I_{xx} to obtain the Hall resistance

$$R_H = \frac{dV_{xy}}{dB} \frac{t}{I_{xx}} = \frac{r}{en_s}, \tag{2.36}$$

where t is the thickness of the Hall bar in the z direction, e is the fundamental charge, n_s is the sheet carrier concentration, and r is an ideality factor typically set equal to unity. Solving this for sheet density gives

$$n_s = \frac{I_{xx}}{e(dV_{xy}/dB)}. \tag{2.37}$$

Assuming the charge carriers are uniformly distributed and the thickness is a well-known value, the bulk charge carrier concentration is $n_{bulk} = n_s/t$.

The Hall mobility can also be found from the Hall resistance, and then simplified to obtain

$$\mu_H = \frac{|R_H|}{\rho_{xx0}} = \frac{dV_{xy}}{dB}\frac{l}{w}\frac{1}{V_{xx0}}, \tag{2.38}$$

where ρ_{xx0} and V_{xx0} are the resistivity and voltage values taken at zero field.

2.10 Angle-resolved photoemission spectroscopy

Angle-resolved photoemission spectroscopy (ARPES) can be used to experimentally measure the electronic band structure of a material [116]. Like XPS, ARPES is based on the photoelectric effect and can measure the initial binding energy of photoemitted electrons. However, ARPES uses a hemispherical electron analyzer instead of the simpler cylindrical one depicted in Fig. 2.9. The two concentric hemispheres of the detector are held at different voltages, which produces a radially aligned electric field that curves and disperses the trajectories of photoelectrons traveling through the space between them depending on their kinetic energy. The key difference in ARPES is that the spherical symmetry of the detector accurately preserves the angles with which the photoelectrons enter the detector. At the far end of the detector, the photoelectrons will have dispersed in energy in the radial axis, and in emission angle in the transverse axis, producing

a two-dimensional image. The photoelectrons then strike a two-dimensional electron multiplier called a multi-channel plate, which amplifies the number of electron counts. The multiplied electrons are then accelerated onto a phosphor screen, which is viewed by a CCD camera. The camera records the electron counts with kinetic energy on one axis, and the angle of emission on the other.

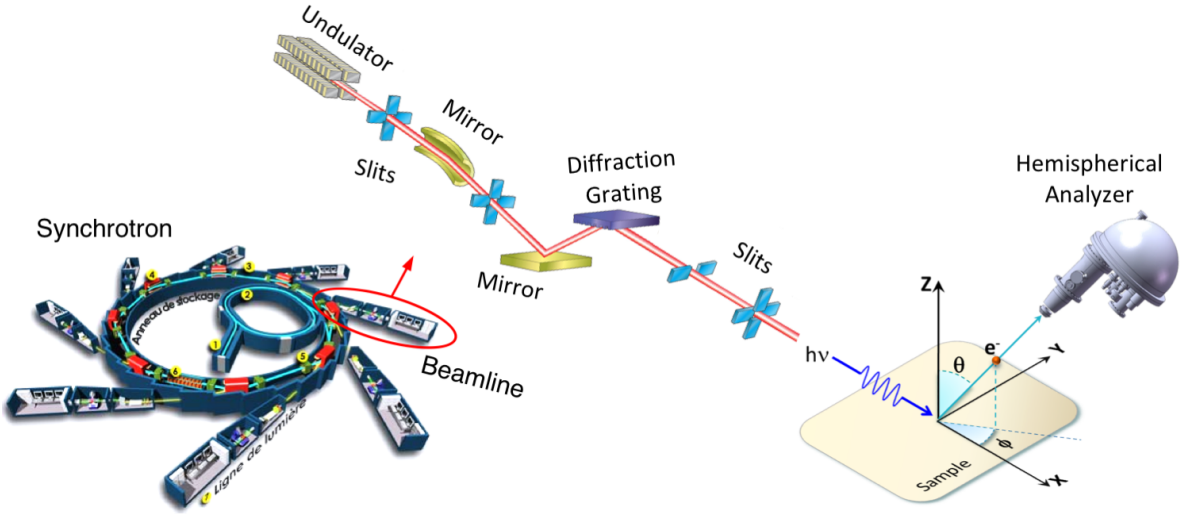

Figure 2.14: ARPES is typically performed at a synchrotron, which provides an extremely bright, monochromatic UV photon beam with energy $h\nu$ that can be varied on-demand. These photons excite electrons in a sample surface. These electrons escape the sample and enter the hemispherical analyzer, which measures their kinetic energy and angle of emission with respect to sample normal. Figure adapted from [117, 118, 119] under Fair Use (Section 107 of the U.S. Copyright Act).

The kinetic energy and emission angle of a photoelectron are determined by the initial state of the bound electron within the sample material before excitation, and by the energy of the photon that excites it out of the material into the detector. The original state is determined by the band structure of the material. Hence, the band structure can be back-calculated from the kinetic energy and emission angle of the photoelectrons. However, the key point to remember about this initial state is that it is taken to be in the two-dimensional surface Brillouin zone, rather than the familiar bulk Brillouin

zone. Heusler compounds have bcc-like symmetry, giving them an fcc-like Brilloun zone in reciprocal space, as shown in Fig. 2.15. The surface Brillouin zone includes two main contributions [116]: (i) electron states that are projected into it from the bulk Brillouin zone, and (ii) states that are unique to the surface that can arise from dangling bonds, surface reconstructions, and the far more exotic topologically protected states of interest in this work. The challenge of ARPES is finding ways to distinguish the interesting contributions from the more mundane ones. Much information is lost when the bulk states are projected into the surface Brillouin zone, making it difficult to know exactly which part of the bulk band structure is being measured. Usually, ARPES results must be augmented with density functional theory calculations, which can be mathematically projected into the surface Brillouin zone and overlaid on top of the experimental data for comparison.

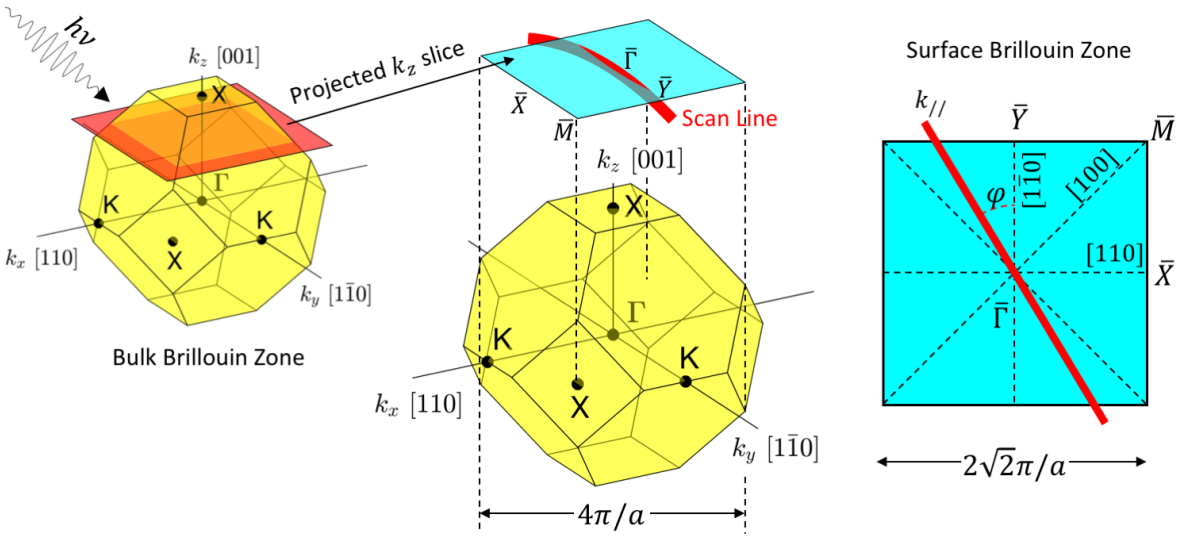

Figure 2.15: (Left) A photon with energy $h\nu$ excites electrons from states intersecting a planar slice (red plane) of the bulk Brillouin zone with k_z given by equation (2.41). (Center) Electron states from the bulk Brillouin zone are projected into the surface Brillouin zone, superimposing with states unique to the surface of the material. ARPES resolves electrons with momenta along the red line. (Right) The in-plane momentum direction $k_{//}$ detected by ARPES is selected by the azimuthal angle φ.

Once again, the relevant energetic terms for the photoemission process are related by

$$E_{kin} = h\nu - E_{bind} - \phi_{wf} \tag{2.39}$$

The initial in-plane momentum of an electron is preserved during photoemission and is directly related to the emission angle from the sample surface, giving

$$k_{//} = \sqrt{\frac{2m_e E_{kin}}{\hbar^2}} \sin\theta, \tag{2.40}$$

where m_e is the mass of the free electron and θ is the polar angle measured from the sample normal direction. The notation $k_{//}$ indicates in-plane momenta in the sample azimuthal direction φ. On the other hand, out-of-plane electron momentum is not conserved during photoemission due to inelastic processes at the interface of the sample and vacuum. The out-of-plane momentum is given by

$$k_z = \sqrt{\frac{2m_e}{\hbar^2}(E_{kin}\cos^2\theta + U_0)}, \tag{2.41}$$

The inner potential U_0 determines the amount of out-of-plane momentum lost at the surface. Inner potential varies from material to material and must be determined experimentally. However, for the purposes of this work it can be assumed to be close to that of other Heusler compounds, around $U_0 = 12$ eV [20, 120].

Experimental $E - k_{//}$ dispersion diagrams can be measured with a single ARPES scan. From these, it is possible to identify linearly dispersing features that may correspond to Dirac cones or topological surface states. However, a single line scan gives a highly restricted view of the band structure. A more complete view can be obtained by performing a Fermi map, where multiple line scans taken at different sample orientations are stitched together to produce a complete energy dispersion map of the surface Bril-

louin zone. This is a time-consuming, laborious, and computationally expensive process. Once the Fermi map is obtained, the in-plane momenta of all the electrons at the Fermi level, and at all binding energies below it, can be determined.

However, even a Fermi map gives a fairly limited view, because the surface Brillouin zone only contains bulk states from a single value of k_z. In order to scan the entire bulk Brillouin zone, a Fermi map would need to be completed for many different photon energies, which would require at least several days of continuous scanning. Instead, the sample should be oriented so that interesting features from the Fermi map are probed by a line scan. Then, photon energy $h\nu$ can be varied. The bulk states with k_z corresponding to equation (2.41) are projected into the surface Brillouin zone, and these change dramatically as $h\nu$ varies. Meanwhile, states confined to the real-space surface of the sample have no out-of-plane momentum, and so do not change with photon energy. By comparing which states disperse with photon energy and which do not, bulk states can be separated from surface states.

ARPES uses photon energies in the extreme ultraviolet range from $h\nu = 10$ eV to 120 eV. Helium discharge lamps can be used as photon sources in lab-based ARPES, but these have fixed photon energies, making the separation of bulk states from surface states difficult. Instead, ARPES is typically performed at a synchrotron, where the photon energy can be varied continuously and on-demand. The high brightness of the photon beam increases electron count rates, making data collection relatively expedient.

2.11 Spin-resolved photoemission spectroscopy

Spin-resolved photoemission spectroscopy (SRPES) is performed using an ARPES system that has a spin detector at the far end of the hemispherical analyzer. Spin detectors take several forms, but the most common variety is the Mott detector, which is

composed of an electron accelerator, a gold anode, and several electron detectors known as channeltrons.

Bound electrons in a sample not only have an initial binding energy and crystal momentum, but also a spin orientation. In itinerant ferromagnets such as Heusler compounds, the sample remanent magnetization direction is the orientation of the majority spins. Certain topologically protected surface states also possess distinct spin orientations [20]. The initial spin direction is preserved during the photoemission process and throughout the path inside the hemispherical analyzer. After passing through the analyzer, a known range of photoelectron energies and momenta are allowed to pass through an aperture. These electrons are accelerated through approximately 50 keV to bring them to relativistic velocities, and these slam into the gold anode of the Mott detector. The electrons scatter from the gold target and a fraction of them are detected by a pair of channeltrons on opposite sides of the target.

The asymmetry in the electron count is related to the spin polarization of the electron beam perpendicular to the scattering plane. The scattering plane is defined by the pair of channeltrons and the gold anode, so spin polarization along various sample directions can be measured by changing the orientation of either the sample or the Mott detector. Typically the Mott detector contains two pairs of channeltrons that define two orthogonal scattering planes simultaneously. One pair detects in-plane spin polarization along the sample axis transverse to the path through the hemispherical analyzer, and the other pair detects spin polarization oriented out-of-plane to the sample.

Physically, the scattering asymmetry occurs because a relativistic photoelectron has a chance of passing very close to the nucleus of a gold atom. The gold nucleus has an enormous positive charge, and it generates a strong magnetic field in the reference frame of the photoelectron. The electron scatters from the gold atom, but the spin interaction skews the probability of scattering to the right vs. to the left by a tiny amount [121].

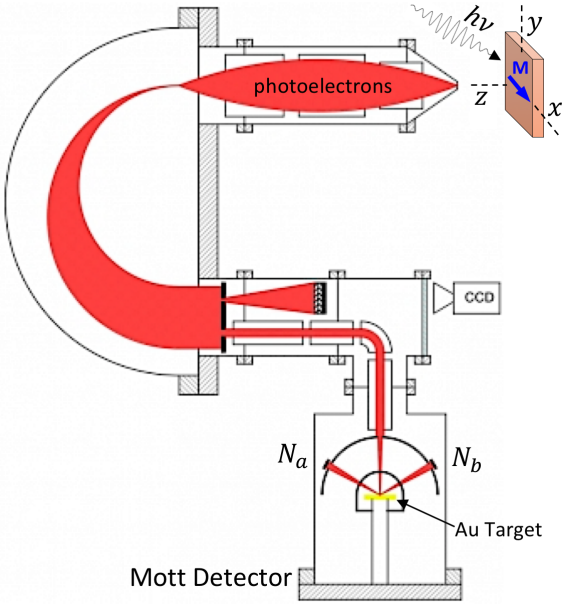

Figure 2.16: Spin-resolved photoemission spectroscopy geometry. The Mott detector here is aligned to measure spin polarization along the x direction of the sample. Normally there is also a pair of detectors orthogonal to the ones depicted here, which would measure the spin polarization along the sample z direction. Image adapted from [117] under Fair Use (Section 107 of the U.S. Copyright Act).

The asymmetry of the electrons is given by

$$A = \frac{N_a - N_b}{N_a + N_b}, \tag{2.42}$$

where N_a and N_b are the counts from the channeltron pair. The spin polarization of the electron beam, and thus the sample surface, is given by

$$P = \frac{A}{SR}, \tag{2.43}$$

where $R = M/M_S$ is the magnetic remanence perpendicular to the Mott scattering plane, and S is the Sherman function or counting efficiency of the Mott detector [122], which

usually has a value of about 0.12. The statistical error of the measurement is given by

$$\sigma_P = \frac{\sqrt{N_a + N_b}}{SR} \tag{2.44}$$

The systematic error is that of the Sherman function, S. Unfortunately, this error is not usually well-known.

Based on the calculated spin polarization and the total counts $N_a + N_b$, the spin-dependent density of states in the sample can be determined. The definition of spin-polarization is

$$P = \frac{N_\uparrow - N_\downarrow}{N_\uparrow + N_\downarrow}, \tag{2.45}$$

where $N_\uparrow$ and $N_\downarrow$ are the spin up and spin down density of states. Combining this with equation (2.43) gives

$$N_\uparrow = \frac{N_a + N_b}{2} + \frac{N_a - N_b}{2SR} \tag{2.46}$$

$$N_\downarrow = \frac{N_a + N_b}{2} + \frac{N_b - N_a}{2SR} \tag{2.47}$$

Finally, in order to ensure that the spin polarization measured by a Mott detector is due to scattering asymmetry rather than simply asymmetric placement or sensitivity of the Mott detector, two separate measurements are performed. One set of data is taken after the sample is magnetized in a positive field (+) along some direction, and the other set of data is taken after reversing the field (−) in the same orientation. The two sets of measurements are combined via the relations

$$N_a = \sqrt{N_{a+} N_{b-}} \tag{2.48}$$

$$N_b = \sqrt{N_{a-} N_{b+}}, \tag{2.49}$$

where $N_{a,b+}$ and $N_{a,b-}$ are the a and b channeltron counts taken for positive and negative magnetization. The previously defined equations are then used to determine the spin polarization corrected for detector misalignment, etc.

2.12 Preparation and use of MgO substrates

A large fraction of the growth studies detailed here utilized MgO (001) single crystal substrates. MgO has a rocksalt crystal structure with lattice parameter $a = 4.212$ Å. Many Heusler compounds can be grown directly on MgO (001) due to a $1 : \sqrt{2}$ coincident lattice that results in a 45° rotation about the [001] axis. This gives MgO an effective in-plane lattice parameter of $a\sqrt{2} = 5.957$ Å, which typically has a few percent lattice mismatch with the Heusler compounds considered in the following chapters. However, MgO substrates suffer from four important limitations that directly impact the epitaxy of ferromagnetic metals.

First, the arc fusion method currently used to synthesize bulk MgO single crystals results in crystal quality far inferior to that of Si or III-V substrates. The high degree of mosaic and crystal twinning in MgO is reflected in the poor crystal quality of epitaxial thin films grown on its surface. This is a fundamental limitation that must be taken for granted until the technology improves.

Second, MgO is hygroscopic and forms hydrated $Mg(OH)_2$ in the presence of water vapor in the atmosphere. Atomic force microscope has revealed the presence of a large number of surface particles on as-received MgO substrates that are not removed by ultrasonic solvent cleaning, as shown in Fig. 2.17. Instead, MgO substrates must be annealed at 800 °C for 12 hours in an oxygen/nitrogen furnace to remove the water and restore a smooth surface with $\sim$ 2 Å RMS roughness [123]. The annealed substrates must then be loaded into UHV immediately, or stored in a vacuum desiccator. Samples

stored in a desiccator will degrade slowly and are viable for growth studies for at least two months. On the other hand, annealed MgO stored in nitrogen ambient degrades quickly, roughening and forming patches of the hydrate within a week or two.

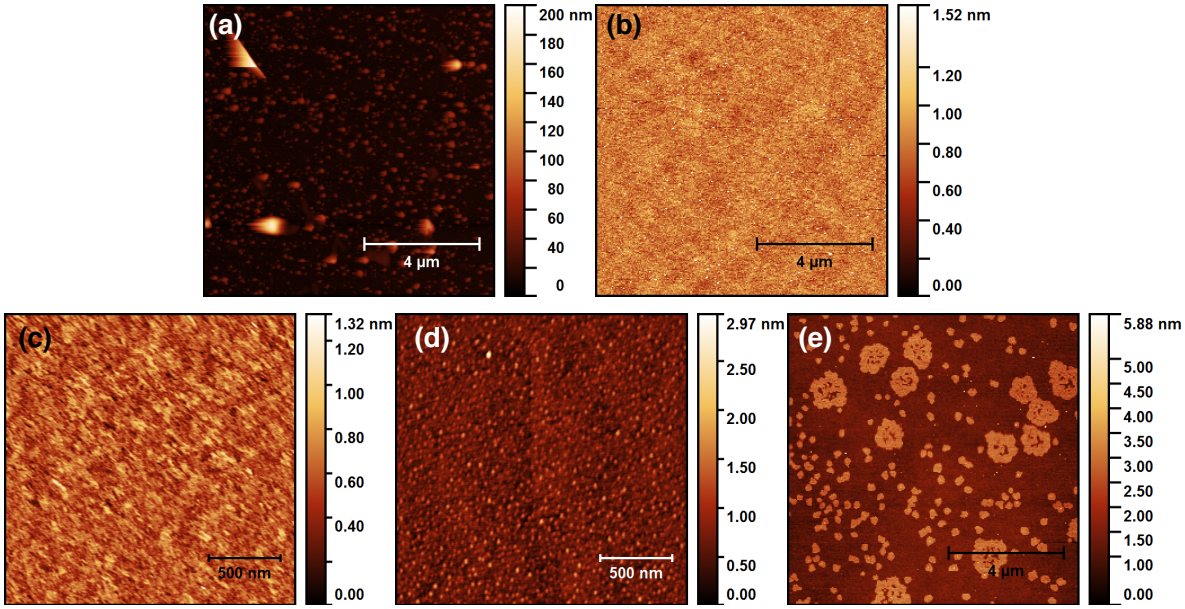

Figure 2.17: Atomic force micrographs of MgO substrates that are (a) as-received, (b) 800 °C furnace annealed, (c) annealed and stored in a vacuum desiccator for 1 month, (d) annealed and stored in a vacuum desiccator for 2 months, and (e) annealed and stored in nitrogen ambient for two weeks.

Third, MgO substrates often have magnetic or other chemical impurities. While dilute, the paramagnetic background of some commercially available MgO substrates can be comparable to the total magnetization of a strongly magnetized but thin ferromagnet deposited on the surface, which complicates analysis of SQUID measurements. It was found that MgO obtained from CrysTec GmbH exhibited far less paramagnetic background than other sources of MgO. Other chemical impurities such as carbon, calcium, and residual $Mg(OH)_2$ must be eliminated by annealing the substrates in UHV at 600 °C for 30 min, then depositing a 10-nm-thick MgO buffer layer using e-beam evaporation with the substrate held at 530 °C.

Fourth, as an oxide, MgO has a low surface energy due to the high chemical strength

and ionic character of the Mg–O bond. Metals typically have much higher surface energy, reflecting the reactivity of the atoms at the surface. Covering a metal surface with an oxide is energetically favorable because it lowers the overall surface energy [124]. On the other hand, deposition of a metal on an oxide surface results in higher overall surface energy, and can result in dewetting of the metal film to maximize the exposed oxide surface area. The dewetting process is driven by surface diffusion of metal adatoms, which increases with temperature. Therefore, lower substrate temperatures are needed when depositing metals on oxides to prevent dewetting. Alternatively, a metallic buffer layer such as Cr or CoFe can be deposited on the MgO at room temperature, and subsequently annealed at 500 °C for 45 min to give an atomically smooth surface with similar surface energy to that of Heusler compounds, as shown in Fig. 2.18

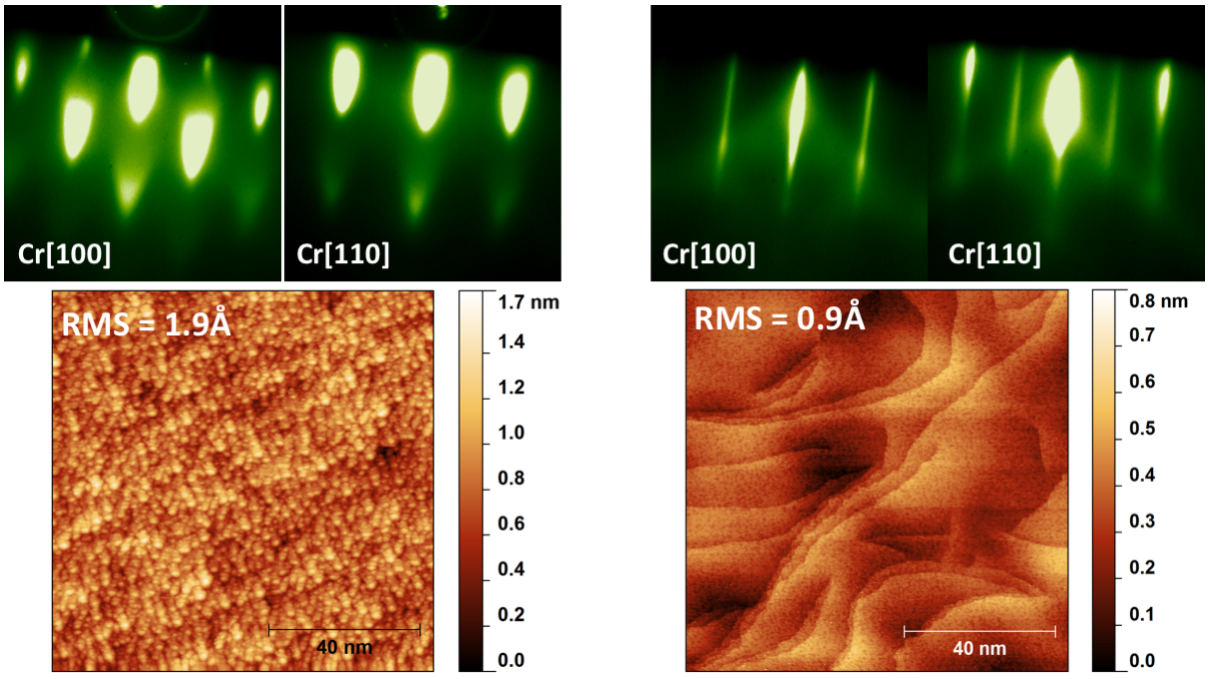

Figure 2.18: Reflection high energy diffraction images and scanning tunneling micrographs of a 20-nm-thick Cr layer deposited on MgO (001) at room temperature. (Left) Immediately after Cr deposition. (Right) After 500 °C 45 min anneal.

Chapter 3

In-situ study of magnetic anisotropy in Fe/MgO(001) ultra-thin films

Interfaces bond,

a pristine surface beckons.

Islands steer the way.

3.1 Introduction

Ferromagnetic contacts exhibiting perpendicular magnetic anisotropy (PMA) are needed for a wide range of spintronic devices, namely technologically relevant magnetic tunnel junctions (MTJ) for use in system-on-chip memory. Perpendicularly magnetized contacts have been shown to reduce spin transfer torque critical current, an important step toward increased energy efficiency [42]. Perpendicular contacts can also possess higher magnetic thermal stability as compared with in-plane magnetized contacts due to increased interface magnetic anisotropy, as seen in ultra-thin ferromagnetic films of CoFeB/MgO (001) [45]. These properties allow fabrication of perpendicular MTJs of

sufficient quality and scale to form the basis of next-generation magnetic random access memory [45].

Recent *ab initio* calculations by Hallal *et al.* predicted the presence of strong interfacial PMA at pure Fe-MgO (001) interfaces due to rehybridization of the iron 3*d* and oxygen 2*p* orbitals [125, 126, 40]. They suggested that an epitaxial MgO/Fe/MgO (001) heterostructure may exhibit dominant PMA for iron thicknesses below 12 Å due to a surface anisotropy constant $K_S = 3.4$ erg/cm^2. This value of K_S is roughly three times higher than that reported for Ta/CoFeB/MgO (001) used in MTJs with a high tunnel magnetoresistance ratio of 604% at room temperature (RT) [42]. Furthermore, the Fe/MgO (001) system would provide a key advantage over Ta/CoFeB/MgO (001) in that it lacks both boron and tantalum, which have been shown to decrease PMA and tunnel magnetoresistance ratio when present in the MgO tunnel barrier or at the Fe-MgO interface [40, 64, 127, 128].

Several prior reports have focused on characterization of PMA in structures such as MgO/Fe/(Cr,V)/MgO (001) and find high surface anisotropy energies of approximately 1 erg/cm^2 [129, 56]. These reports treat chromium and vanadium primarily as a buffer or seed layer to enable growth of a smoother iron film and consequently enables a high quality upper MgO/Fe interface to form, from which the PMA is assumed to arise. These studies avoid the wetting issues during the growth of ultra-thin metal on oxides, an important fabrication step for MTJs, and must assume that the lower Fe/(Cr,V) interface anisotropy contribution is small or zero. Additionally, previous studies of the Fe/MgO system have involved *ex-situ* magnetic characterization techniques that require capping layers to protect the iron from oxidizing in air [130, 131, 132, 133]. It is often assumed that a magnetically inert capping layer of gold, or, perhaps counterintuitively, an oxide such as MgO deposited at RT, will have a negligible effect on the underlying film properties. Consequently, magnetic measurements are assumed to be primarily a

result of the lower Fe/MgO interface [134, 135].

3.2 Experiment

In contrast with these prior reports, an extensive suite of ultra-high vacuum (UHV) interconnected growth and measurement systems are utilized for this study. These systems enable *in-situ* characterization of isolated iron thin films grown epitaxially on MgO(001). Furthermore, this allows the effect of any subsequent capping layers to be determined. MgO (001) single-side-polished substrates $(10 \times 10 \times 0.5)$ mm^3 from CrysTec GmbH were ultrasonically solvent cleaned, then loaded into the UHV system and annealed *in-situ* for 1 hour at 600 °C. A 10-nm-thick MgO buffer layer was then deposited with the sample held at 550 °C as estimated by a calibrated thermocouple mounted near the substrate heater. The MgO buffers and capping layers were grown using an *in-situ* e-beam evaporator from stoichiometric source material. The buffer served to minimize surface carbon and hydroxide (-OH) contamination of the as-received MgO substrates observed via *in-situ* X-ray photoemission spectroscopy. Iron films were deposited from an effusion cell containing 99.999% purity elemental source material in a modified Gen II molecular beam epitaxy system with base pressure of $< 5 \times 10^{-11}$ Torr. Layers were grown at a rate of 6.1×10^{14} atom cm^{-2} min^{-1}, equivalent to 0.5 monoatomic layers (MLs) per minute or 0.7 Å/min.

The substrate was held at RT during iron growth to attempt to suppress the Volmer-Weber (island) growth mode typical for metals deposited on oxides due to high surface energy mismatch and epitaxial strain. Fe is body centered cubic with bulk lattice parameter $a = 2.8665$ Å and has a $\sqrt{2}$:1 coincident lattice with the MgO rocksalt crystal with lattice parameter $a = 4.212$ Å. After 45° in-plane rotation (Fig. 3.1) of the unit cells, iron grows epitaxially on MgO with 3.8% tensile mismatch. The ML thicknesses used in

this report are the total areal atomic densities measured via Rutherford backscattering spectrometry (RBS) divided by the bulk value for body-centered cubic iron of 1 ML = 1.217×10^{15} atom/cm^2. Assuming a uniform, planar film with a bulk lattice constant out-of-plane, one ML of iron has a thickness of 1.433 Å. Consequently, the thicknesses reported here are proportional to the atomic areal density of iron, rather than a strict measure of the physical extent of the films.

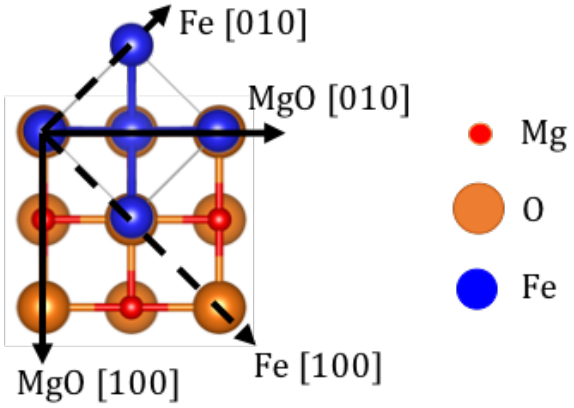

Figure 3.1: Fe [100](001) // MgO [110](001) epitaxial relationship.

The surface crystal quality and Fe [100](001) // MgO [110](001) epitaxial relationship was monitored by *in-situ* reflection high-energy electron diffraction (RHEED) during growth and low energy electron diffraction after growth. Surface morphology was studied by *in-situ* atomic force microscopy (AFM) using an Omicron variable temperature scanning probe microscope with needle sensor. RBS was performed to calibrate growth rates and measure the final thickness (via areal atomic density) of the iron films. Magnetic data were obtained using an *in-situ* magneto-optic Kerr effect (MOKE) system, and an *ex-situ* Quantum Design MPMS XL superconducting quantum interference device (SQUID).

3.3 Surface crystal quality

MgO substrates are hygroscopic and require surface preparation to improve surface crystal quality and chemical purity before use in MBE. *In-situ* RHEED patterns show a marked improvement for substrates with ebeam evaporated MgO buffer layers over those which were only cleaned in acetone and isopropanol. Streaky RHEED patterns and strong Kikuchi lines seen in Fig. 3.2 for the MgO buffer layers indicate a highly crystalline and relatively smooth surface.

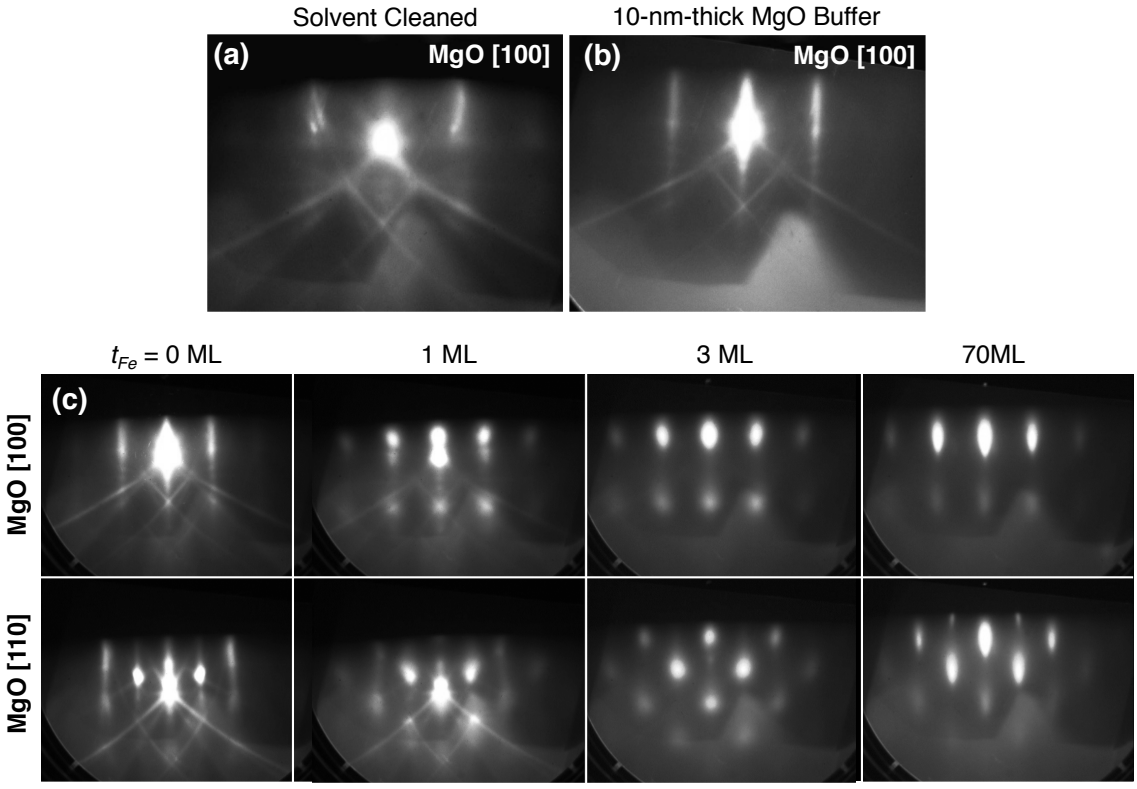

Figure 3.2: RHEED images showing improvement in surface crystal quality between an MgO substrate that was (a) solvent-cleaned only and (b) after annealing and deposition of a 10 nm thick MgO buffer. The bottom rows (c) show various thicknesses of iron deposited on MgO buffer layers.

Upon deposition of the first few MLs of Fe, the RHEED patterns become somewhat diffuse and spotty, which indicates a slight roughening, but still an epitaxial film. Further

iron deposition results in a reduction of the diffuse background in RHEED, but the diffraction pattern remains spotty along the Fe [100] direction. Annealing the free surface up to 400 °C after iron deposition does not eliminate the diffraction spots, but does result in a slight increase in sharpness of the RHEED pattern, indicating improved atomic crystallinity.

Surface morphology was monitored using AFM at each processing step, and is shown in Fig 3.3. High temperature *ex-situ* furnace annealing was performed at 1050 °C for 15 hours with 1 atm O_2 flow. This was found to produce smooth surface steps as per reference [133]. Results in Fig 3.3 show significant step bunching at 1050 °C with some regions of flatness and others that are highly textured. Depositing 8ML Fe directly onto this surface with no MgO buffer layer results in a film with roughness on the order of the film thickness. MgO has also been annealed at 800 °C for 15 hours in 1 atm O_2 flow (see Section 2.12), which produces a uniformly textured surface of much higher overall smoothness. More work is needed to fully characterize Fe films grown on these highly annealed substrates and correlate morphology to their magnetic properties.

3.4 Stoner-Wohlfarth model

In order to better understand the results of magnetic measurements, a Stoner-Wohlfarth model representing coherent magnetic domain rotation was utilized [37]. Generally, the total magnetic energy density of a thin film can be written as a combination of effective in-plane ($K_{eff}^{||}$) and effective out-of-plane ($K_{eff}^{\perp}$) anisotropy constants and a Zeeman term controlled by applied field (H). Magnetization (M) prefers to reside in the direction of the global minimum in the energy surface:

$$E(\theta, \phi) = K_{eff}^{||} \sin^2(\theta) - K_{eff}^{\perp} \cos^2(\theta) - \mu_0 \boldsymbol{M} \cdot \boldsymbol{H}, \tag{3.1}$$

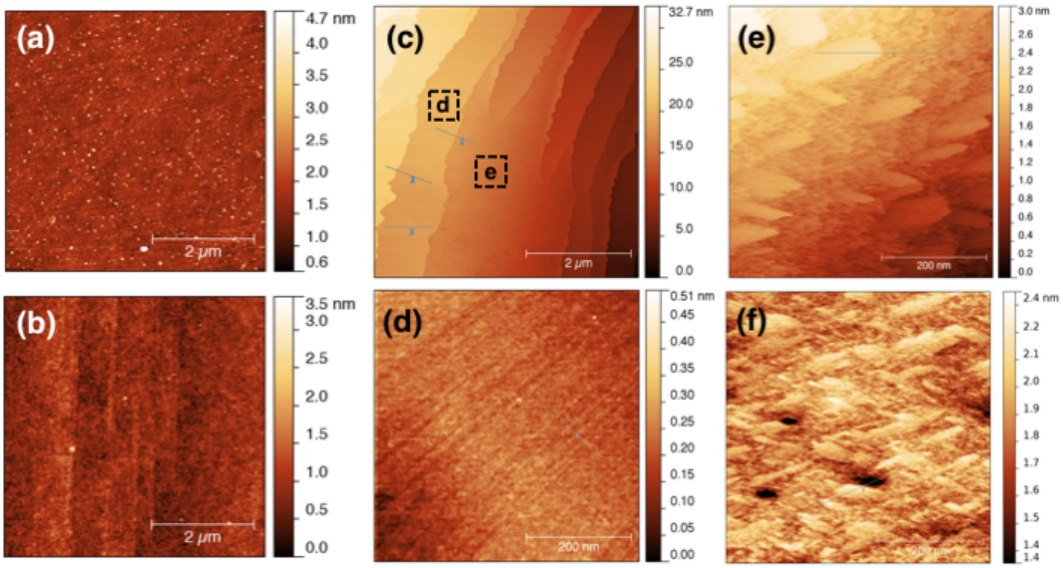

Figure 3.3: *Ex-situ* AFM for MgO substrates that have been (a) solvent cleaned, and (b) subsequently buffered with 15-nm-thick MgO. An improved starting surface is seen in *in-situ* AFM by (c) annealing MgO in 1 atm O_2 at 1050 °C for 15 h. This results in a mixed surface with regions of (d) smooth (001) surfaces and (e) rough transition areas between steps. (f) Deposition of 8ML-thick (1.1nm) Fe directly on the surface in (c) results in a fairly rough surface with corrugations aligned preferentially with the oblique incident direction of the iron effusion cell.

where θ is the angle subtended by M and the film normal direction. The in-plane anisotropy, including an in-plane uniaxial anisotropy term, is given by:

$$K_{eff}^{||} = \frac{K_1}{4}\sin^2(2\phi) + K_U \sin^2(\phi), \tag{3.2}$$

where ϕ is the angle subtended by **M** and the in-plane preferred direction, defined here as Fe [100] [133]. In-plane cubic magnetocrystalline anisotropy is given by K_1, and a small in-plane uniaxial magnetic anisotropy (UMA) (K_U) is assumed to act along Fe [100]. The out-of-plane anisotropy is given by:

$$K_{eff}^{\perp} = K_V + \frac{K_S}{t_{Fe}} = K_{MCA}^{\perp} + \frac{K_S}{t_{Fe}} - 2\pi M_S^2, \tag{3.3}$$

where K_V is the overall volume anisotropy and K_S is the perpendicular surface or interface anisotropy. In general, PMA is dominant when $-K_{eff}^{\perp} < K_{eff}^{||}$. This occurs when the iron thickness (t_{Fe}) is less than the critical thickness ($t_{cr} = -K_S/K_V$), and this condition requires that the surface energy contribution is greater than the combined shape anisotropy ($2\pi M_S^2$) and out-of-plane magnetocrystalline anisotropy (K_{MCA}). From the outset, this condition is more difficult to achieve in pure iron films due to their high saturation magnetization (M_S) as compared to films of CoFeB [64]. This fact makes the predictions of high interface anisotropy energy in Fe/MgO (001) even more interesting.

3.5 Magnetic characterization

A variety of thicknesses of iron films were grown, and M vs. H hysteresis loops were collected using both polar MOKE (sensitive to out-of-plane magnetization only) and transverse MOKE (sensitive to in-plane magnetization along a chosen crystallographic direction).

As seen in Fig. 3.4, *in-situ* MOKE magnetometry revealed a significant in-plane UMA superimposed onto the iron cubic anisotropy, the behavior of which followed equation (3.2). This manifested itself in plots of M vs. H as a square hysteresis loop for measurements along Fe [100] and a split loop for Fe [010]. For a film with dominant in-plane anisotropy ($\theta = \pi/2$), equation (3.1) can be solved for the $\sim$90° magnetization rotation that occurs for H parallel to Fe [010]. This gives $K_U \approx M_S H_{split}$, where H_{split} is the split field from $H = 0$ to the center of the split loop. H_{split} was measured for varying thicknesses of iron using *in-situ* MOKE magnetometry before and after capping the Fe/MgO (001) films with 5-nm-thick MgO. Saturation magnetization was measured by *ex-situ* SQUID magnetometry after capping and removing samples from UHV. From these, K_U was computed and is summarized in Fig. 3.5. The measured

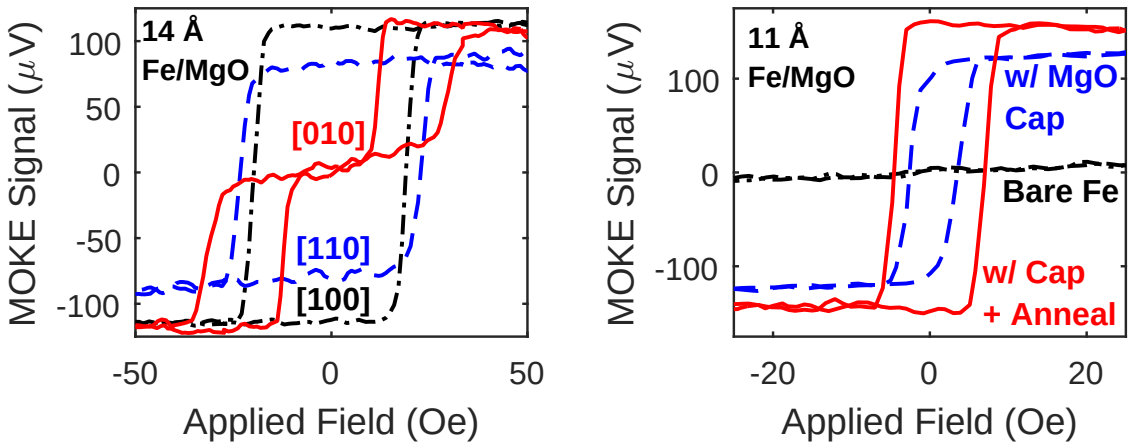

Figure 3.4: *In-situ* transverse MOKE vs. field hysteresis curves of (left) bare 14 Å (10 ML) Fe/MgO (001) along several crystallographic directions and (right) 11 Å (7.6 ML) Fe/MgO (001) for several processing conditions. The split loop along bare Fe [010] arises from strong in-plane UMA acting along Fe [100]. Split field H_{split} is half the distance between the split loop centers. The bare 11 Å Fe film is superparamagnetic, but becomes ferromagnetic in-plane after capping with 5-nm-thick MgO. Anneal was 300° for 1 hour in UHV after cap deposition.

K_U for Fe/MgO (001) has values within an order of magnitude of those reported for Fe/MgO/GaAs (001) [136]. UMA in Fe/MgO/GaAs has been attributed to a "bleed-through" effect since Fe/GaAs is known to exhibit extremely strong in-plane UMA due to preferential bonding to arsenic surface dimers [135, 136]. In contrast, the observation of UMA in Fe/MgO (001) lacks this type of crystal symmetry breaking, which suggests that film growth conditions and morphology better explain UMA observed in this work.

Initially, it was surprising to observe UMA in the Fe/MgO(001) system, since both crystals possess in-plane four-fold symmetry. The source of the additional anisotropy became clear when correlating the UMA direction with the growth geometry. Iron was deposited from an effusion cell mounted 33° from sample normal, and the projection of this growth direction onto the sample plane is parallel to the observed UMA. Additionally, no strong correlation was found for the MgO step edge direction as measured by *in-situ* AFM. This suggests that the UMA does not arise from the surface Néel effect

caused by substrate miscut. These findings are corroborated by previous reports attributing in-plane UMA to symmetry breaking due to oblique-angle deposition [130, 133, 137]. However, the role of film morphology in producing the UMA had not been previously explored experimentally. Here, *in-situ* AFM shown in Fig 3.3(f) revealed iron corrugations with their long axes preferentially aligned along the in-plane projection of the growth direction. Such corrugations would contribute a magnetic shape anisotropy term causing the magnetization to prefer the long corrugation axis, which explains the origin of the in-plane UMA in the Fe/MgO system. This suggests a growth mode beginning with the nucleation of small islands of iron due to surface energy mismatch and lattice strain between iron and MgO, followed by island elongation due to a self-shadowing effect. This growth model is consistent with both SQUID and MOKE magnetometry data showing only superparamagnetic behavior for MgO/Fe/MgO(001) films with less than 9 Å thick iron, which is presumably less than the film coalescence limit.

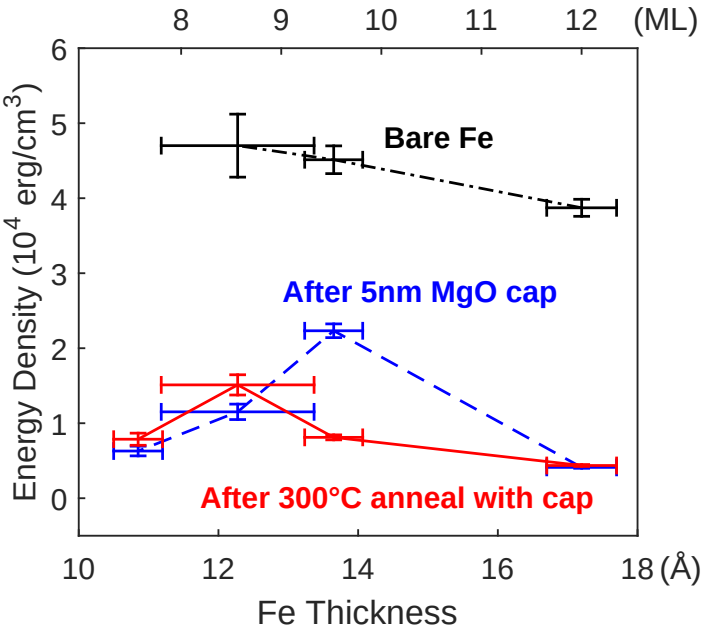

Figure 3.5: Volume normalized in-plane UMA energy vs. thickness of Fe/MgO (001) for several process conditions. In-plane UMA decreases dramatically after capping with 5-nm-thick MgO. Anneal was 1 hour in UHV after cap deposition.

The effect of an MgO capping layer had not been previously reported for the Fe/MgO system. The *in-situ* MOKE magnetometer allowed direct comparison of films before and after capping, which led to the observation of several interesting phenomena. First, a significant reduction of in-plane UMA was generally observed for samples capped with 5-nm-thick MgO, as shown in Fig. 3.5. From this it can be inferred that the MgO acts to dampen or counteract the shape anisotropy caused by iron corrugations.

Second, the direction along which split hysteresis loops occurred rotated by 90° for iron with ∼13 Å thickness after capping with 5-nm-thick MgO. This can be modeled in equation (3.2) as either a 90° rotation of the UMA preferred direction or as a negative value for K_U. This implies that the MgO capping layer can induce a shape or interface anisotropy at a right angle to the original long iron corrugation direction. Note that the e-beam evaporator was mounted at near-normal incidence to the sample during MgO deposition so this effect is unlikely to be due to oblique incidence growth. However, preferential self-shadowing of the MgO may still occur due to the existing corrugation of the iron films.

Third, and perhaps most interestingly, transitions from superparamagnetic to ferromagnetic behavior have been observed for iron films between 9 Å and 12 Å thickness after capping with 5-nm-thick MgO. Such a transition is illustrated in Fig. 3.4. No such transitions were seen for films under 9 Å, which remained superparamagnetic for all processing conditions. MgO capping layers are often assumed to be magnetically inert, which allows simple *ex-situ* magnetic measurements to be used [130, 131, 132, 133, 134, 135]. Critically, these results indicate that MgO capping has several non-trivial effects on iron films, in particular for the ultra-thin limit where interfaces dominate the behavior. It is, so far, unclear whether the change in UMA is related to predictions of orbital rehybridization at the Fe-MgO interface. Alternate explanations for the change in anisotropy include magnetostriction or a thin, magnetically active oxide reaction layer that modifies

ferromagnetic coupling between neighboring iron islands.

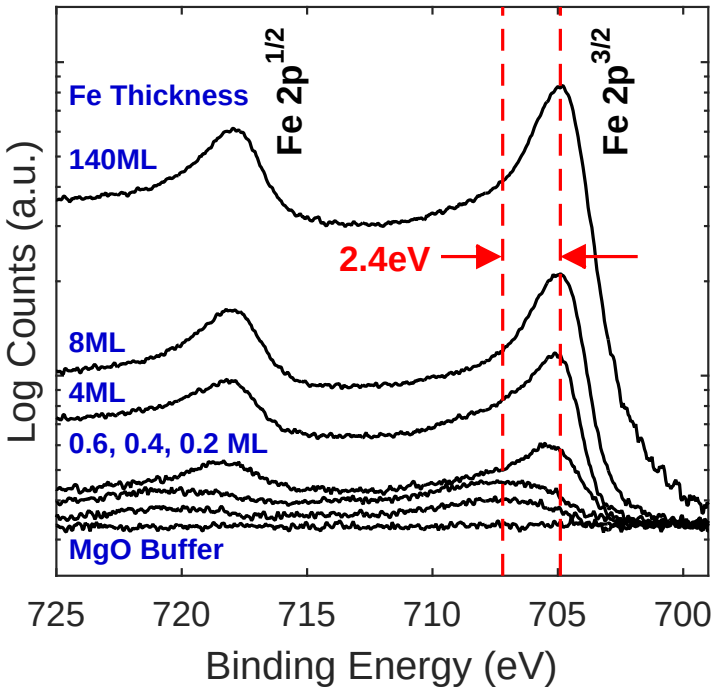

Figure 3.6: *In-situ* X-ray photoemission spectra in the Fe 2*p* region for bare MgO, relatively thick Fe/MgO, and several ultrathin Fe/MgO samples. A 2.4 eV shift to higher binding energy for Fe 2*p* states is apparent for films thinner than 1 ML. This shift is consistent with Fe-O bonding.

3.6 Interface chemistry

To better understand the magnetic anisotropy near the Fe-MgO interface and check for interface reactions between iron and MgO, *in-situ* X-ray photoemission spectroscopy was used to probe for any changes in binding energy for iron, magnesium, and oxygen atoms. To counteract electrical charging effects during XPS measurements, all spectra were aligned to the prominent magnesium 1*s* peak of MgO, then shifted so that the carbon 1*s* peak position on as-received MgO was defined as 284 eV to provide a standard reference energy. However, depending on the species of organic adsorbate, the true

reference value could be shifted by a constant as high as 6 eV to higher binding energy, as in the case for CO_2. As shown in Fig. 3.6, a significant 2.4 eV chemical shift to higher binding energy was detected for iron $2p$ states within one ML of the MgO surface. This shift is consistent with FeO bonding, but is $\sim$1 eV lower than expected for Fe_2O_3 bonding. Simple electrical charging of the sample does not account for the observed shift since it was not observed for any other peaks such as the oxygen $1s$ or magnesium KLL Auger peak. This suggests that a thin oxide layer formed at the lower Fe/MgO interface. Such an oxide had been previously excluded by Mößbauer spectroscopy [131]. However, it is known that magnesium can migrate significant distances into Fe_3O_4/MgO (001) films at elevated temperatures, so a very thin reaction layer at room temperature is a reasonable possibility [138]. XPS analysis of pure $MgFe_2O_4$ by X. Yuan *et al.* [139] reveals an iron $2p^{3/2}$ binding energy of 710.1 eV, or a chemical shift of close to 5 eV from elemental iron. Such a large shift is not observed in the present work, but may be accounted for if the reaction layer is very iron-rich. A thin spinel-like $MgFe_xO_y$ layer may explain the observed changes in magnetic behavior of iron films after MgO capping because disordered spinels are known to be ferrimagnetic [140]. If such a reaction layer were magnetically active, it could serve to couple adjacent iron islands with sufficiently small inter-island spacing. Modified island coupling would alter the iron film shape anisotropy and coercivity, as well as induce a superparamagnetic to ferromagnetic transition after capping for certain critical thicknesses of iron.

Despite the evidence in favor of non-trivial magnetic behavior at the Fe-MgO interface discussed above, iron films failed to exhibit out-of-plane easy axes for any thickness from 1 Å to 50 Å within 800 Oe of applied field as measured by *in-situ* polar MOKE magnetometry. Neither capping with MgO nor annealing before or after MgO capping caused the iron films to exhibit out-of-plane easy axes. To explore why this was the case, the effective PMA energy of MgO-capped films was measured as the area between

the in-plane and out-of-plane SQUID hysteresis loops, using the method described in Section 2.5. Linear fit of the experimental values of effective perpendicular anisotropy ($K_{eff}^{\perp}$) allowed extraction of the surface anisotropy and critical thickness, which were found to be $K_S = 0.17 \pm 0.19$ erg/cm^2 and $t_{cr} = 3.2 \pm 3.7$ Å, respectively. This value of t_{cr} is far lower than that predicted by Hallal *et al.* [40]. and is consistent with near zero interface anisotropy. However, even if the best case value of $t_{cr} = 7$ Å is assumed, a practical problem presents itself. As shown in Fig. 3.7, the iron films grown at RT exhibited only superparamagnetism for all thicknesses below 9 Å. Note that this general behavior was observed for many more samples than were used to measure $K_{eff}^{\perp}$ in Fig. 3.7. Therefore, under these conditions, any iron film thicker than the island coalescence limit will be ferromagnetic but will have in-plane magnetic preferred axes. Consequently, for films without active substrate cooling during growth, dominant PMA is inaccessible in the Fe-MgO system due to unfavorable film growth dynamics.

The discrepancy between the experimental results and the predicted values for PMA can be accounted for in several ways. First, the oxidation state of the MgO surface may not be ideal for e-beam evaporated MgO [125, 126, 40]. Second, a reacted interfacial FeO_x or spinel-like $MgFe_xO_y$ compound may interfere with the desired rehybridization needed for interface PMA, and this is difficult to address due to the high oxidation potential of iron [140]. Third, island formation or crystal defects in these films may disrupt long-range magnetic ordering near the Fe-MgO interface, which is difficult to mitigate due to the high surface energy mismatch and strain between iron and MgO [134]. Further study is needed to determine if low temperature growth is the key to producing contiguous iron films at low temperature [141]. Another avenue for exploration would be to determine the extent to which continuous sample rotation during growth suppresses the formation of iron corrugations, producing a more uniform initial iron film.

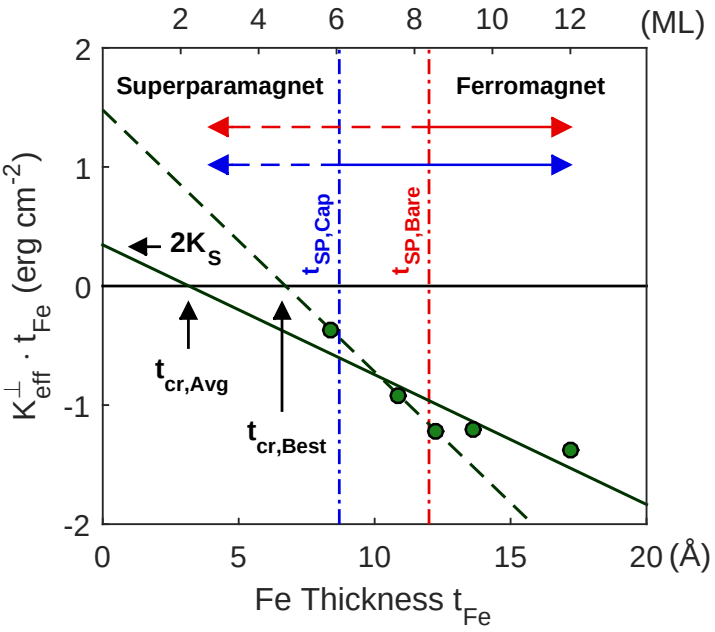

Figure 3.7: Volume-normalized effective perpendicular anisotropy times iron thickness vs. iron thickness for MgO/Fe(t)/MgO (001). PMA is dominant for $K_{eff}^{\perp} > 0$. Experimental data are shown as solid green circles, linear least squares fit is the solid green line, and the most optimistic fit (using only the three data points at low thickness) is the dashed green line. Surface anisotropy K_S and critical thickness t_{cr} are extracted from linear fits. Superparamagetism is observed for Fe thicknesses $t_{SP,Bare} < 12$ Å and for $t_{SP,Cap} < 9$ Å. MgO capping induces a transition to ferromagnetism for Fe thicknesses between 9 Å and 12 Å. The optimistic value of t_{cr} lies below the thickness where only superparamagnetism is observed for all films. Therefore, dominant PMA is inaccessible for the processing conditions used here.

3.7 Summary

It has been shown that ultra-thin iron grown epitaxially on MgO(001) at RT via molecular beam epitaxy formed an interfacial Fe-O-like chemical bond that leads to a significant chemical shift for the iron $2p$ orbital relative to that of bulk iron as evidenced by *in-situ* X-ray photoemission spectroscopy. *In-situ* polar MOKE magnetometry revealed that Fe/MgO (001) did not exhibit PMA before or after capping with MgO, or after a subsequent 300 °C UHV anneal. Generally, the MgO/Fe(t)/MgO(001) films are superparamagnetic for $t_{Fe} < 9$ Å, and strongly in-plane magnetized for $t_{Fe} > 9$ Å. If a

PMA spin reorientation transition exists for this system, it occurs at thicknesses below the experimentally observed superparamagnetic limit and is therefore inaccessible with growth conditions typically employed in magnetic thin film growth. Instead, the in-plane uniaxial magnetic anisotropy induced by oblique incidence Fe growth was found to be dampened or reversed after deposition of MgO capping layers. Additionally, a transition from superparamagnetism to ferromagnetism was observed for films within the thickness range of 9 Å $< t_{Fe} <$12 Å. All of these observations may be explained by the formation of a thin, magnetically active oxide at the Fe-MgO interface that helps to couple iron islands produced by a Volmer-Weber growth mode and self-shadowing.

Chapter 4

Perpendicular magnetic anisotropy in Mn_3Ge

Distort the structure,

magnetism follows suit.

Can you make a film?

4.1 Introduction

The work detailed in the previous chapter attempted to exploit interface anisotropy to produce perpendicular magnetic anisotropy (PMA) in ultra-thin Fe films deposited on MgO (001) substrates. In this chapter, a new strategy for achieving PMA is presented, which takes advantage of strong bulk magnetocrystalline anisotropy. Mn_3Ge has $D0_{22}$ crystal structure with lattice parameters $a = b = 3.82$ Å and $c = 7.26$ Å, as shown in Fig. 4.1(a) [18]. Mn_3Ge can be thought of as Heusler-like, with the equivalent $L2_1$ crystal structure corresponding to a Mn_2MnGe formula unit. Taken on its own, the loss of uniqueness of the Y atom in the X_2YZ formula unit would give $D0_3$ crystal structure.

However, in Mn_3Ge this combines with an expansion between atomic planes layered in the [001] direction. This breaks the cubic $Fm\bar{3}m$ space group symmetry of the $L2_1$ phase into the tetragonal $I4/mmm$ space group of the $D0_{22}$ phase. The unique axis of the tetragonal crystal becomes the magnetic easy axis because crystal symmetry is reflected in magnetocrystalline anisotropy [23].

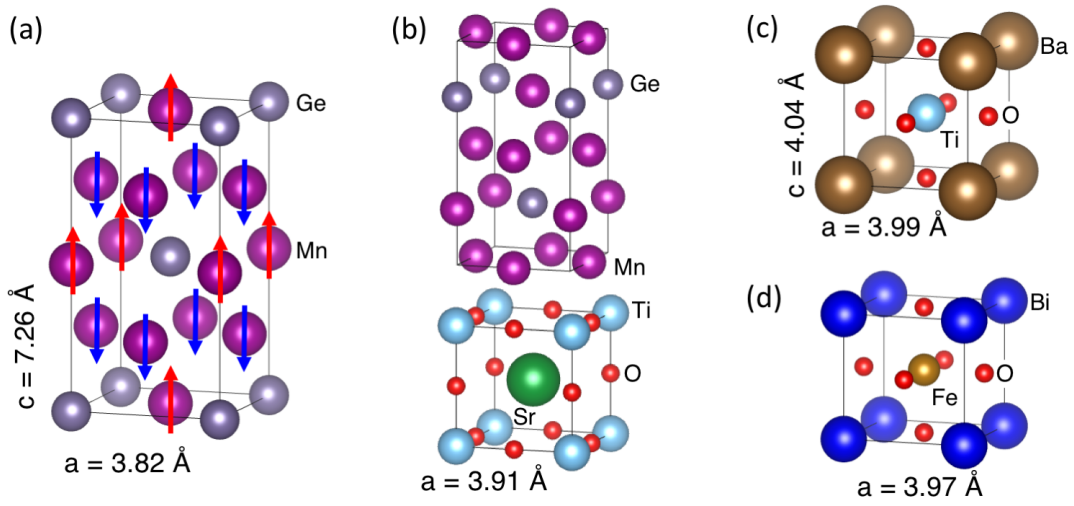

Figure 4.1: Crystal structure diagrams for (a) stoichiometric $D0_{22}$ Mn_3Ge showing ferrimagnetic spin texture as red and blue arrows, (b) likely interface termination arrangement for $Mn_3Ge/SrTiO_3$ (001), (c) tetragonal $BaTiO_3$, and (d) pseudo-cubic (rhombohedral) $BiFeO_3$.

Due to the atomic basis of the Ge atoms, the Mn atoms in the X_2-like sites and XZ-like sites have different chemical environments. This causes different magnetic moments to develop on each type of Mn atom. The Mn atoms in the X_2-like sites ($4d$ Wyckoff position) have a moment of $\mu_{4d} = 1.8\ \mu_B$, while those in the XZ-like sites ($2b$ Wyckoff position) have a moment of $\mu_{2b} = -2.6\ \mu_B$, each aligned along the c axis [18]. The total moment is the sum of the moments in the formula unit, $m = 2\mu_{4d} + \mu_{2b} = 1.0\ \mu_B$. This is in accordance with the Slater-Pauling rule for full-Heuslers, $m = N_V - 24 = 3 \times 7 + 4 - 24 = 1$. The anti-alignment of these two inequivalent spin lattices produces ferrimagnetic behavior, which increases the magnetic anisotropy along the c axis. The uniaxial anisotropy is

reported as $K_U = 2.3 \times 10^7$ erg/cm^3 [142], two orders of magnitude higher than typical values found in ferromagnets with cubic crystal symmetry.

In a polycrystalline film, this uniaxial anisotropy would be randomly aligned with small crystallites and would not provide much benefit for devices. On the other hand, Mn_3Ge epitaxially grown on substrates lattice-matched to its basal plane would effectively pin the unique axis out-of-plane, thereby making the uniaxial anisotropy useful for spintronic applications. Previously, this has been accomplished by growing Mn_3Ge on $SrTiO_3$ (STO) substrates, which gives 2.3% tensile lattice mismatch with a 1:1 coincident lattice for the basal plane [142, 18]. In contrast, the c axis would provide 7.0% tensile lattice mismatch with a 2:1 coincident lattice, which is far more unfavorable. Thus, preference is established for epitaxy with cube-on-cube orientation Mn_3Ge[100](001)//STO[100](001). This and several other epitaxial relationships are summarized in Table 4.1.

Material	Orientation	Structure	a (Å)	c (Å)	ϵ_{aa} (%)	ϵ_{ac} (%)
Mn_3Ge	[100](001)	$D0_{22}$	3.816	7.261	0.0 (1:1)	-4.9 (2:1)
$SrTiO_3$	[100](001)	perovskite	3.905	-	-2.3 (1:1)	-7.0 (2:1)
$BaTiO_3$	[100](001)	perovskite	3.992	4.036	-4.4 (1:1)	-9.1 (2:1)
$BiFeO_3$	[100](001)	∼perovskite	3.965	-	-3.8 (1:1)	-8.4 (2:1)
MgO	[100](001)	rocksalt	4.212	-	-9.4 (1:1)	-13.8 (2:1)
Cr	[110](001)	bcc	2.91	-	-7.3 ($\sqrt{2}$:1)	-11.8 ($2\sqrt{2}$:1)
Co_2MnAl	[110](001)	Heusler	5.75	-	-6.1 (1:$\sqrt{2}$)	-10.7 ($\sqrt{2}$:1)

Table 4.1: List of materials used in this chapter, along with their epitaxial orientation with respect to the Mn_3Ge basal plane, crystal structure type, lattice parameters, lattice strain and related coincident lattice (in parentheses) for epitaxy with the Mn_3Ge $a-a$ basal plane, and with respect to the Mn_3Ge $a-c$ plane. Negative strain values indicate the film is under tensile strain. Larger strain is more unfavorable. Since all strain values for the Mn_3Ge $a-c$ plane are higher in magnitude than that of the $a-a$ basal plane, epitaxy for a (001) basal plane is established. Coincident lattices containing a $\sqrt{2}$ have a 45° rotation between substrate and film.

In addition to its favorable crystalline and magnetic properties, Mn_3Ge has an electronic structure that, at first glance, makes it a strong candidate as an electrode in magnetic tunnel junctions. As shown in Fig. 4.2, the Δ_1 Bloch band is fully spin-polarized

for electrons with momentum along the z axis, allowing Mn_3Ge-based magnetic tunnel junctions to take advantage of the spin-filtering effect when using MgO tunnel barriers [62], as discussed in Section 1.7. On the other hand, there is also a report that the spin-polarization of Mn_3Ge depends on interface termination [60]. A Mn-Mn terminated interface with MgO produces large positive tunneling magnetoresistance, while a Mn-Ge terminated interface gives a smaller, negative tunneling magnetoresistance due to the anti-alignment of the two inequivalent spin sublattices. Since it is difficult to control the interface termination over wide areas due to atomic-scale roughness, Mn_3Ge may not be suitable as an electrode in spin-transfer torque magnetic tunnel junction applications [60].

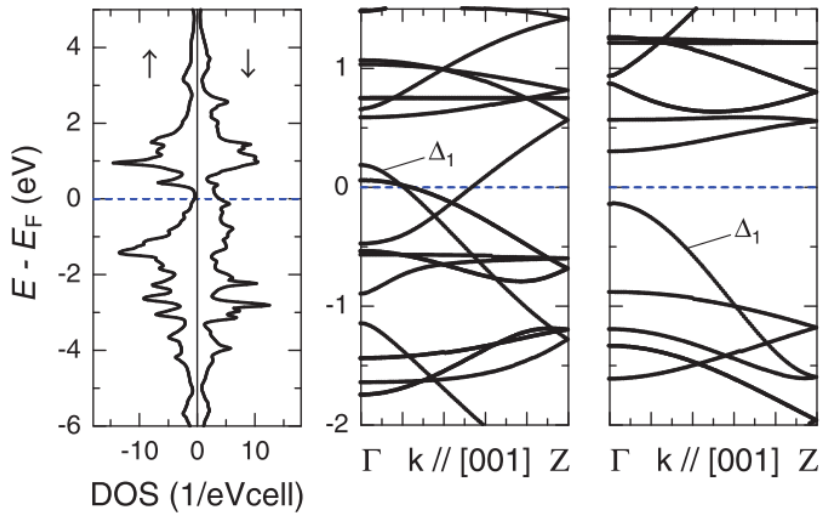

Figure 4.2: Density functional theory calculations for Mn_3Ge showing (Left) spin-resolved density of states, and (center) spin-up and (right) spin-down energy dispersion in the tunneling direction. The Δ_1 Bloch state is fully polarized, which means that Mn_3Ge can take advantage of the spin-filtering effect in MgO tunnel barrier based magnetic tunnel junctions. Figure reprinted with permission from [142].

As previously described in Section 1.8, spin transfer torque is the industry standard for changing the state of magnetic tunnel junctions. However, magnetoelastic switching is expected to require orders of magnitude less power, with dissipation in the range of

several attojoules (10^{-18} J = 6.2 eV) per bit writing operation [76]. This motivates the exploration of magnetic materials with strong perpendicular magnetic anisotropy such as Mn_3Ge that can be deposited epitaxially on ferroelectric substrates such as $BaTiO_3$ and $BiFeO_3$.

Finally, the stoichiometry of Mn_3Ge must be addressed. While it is true that stoichiometric $Mn_{3.0}Ge$ can be stabilized in epitaxial form, the formation of the tetragonal phase from a melt or other bulk synthesis technique requires a slight off-stoichiometry of $Mn_{3+x}Ge$ with $x = 0.26$–0.55 [143]. This bulk phase stability region can be seen clearly in Fig. 4.3. Additionally, K_U has been measured to increase in the bulk phase stability region [142]. For these reasons, much of the work done in this chapter utilizes a $Mn_{3.4}Ge$ alloy. This should provide some versatility for the films, allowing them to be deposited to much greater thicknesses if required. However, no evidence of phase segregation was found for any of the stoichiometric $Mn_{3.0}Ge$ films. For this reason, the general material system will be referred to nominally as Mn_3Ge in the text, unless referring to a specific film with composition of either $Mn_{3.0}Ge$ or $Mn_{3.4}Ge$.

4.2 Substrate surface preparation

To provide the highest quality starting surfaces for growth, the cleaning regimen for each substrate type was optimized. As-received STO was etched in aqua regia (3:1 HCl:HNO_3) to remove surface impurities and a Sr–O layer, preferentially exposing the Ti–O termination [144]. The STO was then annealed in an oxygen furnace at 1050 °C for at least 8 hours, producing high quality step edges as seen in atomic force microscope in Fig. 4.4(a).

$BaTiO_3$ (BTO) substrates were cleaned using a piranha etch (4:1 H_2SO_4:H_2O_2), and subsequently annealed at 1050 °C in an oxygen furnace to promote smoothness and

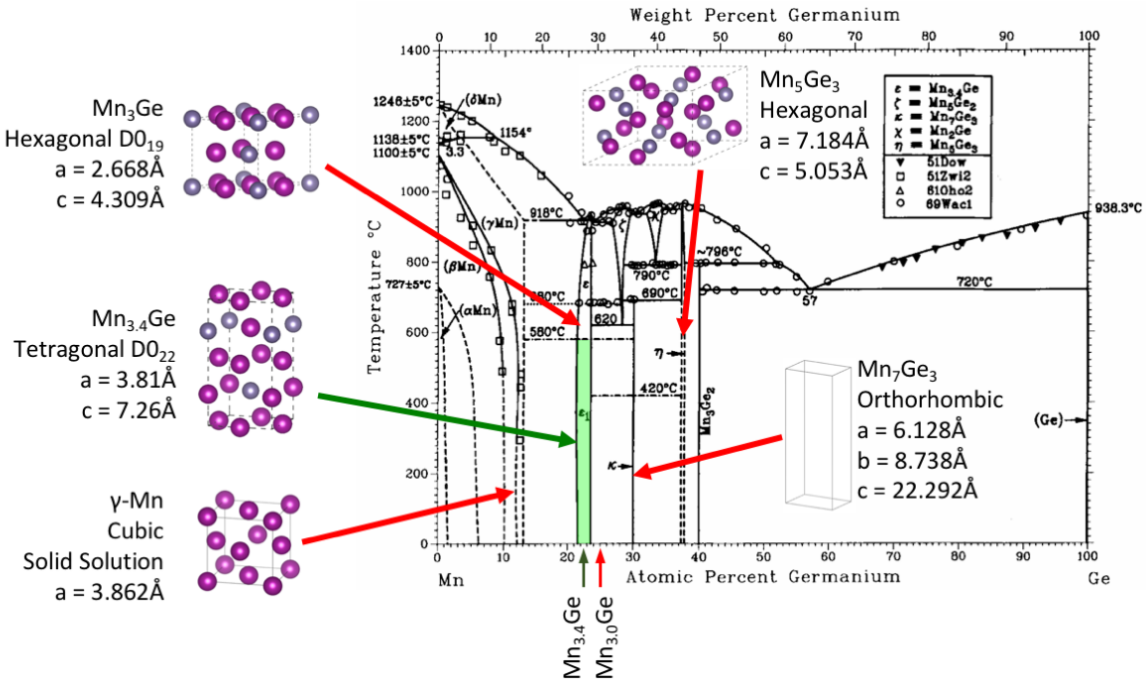

Figure 4.3: Mn–Ge phase diagram showing 11 stable phases. The crystal structures associated with phases likely to result from poorly calibrated growth flux are also shown. Stoichiometric $Mn_{3.0}Ge$ lies in a coexistence region between the desired $D0_{22}$ ϵ_1 phase and the orthorhombic κ phase. $Mn_{3.4}Ge$ lies within the desired ϵ_1 region. Figure adapted from [143].

eliminate water absorbed in the hygroscopic surface [145]. The overall surface morphology of BTO did not change significantly, with flat terraces and deep trenches present as seen in Fig. 4.4(b). However, particulates observed in AFM on as-received substrates vanished after the cleaning procedure. Furthermore, annealing in UHV to 500 °C was found to be beneficial for removing much of the residual hydrocarbon contamination measured by X-ray photoemission spectroscopy (XPS), as shown in Fig. 4.5. UHV ozone cleaning was also tried, but this provided only a marginal benefit. Future studies using BTO substrates would benefit from further optimization of the starting surface to eliminate the terrace/trench morphology.

$BiFeO_3/SrRuO_3/SrTiO_3$/Si (001) substrates grown using pulsed laser deposition were provided by Ramamoorthy Ramesh Group at University of California Berkeley. $BiFeO_3$

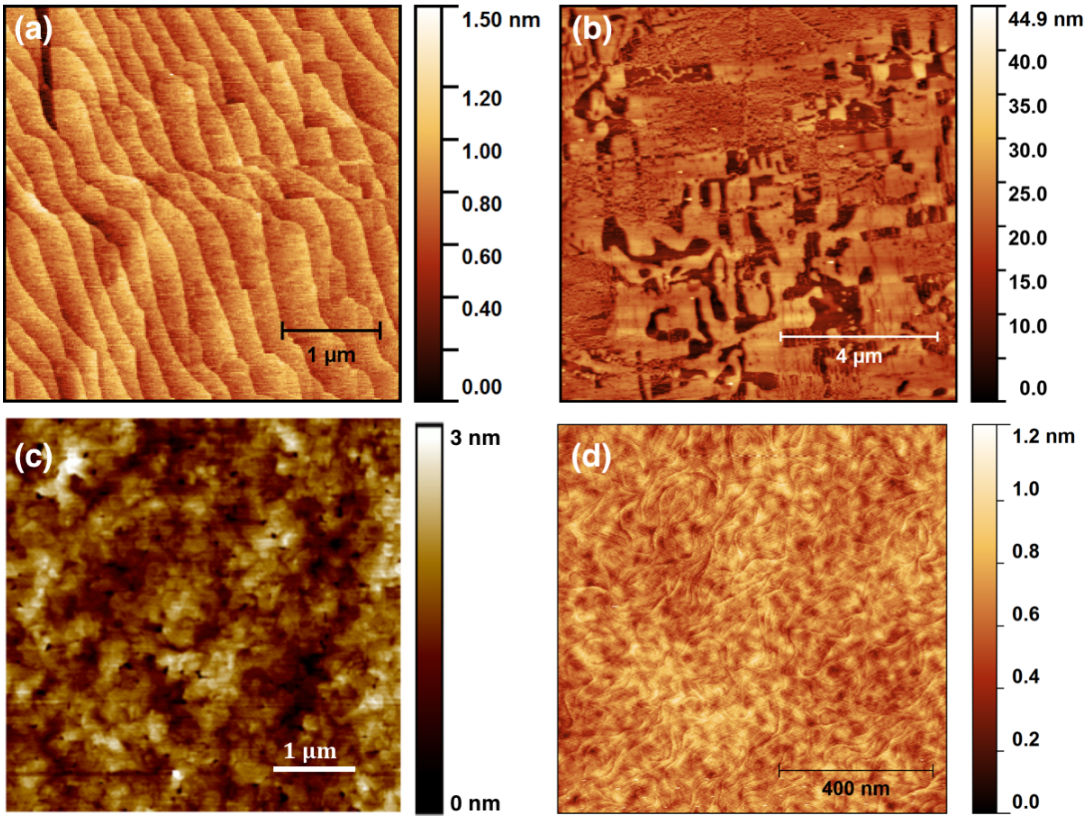

Figure 4.4: (a) AFM of STO substrate after 5 min etch in aqua regia and subsequent 10 hr 1050 °C anneal in a tube furnace with oxygen ambient. (b) AFM of BTO substrate after 5 min piranha etch and 1050 °C oxygen furnace anneal. (c) AFM of BFO substrate immediately after pulsed laser deposition. (d) Scanning tunneling micrograph of 20-nm-thick Cr deposited on MgO at room temperature, then annealed to 500 °C for 45 min.

(BFO) is a strong ferroelectric but is susceptible to various forms of decomposition and phase segregation. Heating above 300 °C in UHV was suspected to result in oxygen loss, limiting options for cleaning and growth conditions. Exposure to residual water vapor and other contaminants in the atmosphere, and in nitrogen ambient storage to a lesser degree, degrades the films over time. This degradation did not respond to UHV ozone cleaning or outgassing. The pulsed laser deposition technique used to grow BFO substrates could only produce small samples (5×5 mm^2) with great effort. Thus, attempts to wet etch the BFO surface before loading in were discouraged. The best method found to prepare

BFO substrates for Mn_3Ge growth was to load them into UHV as soon as possible after the substrates were shipped to UCSB.

Finally, preparation of MgO and Cr/MgO substrates is described in Section 2.12. A scanning tunneling microscope image of a typical prepared Cr/MgO (001) surface is shown in Fig. 4.4(d).

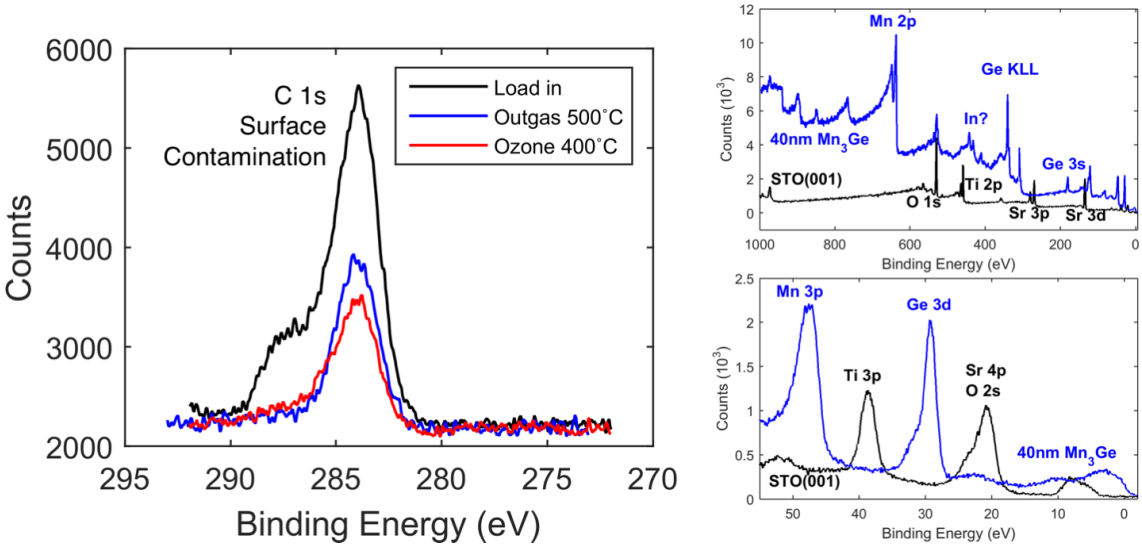

Figure 4.5: X-ray photoemission spectroscopy for a BTO surface showing a decrease in the area under the carbon 1s peak after a 500 °C anneal in UHV, and after a UHV ozone surface cleaning step. Common core level peaks for STO and Mn_3Ge are also shown.

4.3 Epitaxial growth of Mn_3Ge

Previous work on this topic utilized Mn_3Ge co-sputtered onto STO [18], MgO [27], Cr or TaN [60] layers, after which the films were annealed to high temperatures to obtain the $D0_{22}$ phase. In contrast, here Mn_3Ge is codeposited onto various substrates using MBE, with each substrate requiring different growth conditions. Growth studies in this work began using STO substrates due to their low cost and high availability. The low lattice mismatch (see Table 4.1) and low surface roughness (see Fig. 4.4) of STO enabled

high quality growth of $Mn_{3.0}Ge$ and $Mn_{3.4}Ge$. A 1-unit-cell-thick nucleation layer was deposited at room temperature and subsequently annealed to 425 °C. The remainder of the film thickness was deposited at 400 °C. This was done to try to minimize the Volmer-Weber (island) growth mode that is commonly observed when depositing metals on oxides due to surface energy mismatch and preferential bonding to other adatoms [146]. High film strain also tends to produce islands in epitaxial films, which serve to relax strain [147]. During growth, reflection high energy electron diffraction (RHEED) was used to monitor the surface crystal quality. Mn_3Ge grown on STO substrates consistently gave bright, streaky RHEED patterns indicative of high crystal quality and low film roughness, as shown in Fig. 4.6.

The use of ferroelectric BTO substrates was limited due to their high cost. A single $10 \times 10 \times 0.5$ mm^3 wafer presently costs $350. The solution to this problem was to dice each wafer into nine equal $3 \times 3 \times 0.5$ mm^3 sections. The small area made the collection of RHEED images difficult. More importantly, the small size prevented use of indium-free sample holder blocks. The use of indium to bond the substrate, combined with the large perimeter-to-area ratio, allowed indium metal from the substrate-sample block bond to creep over the substrate and onto the film. The indium contamination was common, and visible to the eye as patches of dark reaction region near the edges of the sample. Gallium metal was also tried for bonding, but had similar effects on the film. It is unclear how much this affected the growth mechanics, although visible indium reaction regions were often seen on the substrate surface after growth. The RHEED patterns for Mn_3Ge/BTO typically contained rings indicating polycrystalline growth. Additional faint, diffuse vertical streaks were also present, but these did not depend on the in-plane orientation of the sample with respect to the RHEED beam. The presence of this additional structure in the RHEED pattern suggests that the films were textured, at best in the out-of-plane direction with random in-plane misorientations.

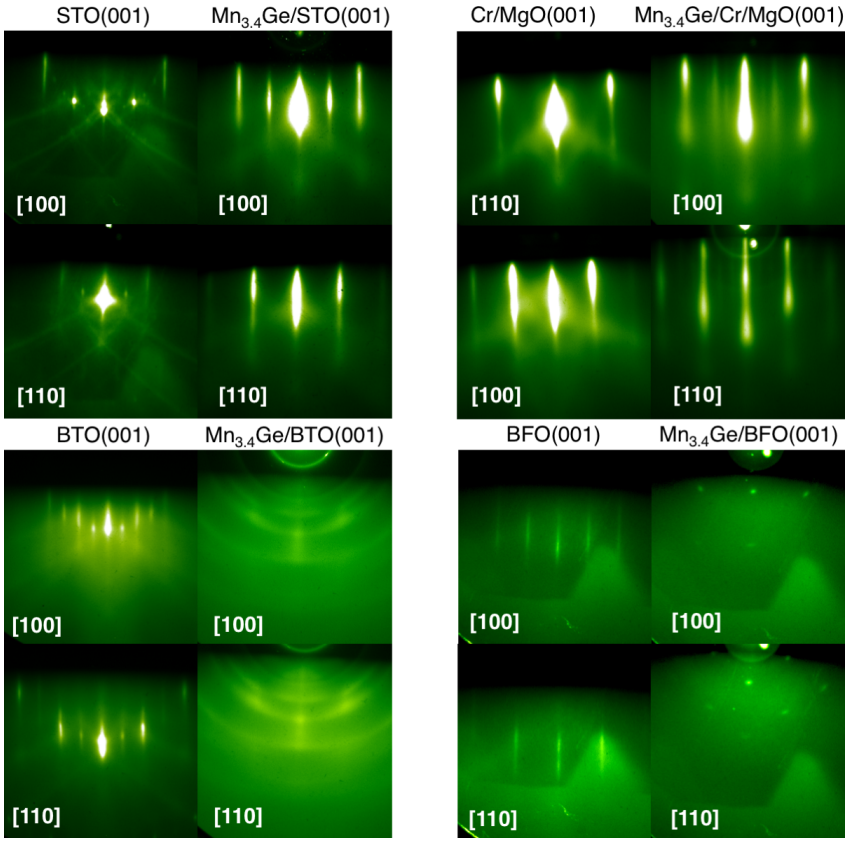

Figure 4.6: Reflection high energy electron diffraction patterns for the starting surfaces and for 20-nm-thick $Mn_{3.4}Ge$ grown on the four indicated substrates. Vertical streaks indicate high crystal quality and smoothness. Spots indicate surface roughness. Rings indicate polycrystalline growth. A diffuse background indicates high surface roughness and/or crystal disorder.

The lack of epitaxy on BTO substrates led to the use of a complex growth scheme where each monoatomic layer was deposited manually using precisely timed shutter operations. First, a Mn_2 monolayer (ML) was deposited to establish interface termination, then a MnGe monolayer, then a Mn_2 monolayer, etc. This allowed control over the out-of-plane crystal order despite the lack of rotational order of the crystallites. Growth conditions that led to out-of-plane magnetic easy axes were: 8 ML deposited at $T_{sub} = 100$ °C, followed by 8 ML deposited at 200 °C, followed by 10 ML deposited at 300 °C, and whatever remainder of the desired thickness deposited at 360 °C.

For Mn_3Ge deposited on BFO substrates, a 1-unit-cell-thick nucleation layer was deposited at 200 °C, and the remainder of the film was grown at 300 °C. Spots and a very diffuse background seen in RHEED indicate the film was at least partially epitaxial, but had either high roughness, low crystal ordering, or both.

4.4 Film morphology

A previous study of thin-film growth of Mn_3Ga by RF sputtering showed that the surface has a terrace/trench morphology [148]. Another study of Mn_3Ge-based magnetic tunnel junctions utilized DC magnetron sputtering and found similar roughness when the growth occurred at high substrate temperatures [60]. This is very similar to the morphology observed in Mn_3Ge studied in the present work. As shown in Fig. 4.7, the films exhibit an island growth mode that can best be described as a densely packed cobblestone network of nano-nuggets. Each nugget is about 100 nm wide and slightly taller than the nominal film thickness, with an approximately flat top corresponding to the (001) crystal facet. The island growth mode is typically found when a film is attempting to relieve strain or to expose a substrate with lower surface energy. Since all the substrates used here have lattice parameter slightly larger than that of the Mn_3Ge basal plane, all the films are under tensile strain. Films deposited on the oxides STO, BTO, BFO, and MgO likely suffer from dewetting related to surface energy mismatch, although the same morphology is observed for films grown on metallic Cr layers, suggesting that the island morphology in Mn_3Ge is primarily due to high film strain, as shown in Table 4.1.

High growth temperatures are needed to maintain a high degree of crystal order during growth, but also likely contribute to the formation of nano-nuggets due to enhanced mass transport via surface diffusion. The solution found by Jeong *et al.* [60] was to grow 2-nm-thick Mn_3Ge at T_{sub} = 450 °C, then grow the remainder of the film at 150 °C to

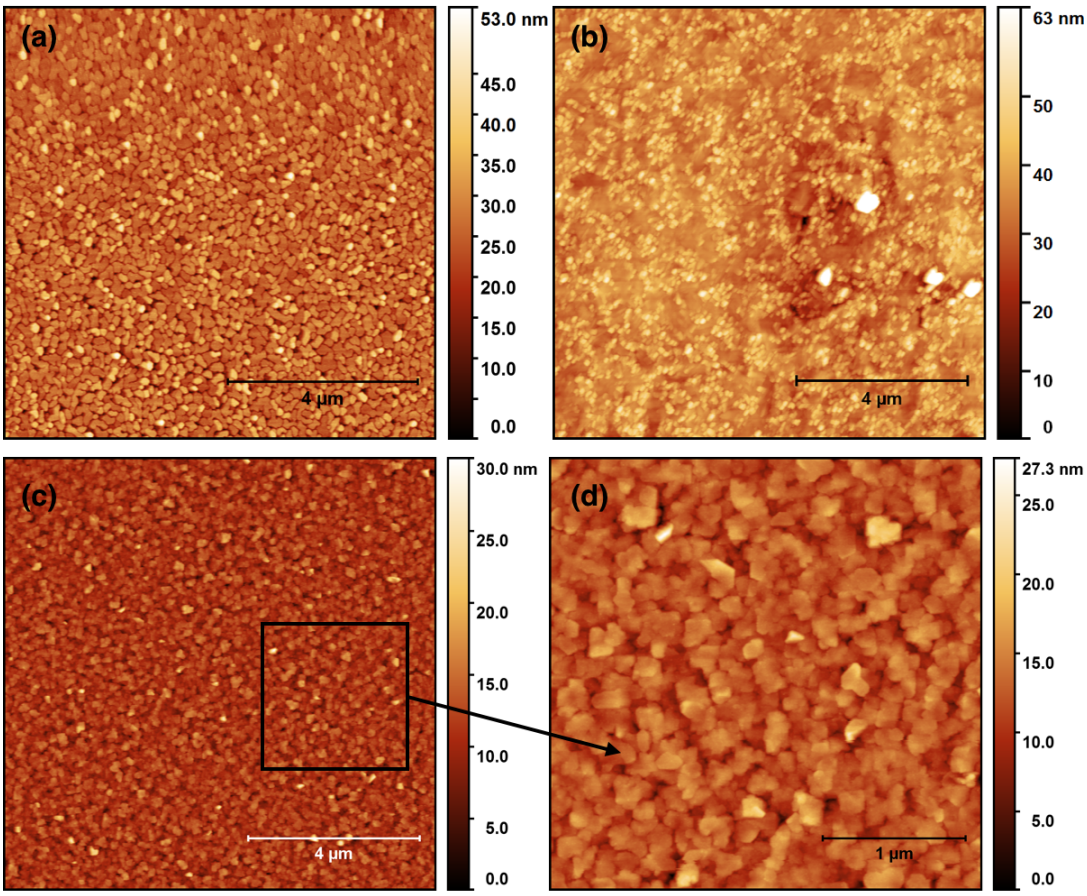

Figure 4.7: Atomic force micrographs showing 20-nm-thick $Mn_{3.4}Ge$ deposited on (a) STO (001) at T_{sub} = 400 °C, (b) BTO (001) using a growth temperature ramping recipe ranging from T_{sub} = 100 to 360 °C, (c,d) Cr/MgO (001) at T_{sub} = 200 °C.

promote smooth film growth . A final 450 °C anneal for 1-2 hrs resulted in smooth films with high perpendicular magnetic anisotropy. It may be worth applying this three step growth recipe in future studies of Mn_3Ge, though it is likely exact recipe will need to be adjusted for synthesis via molecular beam epitaxy. However, the growth recipe described in the previous section for BTO substrates used a similar tactic and resulted in high perpendicular magnetic anisotropy, but no Mn_3Ge diffraction peaks were observed in XRD and the nano-nugget morphology persisted.

4.5 Structural characterization

A summary of the high resolution X-ray diffraction (XRD) results is shown in Fig. 4.8. Mn_3Ge films deposited on STO (001) had high crystal quality as indicated by the presence of both a (002) and (004) Bragg reflection and the absence of any stray peaks corresponding to reaction phases or crystal misorientations. High angle annular dark field scanning transmission electron microscope (STEM) images shown in Fig. 4.9 show that Mn_3Ge has reasonable crystal registry with the STO substrate despite the presence of a dark line between the two materials suggesting interface disorder or contamination. Crystallites with small random rotational mismatches can also be seen throughout the film. The terrace/trench morphology is confirmed, and the trenches are observed to reach all the way to the substrate. Despite this, each island is sufficiently connected to its neighbors to allow percolation of electrical current and magnetotransport analysis, which will be discussed later.

No Bragg peaks were initially observed in XRD for Mn_3Ge films deposited on BTO (001), indicating a high degree of crystal disorder. Extremely long measurement times (12 hours) did reveal the presence of a weak (004) reflection, confirming that the manual shutter sequence growth recipe did produce some out-of-plane (001) crystal texture.

Mn_3Ge films deposited directly on MgO (001) were epitaxial with high crystal quality, but the (002) Bragg reflection is weak compared to growths on STO substrates. On the other hand, growth on Cr/MgO (001) substrates lacked any (002) diffraction peak, indicating a high amount of disorder between the Mn_2 and MnGe monolayers.

BFO substrates, perhaps unsurprisingly, proved to be the most susceptible to reactions during growth. Fig. 4.8(d) shows rocking curves of the same BFO/$SrRuO_3$/$SrTiO_3$/Si (001) substrate both before and after growth of a 20-nm-thick $Mn_{3.0}Ge$ layer. Multiple peaks from reaction or decomposition phases are labeled with a (?). None of these peaks corre-

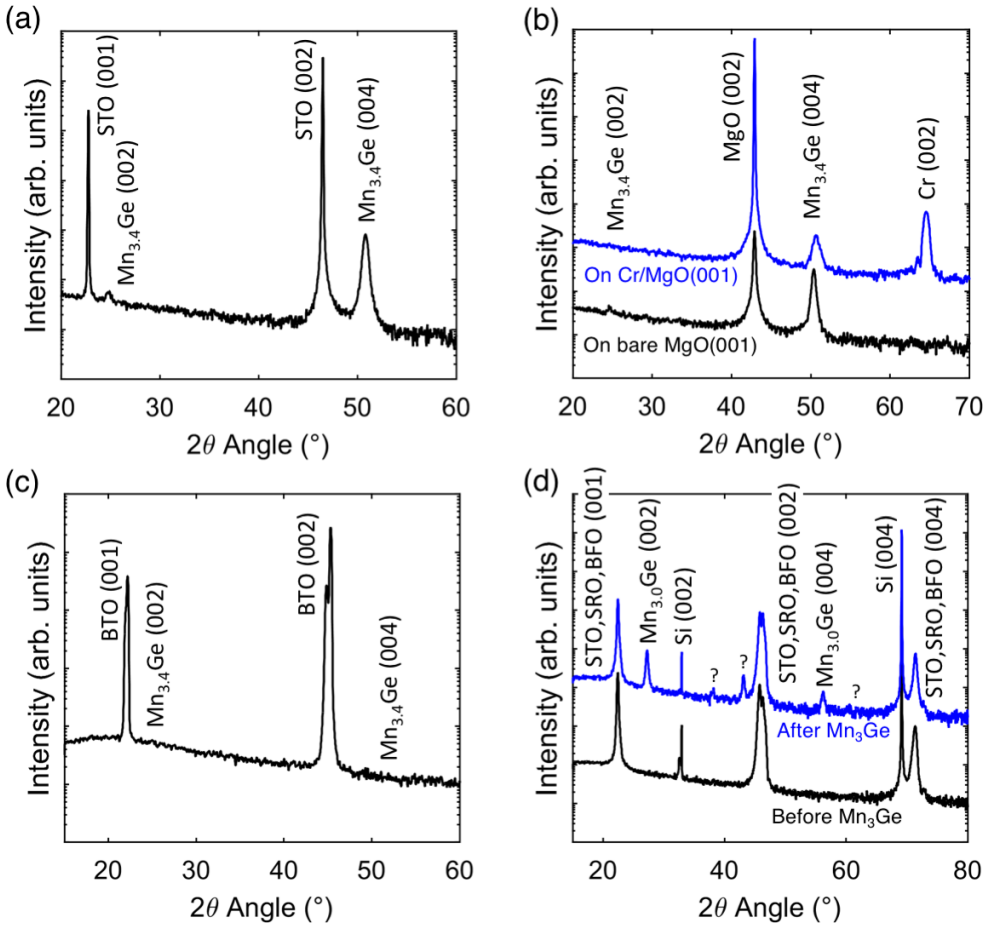

Figure 4.8: On-axis X-ray diffraction rocking curves for 20-nm-thick $Mn_{3+x}Ge$ films deposited on cleaned and prepared (a) $SrTiO_3$ (001), (b) Cr/MgO (001), (c) $BaTiO_3$ (001), and $BiFeO_3$ (001) substrates. Anomalous peaks indicating mixed phase and/or orientation are marked with a (?).

spond to misorientations of $D0_{22}$ Mn_3Ge. Furthermore, the peaks labeled as Mn_3Ge (002) and (004) correspond to an out-of-plane lattice parameter of 6.54 Å, far lower than the expected 7.261 Å. The peaks do not correspond to any of the likely decomposition phases in the Mn–Ge phase diagram, or Bi–Fe–O phase diagram [143, 149]. None of the peaks seem to correspond to the most stable reaction products such as Mn_2O_3, MnO, GeO_2, $MnFeO_3$, or Bi_2O_3, although there are hundreds of other candidate compounds in the Bi–Fe–O–Mn–Ge system [149]. This suggests that growth of Mn_3Ge is unfavorable on BFO substrates under the conditions described above. Further work is needed to develop

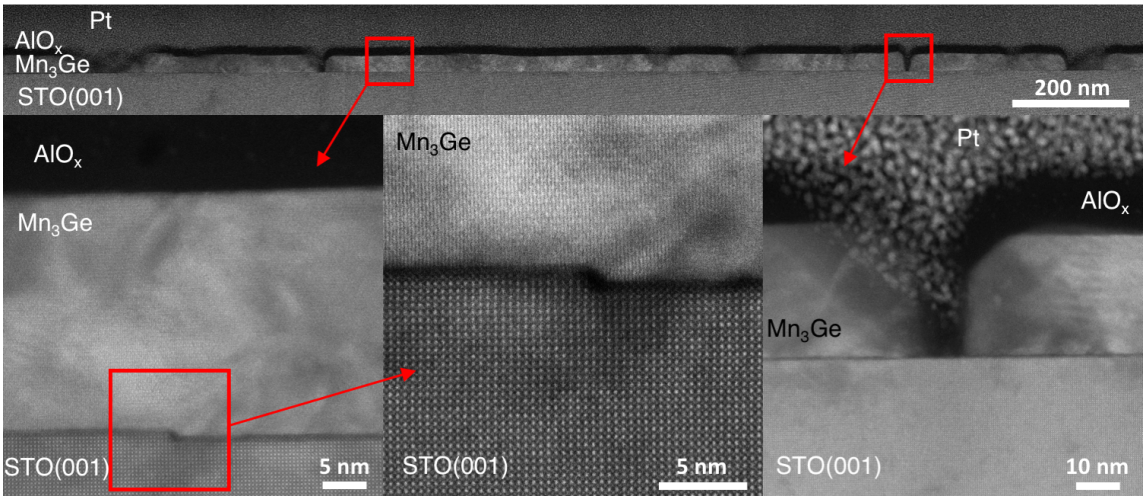

Figure 4.9: High angle annular dark field scanning transmission electron microscopy for 20-nm-thick $Mn_{3.0}Ge$/STO (001). The island growth mode observed in AFM can also be seen here as large valleys in the cross section image. The alternating columns of Mn and Ge atoms corresponding to $D0_{22}$ structure can be clearly seen in Z-contrast in the center image. Despite a thin reaction or disordered layer indicated by the dark interfacial region, good crystal registry seems to be preserved between Mn_3Ge and the STO substrate.

growth conditions that prevent interfacial reactions. Alternatively, a diffusion barrier layer may be helpful for preventing reactions between BFO and Mn_3Ge [21].

4.6 Magnetic properties

The magnetic properties of Mn_3Ge films were measured using a superconducting quantum interference device (SQUID) magnetometer. The summary of the results is shown in Fig. 4.10. Mn_3Ge deposited on STO (001) substrates exhibited strong perpendicular magnetic anisotropy, with magnetization consistent with prior reports [18, 142, 60]. The coercive field was found to be 7T for $Mn_{3.0}Ge$, and 4T for $Mn_{3.4}Ge$. A small paramagnetic signal can be seen at low field in the SQUID data, but this is likely to be an impurity in the substrate since it appears to be the same shape and magnitude in both the in-plane and out-of-plane hysteresis loops. A bare STO substrate without a Mn_3Ge

film was also found to possess a small paramagnetic background with approximately the same magnitude as seen in Fig. 4.10(a), suggesting that the paramagnetic signal is due to a substrate impurity.

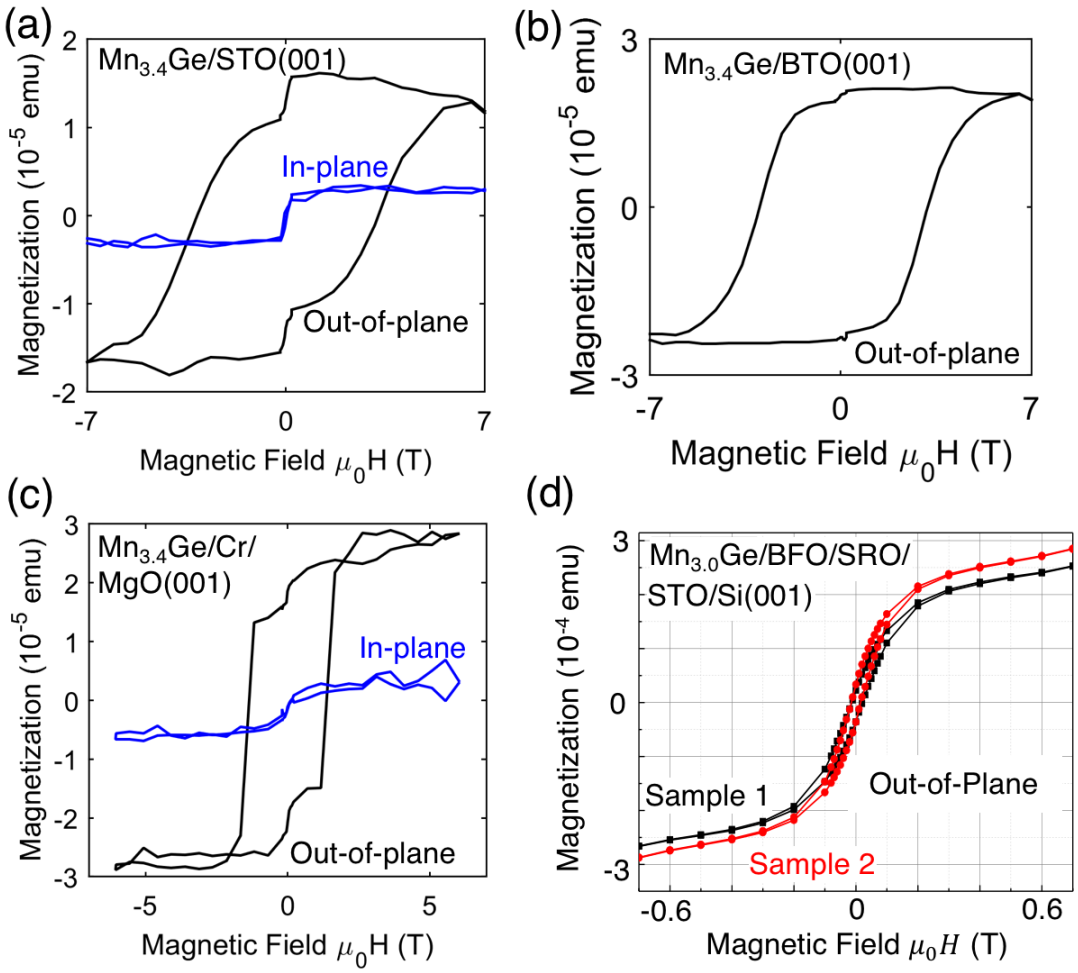

Figure 4.10: SQUID magnetometer data showing magnetization for the indicated films. Each film is approximately 20-nm-thick.

Mn_3Ge deposited on ferroelectric BTO (001) substrates had high quality out-of-plane hysteresis loops with coercive field of 4T and strong perpendicular magnetic anisotropy. This result was one of the primary goals of the present study. The dominant out-of-plane magnetization of films grown on both STO (001) and BTO (001) was confirmed using anomalous Hall effect measurements as shown in Fig. 4.11. Since anomalous Hall effect

measures only the conductive film, and not the substrate, the absence of the paramagnetic signal confirms that it likely originates from substrate impurities.

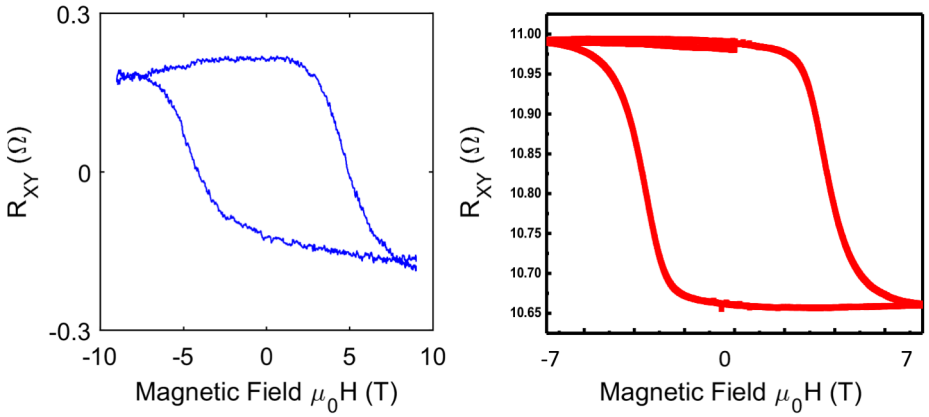

Figure 4.11: Anomalous Hall effect data for (Left) 20-nm-thick $Mn_{3.4}Ge$/STO (001), and (right) 20-nm-thick $Mn_{3.4}Ge$/BTO (001).

Mn_3Ge films deposited on Cr/MgO (001) substrates had an out-of-plane easy axis indicating strong perpendicular magnetic anisotropy, but the coercive field of 2T is much smaller than the expected 4T. This could be due to easier domain wall motion in Mn_3Ge due to the metallic interface with the substrate. Substantial reactions between Cr and Mn_3Ge are unlikely due to the absence of extra peaks in XRD. Additionally, the sample magnetization is consistent with expectations, suggesting that Cr did not incorporate into the Mn_3Ge in large amounts, which would result in lower magnetization according to the Slater-Pauling rule (see Section 1.3).

Mn_3Ge films deposited on BFO (001) substrates did not possess out-of-plane easy axes or any indications of strong perpendicular magnetic anisotropy. This is likely due to the presence of reaction phases that interfere with growth of the $D0_{22}$ Mn_3Ge phase. The reaction may also interfere with the ferroelectric properties of BFO, making this system non-ideal for ferroelectric switching of magnetization without significant future work to optimize growth conditions.

4.7 Ferroelectric switching of magnetization

The magnetic properties of the $Mn_{3.4}Ge$ films grown on BTO substrates were deemed sufficiently successful to attempt experiments related to ferroelectric switching of magnetization. These experiments were carried out at UC Berkeley by Nikita Gaur, advised by Professor Ramamoorthy Ramesh.

After growth, the $Mn_{3.4}Ge$ films were allowed to cool, and Pt electrodes were deposited on top by ebeam evaporation. After shipping the samples to Berkeley, Pt was also deposited on the back of the BTO wafer to form a capacitor structure. Applying a large voltage to this structure should switch the ferroelectric domains of the BTO, introducing strain into the overlaying $Mn_{3.4}Ge$ film. It was hoped that the strain would be sufficient to switch the magnetization state of Mn_3Ge via magnetostriction effects [74, 75, 76]. This voltage was applied in the absence of any magnetic field to avoid the possibility of trivial magnetic switching. Meanwhile, the anomalous Hall voltage of the $Mn_{3.4}Ge$ film was measured while applying an in-plane DC current of 10 μA. Any changes in magnetization would be detected as a change in anomalous Hall voltage. As shown in Fig. 4.12, a hysteresis loop in anomalous Hall resistance is observed as a function of applied out-of-plane voltage. This initially seemed to indicate that the $Mn_{3.4}Ge$/BTO system does, in fact, exhibit ferroelectric switching of magnetization.

Unfortunately, it was later discovered that the application of large voltages across the capacitor structure created microscopic cracks in the Pt/$Mn_{3.4}Ge$ layer above the BTO substrate due to the large changes in strain. Cycling the applied voltage formed cracks and resealed them hysteretically, creating alternating labyrinthine networks of conductive pathways through the upper electrode. This crack formation is what produced the hysteresis loop in Fig. 4.12. After this realization, the ferroelectric magnetization switching project was suspended.

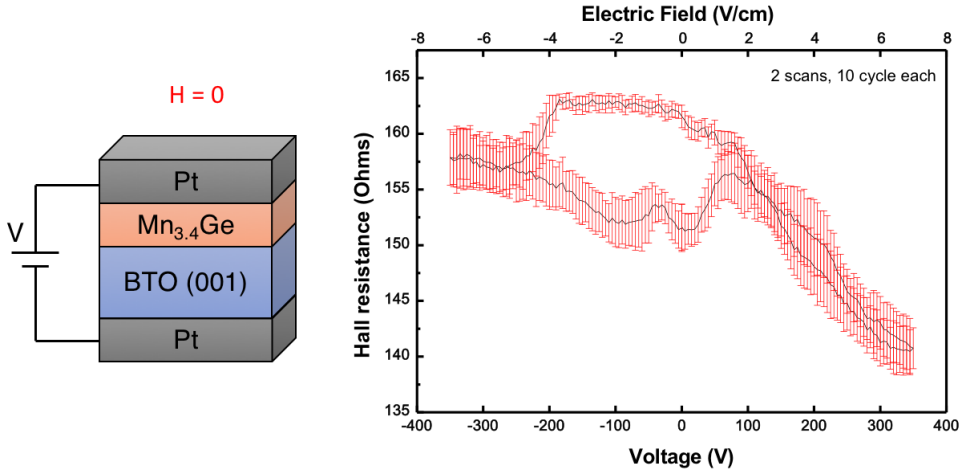

Figure 4.12: A variable voltage was applied out-of-plane to $Mn_{3.4}Ge$/BTO (001) using Pt electrodes. A hysteresis loop in the Hall voltage is observed in response.

4.8 Growth of Mn_3Ge on Co_2MnAl

Despite the lack of evidence of ferroelectric switching of magnetization, Mn_3Ge could potentially be used as an out-of-plane pinning layer for a weaker ferromagnet in a device such as a magnetic tunnel junction. To explore this possibility, $Mn_{3.4}Ge$ was grown on a [Co_2MnAl/Fe_2MnAl] (CFMA) superlattice-based magnetic tunnel junction structure. The superlattices themselves will be discussed in Chapter 5. The important detail here is that the surface termination layer of the superlattice was Co_2MnAl, and it was this surface on which $Mn_{3.4}Ge$ was grown at $T_{sub} = 300$ °C. The device structure was Pt(3nm)/ $Mn_{3.4}Ge$(10nm)/ CFMA(5nm)/ MgO(2nm)/ CFMA(20nm)/ Cr(20nm)/ MgO (001), as shown in Fig. 4.13.

RHEED images were bright and streaky throughout the growth, indicating a smooth film with high crystal quality. However, it is clear from the AFM image in Fig. 4.13 that the growth conditions used were not ideal. The tendency for $Mn_{3.4}Ge$ to form islands was greatly enhanced on the Co_2MnAl surface, even though the growth temperature was lower than that used for oxides. The tensile biaxial strain of 6.1% is the likely cause of this

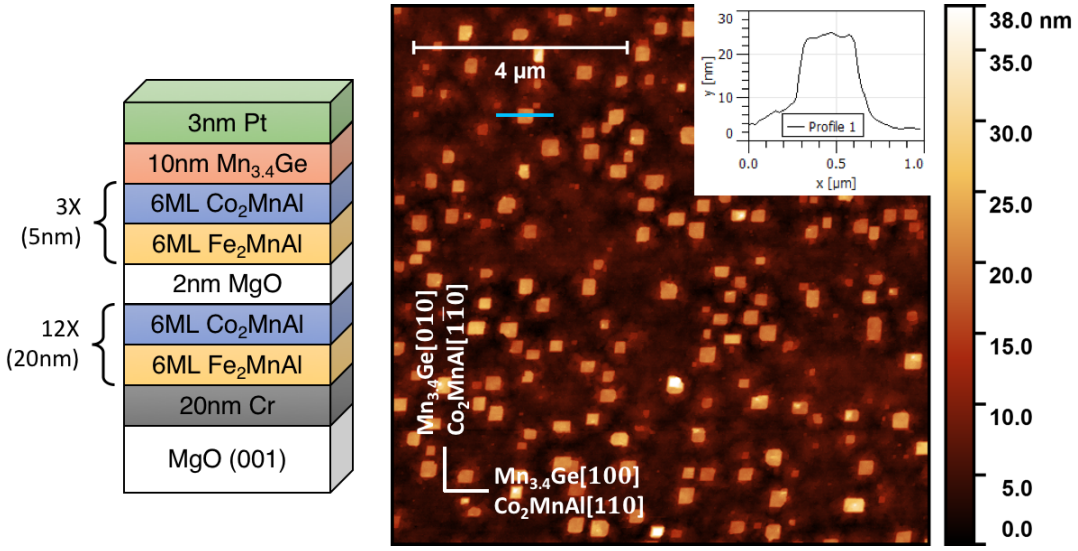

Figure 4.13: (Left) Schematic of the magnetic tunnel junction device stack grown. ML = monoatomic layer. (Right) Atomic force microscope image showing 10-nm-thick $Mn_{3.4}Ge$ deposited on the Co_2MnAl surface at 300 °C substrate temperature. The material arranges into square mesas aligned with the $Mn_{3.4}Ge < 100 >$ directions at this growth temperature. A line scan is shown in the inset, corresponding to the horizontal blue line shown in the main image.

behavior, perhaps combined with increased adatom mobility on a Heusler-like surface. Future growths should employ low substrate temperatures followed by a post-growth anneal to obtain high crystal quality, which should help to avoid dewetting.

The average height of the AFM image was found to be 6.5 nm. This is the approximate thickness of the material in the mesas if it were deposited uniformly. This is less than the 10 nm of Mn_3Ge deposited, which may indicate that the growth exhibited Stranski-Krastanov growth. A relatively smooth nucleation layer, followed by the growth of the rectangular mesas to relieve strain, would account for the observed AFM image.

XRD results indicate that the device structure had high crystal quality, and the Pt capping layer maintained epitaxial orientation with the top electrode. However, no peaks corresponding to $D0_{22}$ $Mn_{3.4}Ge$ were observed. This could be due to low crystal quality as a result of the low growth temperature used, or possibly because the total areal coverage of the $Mn_{3.4}Ge$ islands was low.

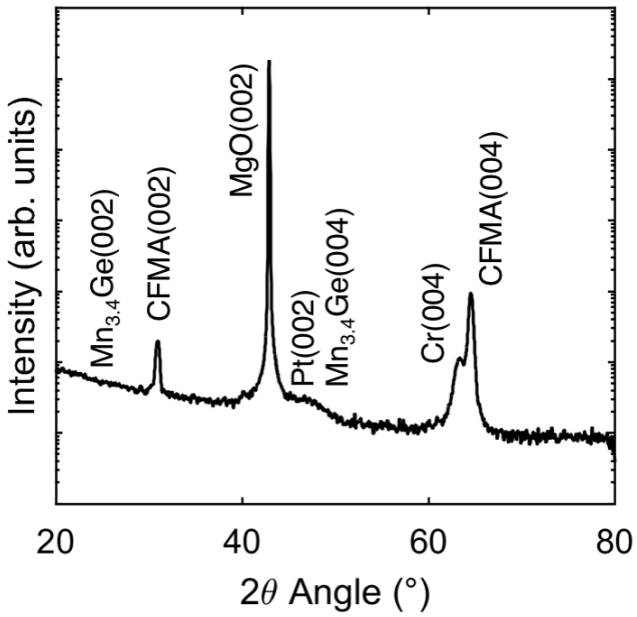

Figure 4.14: XRD on-axis rocking curve for the device stack shown schematically in Fig. 4.13.

Despite the non-ideality of the morphological and structural characteristics, the magnetization data are promising. As shown in Fig. 4.15, the two ferromagnetic layers of the magnetic tunnel junction switch at different coercive fields, resulting in an in-plane hysteresis loop with two segments. The larger of the switches corresponds to the 20-nm-thick CFMA bottom electrode, while the smaller switch corresponds to the upper $Mn_{3.4}Ge$/CFMA electrode. The magnetization contribution from the upper electrode is $\sim 1 \times 10^{-4}$ emu. Note that the ferromagnetic switch of the bottom electrode is sharp, while that of the top electrode is gradual, suggesting a partially hard axis in-plane.

On the other hand, the out-of-plane data show mainly a hard axis due to the in-plane magnetized lower CFMA electrode. A central loop is also observed possibly corresponding to the switching of the upper electrode with an out-of-plane component of magnetization. This explanation is bolstered by looking at the inset of Fig 4.15(b), where the hard axis signal has been subtracted away. The total remaining signal has a range of $\sim 0.8 \times 10^{-4}$ emu, close to the magnitude observed for the upper electrode in the in-plane

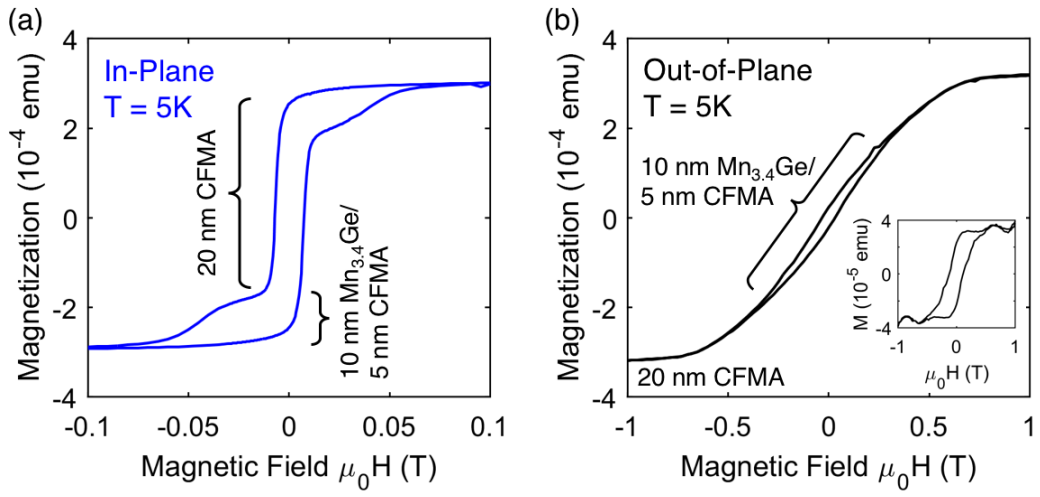

Figure 4.15: SQUID magnetization data for the CFMA-based magnetic tunnel junction structure with $Mn_{3.4}Ge$ pinning layer. (a) In-plane hysteresis loop and (b) out-of-plane hysteresis loop. The inset shows the out-of-plane hysteresis loop with the hard axis subtracted, leaving only the contribution of the upper electrode.

data. This would seem to suggest that the $Mn_{3.4}Ge$ does act as a pinning layer, even in this case of extreme island morphology. Future work should involve further optimization of the growth conditions of $Mn_{3.4}Ge$ on Heusler compounds.

Chapter 5

Epitaxial Heusler Superlattice Co_2MnAl/Fe_2MnAl with Perpendicular Magnetic Anisotropy and Termination-Dependent Half-Metallicity

5.1 Introduction

Spintronic devices require a source of spin-polarized current, and ferromagnetic metals are commonly used for this purpose due to their imbalance of spin up and spin down electron density of states near the Fermi level [4]. Two physical phenomena useful for the improvement of ferromagnetic electrodes used in magnetic tunnel junctions are perpendicular magnetic anisotropy (PMA) [42] and half-metallicity [36, 61]. Extensive research has been conducted to realize these features independently, for example in CoFeB/MgO

[42], Co_2MnSi [36], and Co_2MnSi/MgO [61]. Others have combined separate material systems into hybrid electrodes where a thin half-metal is magnetically pinned in the out-of-plane direction by an adjacent layer with strong PMA [150]. The compensated ferrimagnet Mn_2Ru_xGa can be integrated into perpendicular magnetic tunnel junctions and is predicted to be half-metallic under specific conditions [151, 152]. However, thus far, a single material exhibiting both PMA and half-metallicity has yet to be experimentally confirmed. In this work, we present a promising Heusler atomic superlattice that exhibits both PMA and half-metallicity, albeit for separate samples with different growth conditions.

Half-metals are ferromagnets that possess an energy gap in the minority spin density of states and a Fermi level position that lies within that gap. Consequently, they behave like a metal for one spin channel and a semiconductor for the other, resulting in 100% spin-polarized conduction electrons. Many half-metals have been predicted to exist within the cobalt-based full-Heusler family of materials. Full-Heuslers have molecular formula X_2YZ, where X and Y are typically d- or f-block elements and Z is typically an sp element. In the ideal $L2_1$ crystal structure, the Y and Z atoms form a rocksalt lattice that is filled with X atoms in each of the eight tetrahedral sites, resulting in $Fm\bar{3}m$ space group symmetry. Full-Heusler compounds also commonly crystalize in the B2 (CsCl) structure that represents disorder between the Y and Z atomic sites, which changes to $Pm\bar{3}m$ space group symmetry. In both cases, full-Heusler compounds possess cubic symmetry that gives rise to cubic magnetocrystalline anisotropy that, on its own, cannot overcome thin film magnetic shape anisotropy to yield PMA.

Recently, it was predicted that atomic superlattices of certain pairs of Heusler materials could be perpendicularly magnetized half-metals [153]. Heusler superlattices are distinct from other magnetic multilayers because they maintain the same crystal structure and, in many cases, several of the same atomic species in both constituent layers. The

uniaxial anisotropy in the growth direction arises from changes in electronic structure between layers, and from lattice distortions produced by variations in lattice constant between parent bulk crystals [153]. Equivalently, symmetry breaking due to the layer structure results in tetragonal space group symmetry, which gives rise to tetragonal magnetic anisotropy with the unique axis aligned out-of-plane. In addition, the mixing of electronic states across sublayers is calculated to have a Fermi level tuning effect. Two Heusler compounds that are not half-metallic may combine into a superlattice with the Fermi level within the minority spin gap, forming a half-metal [153].

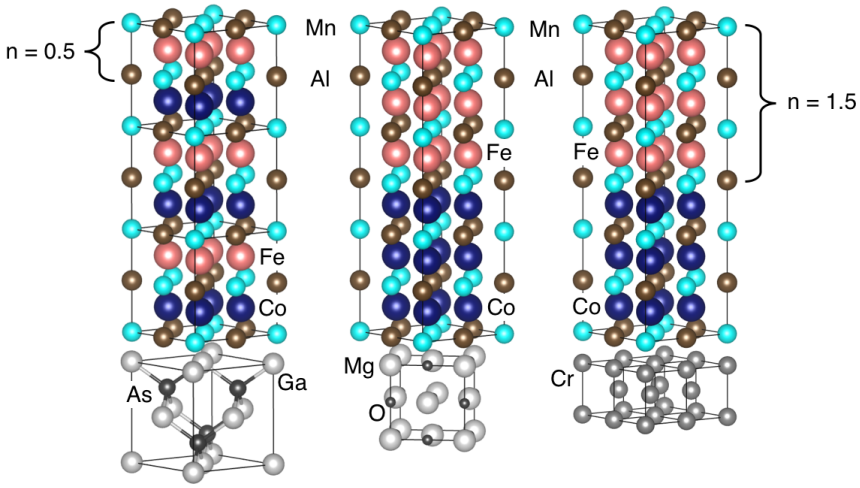

Figure 5.1: Schematics of crystal structure and epitaxial relationship for (left) $[CMA_{0.5}/FMA_{0.5}]_3$/GaAs (001), (center) $[CMA_{1.5}/FMA_{1.5}]_1$/MgO (001), and (right) $[CMA_{1.5}/FMA_{1.5}]_1$/Cr (001) viewed along the Heusler [110] direction.

The superlattice composed of Co_2MnAl (CMA) and Fe_2MnAl (FMA) layered along the [001] direction is predicted to exhibit both PMA and half-metallicity for specific superlattice periodicities [153]. We adopt the convention of Azadani *et al.* [153] and grow superlattices with nominal layering of n = 0.5 and n = 1.5, where n is the thickness of each CMA or FMA sublayer in fractions of a Heusler unit cell. These are stacked to produce $[CMA_n/FMA_n]_q$ films, where q is the total number of bilayers in the superlattice,

as shown in Fig. 5.1. Defined in this way, the reduced space group symmetry of the superlattice is $P4/nmm$ [154]. However, in this work, all Heusler lattice parameters and Bragg reflections are given in terms of the $L2_1$ structure.

5.2 Experiment

The $[CMA_n/FMA_n]_q$ films were deposited on GaAs (001), MgO (001), and chromium-buffered Cr (001)/MgO (001) via molecular beam epitaxy in a modified Veeco Gen II growth chamber with base pressure $< 5 \times 10^{-11}$ Torr. For growth on GaAs, epi-ready GaAs (001) wafers were prepared by thermal desorption of the surface oxide under As_4 overpressure in a VG V80H growth chamber, after which a GaAs buffer was grown. After cooling, a sacrificial arsenic capping layer was deposited *in-situ*. The wafer was then loaded out of ultra-high vacuum (UHV) and stored in inert atmosphere. Before growing a Heusler film, a cleaved section of the As/GaAs (001) wafer was loaded back into UHV where the arsenic cap was thermally desorbed, resulting in a (2x4)/c(2x8) reconstruction in reflection high energy electron diffraction (RHEED). For growth on MgO, MgO (001) substrates were annealed at 800°C for 12 hours in an oxygen ambient furnace to reduce root mean square (RMS) surface roughness to 2 Å [123]. The MgO substrates were then annealed in UHV at 600°C for 30 min, followed by deposition of a 10 nm thick MgO buffer layer at 530°C substrate temperature by e-beam evaporation of stoichiometric source material to bury any remaining surface contamination. For MgO with a chromium buffer layer, a 25 nm thick chromium layer was then deposited from a standard effusion cell onto the prepared MgO (001) substrate held at room temperature. The Cr/MgO (001) was subsequently annealed at 500°C for 45 min until the surface became smooth, as indicated by streaky RHEED patterns. *In-situ* scanning tunneling microscopy of the annealed chromium surface showed atomic steps and RMS roughness

of 1.2 Å, which is a favorable starting surface for growth of magnetic tunnel junction layers. A scanning tunneling microscope image of this surface can be seen in Fig. 2.18.

The Heusler films were grown by co-evaporation of elemental source material from standard effusion cells. Superlattices were grown by setting atomic fluxes such that $\Phi_{Co} = \Phi_{Fe} = 2\Phi_{Mn} = 2\Phi_{Al}$. In addition, some samples were grown with an increased aluminum flux up to 50% excess, while keeping other fluxes constant. This allowed for constant co-deposition of the MnAl rocksalt sublattice, while shutters were used to select either cobalt or iron to grow CMA or FMA, respectively. Fluxes were calibrated before each growth using a beam flux gauge mounted to the sample manipulator. The beam equivalent pressure of each effusion cell was calibrated to its true atomic flux calculated from measurements of total elemental atomic layer deposition using Rutherford backscattering spectrometry (RBS) on MgO calibration samples. Superlattice $[CMA_n/FMA_n]_q$ films with periodicity n = 0.5 and 1.5 were grown with q = 34 and 12 full periods, respectively, which gave a film slightly over 20 nm thick in each case. Growth temperatures depended on the substrate chosen, and will be discussed in the following section.

During Heusler growth, surface crystal quality was monitored by *in-situ* RHEED. After growth, samples were capped with 10 nm AlO_x deposited by *in-situ* e-beam evaporation of Al_2O_3 source material to prevent film oxidation, and loaded out of UHV for *ex-situ* characterization. Film morphology was measured with atomic force microscopy (AFM) in tapping mode. Initial crystal quality was measured by Cu $K_{\alpha 1}$ X-ray diffraction (XRD) open detector rocking curves, while lattice parameters were extracted from XRD reciprocal space maps (RSM) collected with a CCD line detector, as described in Section 2.8. Magnetic hysteresis loops were collected using a Quantum Design MPMS XL SQUID. Anomalous Hall effect was measured in a Quantum Design PPMS for Hall bars defined using photolithography and argon ion milling. Film thicknesses were measured by X-ray reflectometry (XRR). Sample areas were determined photographically.

5.3 Structural Quality

For growths on GaAs (001), $[CMA_n/FMA_n]_q$ films were grown from 150°C to 300°C substrate temperature, resulting in films with a (002) Bragg reflection in XRD indicating at least partial B2 ordering as shown in Fig. 5.6. Fast diffusion of adatoms along arsenic dimer rows produced corrugations visible in AFM along GaAs $[1\bar{1}0]$, which resulted in root mean square (RMS) surface roughness of 8.3 Å for the final AlO_x-capped Heusler films. The roughness is also apparent in RHEED images, indicated by spottiness along the diffraction streaks as shown in Fig. 5.3(a) and (d). For growths on MgO (001), $[CMA_n/FMA_n]_q$ films with a (002) reflection present were obtained both for samples grown at 300°C, and for those grown at room temperature and subsequently annealed at 300°C for 15 min. Islands 40 nm wide and 1 to 4 nm tall visible in AFM resulted from surface energy mismatch and 2.9% tensile lattice mismatch, giving an RMS roughness of 6.0 Å. These islands were also present for A2 (bcc solid solution) films lacking a (002) Bragg reflection, grown at room temperature with no subsequent anneal, suggesting the island morphology was not caused by dewetting at high temperatures. RHEED images showing a c(2x2) reconstruction with prominent half-order streaks along [110] indicated high quality Heusler growth and suggested an $L2_1$-like surface unit cell [155]. Finally, $[CMA_n/FMA_n]_q$ grown on Cr/MgO (001) at 250°C had a (002) Bragg reflection and exceptionally smooth surface morphology with 2.4 Å RMS roughness. Bright half-order streaks and Kikuchi lines in RHEED images confirmed smooth surfaces and high crystal quality suitable for fabrication of devices such as magnetic tunnel junctions. These results are summarized in Table 5.1.

Aluminum content had no significant effect on RHEED patterns, which were determined primarily by the substrate chosen and the growth temperatures used. No surface reconstructions other than (1x1) or c(2x2) were observed for any of the epitaxial Heusler

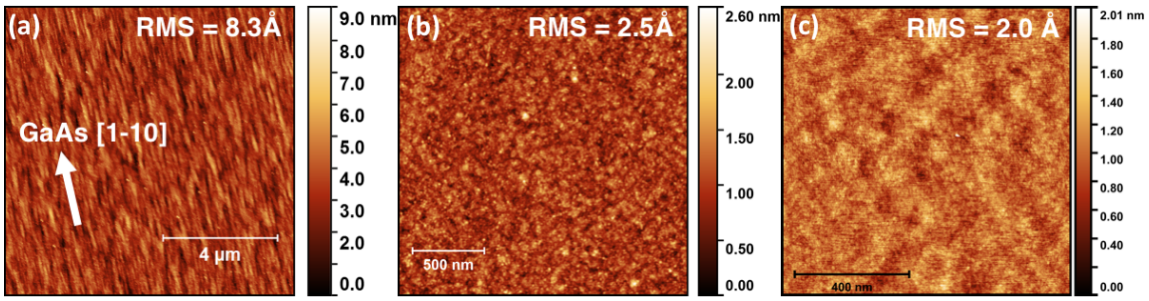

Figure 5.2: 20-nm-thick $[CMA_n/FMA_n]_q$ grown on (a) GaAs (001), (b) MgO (001), and (c) Cr/MgO (001) substrates.

Substrate	a (Å)	ϵ_{xx} (%)	c/a	T_g (°C)	σ_{RMS} (Å)
GaAs (001)	5.653	-2.4	1.02–1.06	150	8.3
MgO (001)	4.212	2.9	0.96–0.99	300	6.0
Cr/MgO (001)	2.91	0.5	1.00	250	2.4

Table 5.1: Summary of substrate lattice parameters, in-plane biaxial strain for superlattice films with $a_0 = 5.79$ Å, typical tetragonal distortion values, optimized substrate temperature during growth (T_g), and RMS roughness determined by AFM for 20 nm thick superlattice films.

films. High aluminum content was associated with higher (002)/(004) Bragg peak area ratios in XRD, but this could also be accounted for by variations in growth temperatures and thus higher or lower degrees of chemical ordering.

XRD reciprocal space maps of the $[CMA_n/FMA_n]_q$ (224) reflections shown in Fig 5.4 were collected along with a nearby substrate reflection. Using these off-axis peaks, the in-plane and out-of-plane lattice parameters of the superlattice were calculated using the method described in Section 2.8. The $[CMA_n/FMA_n]_q$ films were partially to fully strained to the substrates, with the degree of relaxation increasing slightly with higher growth and annealing temperatures. This resulted in tetragonal distortion c/a = 1.02 to 1.06 for films deposited on GaAs (001), c/a = 0.96 to 0.99 for films deposited on MgO (001), and c/a = 1.00 for films deposited on lattice matched Cr/MgO (001). The $[CMA_n/FMA_n]_q$ relaxed cubic lattice parameter $a_0 = 5.79$ Å was extracted from a linear fit of a vs. c.

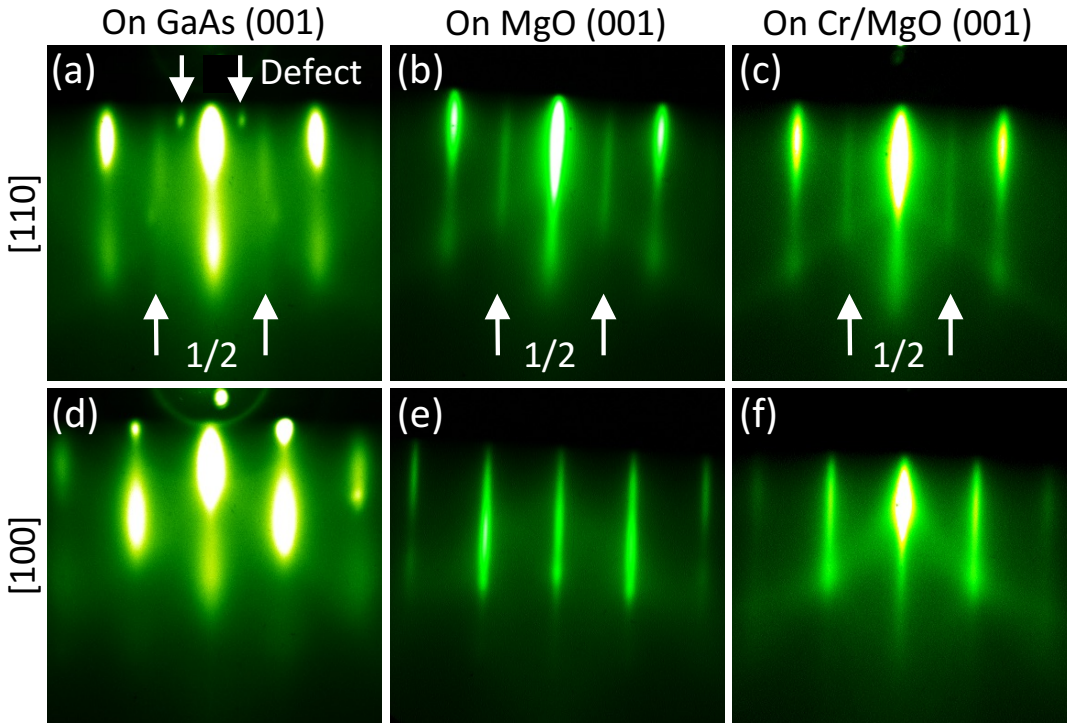

Figure 5.3: RHEED images of 20 nm thick $[CMA_n/FMA_n]_q$ films grown on indicated substrates along Heusler (a-c) [110] and (d-f) [100] directions. Half-order streaks along [110] indicate an $L2_1$-like surface unit cell. Faint spots visible in (a), which vanish after annealing to 300°C, are attributed to crystal twinning at low growth temperatures.

Based on diffraction structure factor calculations discussed in Section 2.7, the presence of a Heusler (111) Bragg reflection indicates at least partial $L2_1$ ordering. A (111) reflection was observed in XRD RSMs for pure Fe_2MnAl films but was not observed for any Co_2MnAl or superlattice films. Additionally, cross-sectional high angle annular dark field scanning transmission electron microscope (HAADF-STEM) images shown in Fig. 5.5(a) indicate B2 ordering for a $[CMA_{1.5}/FMA_{1.5}]_{12}$/GaAs (001) film grown at 150°C substrate temperature. This is apparent from the lack of a characteristic brickwork pattern expected from the alternating manganese and aluminum atomic columns when viewed along the [110] direction in the $L2_1$ structure [17], as shown in Fig. 5.1. Nevertheless, diffuse half-order streaks observed in RHEED shown in Fig. 5.3 along the Heusler [110] direction during and after growth suggest the surface unit cell is at least

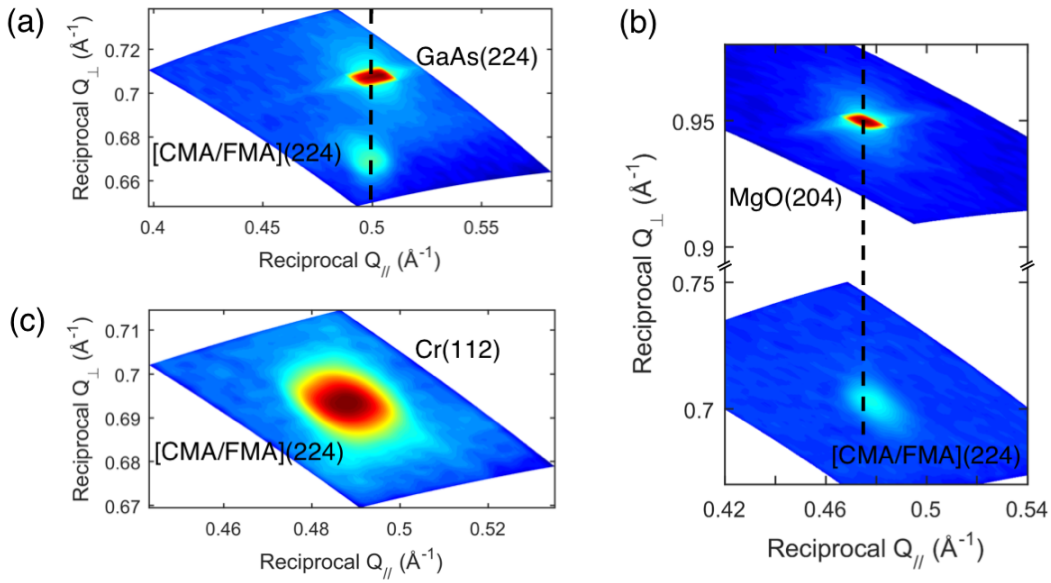

Figure 5.4: Reciprocal space maps (RSM) of 20-nm-thick $[CMA_n/FMA_n]_q$ deposited on (a) GaAs (001), (b) MgO (001), and (c) Cr/MgO (001) substrates.

partially $L2_1$-like. STEM electron energy loss spectroscopy (STEM-EELS) maps of the same region shown in Fig. 5.5(a) reveal that the superlattice structure is intact, cobalt and iron interdiffusion is low, and the thin Co_2MnAl – GaAs interface layer is gallium and cobalt rich, which could indicate an epitaxial CoGa B2 interfacial layer [156].

This analysis was then repeated for $[CMA_n/FMA_n]_q$ grown at 300°C on MgO (001). Spottiness along the diffraction streaks observed in RHEED during superlattice nucleation suggested an island growth mode and possibly the presence of microtwins, which can form during island coalescence due to slight misorientations between neighboring islands [157]. A (111) Bragg reflection was not observed in XRD RSMs, suggesting that the films are B2 ordered. However, STEM shown in Fig. 5.5(b) reveals some regions with the characteristic $L2_1$ brickwork pattern, but the pattern is not uniform across the image, suggesting mixed B2/$L2_1$ order. Additionally, a disordered region is visible within 2–3 nm of the interface with MgO. Crystallites in this region had small, random rotational mismatches, which were likely caused by the large 2.9% tensile lattice strain.

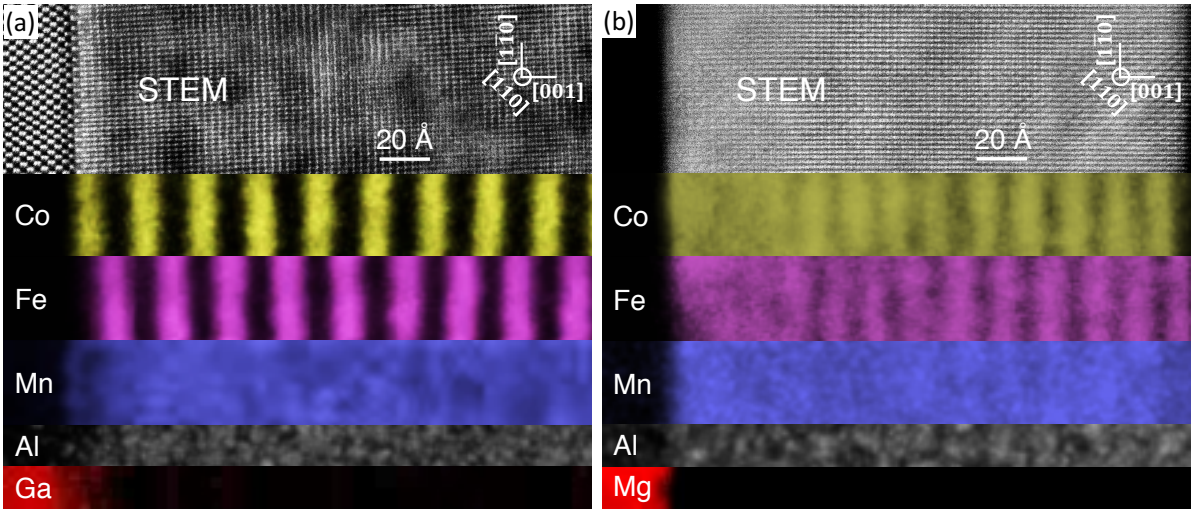

Figure 5.5: (Top row) Cross-sectional HAADF-STEM and (bottom five rows) EELS maps along the [110] direction of $[CMA_{1.5}/FMA_{1.5}]_{12}$ superlattices grown on (a) GaAs (001) at 150°C substrate temperature, and (b) MgO (001) at 300°C substrate temperature. A weak superlattice satellite peak was observed in XRD rocking curves for (a) but not for (b).

This disorder is best described as mosaic rather than polycrystalline nucleation. STEM-EELS measured complete sublayer intermixing in this interfacial region. The superlattice structure became visible further from the MgO interface, but significant apparent sublayer intermixing remained. There are two explanations for this behavior. First, diffusion of cobalt and iron within the Heusler matrix during growth could cause sublayers to mix. Layers near the MgO interface were exposed to 300°C for one hour longer than those near the surface, which could result in the observed mixing gradient. Second, the island growth morphology indicated by RHEED during Heulser growth initiation may produce height variations greater than the thickness of individual sublayers near the MgO interface. As the film becomes thicker and smoother, the roughness may drop below the sublayer thickness, allowing a superlattice structure to be observed in STEM-EELS. If the average island size is much smaller than the TEM sample thickness, this growth mode would be imaged in EELS as a mixing gradient between the bottom and top surfaces of the superlattice.

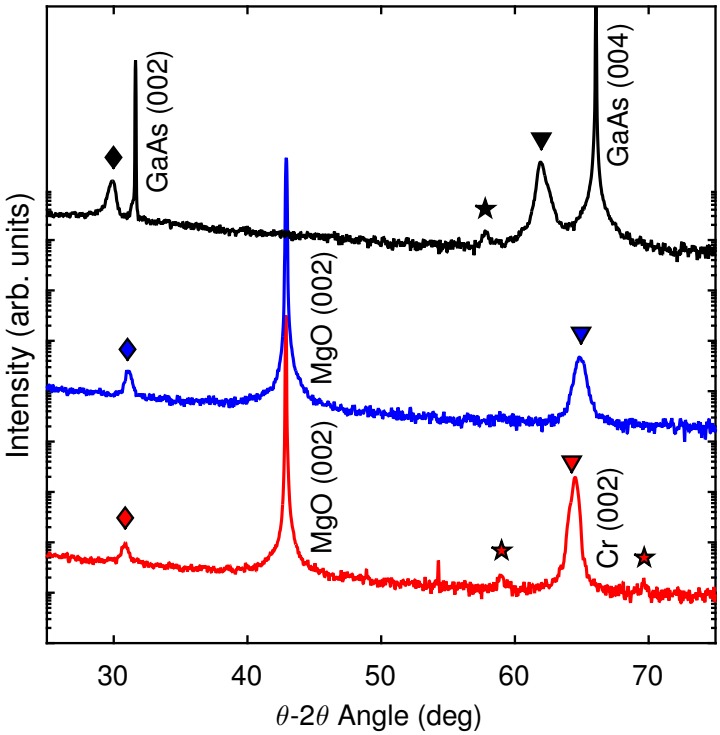

Figure 5.6: XRD on-axis rocking curves for $[CMA_{1.5}/FMA_{1.5}]_{12}$ films grown on (black line) GaAs (001), (blue line) MgO (001), and (red line) Cr/MgO (001). Atomic ordering that is at least B2 is confirmed by the presence of a Heusler (002) peak (♦) along with the (004) peak (▼). The superlattice satellite peak (★) corresponds to a periodicity of 24.6 Å for the film grown on GaAs (001), and 20.7 Å for the film grown on Cr/MgO (001). Only one satellite peak was distinguishable for films grown on GaAs (001) due to overlap with the substrate (004) peak. Satellite peaks were not observed for films grown on MgO (001) due to film roughness and/or diffusion effects.

The superlattice structures were further analyzed using superlattice satellite peaks observed in XRD. The satellite peaks are expected to be weak because the X-ray scattering form factors of cobalt and iron are quite similar. The satellite peak for the film grown on GaAs (001) shown Fig. 5.6 corresponds to a periodicity of 24.6 Å, which matches well with the periodicity measured by EELS in Fig. 5.5(a) for the same sample. The periodicity was larger than the expected $2na_0 = 17.4$ Å primarily because the sample was grown with an aluminum excess of x = 33% (see section III.B.). Satellite peaks were observed for all superlattice samples with n = 1.5 grown on GaAs (001) at 200°C or below.

The absence of a satellite peak for films with higher growth and annealing temperatures suggests that sublayer interdiffusion degrades the superlattice structure. A satellite peak was also observed for a film grown on Cr/MgO (001) at 250°C, suggesting that the superlattice structure survives up to slightly higher growth temperatures than for films grown on GaAs (001). However, films grown or annealed above 300°C on Cr/MgO (001) had no satellite peaks, confirming that high temperatures tend to mix the superlattice sublayers. On the other hand, no films grown directly on MgO (001) at any temperature possessed a satellite peak, suggesting that roughness caused by island growth during nucleation also plays a major role in superlattice sublayer quality. Additionally, the presence of XRD satellite peaks correlated with excellent sublayer contrast for samples also measured in STEM-EELS. Superlattice periodicity calculated from satellite peaks also agreed well with total film thickness measurements using XRR divided by the number of deposited superlattice periods.

Superlattice films grown at 150°C, including the film shown in Fig. 5.5(a), had additional faint RHEED diffraction spots in the [110] direction as seen in Fig. 5.3(a). These spots were also observed during room temperature growth of Fe_2MnAl and may be due to crystal twinning or the presence of nanoscale crystallites at the surface. A secondary bulk crystal phase is unlikely due to the lack of additional peaks in XRD rocking curves, and cross-sectional TEM showed no indication of surface crystal phase segregation. The extra RHEED spots vanished if the sample was annealed to 300°C after deposition. Spots in RHEED are often associated with bulk diffraction due to surface roughness, but RMS roughness measured in AFM was the same for samples with and without the post-growth anneal, suggesting that any changes in roughness occurred on the nanoscale.

5.4 Magnetic Anisotropy Energy

The effective PMA energy, $K_{eff}^{\perp}$, was experimentally quantified for each sample as the area between the out-of-plane and in-plane SQUID hysteresis loops [37]. Positive values of $K_{eff}^{\perp}$ indicated dominant PMA, while negative values indicated in-plane dominated anisotropy. $K_{eff}^{\perp}$ may be written as a sum of independent anisotropy contributions,

$$K_{eff}^{\perp} = K_{MCA}^{\perp} + \frac{K_S}{t_{film}} - 2\pi M_S^2 \tag{5.1}$$

where $K_{MCA}^{\perp}$ is out-of-plane magnetocrystalline anisotropy, K_S is interface anisotropy, t_{film} is the total thickness of the ferromagnetic layer, and M_S is saturation magnetization. Typically, the interface anisotropy term is exploited in ultra-thin films to obtain PMA, for example in CoFeB/MgO films less than 1.5 nm thick [42]. Following this reasoning, it is tempting to consider there to be a large anisotropy contribution present at each superlattice sublayer interface. The sublayers are sufficiently thin (0.85 nm in the case of n = 1.5) for interface anisotropy to be considered important. However, the primary motivation for the superlattice is to create a material that has uniaxial anisotropy in the bulk, rather than at an interface. For this reason, $[\mathrm{CMA_n/FMA_n}]_\mathrm{q}$ is viewed as possessing superlattice-related $K_{MCA}^{\perp}$ due to $P4/nmm$ space group symmetry rather than a cumulative K_S summed up at each sublayer interface. Taking this view, interface anisotropy exists only between $[\mathrm{CMA_n/FMA_n}]_\mathrm{q}$ and the substrate. To obtain PMA from the bulk of a $t_{film} = 20$ nm thick superlattice film, two conditions must be satisfied: (i) shape anisotropy magnitude must be minimized by reducing the saturation magnetization, and (ii) $K_{MCA}^{\perp}$ must be maximized via tetragonal distortion and superlattice effects.

To address condition (i), the shape anisotropy term $2\pi M_S^2$ (in cgs units) was reduced by increasing the aluminum content. This is possible because the M_S of Heusler

compounds is directly related to composition via the Slater-Pauling curve,

$$m = M_S/f.u. = N_V - 6N_a \tag{5.2}$$

where m is the moment per molecular formula unit ($f.u.$) in units of Bohr magnetons (μ_B), N_V is the average number of valence electrons per $f.u.$, and N_a is the number of atoms per $f.u.$ [32]. For full-Heuslers with no vacancies, (5.2) reduces to the familiar $m = N_V - 24$. However, generally, estimation of N_V and N_a is model-dependent, and here we choose the model with stoichiometry given by $Co_{2\eta}Mn_{\eta}Al_{1+x}/Fe_{2\eta}Mn_{\eta}Al_{1+x}$, where x is aluminum excess and $\eta = (3 - x)/3$ is a normalization factor required to maintain four atoms per full-Heusler formula unit without vacancies, while maintaining growth fluxes as $\Phi_{Co} = \Phi_{Fe} = 2\Phi_{Mn}$. Alternative models incorporating preferential site occupancy and vacancies ($N_a < 4$) overpredicted the reduction in M_S for estimated aluminum excess based on Rutherford backscattering spectrometry calibration samples.

The Slater-Pauling curve for this model can be simplified to $m = 3 - 5x$, where x is the aluminum excess. For $x = 0$ and cubic lattice parameter $a_0 = 5.79$ Å, we expect $m = 3.0\ \mu_B$, which gives a saturation magnetization $M_S = 573$ emu/cm^3. However, for 10% aluminum excess, M_S is lowered by 17% according to the Slater-Pauling curve. This, in turn, decreases shape anisotropy magnitude by 31%. To illustrate this point, $K_{eff}^{\perp}$ vs. M_S is plotted in Fig. 5.7. It is important to note that this figure contains data from samples grown on all three substrate types at various growth and annealing temperatures. Nevertheless, saturation magnetization is clearly an important factor in determining in-plane vs. out-of-plane magnetization for this system. A least-squares fit for the full data set is also shown. It is unclear whether the magnetocrystalline or interface anisotropy terms have some hidden dependence on M_S. Therefore, the linear fit term was assumed to be zero, giving a regression model of $K_{eff}^{\perp} = AM_S^2 + B$, with

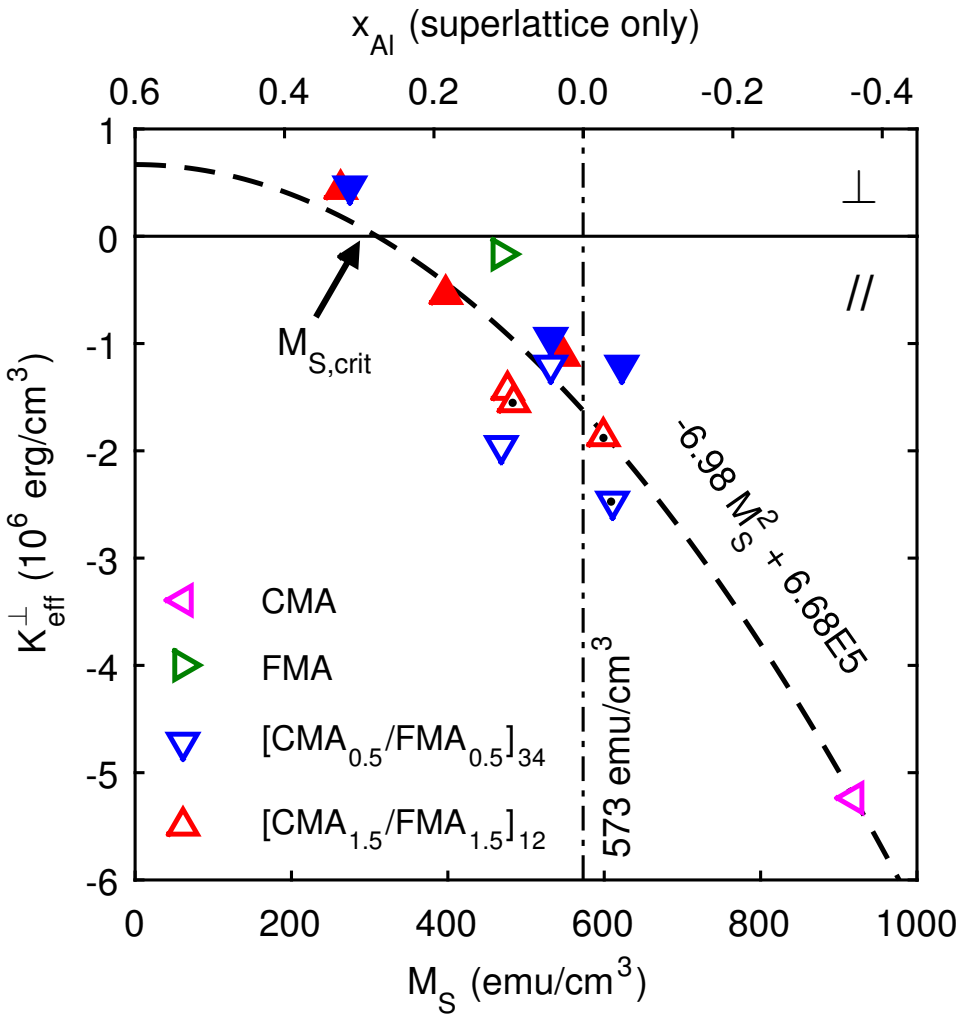

Figure 5.7: Effective perpendicular anisotropy vs. saturation magnetization at $T = 5\ K$. Filled markers are films grown on GaAs (001), unfilled markers are films grown on MgO (001), and markers with a black center dot are films grown on Cr/MgO (001). The constrained (see text) least squares fit (black dashed line) and the experimental fit parameters include all the data points shown. The upper x_{Al} scale indicates the calculated superlattice aluminum excess based on M_S measurements and is not valid for pure CMA or FMA since they follow a different Slater-Pauling model. Out-of-plane easy axes are observed for $[CMA_n/FMA_n]_q$ with high aluminum content grown at 150°C on GaAs (001). Sample volumes were determined using XRR and photographic area measurements.

$A = -6.98 \pm 1.79$ and $B = (6.68 \pm 6.09) \times 10^5$ erg/cm^3. The large standard deviation of the fit parameters is related to the number of uncontrolled variables such as growth temperature in Fig. 5.7, but A is consistent with 2π in equation (5.1). Fits constrained to pass through the origin, as well as unconstrained fits, produced qualitatively similar results. From the fit parameters, the critical saturation magnetization was determined to be $M_{S,crit} = 309$ emu/cm^3, or $m_{crit} = 1.62\ \mu_B$. For magnetizations below $M_{S,crit}$, films were preferentially magnetized out-of-plane at temperatures below 200 K, and magnetized in-plane at temperatures above 200 K. The Curie point was above room temperature for all films measured in SQUID, so the transition observed at 200 K is a spin reorientation transition. Assuming the stoichiometry model above, $M_{S,crit}$ corresponds to an aluminum excess of x $>$ 0.28. Therefore, PMA is observed for superlattices with greater aluminum excess than $Co_{1.81}Mn_{0.91}Al_{1.28}/Fe_{1.81}Mn_{0.91}Al_{1.28}$. This aluminum excess value matches well with estimated fluxes based on RBS calibrations used for the sample set.

It is mentioned in Ref. [153] that small values of M_S can give large anisotropy fields for relatively small K_{MCA}. This fact is exploited to achieve PMA in the present work. However, the original prediction of PMA in this Heusler superlattice did not include the necessity of lowering the saturation magnetization or introducing tetragonal distortion. Rather, $K_{eff}^{\perp}$ is predicted to be positive for stoichiometric $[CMA_{0.5}/FMA_{0.5}]_q$, with a value of $K_{eff}^{\perp} = 4.73 \times 10^6$ erg/cm^3 (given as $\mu_0 H_{eff} = 1.50$ NA^{-1}m^{-1} in Ref. [153]). Instead, we find that the maximum PMA is obtained for $[CMA_{1.5}/FMA_{1.5}]_q$ with 33% aluminum excess, giving a value of $K_{eff}^{\perp} = 4.4 \times 10^5$ erg/cm^3 at T = 5 K, an order of magnitude lower than the predicted value. This low value is insufficient to produce a completely hard axis in-plane, resulting in canted magnetization with slight preference along the [001] direction as shown in Fig. 5.8.

To address condition (ii), $K_{MCA}^{\perp}$ was enhanced in samples with well-defined superlattice layers and tetragonal distortion c/a $>$ 1. The two samples in Fig. 5.7 with dominant

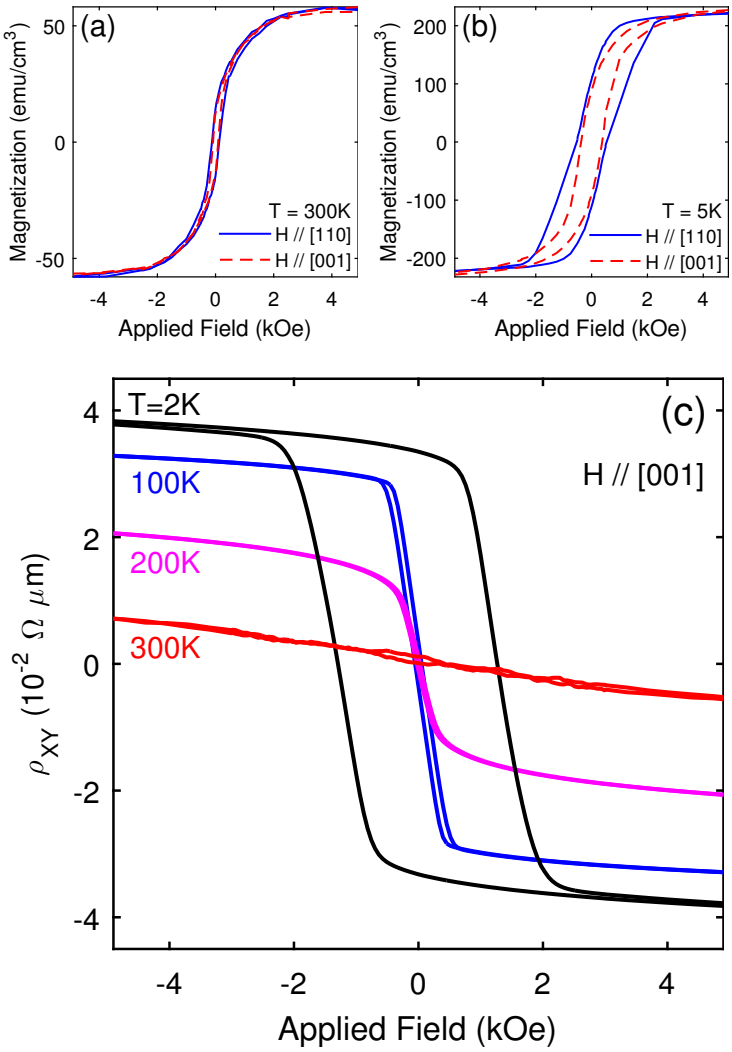

Figure 5.8: Magnetization hysteresis data for the sample with n = 1.5 and dominant PMA shown in Fig. 5.5(a) and Fig. 5.7. SQUID data was collected at (a) 300 K and (b) 5 K. (c) Anomalous Hall resistivity curves show the out-of-plane spin reorientation transition below 200 K.

PMA ($K_{eff}^{\perp} > 0$) were grown at low temperature on GaAs (001) under conditions where superlattice sublayer interdiffusion and the degree of film relaxation was low, as described previously. The sample with n = 0.5 had c/a = 1.022, while the sample with n = 1.5 had much larger c/a = 1.054. Both samples had approximately the same saturation magnetization and $K_{eff}^{\perp}$. Since less tetragonal distortion is required to produce nearly the same $K_{eff}^{\perp}$ for n = 0.5, it is possible that the superlattice structure with n = 0.5 provides more superlattice-related $K_{MCA}^{\perp}$ than that of the superlattice with n = 1.5. An additional strain-dependent sample series would be required to confirm this. A separate sample series (not shown) grown only on MgO (001) substrates at 300°C did not experience a spin reorientation transition below $M_{S,crit}$, further supporting the conclusion that $K_{eff}^{\perp}$ is maximized for $[\mathrm{CMA_n/FMA_n}]_\mathrm{q}$ with high aluminum excess grown on GaAs (001) at 150°C with no subsequent anneal. This combines the advantages of the superlattice structure with compressive strain resulting in c/a > 1, both of which are expected to enhance $K_{MCA}^{\perp}$ [153, 158]. This factor is then allowed to dominate by increasing the aluminum content, thereby lowering the shape anisotropy contribution.

5.5 Surface Spin Polarization

A discussion of spin-resolved photoemission spectroscopy (SR-PES) can be found in Section 2.11. For this work, SR-PES was conducted at the Cassiopée beamline at Synchrotron SOLEIL in Saint-Aubin, France. SR-PES has a probing depth of approximately 10–15 Å for photoelectron kinetic energies considered here, making it an ideal technique to measure spin polarization near the surface of thin films. The samples were grown in an MBE chamber with base pressure $< 5 \times 10^{-10}$ Torr, then transferred under UHV conditions to an analysis chamber with base pressure $< 5 \times 10^{-11}$ Torr. Cobalt and iron were deposited from dual e-beam evaporators, while manganese and aluminum were de-

posited from standard effusion cells. Fluxes from each source were calibrated with a retractable quartz crystal microbalance in the sample position before each growth, and the microbalance tooling factors were calibrated by RBS measurements for each element. Samples were grown close to stoichiometry, resulting in films that were magnetized in-plane. Substrates and superlattice films were prepared as previously described. Iron and FMA buffer layers were grown on MgO (001) substrates at room temperature, then annealed at 600°C for 20 min until *in-situ* RHEED patterns became streaky, indicating a smooth surface. All superlattice samples measured in SR-PES had n = 1.5 and were annealed at 300°C, resulting in preferential B2 ordering as measured in XRD. However, again, bright half-order streaks were observed in RHEED, suggesting that the surface unit cell was at least partially $L2_1$-like. As described earlier, these growth conditions caused sublayer intermixing. Nevertheless, as will be discussed below, the surface spin polarization was found to depend strongly on whether the superlattice was terminated with a CMA or an FMA layer, suggesting that the superlattice structure remained at least partially intact.

SR-PES measurements were performed at constant photon energy $h\nu = 35$ eV. Assuming that CMA and FMA possess an inner potential V_0 that is similar to other Heusler compounds [20, 120], out-of-plane photoelectron momentum k_z was near the X point in the bulk Brillouin zone. The analyzer was set to angle-averaging transmission mode, which integrated 52% of the width of the surface Brillouin zone along the $\bar{X}_1$ axis (parallel to [110]), centered about the surface $\bar{\Gamma}$ point. Samples were magnetized along the Heusler [110] direction in a 200 Oe applied field prior to each measurement, and data were collected at remanence. The Mott detector measured spin polarization in the Heusler [110] (in-plane) and [001] (out-of-plane) directions. After measurement, samples were capped with 10 nm thick gold and loaded out of UHV for further characterization. Spin polarization was calculated as $P = A/(SR)$, where A is the photoelectron scattering

asymmetry in the Mott detector, S is the Sherman function of the detector, and R is the magnetic remanence of each sample along the Heusler [110] direction.

From SR-PES and SQUID magnetization data, several trends emerge. First, the magnetic easy axis was found to be along [110] for CMA and $[CMA_n/FMA_n]_q$ deposited directly on MgO (001) and GaAs (001). An easy axis along [100] was found for FMA and $[CMA_n/FMA_n]_q$ films deposited on a 20 nm thick iron or FMA buffer layer. Furthermore, spin polarization did not depend on the substrate used, but was found to depend strongly on the surface termination layer, as shown in Fig. 5.9. Pure FMA films and FMA terminated $[FMA_n/CMA_n]_q$ had low spin polarization near the Fermi level, $P(E_f) = 25\%$, which contradicts predictions of half-metallicity for this system [159, 160, 161, 162]. Pure CMA had relatively high $P(E_f) = 65\%$, which falls short of predictions of half-metallicity for CMA [163, 164, 165], but corroborates claims of near half-metallicity with Fermi level position at the bottom of the minority spin gap [166, 167, 168, 169].

Finally, and most importantly, CMA-terminated superlattice with $P(E_f) = 95\%$ shown in Fig. 5.9(b) and (f) had significantly higher Fermi level spin polarization than a pure CMA film. The enhancement is speculated to arise due to Fermi level tuning by the superlattice structure [153]. Additionally, given the termination dependence of the enhancement, any heterostructure interface such as superlattice/Ag for GMR devices or superlattice/MgO for tunnel junction devices should have CMA termination to maximize magnetoresistance. This conclusion is exciting because the Co_2MnAl/MgO interface is also expected to preserve coherent tunneling of the Δ_1 Bloch band, which is a requirement for the spin filtering enhancement to tunnel magnetoresistance [170, 62].

The $[CMA_n/FMA_n]_q$ superlattice has been demonstrated to exhibit both perpendicular magnetization and near half-metallicity. However, so far these properties have been observed for samples with different growth conditions. Low saturation magnetization, low growth temperatures, and compressive substrates are required to overcome shape

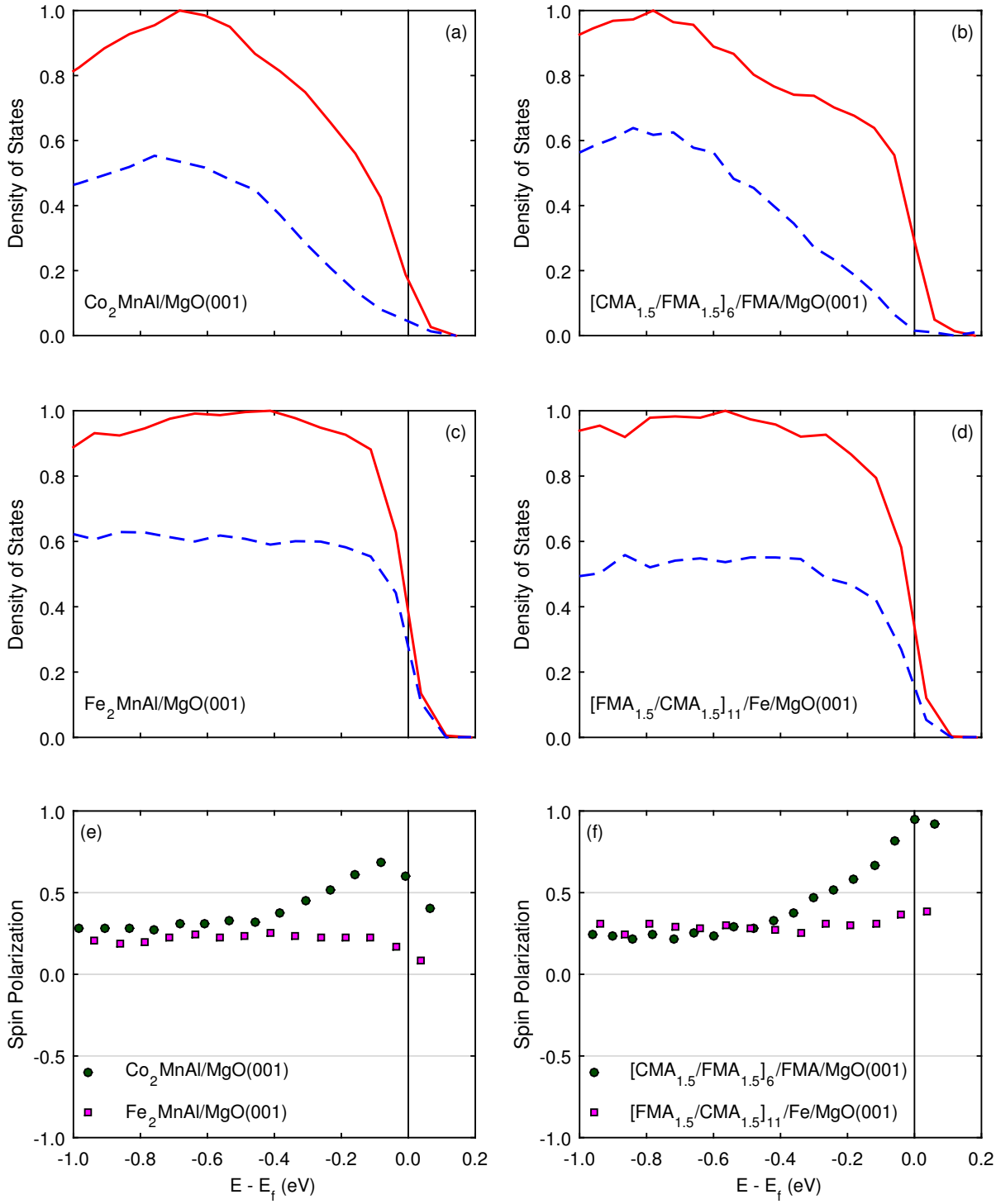

Figure 5.9: SR-PES vs. photoelectron energy collected at $h\nu = 35$ eV for four different samples, as indicated in each subplot. Normalized density of states in (a)-(d) are separated into majority (solid red line) and minority (dashed blue line) spins. The spin polarizations for pure films (a) and (c) are summarized in (e), while superlattice films (b) and (d) are summarized in (f).

anisotropy and produce out-of-plane easy axes, as demonstrated for $[CMA_n/FMA_n]_q$ with an excess of aluminum grown at 150°C on GaAs (001). Near-half-metallic samples measured in SR-PES were grown close to stoichiometry on FMA/MgO (001) substrates at 300°C. Future work includes measuring the spin polarization of out-of-plane magnetized superlattice films with high aluminum content. Theory predicts that B2 ordering and manganese excess both preserve half-metallicity, but cobalt antisite disorder should destroy half-metallicity in CMA [164, 171]. The effects of excess aluminum in CMA or FMA have not been reported in literature. This issue may be circumvented by growing superlattice films with $(Co, Fe)_2Mn_{1-x}Al_{1+x}$ layers, which would allow for M_S tuning, preserve B2 order, and minimize any potential for aluminum in the cobalt or iron sites. On the other hand, excess aluminum may be beneficial in this system as it is in Co_2Mn_xSi, where it is argued that excess manganese prevents cobalt antisite disorder [54].

5.6 Conclusion

MBE growth of single crystal epitaxial $[CMA_n/FMA_n]_q$ superlattices on GaAs (001), MgO (001), and Cr/MgO (001) substrates was successfully demonstrated. Mixed B2/$L2_1$ atomic order was determined with a combination of RHEED, XRD, and HAADF-STEM. Superlattices with high sublayer structure integrity seen in STEM-EELS also possessed a weak superlattice satellite peak in XRD rocking curves. Substrate-dependent strain and tetragonal distortion was quantified by XRD RSMs, from which the relaxed cubic lattice parameter $a_0 = 5.79$ Å was extracted. PMA measured in SQUID depended largely on film stoichiometry, with higher aluminum content corresponding to higher PMA. The films under the critical magnetization of 309 emu/cm^3 grown at 150°C substrate temperature on GaAs (001) exhibited out-of-plane magnetization for $T < 200$ K. Assuming the excess aluminum is randomly substituted on cobalt, iron, and manganese atomic sublattices, this

magnetization corresponds to an aluminum excess of 28%. Synchrotron-based SR-PES measurements show the spin polarization of stoichiometric, in-plane magnetized FMA is 25% and that of CMA is 65% at the Fermi level near the bulk X point. Superlattice $[\mathrm{CMA_n/FMA_n}]_\mathrm{q}$ adopted the electronic character of the termination layer, but provided an additional improvement in spin-polarization for CMA termination, resulting in spin polarization of 95% near the Fermi level.

Chapter 6

Searching for Weyl Semimetallicity in Co_2TiGe

Breaking symmetry,

Berry curvature gives rise.

The Weyl fermion!

6.1 Introduction

For a comprehensive overview of the motivations behind research into Weyl semimetals, see Section 1.9. The accidental degeneracies in band structures that produce Weyl nodes are actually quite common, but the theory that established them as a potentially interesting condensed matter system was not developed until 2011 [80, 89]. As a result, there are a number of materials that have been studied in the past that are now experiencing a renewal of interest as Weyl semimetal candidates. This is exactly the case for Co_2TiX (X = Si, Ge, Sn) compounds, which were originally studied in bulk polycrystalline form due to predictions that they are half-metallic with minority spin

gaps of $\sim 0.5\ eV$ [172]. Five years later, in 2016, two groups predicted the existence of type II Weyl nodes in the same systems [9, 10]. The accidental degeneracies in the band structure are quite clear, in retrospect, as shown in Fig. 6.1. Of course, it is not possible to identify Weyl nodes simply by finding band crossings. Instead, the chirality of certain crossings has been calculated and found to be $C = \pm 1$ or ± 2 according to equation (1.13) [10].

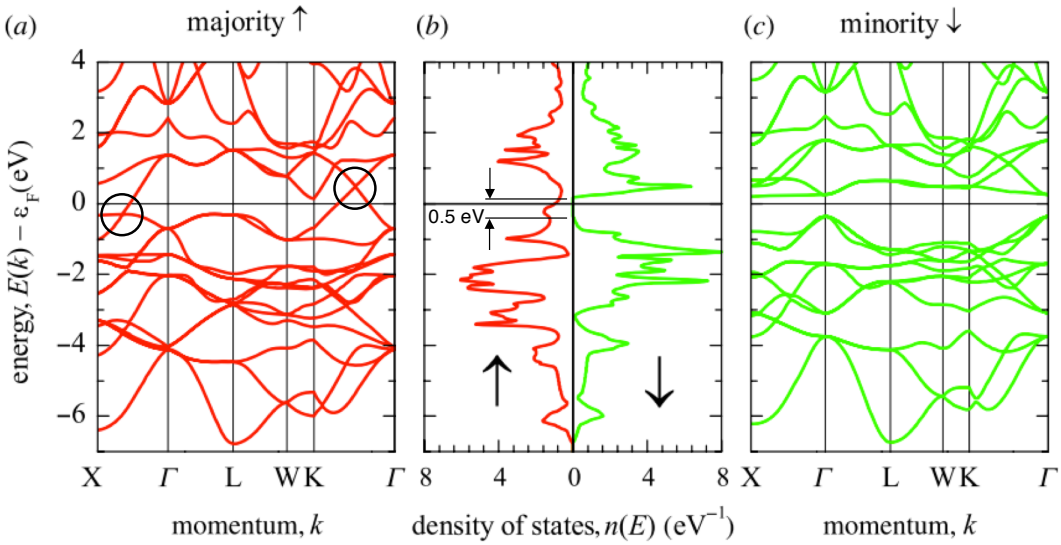

Figure 6.1: Spin-resolved band structure calculation for Co_2TiGe showing (a) majority spins (b) density of states (DOS), and (c) minority spins. The minority spin gap at the Fermi level is 0.5 eV wide, making this a strong half-metal candidate. The accidental degeneracies enclosed by the black circles in (a) were later identified as Weyl nodes. Figure adapted with permission from [172].

It is important to note a few other features in the electronic band diagram for Co_2TiGe shown in Fig. 6.2. First, the position of the Weyl points depends on the magnetization direction. This is because spin-orbit coupling converts band crossings into gapped or avoided crossings when symmetry is broken by the magnetization vector, destroying the intrinsic chirality of the Weyl node. Only those Weyl nodes with symmetry about the magnetization vector persist. In the case of $\boldsymbol{M}$ along [110], a Weyl node appears roughly halfway between Γ and K in the bulk Brillouin zone, with its chiral opposite appear-

ing at exactly opposite momentum. This Weyl pair is important because Co_2TiGe has been found to have a slightly easier magnetic axis along [110] as compared to the [100] direction, and so will have remanent magnetization along [110] after saturation in an applied magnetic field [21]. This constrains the experimental procedure when performing an ARPES measurement. The trajectory of low energy photoelectrons produced in ARPES can be distorted even by small fields, so it is not feasible to apply a field strong enough to control the magnetization direction of Co_2TiGe during measurement. Instead, one must rely on the remanent magnetization of the thin film. Therefore, for ARPES measurements, we must focus on the Weyl point labeled as W^1_{110}.

The second important detail to note in Fig. 6.2 is that the Fermi level is 0.3 eV below W^1_{110}. Other Weyl points, such as those that appear for $\boldsymbol{M}$ along [100], are also found ± 0.3 eV from the Fermi level. Unfortunately, it is clear from equation (1.14) that signatures of Weyl nodes are damped by large $\mu = E_f - E_{Weyl}$, at least in transport measurements. In fact, it seems likely that any properties linked to the chirality of the Weyl node would be destroyed by this large μ by virtue of the Fermi surface that encloses the nodes. Each Fermi surface pocket carries the sum total of the Chern numbers (equation 1.13) of any Weyl points enclosed within [98]. Weyl-like electronic properties arise from the behavior of electrons that exist on Fermi surfaces with non-trivial total chirality ($\Sigma C \neq 0$). This is a critical point of fact, but the implications of the large μ in Co_2TiGe are not discussed by G. Chang *et al.*, the principle source of specific theory data for this material system at present [10]. It seems unlikely that the metallic Fermi surface will individually enclose isolated Weyl points.

Despite these hurdles, it is still important to investigate the properties of Co_2TiGe to check for any signatures of Weyl nodes. Additionally, it may be possible to modify the Fermi surface and isolate the Weyl points by means of Fermi level tuning, which will be discussed in Section 6.7.

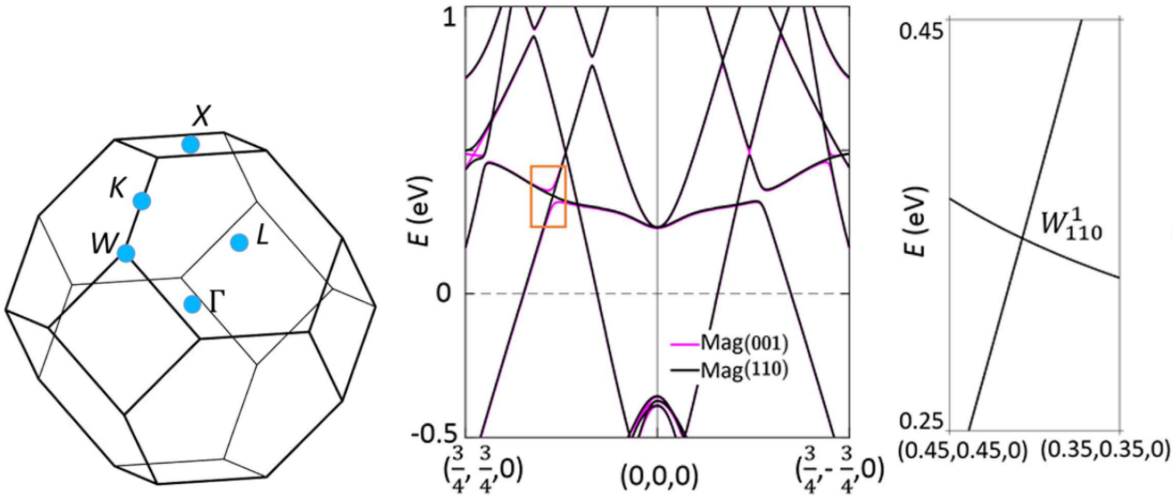

Figure 6.2: (Left) Schematic of the first Brillouin zone of Co_2TiGe with high symetry points labeled. The [110] direction is the axis defined by $\Gamma - K$. (Center) Band structure of Co_2TiGe taking spin-orbit coupling into account for magnetization along [100] and [110] directions. Note that the position of the Weyl nodes changes depending on the magnetization direction. (Right) Zoom in of the Weyl node for magnetization along [110]. Figure reprinted from [10] under the Creative Commons Attribution 4.0 International License.

6.2 Experiment

In this study, we utilize molecular beam epitaxy to grow single-crystal Co_2TiGe thin films on several different substrates. The development of thin film growth techniques is important for all electronic materials because thin films enable the production of useful and reproducible test structures and devices. The substrates were chosen to optimize certain film characteristics depending on the desired measurement. Insulating MgO (001) substrates were used for magnetotransport measurements to eliminate confounding parallel conduction. Chromium buffer layers grown on some MgO (001) substrates were used to smoothen the Co_2TiGe layer, and would be a favorable starting surface for future studies of magnetic tunnel junctions. Finally, a lattice matched, conductive III-V semiconductor buffer structure was used for ARPES measurements. This structure consisted of GdAs(16nm)/$In_{0.52}Al_{0.48}As$(50nm)/$In_{0.53}Ga_{0.47}As$(400nm)/$In_{0.52}Al_{0.48}As$(50nm)/InP (001)

and was developed for Palmstrøm group by J.A. Logan *et al.* specifically for high quality growth of Co_2TiGe. The III-V material was n-type doped with silicon to enhance conductivity, and the composition was chosen to provide lattice match to the 5.83 Å lattice parameter of Co_2TiGe. The GdAs layer was used as a chemical diffusion barrier, and was found to prevent reactions that otherwise occured between Co_2TiGe and the InAlAs layer underneath. Further details of the MBE growth and composition of both Co_2TiGe and the III-V buffer structure can be found in [21].

As discussed in Chapter 5, ideal full-Heusler compounds with formula X_2YZ have an $L2_1$ crystal structure, where the Y and Z elements form a rocksalt lattice that is stuffed with X atoms in each of the 8 tetrahedral sites, as shown in Fig. 6.3. Thin film growth was accomplished by codepositing high-purity elemental Co, Ti, and Ge from effusion cells in an ultra-high vacuum growth chamber. The fluxes of each cell were calibrated using Rutherford backscattering spectrometry (RBS), which is typically accurate to within about ∼5% of composition. An *in-situ* flux gauge was not used for the work presented here. Instead, the effusion cell temperatures were calibrated with RBS before any major measurement, such as ARPES, and the fluxes were found to drift by a negligible amount over time.

After growth, most samples were capped with 10 nm thick AlO_x and loaded out of UHV. These samples were characterized using atomic force microscopy, high resolution X-ray diffraction (XRD), XRD reciprocal space mapping (RSM), and superconducting quantum interference device (SQUID) magnetometry. Resistivity and Hall analysis was performed by fabricating Hall bars with $l = 250\mu m$ and $w = 50\mu m$. Hall bars were measured in a Quantum Design Physical Properties Measurement System (PPMS) with an accompanying sample tilt stage.

A number of samples were also grown for angle-resolved photoemission spectroscopy (ARPES) studies. ARPES was performed at beamline 10.0.1 at the Advanced Light

Source (ALS) in the Lawrence Berkeley National Laboratory in Berkeley, California. In order to preserve the pristine surface of Co_2TiGe from oxidation in atmosphere, a vacuum suitcase was developed to allow transportation of samples grown at UCSB. The vacuum suitcase maintains UHV by means of a small, active ion pump and a passive non-evaporable getter pump, resulting in a base pressure $P < 10^{-10}$ torr. Samples were grown within 48 hours of transport to ALS, and then transferred under UHV into the vacuum suitcase. The suitcase was then removed from the UHV system at UCSB, with the ion pump powered by a battery backup module. The suitcase with samples was transported by automobile to ALS, where it was attached to the beamline end-chamber. After baking and pumping out the intermediary space that had been exposed to atmosphere, the samples could then be transferred safely into the UHV environment of the ARPES chamber. After ARPES, samples were returned to the vacuum suitcase and transported back to UCSB, where they were transferred back into the Palmstrøm lab UHV system for further analysis. X-ray photoemission spectra of the sample surfaces showed minimal contamination of Co_2TiGe surfaces by oxygen after a round trip time span of 7 days.

6.3 Sample growth and crystal quality

The optimized substrate temperature for Co_2TiGe was found to be 390 °C for growth on the III-V buffer, and 400 °C for growth on MgO (001). This was reported as the real temperature as calibrated by the thermal desorption of the arsenic capping layer from the III-V buffer, which is known to occur at 350 °C. These optimized temperatures were based on streaky RHEED patterns and scanning tunneling microscopy measurements indicating a smooth surface favorable for ARPES measurements [21]. In this work, reproducing the growth conditions of Logan *et al.* resulted in a smooth, single crystal film, but the RHEED patterns were more complex. Typical Heusler RHEED patterns

exhibit a c(2x2) reconstruction, which can be viewed as a manifestation of an $L2_1$-like surface unit cell. Instead, here, a c(6x6) or c(9x9) reconstruction was often observed, with chevrons along the <100> directions in RHEED, as shown in Fig. 6.3. The chevron diffraction pattern is often attributed to corrugations in the sample surface, in this case extending along the <100> directions, however no such corrugations were observed using atomic force microscopy after capping the Heusler films with 10-nm-thick AlO_x. The deviation in RHEED patterns for the present work can be explained by a slight excess of Ge flux during growth, as described in Section 6.4.

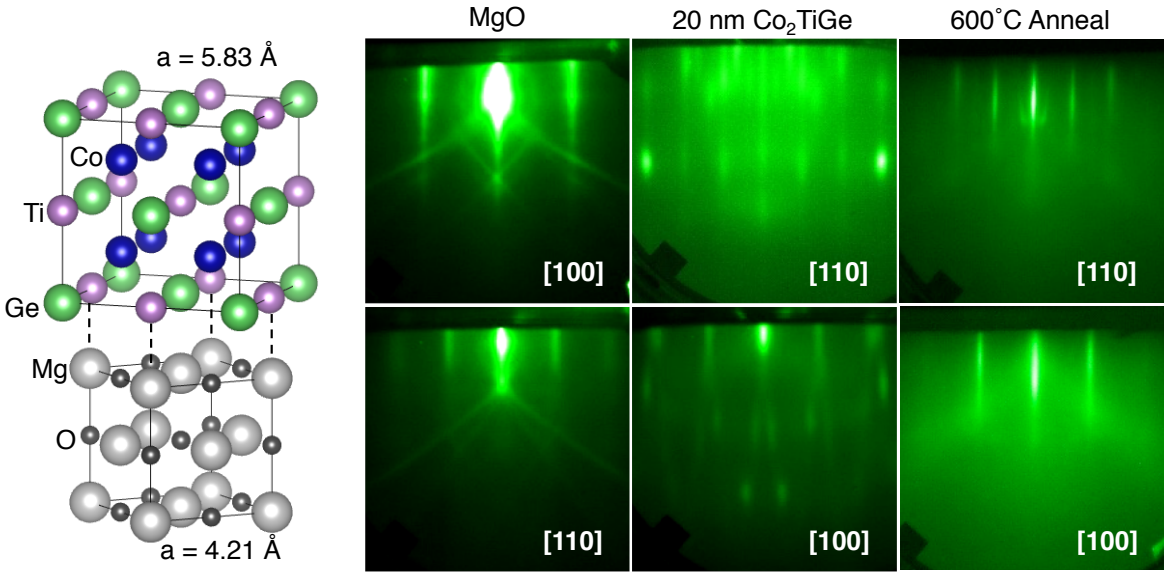

Figure 6.3: (Left) Crystal structure and epitaxial relationship for Co_2TiGe[100](001) // MgO[110](001). Note that the rocksalt and Heusler crystal structures are rotated by 45° to obtain a coincident lattice with 2.1% tensile lattice mismatch for the Heusler. (Right) RHEED images showing the relevant crystallographic directions of the MgO (001) starting surface, a Co_2TiGe film grown at 400 °C, and a Co_2TiGe surface subsequently annealed to 600 °C.

While the growth conditions had been optimized for film smoothness in [21], work remained to be done to verify the presence of the $L2_1$ crystal structure. Heusler compounds are subject to various types of chemical disorder. Disorder between the Ti and

Ge atoms would give B2 (CsCl) order, while complete chemical disorder for Co, Ti, and Ge would give A2 order (bcc solid solution). Similarly to the analysis done in Chapter 5, the degree of chemical order in Co_2TiGe was established to ensure measurement of high quality Heusler films. This was accomplished with XRD RSMs. Taking the $L2_1$ structure as the crystallographic basis, a (004) Bragg peak indicates at least partial A2 order, a (002) peak indicates at least partial B2 order, and a (111) peak indicates at least partial $L2_1$ order. However, Co_2TiGe presents an additional challenge since the (002) Bragg peak intensity is weak even for perfectly ordered samples. This is because of the similarity in X-ray scattering amplitude between Co_2 monolayers and TiGe monolayers layered in the [001] direction. Instead, the (111) Bragg reflection must be used to reliably identify a high degree of chemical ordering.

Unfortunately, no Co_2TiGe films grown using the conditions developed by Logan *et al.* possessed a (111) Bragg reflection in XRD. To promote $L2_1$ order, a high-temperature post-growth anneal was required. Initially, post-growth annealing was found to be important based on changes in RHEED. For samples grown on MgO (001) at 400 °C, the complex c(6x6) or c(9x9) reconstructions and chevrons observed during and after growth vanished upon annealing at or above 550 °C. This can be clearly seen in Fig. 6.4. A post-growth anneal was also found to be important during the growth of Fe_2MnAl buffer layers for use in the work in Chapter 5. Complex spot patterns and half-order streaks along the Fe_2MnAl [110] direction vanished when annealing over 500 °C. Upon cooling, the spots did not return, but the half-order streaks returned with greater brightness than before, indicating high crystal quality. The annealed Fe_2MnAl also exhibited a (111) Bragg reflection in XRD. This reinforces the importance of performing a high temperature anneal to promote $L2_1$ order for Heusler films grown epitaxially at lower temperatures.

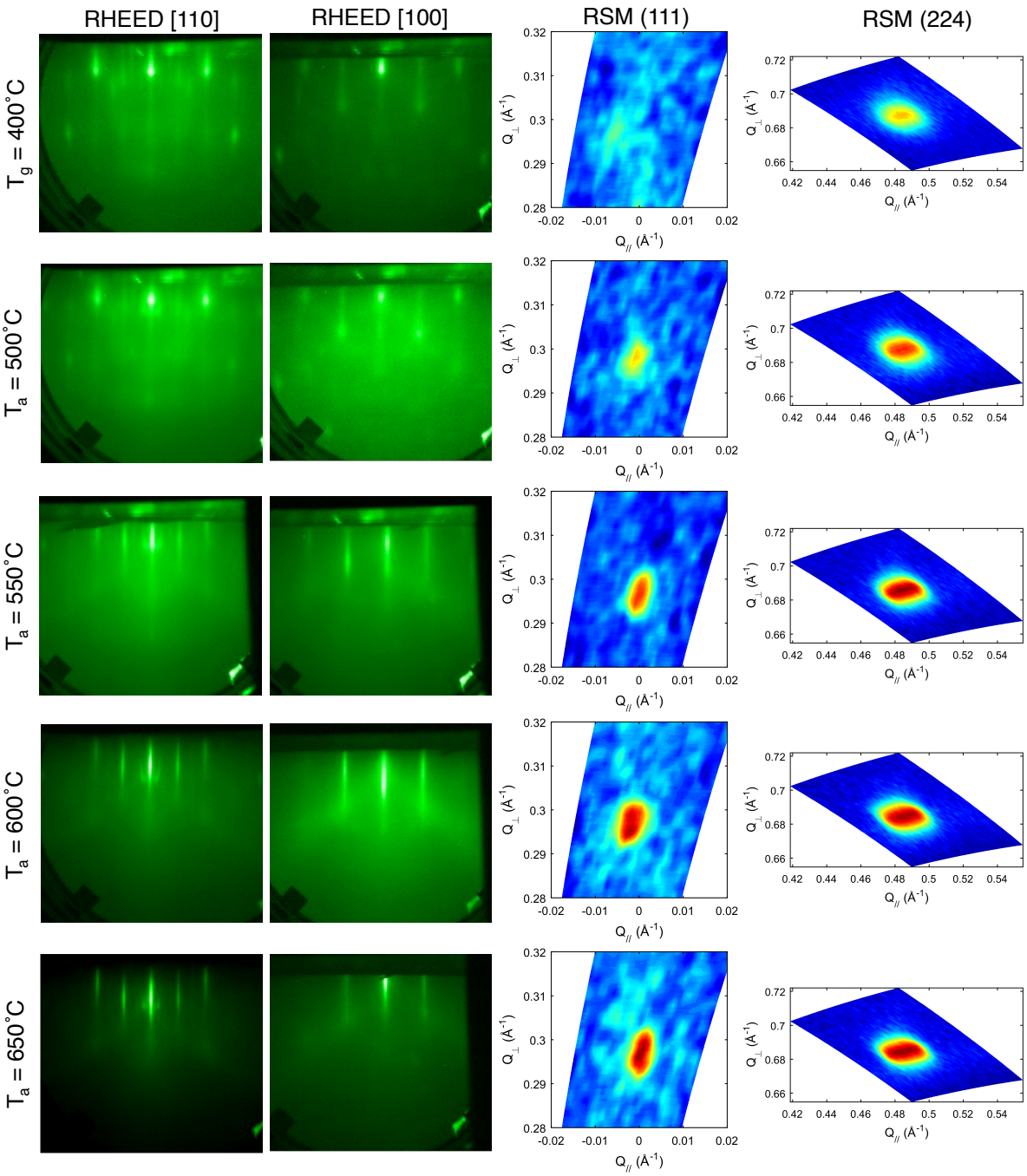

Figure 6.4: 20-nm-thick Co_2TiGe films grown at $T_g = 400$ °C on MgO (001) substrates were subsequently annealed at various temperatures (T_a) for 20 min. (Left) RHEED, (center) XRD-RSMs of the Heusler (111) peak, and (right) XRD-RSMs of the Heusler (224) peak.

6.4 Magnetic analysis using SQUID

To help understand the contributions due to the internal magnetization of the film, it is important to first analyze SQUID measurements. Fig. 6.5 shows magnetization data normalized to sample volume determined using X-ray reflectivity (XRR) and photographic area measurements. The coercive fields at $T = 5K$ and $300K$ are 228 Oe and 168 Oe, respectively. The saturation magnetization at $T = 5K$ of $M_S = 333$ emu/cm^3 agrees well with the expected value based on the Slater-Pauling curve.

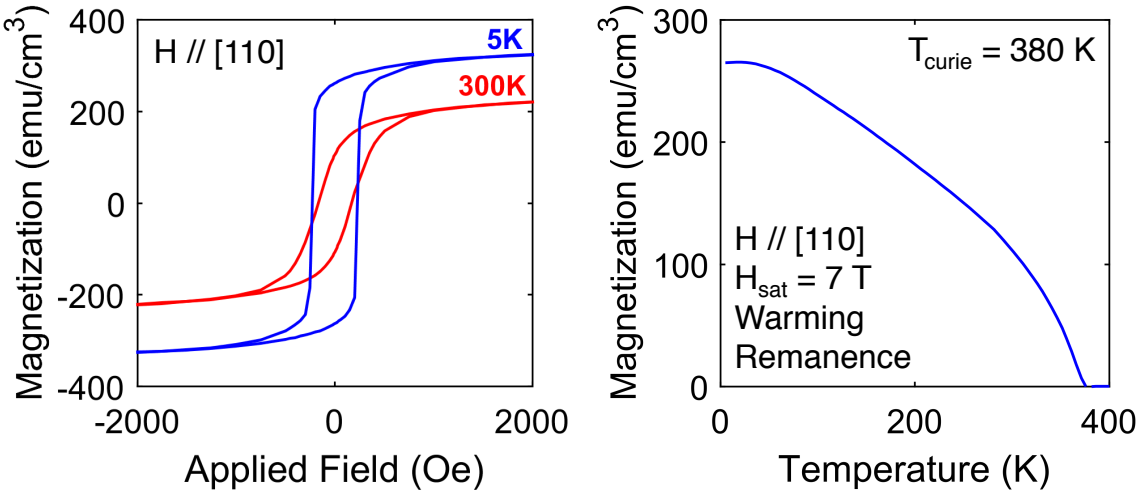

Figure 6.5: (Left) Magnetic hysteresis loops and (right) remanence vs. temperature for a 72-nm-thick Co_2TiGe/MgO (001) film as measured by SQUID. The low temperature saturation magnetization and Curie point agree well with literature values.

In fact, a rough estimate of the composition can be obtained from this value of M_S using the following procedure. Since the number of valence electrons for Ti and Ge are the same (four each) and are thus indistinguishable with this method, consider the composition $Co_{2-x}Ti_{1+x/2}Ge_{1+x/2}$, which preserves four atoms per formula unit but allows some constrained non-stoichiometry. The Slater-Pauling rule should then be

$$m = |N_V - 24| = |9(2-x) + 4(1+x/2) + 4(1+x/2) - 24| = |2 - 5x|, \tag{6.1}$$

where m gives the moment in Bohr magnetons (μ_B) per formula unit. Normalizing this by unit cell volume and accounting for the four formula units per unit cell gives the expected saturation magnetization,

$$M_S = \frac{4\mu_B}{a^3}|2 - 5x|. \tag{6.2}$$

For perfect stoichiometry $x = 0$, $a = 5.83$ Å as determined by XRD, and $\mu_B = 9.274 \times 10^{-21}$ emu, we expect $M_S = 374$ emu/cm^3. Solving (6.2) for x gives a measure of the stoichiometry in terms of M_S,

$$x = \frac{2}{5} \pm \frac{M_S a^3}{20\mu_B}. \tag{6.3}$$

Entering the experimental values for Co_2TiGe gives $x = 0.044$ or $x = 0.76$. It is unlikely that the composition deviated by more than a few percent because the film crystal quality was high and the thickness measured in XRR was approximately what was expected based on RBS calibrations. This means that our films have a composition that is close to $Co_{1.96}Ti_{1.02}Ge_{1.02}$, based on SQUID measurements. This composition agrees well with observations that complex RHEED patterns appear in the presence of excess Ge flux during growth [21]. These patterns can be seen in Figs. 6.3 and 6.4.

Magnons have a direct impact on the bulk magnetization of films, and explain the reduction in measured saturation magnetization at elevated temperatures according to the Bloch equation [173]:

$$M_S(T) = M_{S0}(1 - \beta T^{3/2}), \tag{6.4}$$

which can be fit to the experimental SQUID data shown in Fig. 6.5. The fit is typically poor and higher order terms may be included to capture various magnon and anisotropy effects, but the $T^{3/2}$ dependence captures the majority of the $M_S(T)$ behavior.

6.5 Electrical transport properties

Careful analysis of the magnetotransport data is essential in Co_2TiGe because impurity scattering, phonon scattering, magnetic scattering, half-metallic contributions, enhanced anomalous Hall effect due to high Berry curvature, and the chiral anomaly may all be in competition with one another. It is critically important to fully understand the origins of all magnetotransport signals in Co_2TiGe, so we can confidently identify any otherwise unexplainable signatures of Weyl physics.

The resistivity in ferromagnets arises primarily from the common mechanisms that apply to all metals and semiconductors. Resistance is caused by electrons scattering from other objects within the material, and this includes impurities and defects in the crystal structure, other electrons, and thermal fluctuations in atomic positions known as phonons. Additionally, ferromagnets are host to a complex scattering mechanism that arises from disturbances in spin order. These so-called magnons are collective excitations of large numbers of magnetically coupled spins. They have their own dispersion relations, with the energy of a magnon $E(\boldsymbol{q})$ depending on the effective mass of the electrons involved and on the wavevector $\boldsymbol{q}$ of the spin-wave itself. Magnons are generated by electrons undergoing a spin-flip transition as a result of a collision with either a phonon or another electron. The energy liberated from this transition generates a magnon, which propagates through the material and can go on to facilitate a spin-flip transition in another electron scattering event [174].

6.5.1 Temperature Dependent Resistivity

Generally, the resistivity of a ferromagnet can be described by

$$\rho_{xx}(H,T) \approx \rho_{imp} + \rho_{ee}(T) + \rho_{ph}(T) + \rho_{mag}(H,T), \tag{6.5}$$

where $\rho_{imp} = \rho_{xx0}$ is resistance due to electron-impurity scattering, $\rho_{ee}(T)$ is due to electron-electron scattering, $\rho_{ph}(T)$ is due to electron-phonon scattering, and $\rho_{mag}(H,T)$ is electron-magnon scattering. In typical ferromagnets and metals, electron scattering scales with T^2, while phonon scattering scales with T^5 [173, 175]. Note that magnon scattering depends both on temperature and applied field, and cannot be described by a simple power law alone, although there is one report claiming it should scale with T^2 in certain material systems [173]. In fact, the magnon contribution can only be approximated here in the limits of high field and zero field. First, let us turn our attention to the behavior of equation (6.5) when $H = 0$. The relevant physics in this limit is electrons scattering from magnetically misaligned particles, grains, and domains, and in this sense Co_2TiGe can be called a granular ferromagnet. In this case, the magnetic contribution to the resistivity takes the form

$$\rho_{mag}(H = 0, T) \approx \rho_m(T)[1 - f(M/M_S)], \tag{6.6}$$

where $\rho_m(T)$ is an arbitrary function of temperature, and $f(M/M_S)$ is an arbitrary function of the fractional magnetization [176]. The latter function can be approximated as $f(x) = \alpha x^2$ [177, 176]. Furthermore, when $H = 0$, M/M_S can be approximated by equation (6.4). Finally, assuming $\rho_m(T)$ is roughly constant and neglecting the small phonon scattering contribution gives us

$$\rho_{xx}(T) \approx \rho_{xx0} + a_{ee}T^2 + b_m[1 - \alpha(1 - \beta T^{3/2})^2], \tag{6.7}$$

where ρ_{xx0} is the resistivity at absolute zero due to impurities, a_{ee} is the magnitude of electron-electron scattering, b_m and α give the magnitude of the electron-magnon scattering, and β is related to the Curie temperature.

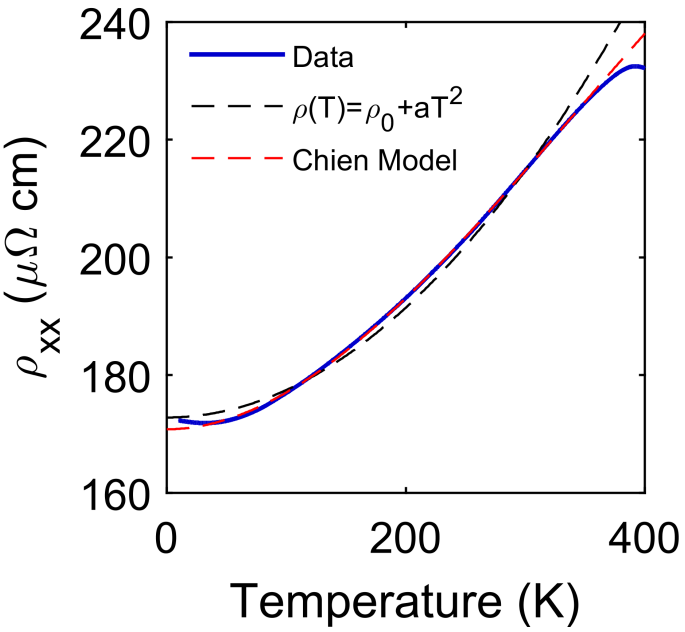

Figure 6.6: Resistivity vs. temperature for a 20-nm-thick Co_2TiGe/MgO (001) film. The blue line is the measured data, the dashed black line is a fit to the electron-electron scattering model only, while the dashed red line is the fit to equation (6.7), which provides excellent agreement with experiment from $T \approx 30\ K$ to 350 K.

Clearly, this result is heavily approximated. However, it does capture the majority of the important scattering physics in Co_2TiGe and provides an excellent fit to the data, as shown in Fig. 6.6. Thus, the temperature dependence can be explained with impurity, electron, and magnon scattering.

6.5.2 Magnetoresistance effects

We now turn to the field-dependence of the resistivity, which is shown on the left of Fig. 6.7. Here, $\rho_{xx}(H,T)$ can be separated into low-field and high-field regions. Let us first examine the low-field region, where the magnetization direction of the sample depends strongly on the strength of the applied field. This is reflected in the resistivity data due to anisotropic magnetoresistance (AMR). Note that the low field region extends approximately from $\mu_0 H = \pm 4\pi M_S$, the saturation field of a thin film. The derivation

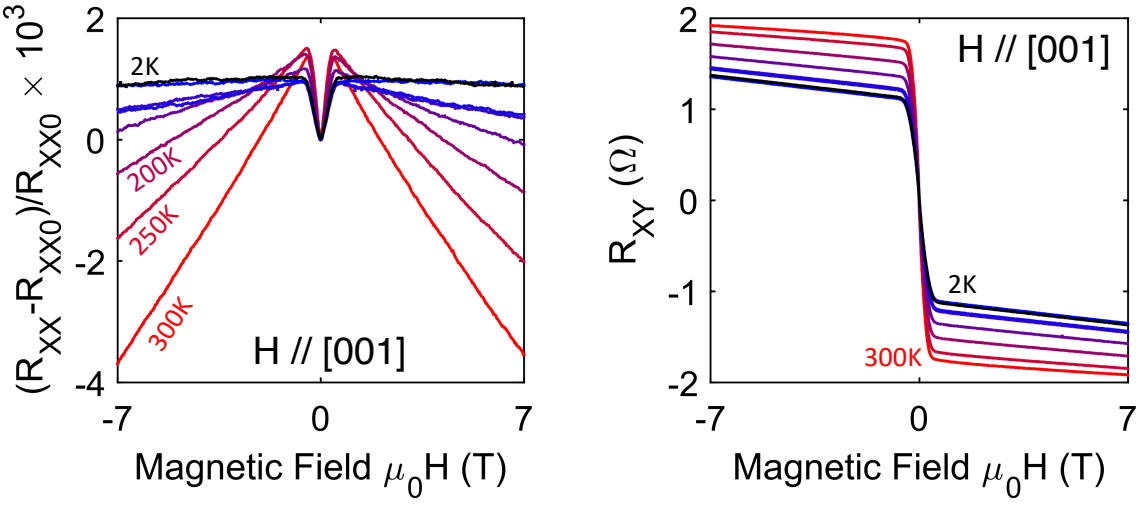

Figure 6.7: (Left) Magnetoresistance and (Right) Hall resistance for 20-nm-thick Co_2TiGe/MgO (001) as a function of applied field. Low-field MR is due to anisotropic magnetoresistance, while the high field behavior is dominated by GMR effects.

supporting this claim can be found in Appendix A.

The high field behavior shown in Fig. 6.7 can be explained by the suppression of magnon scattering. Fundamentally, this occurs because the energy of a magnon depends linearly on the applied field according to

$$E(\boldsymbol{q}) = Dq^2 + g\mu_B[B_{int} + B_A + \mu_B M_S \sin^2(\theta_k)]. \tag{6.8}$$

Here, D is the exchange stiffness or strength of magnetic coupling between spins, $B_{int} = \mu_0 H + \mu_0 M_S$ is the total magnetic induction within the material, B_A is magnetic anisotropy, and θ_k is the magnon propagation angle with respect to the magnetization direction [174]. The consequence of this dependence on applied field B is that the population of magnons can have their lowest energy level tuned above the energy of certain spin-flip transitions using a very large field. Therefore, fewer spin-flip scattering events can occur, since low energy spin-flip transitions do not provide enough energy to generate even the lowest energy magnon. This magnon scattering suppression is clearly visible at high applied

fields in common ferromagnets such as Co, Fe, and Ni [174].

The change in resistance due to magnon scattering suppression has been derived for $3d$ ferromagnets in the high field limit by B. Raquet *et al.* [174] and should follow

$$\Delta\rho_{xx}(H,T) = \frac{\mu_0 HT}{D^2} \ln\left(\frac{\mu_B \mu_0 H}{k_B T}\right), \tag{6.9}$$

which gives an excellent fit to the high field region of $\rho_{xx}(H,T)$, as shown in Fig. 6.8. The fitting parameter inside the logarithm refines to within an order of magnitude of the expected value.

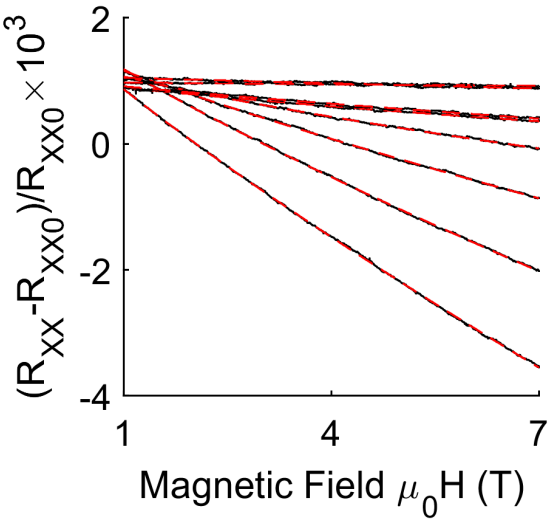

Figure 6.8: Normalized resistivity of Co_2TiGe from Fig. 6.7 showing only the high field region. The data is shown as black lines, while the fit to equation (6.9) is shown as red dashed lines.

The presence of a large amount of magnon scattering seems to present an additional problem for predictions of half-metallicity in Co_2TiGe. Spin-flip scattering that produces magnons must occur between electronic bands of opposite spin close to the Fermi energy [174]. Since no minority spin Fermi surface exists in half-metals, the energy required to produce a magnon would be the distance from the Fermi level to the edge of the minority gap, on the order of hundreds of meV. This energy is orders of magnitude larger than

that of a typical magnon, which suggests that magnons should be entirely suppressed in half-metals. Conversely, ferromagnets with a large amount of magnon scattering seem to be precluded from being half-metals. However, this conclusion is not entirely correct. While it is true that no minority spins exist in the ground state, thermal fluctuations of spins in the majority band can induce a virtual minority band into which majority spins can scatter [178]. Indeed, this is the cause of the reduction in spin-polarization of all half-metals at finite temperatures [179]. Therefore, the large magnon scattering effect in Co_2TiGe cannot be used as evidence that it is not half-metallic in the ground state.

6.5.3 Ordinary Hall effect

Returning to the transport data, the Hall resistance data shown in Fig. 6.7 can also be separated into high-field and low-field regions, which correspond to ordinary Hall effect (OHE) and anomalous Hall effect (AHE) contributions, respectively, according to equation (2.35). The corresponding carrier concentration and mobility for Co_2TiGe are shown in Fig. 6.9. The film thickness was measured using X-ray reflectivity. Since dV_{xy}/dB was found to be negative, we can infer that the Hall carriers were negatively charged electrons. The electron density of $\sim 10^{22}$ cm^{-3} is extremely high, while the electron mobility of ~ 2 cm^2/Vs is very low, indicating that charge transport in Co_2TiGe is metallic, rather than semimetallic as in TaAs or other Weyl semimetals [93]. The low mobility may be beneficial, however, since the current jetting effect that confounds measurements of the Weyl-induced chiral conductance occurs in materials with high mobility.

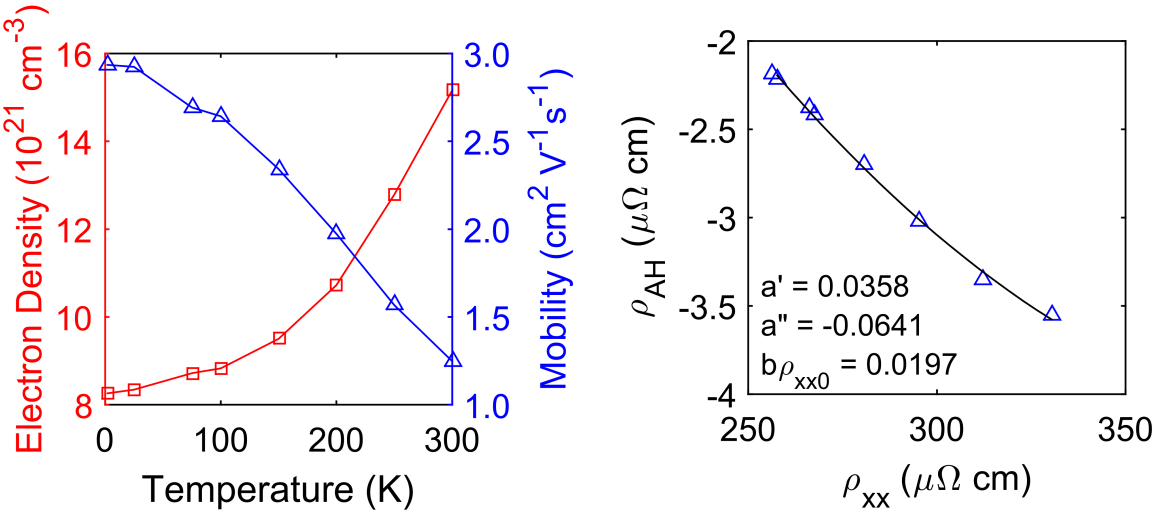

Figure 6.9: Two analyses from Co_2TiGe magnetotransport data shown in Fig. 6.7. (Left) Bulk electron density and carrier mobility values extracted from OHE. (Right) AHE analysis showing contributions from impurity (a') and phonon (a") scattering, and Berry curvature ($b\rho_{xx0}$) contributions.

6.5.4 Anomalous Hall effect analysis

In addition to using OHE to determine charge concentration and mobility, AHE was used to determine the contributions of electron scattering mechanisms related to magnetism in Co_2TiGe. Generally, the AHE can be separated into extrinsic scattering mechanisms due to crystal imperfections and temperature effects, and intrinsic mechanisms that alter the properties of electron wavefunctions due to spin-orbit coupling [180, 115]. The intrinsic AHE is of particular interest for time-reversal symmetry breaking Weyl materials because it arises directly from the Berry curvature, which, as was discussed in the introduction, increases dramatically near Weyl nodes. In fact, for materials in which conduction occurs only at the Weyl points, the AHE is expected to arise solely through the intrinsic mechanism [91, 92].

Over the last few decades there has been a great deal of disagreement on how to separate and quantify the intrinsic and extrinsic AHE mechanisms, but there is general agreement that the anomalous Hall resistivity should scale with the overall longitudinal

resistivity of the material. Extrinsic scattering is typically found to be constant or to scale linearly with ρ_{xx}, while intrinsic contributions are usually given as scaling with ρ_{xx}^2. Finally, Y. Tian *et al.* developed a scaling relationship that encompasses both extrinsic and intrinsic contributions to the AHE [181]. The anomalous Hall effect is thus found to follow

$$\rho_{AH} = R_{AH} \cdot t = a'\rho_{xx0} + a''\rho_{xxT} + b\rho_{xxT}^2, \tag{6.10}$$

where a', a'', and b are fitting constants corresponding to the strength of impurity, phonon, and Berry related contributions, respectively. In order to apply this model, one must go back to equation (2.35). The anomalous Hall resistance R_{AH} was extracted from Fig. 6.7 by extrapolating the OHE back to its y-axis intercept. This finds the overall magnitude of the AHE, which is then normalized by the thickness of the film. This process must then be repeated for several other temperature values. Note that equation (6.10) does not contain the lateral dimensions of the Hall bar w and l, in contrast to (2.32). This is because the Hall voltage that develops transverse to the current and field directions depends only on the thickness of the sample in the z direction.

The result of this analysis is shown in the right side of Fig. 6.9. It is clear that all three scattering types contribute to the AHE in stoichiometric Co_2TiGe. The parameters $a' = 0.0358$, $a'' = -0.0641$ and $b\rho_{xx0} = 0.0197$ are unitless numbers. Thus, it is tempting to conclude that phonon scattering is the dominant mechanism in Co_2TiGe. However, phonons do not contribute to scattering at low temperature, but a significant ρ_{AH} remains at 2K. These numbers merely relate changes in AHE to changes in resistivity. Furthermore, the values are proportional to other Heuslers quantified using the same technique [15]. To draw a strong conclusion, a series of samples would be needed to see how these parameters change with composition, annealing temperature, etc. This will be discussed in further detail in Section 6.7.

6.5.5 Longitudinal Magnetoresistance

As discussed in Section 1.9.2, the chiral anomaly is predicted to enhance conductivity in Weyl semimetals when a large magnetic field is applied parallel to the current transport direction. To determine whether such an enhancement is present in Co_2TiGe, the field-dependent resistivity has been measured for several different applied field angles. The important caveat here is that, due to magnon scattering suppression, the magnetoresistance is expected to decrease at high fields simply by virtue of ferromagnetism in Co_2TiGe. Our task is then to determine whether there is NLMR above and beyond that which is native to all metallic ferromagnets.

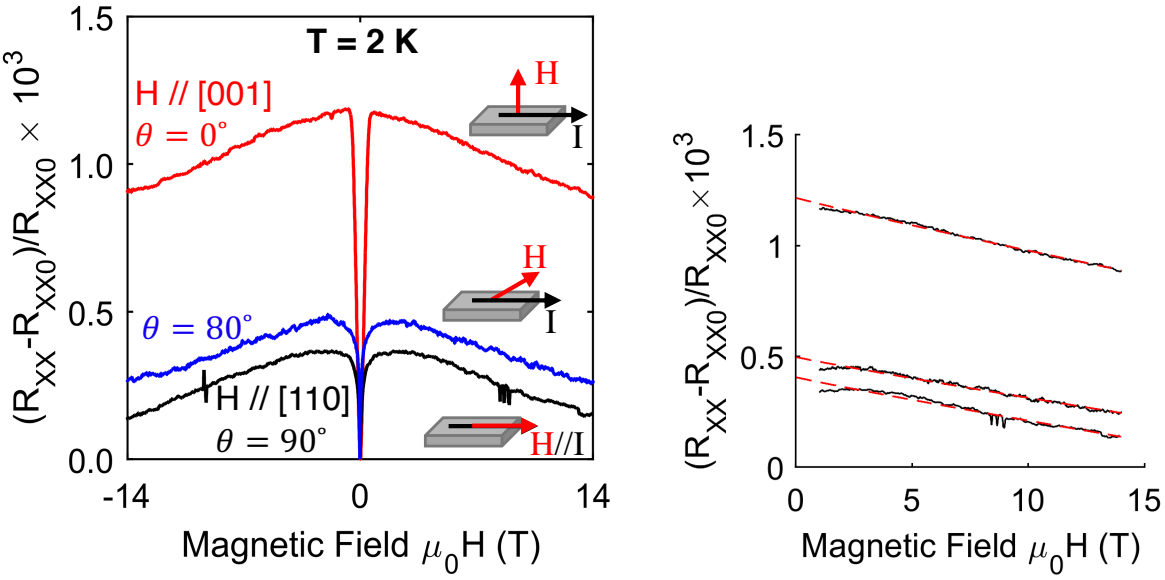

Figure 6.10: (Left) Magnetoresistance as a function of applied field and field angle. The behavior is explained by AMR at low field and magnon suppression at high field. The chiral anomaly would appear as an additional reduction in MR at high field when $\boldsymbol{H}//\boldsymbol{I}$. (Right) High field data from the plot at left (black lines) are plotted against the best fit (red dashed lines) to equation (6.9).

As shown in Fig. 6.10, the magnetoresistance does vary significantly with the applied field angle. However, the main difference in the signal is the magnitude of the AMR in the low field region. The high field region, where the chiral conductance is expected to

contribute, appears to have the same slope and curvature for each field angle. This is confirmed by, once again, fitting the data to equation (6.9). The high quality of the fit suggests that the chiral conductance does not contribute significantly to the longitudinal magnetoresistance in Co_2TiGe. This, in turn, suggests that the conduction electrons are far in energy from the Weyl point, according to equation (1.14). Alternatively, the Fermi surface may contain equal numbers of Weyl points of opposite chiral charge, resulting in a Fermi surface with a Chern number of zero. This null result, while discouraging, is not entirely unexpected due to the calculated Fermi level position of Co_2TiGe. An energy separation of 0.3 eV between the Fermi level and relevant Weyl point W^1_{110} is expected. In order to isolate each of the Weyl points in their own Fermi surface it will be necessary to tune the Fermi level upwards by 0.3 eV. This process will be outlined in Section 6.7.

6.6 Angle-resolved photoemission spectroscopy for stoichiometric Co_2TiGe

While the validity of the chiral anomaly has been called into question by current jetting effects, the presence of Fermi arcs at the surface of Weyl semimetals is, so far, an undisputed phenomenon. ARPES is an ideal technique for measuring these surface states due to its surface sensitivity and excellent energy and momentum resolution. Some samples measured in ARPES were grown on MgO (001) using the conditions that give $L2_1$ ordering, as described above. MgO is an insulator and normally would be unusable as a substrate for photoemission experiments due to charging effects. However, a custom sample block was used that attached the MgO wafer using large clips. After growth of Co_2TiGe, the clips could be moved using a wobblestick in vacuum to electrically short the epitaxial film to the sample block, allowing charge-free measurement in ARPES.

Unfortunately, the crystal quality of MgO (001) substrates is quite poor, with a large amount of crystal twinning and mosaic which can be easily seen in high resolution XRD. This mosaic is reflected in the overlaying epitaxial film, which blurs the observed spectral density measured in ARPES as shown in Fig. 6.11.

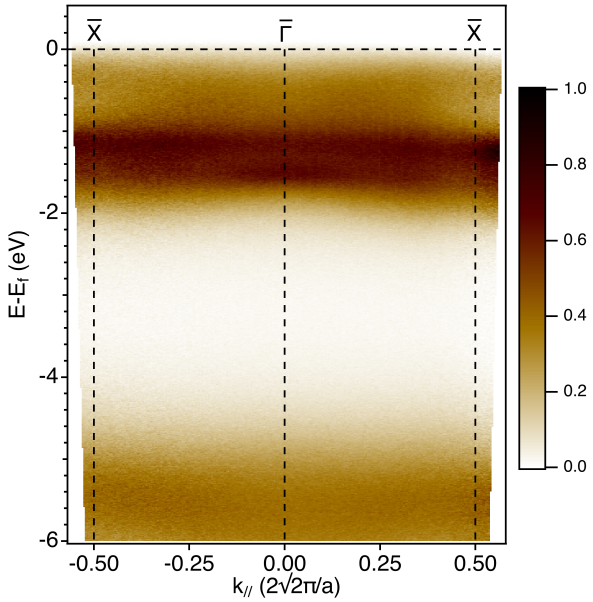

Figure 6.11: ARPES dispersion map for Co_2TiGe/MgO (001) annealed to 600 °C after growth. The mosaic of the MgO substrate is reflected in the quality of the Heusler film, blurring the observed band structure. No dispersive bands are visible.

In contrast, the GdAs/InAlAs/InGaAs/InAlAs/InP (001) structure described in Section 6.2, hereafter referred to as the III-V buffer, was grown on extremely high crystal quality wafers. The buffer should minimize the dislocation density and mosaic of the overlaying Co_2TiGe films. The compromise for using this substrate is that the GdAs diffusion barrier, which prevents reactions with the InAlAs lattice matching layer, does not survive post-growth annealing above temperatures of ∼450 °C. The Heusler film reacts with the GdAs at high temperatures and roughens the film, rendering it useless for ARPES measurements. As a result, the Co_2TiGe grown on III-V buffers did not possess a prominent (111) Bragg reflection in XRD RSMs, indicating they were likely B2 ordered

with nearly complete mixing of the Ti and Ge sites. It is unclear what effect this will have on the Weyl points.

ARPES data was collected at photon energy $h\nu = 60$ eV and the combined work function of the sample and electron detector was $\phi = 3.15$ eV. For electrons from the Fermi level where binding energy is $|E_B| = 0$, the kinetic energy of the ejected photoelectrons was

$$E_{kin} = h\nu - \phi - |E_B| = 56.85\ eV. \tag{6.11}$$

The out-of-plane momentum of the electrons before excitation is then given by

$$k_z = \sqrt{\frac{2m_e}{\hbar^2}(E_{kin}\cos^2\theta + U_0)}, \tag{6.12}$$

where m_e is the mass of the free electron and θ is the polar angle measured from sample normal. The inner potential U_0 is unknown for this material, but can be assumed to be close to that of other Heuslers, around 12 eV [20, 120]. For electrons measured at the center of the surface Brillouin zone ($\bar{\Gamma}$) where $\theta = 0$, the out-of-plane momentum is $k_z = 4.25$ Å^{-1}. Co_2TiGe has lattice parameter $a = 5.83$ Å, and the width of the bulk Brillouin zone along the $X - \Gamma - X$ direction is $4\pi/a = 2.16$ Å^{-1}. This means ARPES probed electrons at a 1.97 Brillouin zone radius from Γ of the first bulk Brillouin zone. Considering symmetry and band folding, k_z is close to Γ of the third bulk Brillouin zone, offset about 6% of the way to the lower X point. The sample manipulator was cooled using liquid He, giving a sample temperature of 30 K as measured by a calibrated resistor mounted to the sample stage. The azimuthal axis was set such that the entrance slit of the detector was aligned with the [110] direction of the Heusler film, which is the $\bar{X} - \bar{\Gamma} - \bar{X}$ axis of the surface Brillouin zone.

The Fermi maps in Fig. 6.12(a) and (b) shows the in-plane momentum dependent

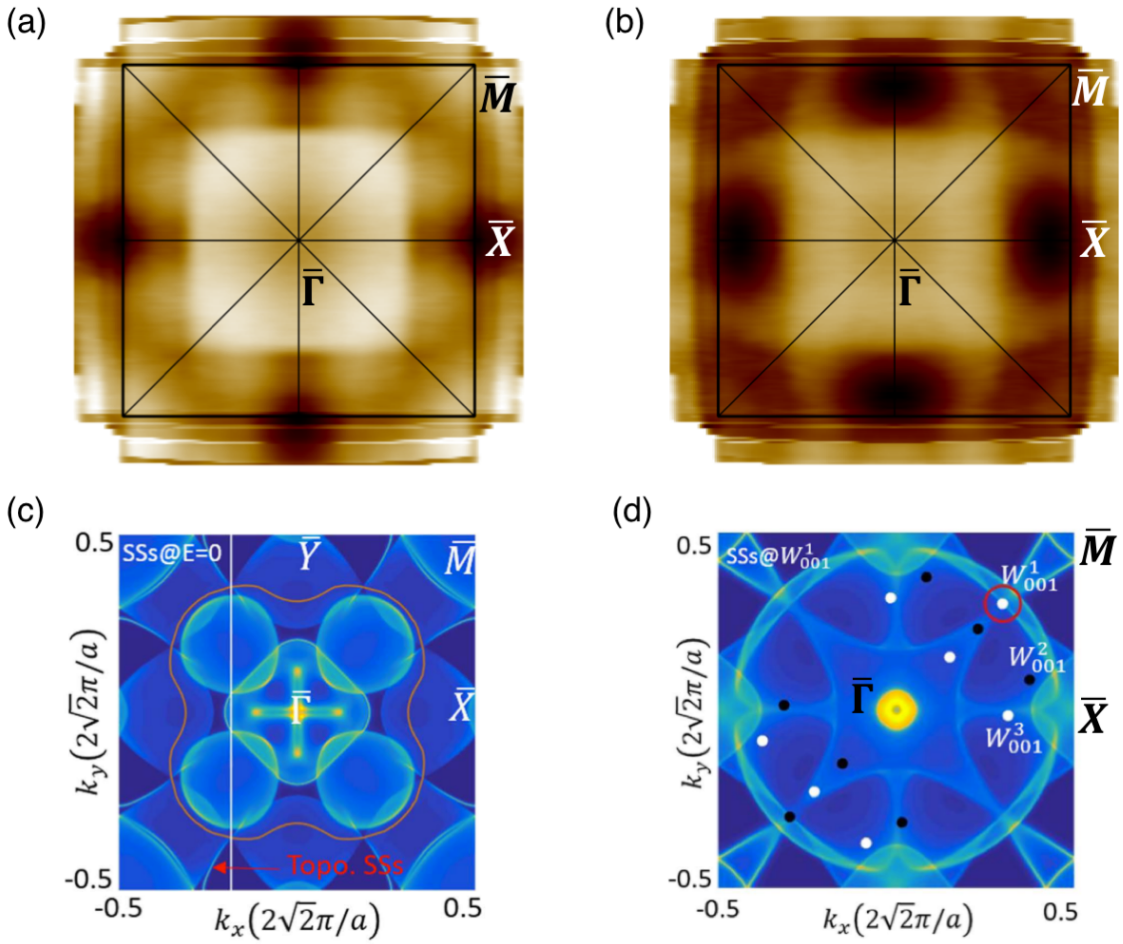

Figure 6.12: ARPES in-plane momentum map for Co_2TiGe collected at $h\nu = 60\ eV$ for electrons at (a) the Fermi level and (b) 300 meV below the Fermi level. Also shown is (c) a calculated Fermi map at $k_z = 0$ in the absence of spin-orbit coupling showing the orange nodal line from which Weyl points arise. (d) Calculated Fermi map at $k_z = 0$ including spin-orbit coupling and magnetization along [100] showing the location of Weyl points as black or white dots, depending on chirality. Figures (c) and (d) are reprinted from [10] under a Creative Commons Attribution 4.0 International License.

density of conduction electrons at this particular k_z slice through the bulk Brillouin zone. The calculated Fermi map for k_z at bulk Γ is also shown. Some features of the theory and experimental Fermi maps match, such as the high intensity at the $\bar{X}$ points. Other features seem to be missing from the experimental result, namely the high intensity at $\bar{\Gamma}$ and ring feature shown in Fig. 6.12(d). It is also notable that no obvious Fermi arcs

exist in either the theory or experimental result. This is discussed briefly by Chang *et al.* [10], who claim that Fermi arcs are likely to be completely obscured by the presence of high intensity bulk-like states projected into the surface Brillouin zone.

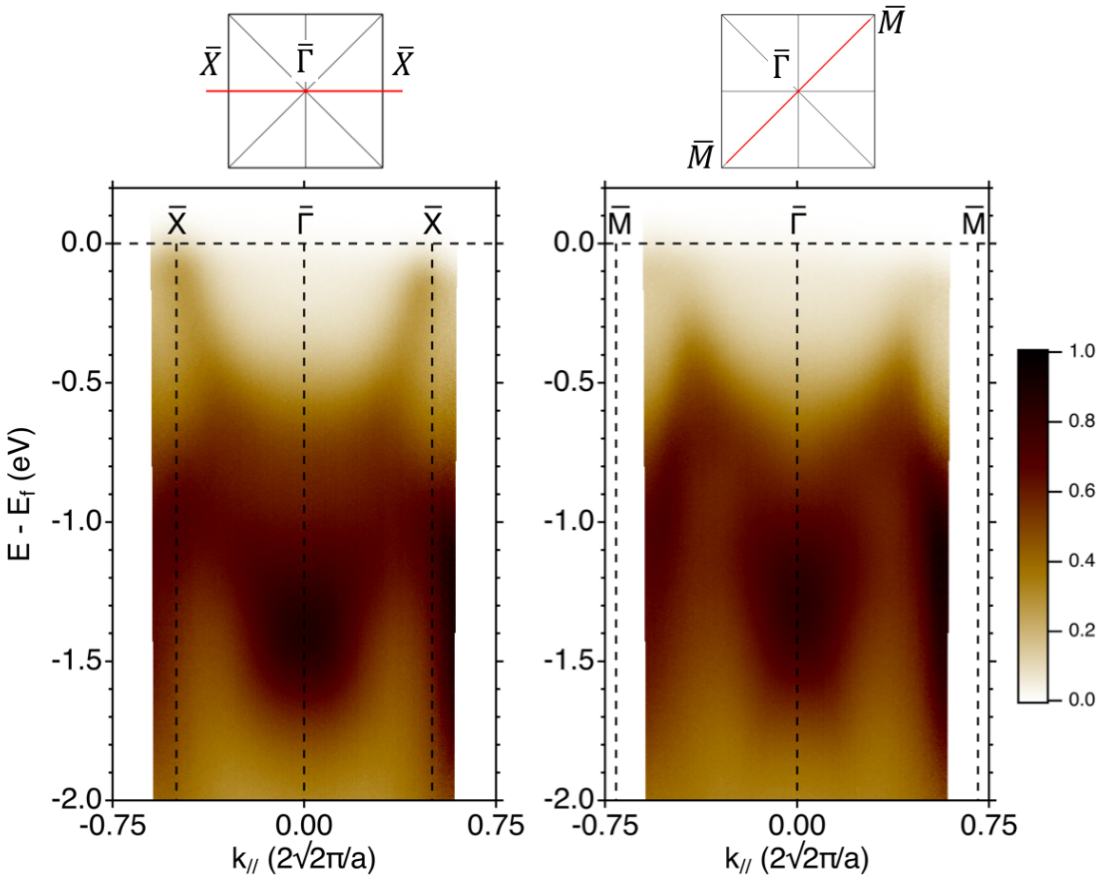

Figure 6.13: ARPES energy dispersion slices for Co_2TiGe collected at $h\nu = 60\ eV$.

This point raises a fundamental problem with the claim that Co_2TiGe is a Weyl material. Experimental confirmation of Weyl semimetallicity requires measuring either negative longitudinal magnetoresistance attributable to the chiral anomaly or observation of Fermi arcs in ARPES data. However, the lack of either of these features doesn't necessarily mean that Co_2TiGe is not a Weyl material, because the measurements can be confounded by Fermi level offset from the Weyl point or overlapping bulk bands, respectively. In other words, the claim that Co_2TiGe is a Weyl metal seems to be unfalsifiable

through standard experimental means, a situation which tends to put experimental scientists in an awkward position.

Instead, we must use other measurements to infer the presence or absence of electronic structure that suggests the existence of Weyl nodes in Co_2TiGe. For example, Fig. 6.13 shows ARPES energy dispersion slices through the $\bar{X}-\bar{\Gamma}-\bar{X}$ and $\bar{M}-\bar{\Gamma}-\bar{M}$ directions. For the latter axis, a pair of Dirac cone-like features around $k_{//} \approx 0.60 \times 2\sqrt{2}\pi/a$ can be seen extending up toward the Fermi level. These could be the manifestation of the nodal line state from which Weyl nodes arise according to the theory [10]. However, this claim is difficult to support with only this data set. To bolster the evidence that Dirac cone features are present, substitutional alloying was performed to shift the Fermi level away from the supposed Dirac point, to allow greater visibility of the band structure there.

6.7 Alloying to achieve isolated Weyl points

As made clear in the previous sections, stoichiometric Co_2TiGe exhibits none of the classic experimental signatures of Weyl semimetals. The chiral conductance is not significant, if present at all, and no Fermi arcs are visible in the surface Brillouin zone. Rather, it is a high crystal quality metallic ferromagnet with high carrier concentration, low mobility, a large amount of electron-electron and electron-magnon scattering, and a modest Berry curvature contribution to the AHE. In other words, Co_2TiGe is a typical magnetic full-Heusler, which may or may not be a half-metal. This seems somehow unsatisfying.

To convert this material into a type II Weyl metal, the Fermi level must be shifted toward the Weyl point. This can be accomplished using electron doping, or substituting an element with one additional electron onto one of the atomic sites. For Co_2TiGe, this means alloying Ni onto the Co site, V onto the Ti site, or As onto the Ge site. Additionally, Sb could be substituted onto the Ge site. Interestingly, Ni_2TiGe, Co_2VGe,

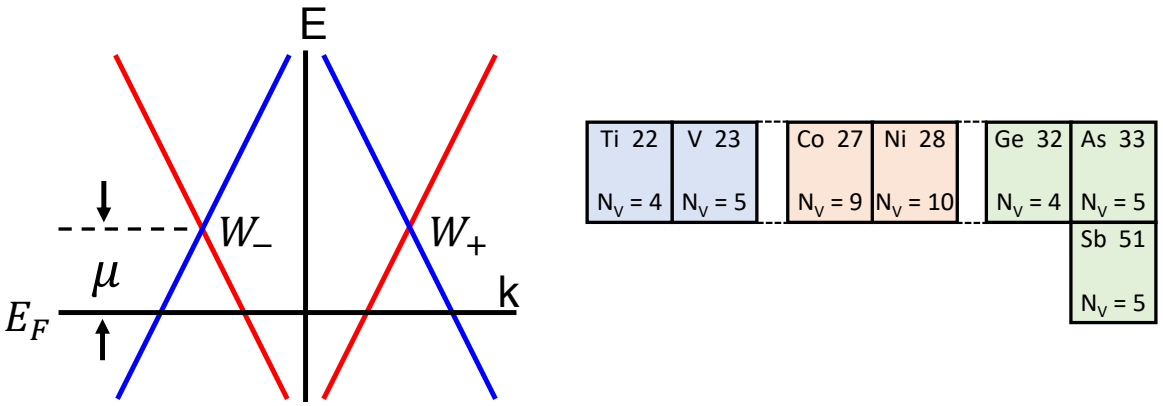

Figure 6.14: (Left) Schematic of the energy dispersion for a pair of Weyl nodes at a distance μ above the Fermi level. (Right) Abbreviated periodic table showing the valence electron counts for relevant elements that could be used in an alloy series.

Co_2TiAs, and Co_2TiSb are all expected to be tetragonally distorted with $D0_{22}$, not $L2_1$, crystal structure [182]. This change in crystal structure causes them to deviate significantly from the full-Heusler Slater-Pauling rule. It also seems exceedingly likely that the broken symmetry in the tetragonally distorted $D0_{22}$ structure would modify or even eliminate the Weyl nodes. However, all the candidate compounds are afflicted by this issue, so the decision of alloying element comes down to availability. Since V and As are not available in the MBE system used, and Sb would likely cause the lattice parameter and spin-orbit coupling to change significantly, Ni was chosen to substitute onto the Co site.

A $Co_{2-x}Ni_xTiGe$ alloy series would need to be carefully monitored for phase segregation and the phase transition to the $D0_{22}$ crystal structure. The relationship between composition x and the increase in Fermi level is not straightforward and must be calculated using DFT. Fortunately, it is likely that the composition x required to move the Fermi level will be small. For example, DFT calculations suggest that $Co_2Zr_{1-x}Nb_xSn$ requires $x = 0.28$ to move the Fermi level upwards by 0.6 eV [9]. A correspondingly

small amount of Ni substituted into Co_2TiGe is unlikely to produce a $D0_{22}$ phase transition. MBE-grown epitaxial thin films also benefit from added stability against such phase transitions due to lattice matching with the substrate.

Assuming $L2_1$ crystal structure is maintained, the magnetic moment of a $Co_{2-x}Ni_xTiGe$ formula unit should follow the Slater-Pauling rule

$$m = |N_V - 24| = |9(2-x) + 10x + 4 + 4 - 24| = |2 + x|. \tag{6.13}$$

This can be used to confirm the stoichiometry of the films via SQUID measurements, as was done in equation (6.2). Any significant deviations from the expected saturation magnetization, along with XRD results, can be used to detect and avoid the $D0_{22}$ phase transition. Furthermore, the AHE analysis defined by equation (6.10) can be applied to quantify the Berry curvature as a function of composition x. When the Fermi level approaches the Weyl node, the Berry curvature is expected to increase dramatically, and it may be possible to detect this using AHE. At the same time, the longitudinal magnetoresistance can be measured as a function of x, which would capture the appearance of the chiral conductance, if it exists. Using these measurements as an indication of Weyl point isolation, a sample with specific Ni composition can be grown, transported to the Advanced Light Source, and examined using ARPES to determine whether Fermi arcs appear in the surface Brillouin zone.

6.8 ARPES of Nickel-doped Co_2TiGe

Fermi level tuning of $Co_{2-x}Ni_xTiGe$ was confirmed by comparing equivalent ARPES energy dispersion slices for $x = 0.0$ and $x = 0.2$. As shown in Fig. 6.15, the bulk-like states near $\bar{\Gamma}$ move downward, or, equivalently, the Fermi level shifts upward by 350 meV

upon substitution of a nickel content of $x = 0.2$. This doping efficiency can be used in future studies of $Co_{2-x}Ni_xTiGe$ to shift the Fermi level to the Weyl point immediately.

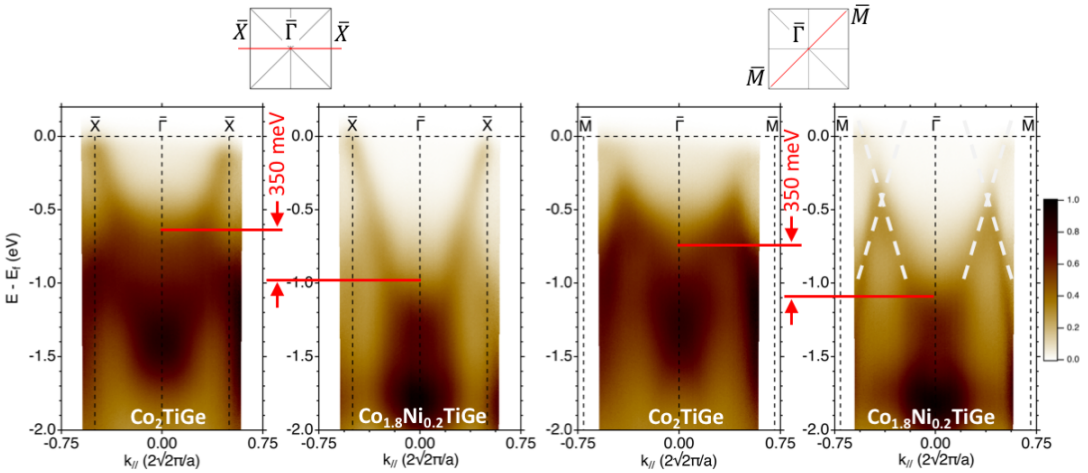

Figure 6.15: ARPES energy dispersion slices collected at $h\nu = 60\ eV$ for for Co_2TiGe and $Co_{1.8}Ni_{0.2}TiGe$ along the (left pair) $\bar{X} - \bar{\Gamma} - \bar{X}$ and (right pair) $\bar{M} - \bar{\Gamma} - \bar{M}$ directions. Dashed white lines have been added as a guide to the eye on the far right image.

In addition to confirming the presence and degree of Fermi level tuning, it is also possible to see clearly the structure of the Dirac cone-like feature in the $\bar{M} - \bar{\Gamma} - \bar{M}$ slice for the $Co_{1.8}Ni_{0.2}TiGe$ film. The Fermi surface map of this film shown in Fig. 6.16(b) also shows clearly the position of this cone-like feature. The four points labeled with red circles indicates the location of the cone. This position coincides with the location of the predicted Weyl point W^1_{001} in the calculated Fermi map in Fig. 6.16(c).

The cone-like feature observed in Fig. 6.16(b) may be a result of surface states rather than the nodal line state in the bulk band structure. To eliminate this possibility, a photon energy sweep from $h\nu = 60$ to 70 eV was performed while measuring the energy dispersion along the $\bar{M} - \bar{\Gamma} - \bar{M}$ direction of the $Co_{1.8}Ni_{0.2}TiGe$ film. The results of the sweep are shown in Fig. 6.17. Note that $h\nu = 60$ eV corresponds to the bulk Γ point, while $h\nu = 70$ eV corresponds to an offset of 22% toward the X point along the Γ-X

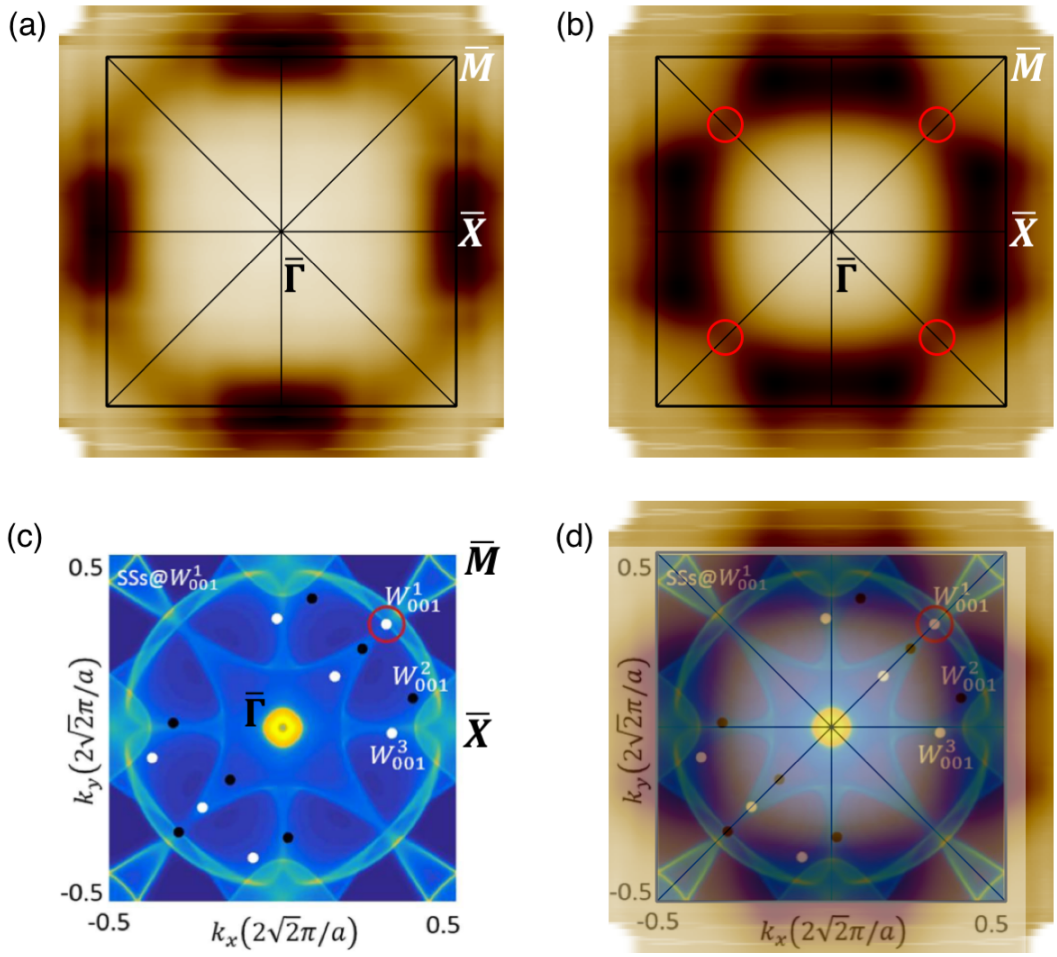

Figure 6.16: ARPES in-plane momentum map for $Co_{1.8}Ni_{0.2}TiGe$ collected at $h\nu = 60\ eV$ for electrons at (a) the Fermi level and (b) 300 meV below the Fermi level. (c) Calculated Fermi map at $k_z = 0$ including spin-orbit coupling and magnetization along [100] showing the location of Weyl points as black or white dots, depending on chirality. (d) Figure (c) overlaid on top of figure (b) showing the correlation of the predicted Weyl nodes with the experimental data. Figures (c) and (d) are reprinted from [10] under a Creative Commons Attribution 4.0 International License.

direction. Electronic states confined to the surface do not disperse in the out-of-plane direction, so surface states should appear constant as a function of photon energy, while bulk-like states should disperse with photon energy.

It is clear from Fig. 6.17 that the Dirac cone-like state disperses with photon energy, and is therefore a bulk-like state. Furthermore, as k_z moves away from Γ, the pair of

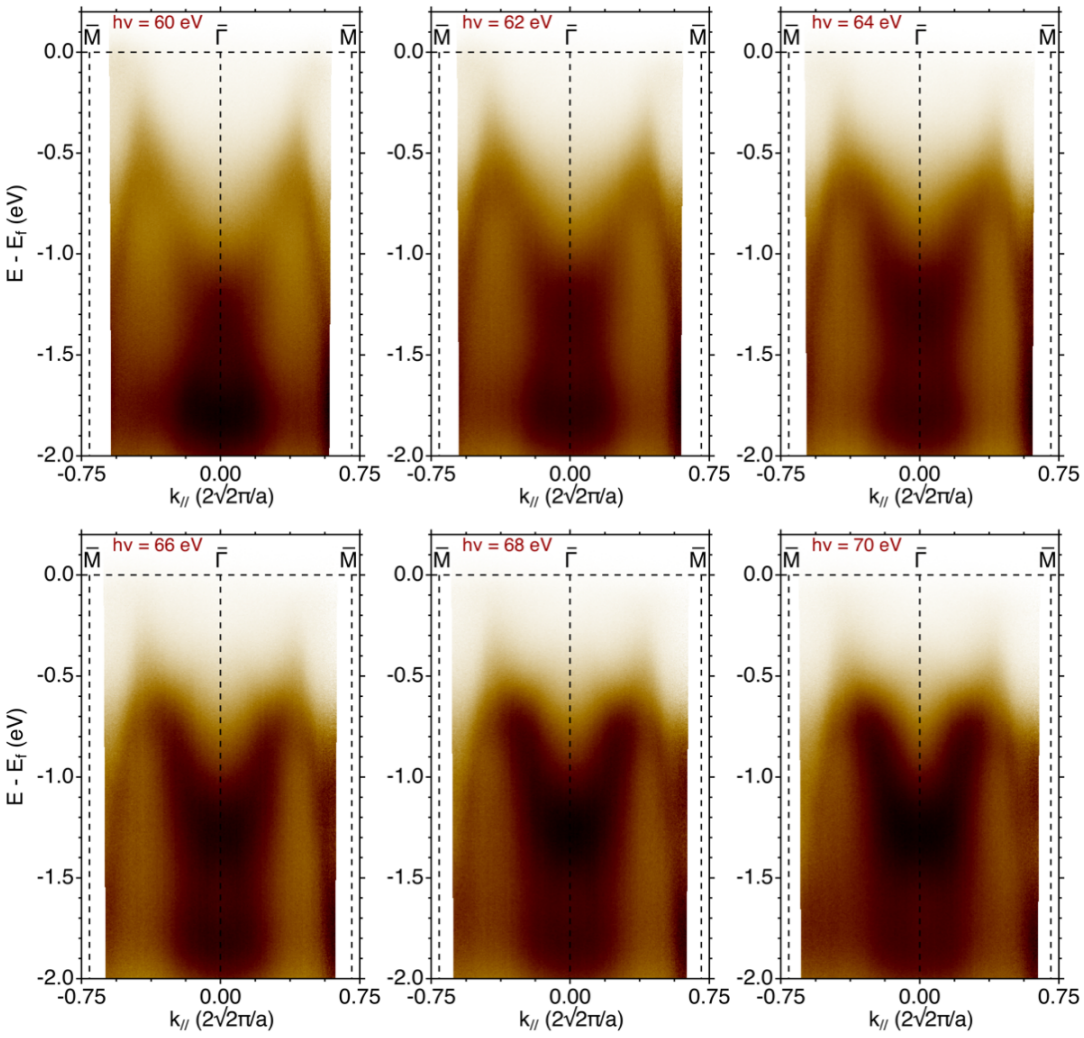

Figure 6.17: ARPES energy dispersion slices along $\bar{M}-\bar{\Gamma}-\bar{M}$ at indicated photon energies $h\nu$. Dispersion with photon energy shows that the cone-like feature is bulk-like, suggesting that it is the nodal line state that gives rise to Weyl nodes.

linearly dispersing intersections become more and more parabolic. This is precisely the behavior expected from a 3D Dirac cone. Therefore, this data strongly suggests that this band dispersion is that of the nodal line state that is expected to give rise to Weyl nodes in the presence of spin-orbit coupling.

6.9 Summary

Time reversal symmetry breaking Weyl metals are an exciting class of materials that serve as analogues through which to study exotic Weyl fermion physics. While several materials such as TaAs and TaP have been shown to exhibit inversion symmetry breaking Weyl semimetallicity, no experimental verification has been completed for the time reversal symmetry breaking varieties. Co_2TiGe, has been predicted to have magnetization direction dependent Weyl nodes, but these nodes are expected to exist ± 0.3 eV from the Fermi energy. Nevertheless, the magnetic, transport, and band structure properties have been examined for any signatures of Weyl physics.

The MBE growth parameters and post-growth annealing temperature was optimized to produce $L2_1$ order. The magnetic moment and Curie point are found to agree with theory and prior reports. The resistivity is found to be dominated by impurity scattering, electron-electron scattering, and electron-magnon scattering. Magnetoresistance is dominated by AMR at low field, and magnon scattering suppression at high field. No evidence was found in longitudinal magnetoresistance data for the chiral anomaly seen in some Weyl semimetals. The Hall effect has been used to find a very high carrier concentration and low mobility consistent with other ferromagnetic metals. Similarly, the magnetic impurity and phonon scattering, as well as the Berry curvature contributions were quantified using AHE and appear to be in proportion with other Heusler compounds. The electronic band dispersion in the surface Brillouin zone was measured using ARPES and found to possess high electron density at the $\bar{X}$ point. However, no Fermi arcs connecting surface projections of the Weyl nodes were observed. A strategy to tune the Fermi level toward the Weyl points using electron doping with a $Co_{2-x}Ni_xTiGe$ alloy was outlined. This allowed observation of a Dirac cone-like feature in a location where a Weyl node is expected to exist based on theoretical calculations.

Chapter 7

Summary and Future Work

7.1 Summary

In this dissertation, it has been shown that the magnetic properties of several technologically promising material systems can be engineered using a combination of interface choice, composition variation, growth condition optimization, and post-growth processing. Each material was grown using molecular beam epitaxy on a substrate that was chosen based on film lattice match, surface energy considerations, and technological relevance. The epitaxial film materials were chosen primarily due to promising predictions of perpendicular magnetic anisotropy, half-metallicity, or Weyl semimetallicity. Each step in the growth, processing, and characterization has been verified using standard techniques adapted to the needs and goals of the specific projects included here.

In Chapter 3 it was shown that ultra-thin Fe films epitaxially grown on MgO (001) substrates by MBE develop an interfacial Fe–O bond consistent with predictions of orbital rehybridization at the Fe/MgO interface. However, lattice mismatch, tensile film strain, and unfavorable surface energy mismatch result in a Volmer-Weber growth mode, even for growths where the substrate is held at room temperature. The islands that form

fail to coalesce at thicknesses where perpendicular magnetic anisotropy is predicted to dominate. Film coalescence is found to occur for 12-Å-thick Fe, while the measured interface anisotropy of $K_S = 0.17 \pm 0.19$ erg/cm^2 would only produce out-of-plane easy axes for films below the critical thickness $t_{cr} = 3.2 \pm 3.7$ Å. Interestingly, the effective film coalescence thickness decreases to 9 Å for Fe films capped with MgO on top. This can be explained by a thin, magnetically active, spinel-like $MgFe_xO_y$ layer that forms at the Fe/MgO interface.

In Chapter 4, Mn_3Ge was found to have high crystal quality and somewhat rough surface morphology. The films were perpendicularly magnetized when grown on prepared $SrTiO_3$ (001), $BaTiO_3$ (001), and Cr/MgO (001) substrates. The films were found to completely react with ferroelectric $BiFeO_3$ (001) substrates. Ferroelectric switching of the out-of-plane magnetization was attempted for Pt/Mn_3Ge/$BaTiO_3$ (001)/Pt structures, but the hysteretic Hall resistance observed was found to be caused by partially reversible crack formation in response to the piezoelectric strain, rather than any magnetization switching effects. Mn_3Ge grown on a full-Heusler Co_2MnAl surface resulted in tall, sparsely distributed square mesas. This enhanced island formation was speculated to arise from high atadom mobility on the Heusler surface. Despite this, the magnetic behavior of the Mn_3Ge/Co_2MnAl structure seemed to possess at least a partially out-of-plane magnetic easy axis. This could be useful for making out-of-plane magnetized magnetic tunnel junctions with half-metallic contacts that do not posses perpendicular magnetic anisotropy on their own.

In Chapter 5, the MBE growth of single crystal epitaxial $[CMA_n/FMA_n]_q$ superlattices on GaAs (001), MgO (001), and Cr/MgO (001) substrates was successfully demonstrated. The films under the critical magnetization of 309 emu/cm^3 grown at 150°C substrate temperature on GaAs (001) exhibited out-of-plane magnetization for $T < 200$ K. Synchrotron-based SR-PES measurements show the spin polarization of stoichiometric,

in-plane magnetized FMA is 25% and that of CMA is 65% at the Fermi level near the bulk X point. Superlattice $[CMA_n/FMA_n]_q$ adopted the electronic character of the termination layer, but provided an additional improvement in spin-polarization for CMA termination, resulting in spin polarization of 95% near the Fermi level.

In Chapter 6, Co_2TiGe was explored as a candidate time reversal symmetry breaking Weyl semimetal. Co_2TiGe has been predicted to have magnetization direction dependent Weyl nodes ± 0.3 eV from the Fermi energy. The magnetic, transport, and band structure properties have been examined for any signatures of Weyl physics. The MBE growth parameters and post-growth annealing temperature was optimized to produce $L2_1$ order. No evidence was found in longitudinal magnetoresistance data for the chiral anomaly seen in some Weyl semimetals. The Hall effect has been used to find a very high carrier concentration and low mobility consistent with other ferromagnetic metals. Similarly, the magnetic impurity and phonon scattering, as well as the Berry curvature contributions were quantified using AHE and appear to be in proportion with other Heusler compounds. The electronic dispersion in the surface Brillouin zone was measured using ARPES and found to possess high electron density at the $\bar{M}$ point. However, no Fermi arcs connecting surface projections of the Weyl nodes were observed.

7.2 Future work

Further study is needed to determine if low temperature growth is the key to epitaxial growth of contiguous Fe films on MgO [141]. A LN_2 cold-stage sample manipulator is available in the Palmstrøm lab, but it is currently used to grow superconductor material. Since Fe would contaminate the superconductors, the present work was unable to gain access to the cold-stage. Once the requirements for superconductors have been relaxed, use of the cold-stage would provide a way to reduce Fe atadom mobility and possibly

prevent Volmer-Weber growth. Another avenue for exploration would be to determine the extent to which continuous sample rotation during growth suppresses the formation of iron corrugations, producing a more uniform Fe film.

The promising initial results of a Mn_3Ge pinning layer grown on a Co_2MnAl surface should be explored further. It seems clear that the growth temperature $T_{sub} = 300$ °C allows too much atadom mobility, resulting in extreme island morphology. Future work should involve further optimization of the growth conditions of Mn_3Ge on other proposed half-metallic Heusler compounds such as Co_2MnAl, Co_2FeAl, Co_2MnSi, and Co_2TiGe.

Future work for $[CMA_n/FMA_n]_q$ superlattices includes measuring the spin polarization of out-of-plane magnetized superlattice films with high aluminum content. This would confirm the coexistence of half-metallicity and perpendicular magnetic anisotropy in a single material. Additionally, the spin polarization should be measured at several different locations in the bulk Brillouin zone. SR-PES measurements presented here measured only electrons at the bulk X point, but electrons on the Fermi surface throughout the Brillouin zone contribute to overall spin polarization. The superlattices should also be incorporated into magnetic tunnel junctions, and a systematic study should be executed to determine the tunneling characteristics on optimized devices.

Co_2TiGe is still being actively studied. A strategy to tune the Fermi level toward the Weyl points using electron doping with a $Co_{2-x}Ni_xTiGe$ alloy has been outlined, and is presently being executed. Preliminary ARPES data seem to indicate that $x = 0.2$ raises the Fermi level by approximately 0.350 eV, exactly the amount required to shift the Fermi level toward the Weyl nodes. Therefore, magnetotransport analysis should be performed on a $Co_{1.8}Ni_{0.2}TiGe$ film to determine the Berry curvature as soon as possible. Additionally, work should begin on Co_2TiSn, which is also expected to be a Weyl material but with a larger degree of spin-orbit splitting due to the heavy Sn atoms.

Appendix A

Anisotropic Magnetoresistance

Chapter 6 contains field-dependent resistivity data that can be separated into low-field and high-field regions. It was argued that the low field region is accounted for by the anisotropic magnetoresistance (AMR). To show this is the case, consider the Stoner-Wohlfarth model

$$E(\theta,\phi) = K_{eff}^{//}(\phi)\sin^2(\theta) + K_{eff}^{\perp}\cos^2(\theta) - \mu_0 \boldsymbol{H}\cdot\boldsymbol{M}. \tag{A.1}$$

In the presence of high magnetic fields applied out-of-plane to a thin film, magnetocrystalline anisotropy becomes negligible. In this limit, in-plane anisotropy is approximately zero and out-of-plane anisotropy is approximately equal to the thin-film shape anisotropy, yielding

$$E(\theta) = 2\pi M_S^2\cos^2(\theta) - \mu_0 H M_S\cos(\theta) \tag{A.2}$$

The magnetic torque equation for this model is given by

$$L(\theta) = \frac{dE}{d\theta} = -4\pi M_S^2\cos(\theta)\sin(\theta) + \mu_0 M_S H\sin(\theta) \tag{A.3}$$

When the system is in equilibrium, $L(\theta) = 0$ and this allows us to find

$$\cos(\theta) = \frac{\mu_0 H}{4\pi M_S}; \qquad \mu_0 H \in [-4\pi M_S, 4\pi M_S] \tag{A.4}$$

The range is inferred from the cancellation of $\sin(\theta)$, which is not allowed when $\theta = 0$. The saturation field value $\mu_0 H_{sat} = 4\pi M_S$ found here is identical to that often used in anomalous Hall effect analysis. Furthermore, the anisotropic magnetoresistance (AMR) is given by

$$\rho(\varphi) = \rho_0 + \Delta\rho\cos^2(\varphi), \tag{A.5}$$

where φ is the angle subtended by the magnetization and charge current directions [183]. For $\boldsymbol{I}//[110]$ and $\boldsymbol{H}//[001]$, it can be assumed that $\varphi = 90° - \theta$, giving

$$\rho(\theta) = \rho_0 + \Delta\rho \sin^2(\theta). \tag{A.6}$$

Recall that $\sin^2(\theta) + \cos^2(\theta) = 1$, which allows us to determine the expected contribution from anisotropic magnetoresistance in the MR data. The extra factor of 1 is absorbed into ρ_0, and the sign is absorbed into $\Delta\rho$.

$$\frac{\rho(\theta) - \rho_0}{\Delta\rho} = \left(\frac{\mu_0 H}{4\pi M_S}\right)^2; \qquad \mu_0 H \in [-4\pi M_S, 4\pi M_S] \tag{A.7}$$

Therefore, the AMR gives approximately parabolic response for field values up to H_{sat}, after which the magnetization saturates. This is precisely what is observed in Fig. 6.7. Additionally, H_{sat} corresponds to a value of M_S of 300 to 350 emu/cm^3, in agreement with M_S determined from SQUID measurements. It should be emphasized that this result is valid only for H applied directly out-of-plane. Introducing an arbitrary tilt angle ξ in H toward the current direction would replace (A.2) with

$$E(\theta) = 2\pi M_S^2 \cos^2(\theta) - \mu_0 M_S H(\cos(\theta)\cos(\xi) + \sin(\theta)\sin(\xi)), \tag{A.8}$$

which ultimately produces a transcendental function that cannot be solved directly. Thus, the low-field MR data are explained by AMR.

Appendix B

Data Analysis Techniques

Throughout this dissertation, raw data has been shown after some type of processing to render it easier to interpret. A few of these processes are given below for transparency and completeness.

B.1 Data smoothing

Smoothing operations were done by convolving raw data with a row of Pascal's triangle, which is approximately Gaussian. This smoothing can be done without sacrificing data integrity as long as the length of the row is smaller than the features being analyzed, and the data is evenly spaced. X-ray diffraction (XRD) rocking curves are a good example, since the convolution will merely appear to increase the FWHM of the Bragg peaks slightly. The MATLAB code is given by

```
x = xData;
y = yData;
halfWidth = someNumber;
boxWidth = 2*halfWidth+1;
boxCar = pascal(boxWidth,2);
boxCar = transpose(abs(boxCar(:,1)));
boxCar = box/sum(boxCar);
x = x(halfWidth+1:end-halfWidth);
y = conv(y,boxCar,'valid');
```

B.2 Evolved multi-parameter fitting

Some simple functions can be easily fit using standard toolboxes included with popular software packages. For example, 2-dimensional Gaussian peaks in X-ray diffraction reciprocal space maps were fit using the MATLAB Curve Fitting Toolbox. Following the instructions in the help files gives reasonable results, and code can be generated by the Toolbox that can be used over and over again in custom scripts.

However, if a fit requires many parameters to be varied independently, it is often helpful to utilize a more robust fitting algorithm. The technique used for multiparameter fitting in the majority of this dissertation can be described as a simple evolutionary algorithm. Instead of using a gradient-based correction for each parameter, the parameters are varied by a random amount about their current values. If the randomly generated new parameters produce a better fit than the old parameters, then the new parameters are kept and used to breed the next set of parameters. In this way, local minima in the fitness function can be avoided, which gives a greater chance that the fit results in parameters representative of the global minimum of the fitness function.

Let $f(x, P)$ be an arbitrary function to be fitted to the experimental data set $g(x_n)$. The independent variable x is sampled at N discrete values $x_1, ..., x_n, ..., x_N$ in the data set. P is an array of parameters that are used to scale and fit the function $f(x, P)$. The rough initial (seed) values P_i can usually be generated automatically from $g(x)$ with a few programming and fitting tricks. They can also simply be set to some constant, reasonable value within a few orders of magnitude of the typical value. The initial guess for the fitting process is then $f(x_n, P_i)$.

To check the goodness of the fit, various fitness functions can be used to generate the χ^2 value. The simplest and most correct method is to sum the variances of each data point:

$$\chi_i^2 = \sum_{n=1}^{N} (f(x_n, P_i) - g(x_n))^2 \tag{B.1}$$

Alternatively, for data that spans across multiple orders of magnitude, a logarithmic fitness function can be used:

$$\chi_i^2 = \sum_{n=1}^{N} [log(f(x_n, P_i)) - log(g(x_n))]^2 \tag{B.2}$$

In both cases, the parameters P must be varied to minimize χ^2, hence the term "least-squares fit".

New guesses for P are generated in the following manner, as written in MATLAB:

$$P_f = P_i. * (1 + \text{randn}(\text{size}(P_i))./M), \tag{B.3}$$

where P_f are the new parameters to compare to the initial parameters, randn() generates an array of values that are randomly distributed about zero according to a Gaussian

distribution, size() returns the dimensions of the argument array. M is an array with the same size as P and represents the resistance of the corresponding parameter to evolution during each step. For example, if $M = 1000$, then $P_f = P_i \pm P_i/1000$. The higher the value of M, the smaller the variation per step in that parameter.

After generating a new set of parameters P_f, they are used to calculate the new χ^2_f value. If $\chi^2_f > \chi^2_i$, then the new parameters are thrown out and P_i are used to generate a new set of parameters P_f. However, if $\chi^2_f < \chi^2_i$, then the old parameters are thrown out and the new parameters become the reference set. In other words, P_i is set equal to P_f. Then new parameters P_f are generated, and so forth.

In this way, random and incremental improvements are added up, resulting in a weighted random walk towards the best fit to the data. While this is not the most efficient way to generate a least-squares fit, it is incredibly robust and versatile.

Appendix C

High quality RBS fitting

This appendix includes instructions to perform a high quality fit to experimental Rutherford backscattering spectrometry (RBS) data using the Genplot RUMP freeware [184]. A nominally stoichiometric 20-nm-thick Co_2TiGe sample grown on Si (001) will be used in this example. Of course, the true thickness and composition are not known during growth, so these will be left as free parameters. This provides an excellent demonstration of the best practices and capabilities of the built-in least-squares fitting algorithm available in RUMP.

Open RUMP and enter the following commands. You should familiarize yourself with the Genplot documentation to understand the functions listed here.

1. `cd (directory)`
   Change directory. Navigate the to the directory containing the RBS data.

2. `ls`
   List stuff. Displays the contents of the current directory.

3. `read (file).rbs`
   Read the file into the data buffer. Note that only .rbs files can be read in, and the accompanying .txt or .asc files cannot be read in directly.

4. `reg 100 325`
   Set the plot region. This should give a reasonable plot containing the substrate plateau and the three film peaks for a 20-nm-thick Co_2TiGe/Si (001) sample.

5. `pl 1`
   Plot the contents of buffer 1 to confirm the quality of the data.

6. `sim`
   Enter simulation mode.

7. `lay 1 c co 2 ti 1 ge 1 / th 100 /cm2`
   Set the top layer to be $Co_2Ti_1Ge_1$ with areal atomic density of $100 \times 10^{15}/cm^2$.

8. `lay 2 c si 1 / th 20000 /cm2`
   Set the bottom layer to be Si with very large areal atomic density because it is the substrate.

9. `pert`
   Enter perturbation mode.

10. `norm`
    Set the normalization region. This should be a well-behaved region of the substrate plateau. Note that [Enter] must be pressed twice for selection crosshairs to appear on the plot. See Fig. C.1(a) for an example region.

11. `wind`
    Set the fitting window. Parameters will be varied to minimize the difference between the data and simulation within the fitting window. This region should contain the leading edge of the substrate and all of the film peaks. Note that [Enter] must be pressed twice for selection crosshairs to appear on the plot. See Fig. C.1(a) for an example region.

12. `vary mev 1.9 2.1`
    Allow the alpha particle beam energy to vary. This is the main scattering variable. Usually this is set by the beamline technician as close to 2 MeV as possible, but each sample run may have a slightly different real energy. This causes an apparent offset and scaling of the data that can be compensated by varying the simulated beam energy by a small amount.

13. `vary fwhm 10 40`
    Allow the full width half max of the beam energy and detector to vary. This can also change from run to run. This value is nominally 20 keV for the Arizona State University beamline but can be as high as 35 keV.

14. `vary th 1 1 200`
    Allow the thickness of layer 1 to vary. Layer 1 is the Co_2TiGe layer in this case. The thickness is in whatever units were chosen when entering the layer in SIM mode.

15. `vary co 1 ti 0 2`
    Allow the composition of the titanium in layer 1 to vary from Co_2Ti_0Ge to Co_2Ti_2Ge.

16. `vary co 1 ge 0 2`
    Allow the composition of the germanium in layer 1 to vary from Co_2TiGe_0 to Co_2TiGe_2.

17. `stat`
    Show the status of the fitting variables. Confirm that all necessary variables are present with the desired fitting ranges on each.

18. `go`
    Execute the multiparameter least-squares fit over the window region. The output for this example can be seen in Fig. C.1(c).

19. `pl 1 ov 0`
    Plot the data and fitted simulation together on the same plot. The result for this example can be seen in Fig. C.1(b).

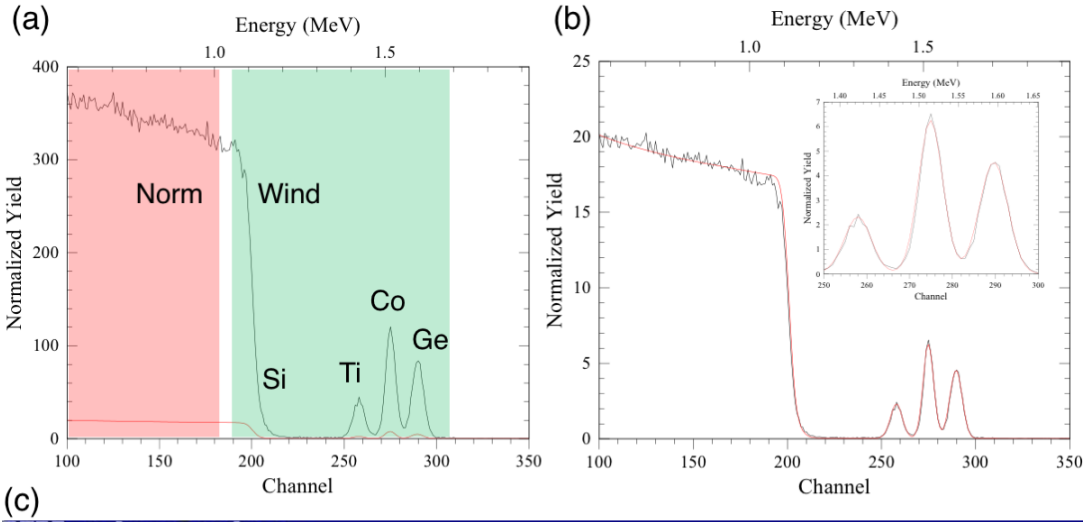

(c)

```
PERT subcommand: go
-------------------------------------------------------------------------------
    CHISQR          mev          fwhm      thickness       comp Ge       comp Ti
-------------------------------------------------------------------------------
     6.324        1.996         34.97          89.72         1.188         1.235
     6.324        1.996         34.97          89.72         1.188         1.235

    Variable                                    Value:                    Sigma
    --------                                    ------                    -----
    Incident energy (MeV)                      1.99578                0.0001878764
    Detector FWHM (keV)                        34.96807                  0.2337606
    Thickness of layer 1      σ_tot = 89.72036 ×10^15/cm^2               0.6872433
    Layer 1, Ge fraction      χ_Ge = 1.187734                          0.02038389
    Layer 1, Ti fraction      χ_Ti = 1.234953                          0.02624743
                              χ_Co = 2.00
Estimated correction factor set for buffer: 0.0541919
```

Figure C.1: (a) RUMP plot showing unfitted data and simulation, along with acceptable normalization and fitting window ranges for perturbation mode. (b) RUMP plot showing a high quality least-squares fit of the simulation to the data. The inset shows the film peaks, and the fit even captures the bridges between peaks. (c) Raw PERT output for the fitting operation. The parameters used to determine film composition are shown in red.

The resulting fit should be of high quality, even if the peaks overlap significantly, as shown in Fig. C.1(b). The fit will return the total areal density of the layer σ_{tot}, as well as the relative compositions χ_{Ti} and χ_{Ge} normalized to Co_2. The factor of 2 comes from

how we defined the layer in SIM. The individual atomic areal densities of each element can be determined using the following formulas.

$$\sigma_{Co} = \frac{2\sigma_{tot}}{2 + \chi_{Ti} + \chi_{Ge}} \tag{C.1}$$

$$\sigma_{Ti} = \frac{\chi_{Ti}\sigma_{tot}}{2 + \chi_{Ti} + \chi_{Ge}} \tag{C.2}$$

$$\sigma_{Ge} = \frac{\chi_{Ge}\sigma_{tot}}{2 + \chi_{Ti} + \chi_{Ge}} \tag{C.3}$$

This strategy results in composition values within a few percent of the gross values obtained from the more standard analysis technique that directly integrates the area under the experimental peaks using the "thick" command. This least squares fitting method has the advantage of being able to deconvolve peaks that overlap significantly, and automatically finds the correction factor during the normalization process.

Bibliography

[1] S. A. Wolf, D. D. Awschalom, R. A. Buhrman, J. M. Daughton, S. von Molnár, M. L. Roukes, A. Y. Chtchelkanova, and D. M. Treger, "Spintronics: A Spin-Based Electronics Vision for the Future," *Science*, **294**(5546), 1488–1495 (2001), doi:10.1126/science.1065389.

[2] D. Morton, "Armour Research Foundation and the Wire Recorder: How Academic Entrepreneurs Fail," *Technology and Culture*, **39**(2), 213–244 (1998), doi:10.2307/3107045.

[3] W. J. Gallagher and S. S. P. Parkin, "Development of the magnetic tunnel junction MRAM at IBM: From first junctions to a 16-Mb MRAM demonstrator chip," *IBM Journal of Research and Development*, **50**(1), 5–23 (2006), doi:10. 1147/rd. 501.0005.

[4] T. Graf, C. Felser, and S. S. P. Parkin, "Simple rules for the understanding of Heusler compounds," *Progress in Solid State Chemistry*, **39**(1), 1 – 50 (2011), doi:10.1016/j.progsolidstchem.2011.02.001.

[5] T. Graf, S. S. P. Parkin, and C. Felser, "Heusler compounds - A material class with exceptional properties," *IEEE Trans. Mag.*, **47**(2), 367–373 (2011), doi:10.1109/TMAG.2010.2096229.

[6] S. Datta and B. Das, "Electronic analog of the electro-optic modulator," *Applied Physics Letters*, **56**(7), 665–667 (1990), doi:10.1063/1.102730.

[7] C. Brüne, A. Roth, H. Buhmann, E. M. Hankiewicz, L. W. Molenkamp, J. Maciejko, X.-L. Qi, and S.-C. Zhang, "Spin polarization of the quantum spin Hall edge states," *Nat. Phys.*, **8**, 485 (2012), doi:10.1038/nphys2322.

[8] P. M. Tedrow and R. Meservey, "Spin-Dependent Tunneling into Ferromagnetic Nickel," *Phys. Rev. Lett.*, **26**, 192–195 (1971), doi:10.1103/PhysRevLett.26.192.

[9] Z. Wang, M. G. Vergniory, S. Kushwaha, M. Hirschberger, E. V. Chulkov, A. Ernst, N. P. Ong, R. J. Cava, and B. A. Bernevig, "Time-Reversal-Breaking Weyl Fermions in Magnetic Heusler Alloys," *Phys. Rev. Lett.*, **117**, 236401 (2016), doi:10.1103/PhysRevLett.117.236401.

[10] G. Chang, S.-Y. Xu, H. Zheng, B. Singh, C.-H. Hsu, G. Bian, N. Alidoust, I. Belopolski, D. S. Sanchez, S. Zhang, H. Lin, and M. Z. Hasan, "Room-temperature magnetic topological Weyl fermion and nodal line semimetal states in half-metallic Heusler Co_2TiX (X=Si, Ge, or Sn)," *Sci. Rep.*, **6**, 38839 (2016), doi:10.1038/srep38839.

[11] C. J. Palmstrøm, "Heusler compounds and spintronics," *Progress in Crystal Growth and Characterization of Materials*, **62**(2), 371 – 397 (2016), doi:10.1016/j.pcrysgrow.2016.04.020.

[12] J. W. Dong, L. C. Chen, J. Q. Xie, T. A. R. Müller, D. M. Carr, C. J. Palmstrø m, S. McKernan, Q. Pan, and R. D. James, "Epitaxial growth of ferromagnetic Ni_2MnGa on GaAs(001) using NiGa interlayers," *Journal of Applied Physics*, **88**(12), 7357–7359 (2000), doi:10.1063/1.1326461.

[13] C. Uher, J. Yang, S. Hu, D. T. Morelli, and G. P. Meisner, "Transport properties of pure and doped MNiSn (M=Zr, Hf)," *Phys. Rev. B*, **59**, 8615–8621 (1999), doi:10.1103/PhysRevB.59.8615.

[14] A. D. Rice, J. K. Kawasaki, N. Verma, D. J. Pennachio, B. D. Schultz, and C. J. Palmstrøm, "Structural and electronic properties of molecular beam epitaxially grown $Ni_{1+x}TiSn$ films," *Journal of Crystal Growth*, **467**, 71 – 76 (2017), doi:10.1016/j.jcrysgro.2017.03.015.

[15] S. D. Harrington, A. D. Rice, T. L. Brown-Heft, B. Bonef, A. Sharan, A. P. McFadden, J. A. Logan, M. Pendharkar, M. M. Feldman, O. Mercan, A. G. Petukhov, A. Janotti, L. Colakerol Arslan, and C. J. Palmstrøm, "Growth, electrical, structural, and magnetic properties of half-Heusler $CoTi_{1-x}Fe_xSb$," *Phys. Rev. Materials*, **2**, 014406 (2018), doi:10.1103/PhysRevMaterials.2.014406.

[16] T. L. Brown-Heft, J. A. Logan, A. P. McFadden, C. Guillemard, P. Le Fèvre, F. Bertran, S. Andrieu, and C. J. Palmstrøm, "Epitaxial Heusler superlattice Co_2MnAl/Fe_2MnAl with perpendicular magnetic anisotropy and termination-dependent half-metallicity," *Phys. Rev. Materials*, **2**, 034402 (2018), doi:10.1103/PhysRevMaterials.2.034402.

[17] A. P. McFadden, T. L. Brown-Heft, D. Pennachio, N. S. Wilson, J. A. Logan, and C. J. Palmstrøm, "Oxygen migration in epitaxial $CoFe/MgO/Co_2MnSi$ magnetic tunnel junctions," *J. Appl. Phys.*, **122**(11), 113902 (2017), doi:10.1063/1.5003089.

[18] H. Kurt, N. Baadji, K. Rode, M. Venkatesan, P. Stamenov, S. Sanvito, and J. M. D. Coey, "Magnetic and electronic properties of $D0_{22}$-Mn_3Ge (001) films," *Applied Physics Letters*, **101**(13), 132410 (2012), doi:10.1063/1.4754123.

[19] J. Winterlik, G. H. Fecher, A. Thomas, and C. Felser, "Superconductivity in palladium-based Heusler compounds," *Phys. Rev. B*, **79**, 064508 (2009), doi:10.1103/PhysRevB.79.064508.

[20] J. A. Logan, S. J. Patel, S. D. Harrington, C. M. Polley, B. D. Schultz, T. Balasubramanian, A. Janet, A. Mikkelsen, and C. J. Palmstrøm, "Observation of a topologically non-trivial surface state in half-Heusler PtLuSb (001) thin films," *Nat. Commun.*, **7**(7), 11993 (2016), doi:10.1038/ncomms11993.

[21] J. A. Logan, T. L. Brown-Heft, S. D. Harrington, N. S. Wilson, A. P. McFadden, A. D. Rice, M. Pendharkar, and C. J. Palmstrøm, "Growth, structural, and magnetic properties of single-crystal full-Heusler Co_2TiGe thin films," *Journal of Applied Physics*, **121**(21), 213903 (2017), doi:10.1063/1.4984311.

[22] A. Rath, C. Sivakumar, C. Sun, S. J. Patel, J. S. Jeong, J. Feng, G. Stecklein, P. A. Crowell, C. J. Palmstrøm, W. H. Butler, and P. M. Voyles, "Reduced interface spin polarization by antiferromagnetically coupled Mn segregated to the Co_2MnSi/GaAs (001) interface," *Phys. Rev. B*, **97**, 045304 (2018), doi:10.1103/PhysRevB.97.045304.

[23] C. Kittel, *Introduction to Solid State Physics*, John Wiley & Sons, Inc., New York, 6th edition (1986), ISBN 9780471874744.

[24] R. M. Bozorth, *Ferromagnetism*, Wiley (1993), ISBN 9780780310322.

[25] P. A. M. Dirac, "The quantum theory of the electron," *Proceedings of the Royal Society of London A: Mathematical, Physical and Engineering Sciences*, **117**(778), 610–624 (1928), doi:10.1098/rspa.1928.0023.

[26] M. Pajda, J. Kudrnovský, I. Turek, V. Drchal, and P. Bruno, "Ab initio calculations of exchange interactions, spin-wave stiffness constants, and Curie temperatures of Fe, Co, and Ni," *Phys. Rev. B*, **64**, 174402 (2001), doi:10.1103/PhysRevB.64.174402.

[27] A. Sugihara, K. Suzuki, S. Mizukami, and T. Miyazaki, "Structure and magnetic properties of tetragonal Heusler $D0_{22}$–Mn_3Ge compound epitaxial films with high perpendicular magnetic anisotropy," *Journal of Physics D: Applied Physics*, **48**(16), 164009 (2015), doi:10.1088/0022-3727/48/16/164009.

[28] J. Kanamori, "Electron Correlation and Ferromagnetism of Transition Metals," *Progress of Theoretical Physics*, **30**(3), 275–289 (1963), doi:10.1143/PTP.30.275.

[29] J. Kübler, *Theory of itinerant electron magnetism*, Internat. Ser. Mono. Phys., Oxford Univ. Press, Oxford (2000), ISBN 9780199559022.

[30] K. H. J. Buschow and F. R. de Boer, *Itinerant-Electron Magnetism*, Springer US, Boston, MA (2003), ISBN 978-0-306-48408-7, doi:10. 1007/0-306-48408-0_7.

[31] J. Kübler, A. R. William, and C. B. Sommers, "Formation and coupling of magnetic moments in Heusler alloys," *Phys. Rev. B*, **28**, 1745–1755 (1983), doi:10.1103/PhysRevB.28.1745.

[32] J. Kübler, G. H. Fecher, and C. Felser, "Understanding the trend in the Curie temperatures of Co_2 -based Heusler compounds: Ab initio calculations," *Phys. Rev. B*, **76**, 024414 (2007), doi:10.1103/PhysRevB.76.024414.

[33] S. Skaftouros, K. Özdoğan, E. Şaşıoğlu, and I. Galanakis, "Generalized Slater-Pauling rule for the inverse Heusler compounds," *Phys. Rev. B*, **87**, 024420 (2013), doi:10.1103/PhysRevB.87.024420.

[34] M. Johnson and R. H. Silsbee, "Spin-injection experiment," *Phys. Rev. B*, **37**, 5326–5335 (1988), doi:10.1103/PhysRevB.37.5326.

[35] R. A. de Groot, F. M. Mueller, P. G. v. Engen, and K. H. J. Buschow, "New Class of Materials: Half-Metallic Ferromagnets," *Phys. Rev. Lett.*, **50**, 2024–2027 (1983), doi:10.1103/PhysRevLett.50.2024.

[36] M. Jourdan, J. Minár, J. Braun, A. Kronenberg, S. Chadov, B. Balke, A. Gloskovskii, M. Kolbe, H. J. Elmers, G. Schönhense, H. Ebert, C. Felser, and M. Kläui, "Direct observation of half-metallicity in the Heusler compound Co_2MnSi," *Nat. Commun.*, **5**(May), 3974 (2014), doi:10.1038/ncomms4974.

[37] M. T. Johnson, P. J. H. Bloemen, F. J. A. den Broeder, and J. J. de Vries, "Magnetic anisotropy in metallic multilayers," *Reports Prog. Phys.*, **59**(11), 1409–1458 (1996), doi:10.1088/0034-4885/59/11/002.

[38] H. B. Callen and E. Callen, "The present status of the temperature dependence of magnetocrystalline anisotropy, and the $l(l+1)^2$ power law," *Journal of Physics and Chemistry of Solids*, **27**(8), 1271 – 1285 (1966), doi:10.1016/0022-3697(66)90012-6.

[39] H. X. Yang, M. Chshiev, B. Dieny, J. H. Lee, A. Manchon, and K. H. Shin, "First-principles investigation of the very large perpendicular magnetic anisotropy at Fe/MgO and Co/MgO interfaces," *Phys. Rev. B*, **84**, 054401 (2011), doi:10.1103/PhysRevB.84.054401.

[40] A. Hallal, H. X. Yang, B. Dieny, and M. Chshiev, "Anatomy of perpendicular magnetic anisotropy in Fe/MgO magnetic tunnel junctions: First-principles insight," *Phys. Rev. B*, **88**, 184423 (2013), doi:10.1103/PhysRevB.88.184423.

[41] S. Ikeda, J. Hayakawa, Y. Ashizawa, Y. M. Lee, K. Miura, H. Hasegawa, M. Tsunoda, F. Matsukura, and H. Ohno, "Tunnel magnetoresistance of 604% at 300K by suppression of Ta diffusion in CoFeB/MgO/CoFeB pseudo-spin-valves annealed at high temperature," *Applied Physics Letters*, **93**(8), 082508 (2008), doi:10.1063/1.2976435.

[42] S. Ikeda, K. Miura, H. Yamamoto, K. Mizunuma, H. D. Gan, M. Endo, S. Kanai, J. Hayakawa, F. Matsukura, and H. Ohno, "A perpendicular-anisotropy CoFeB-MgO magnetic tunnel junction." *Nat. Mater.*, **9**(9), 721–724 (2010), doi:10.1038/nmat2804.

[43] S. Ikeda, J. Hayakawa, Y. M. Lee, F. Matsukura, Y. Ohno, T. Hanyu, and H. Ohno, "Magnetic Tunnel Junctions for Spintronic Memories and Beyond," *IEEE Transactions on Electron Devices*, **54**(5), 991–1002 (2007), doi:10. 1109/TED. 2007.894617.

[44] D. Weller, A. Moser, L. Folks, M. E. Best, W. Lee, M. F. Toney, M. Schwickert, J. U. Thiele, and M. F. Doerner, "High K_u materials approach to 100 Gbits/in^2," *IEEE Transactions on Magnetics*, **36**(1), 10–15 (2000), doi:10. 1109/20. 824418.

[45] L. Thomas, G. Jan, J. Zhu, H. Liu, Y.-J. Lee, S. Le, R.-Y. Tong, K. Pi, Y.-J. Wang, D. Shen, R. He, J. Haq, J. Teng, V. Lam, K. Huang, T. Zhong, T. Torng, and P.-K. Wang, "Perpendicular spin transfer torque magnetic random access memories with high spin torque efficiency and thermal stability for embedded applications (invited)," *Journal of Applied Physics*, **115**(17), 172615 (2014), doi:10.1063/1.4870917.

[46] S.-M. Ahn and G. S. D. Beach, "Crossover between in-plane and perpendicular anisotropy in Ta/Co_xFe_{100-x}/MgO films as a function of Co composition," *Journal of Applied Physics*, **113**(17), 17C112 (2013), doi:10.1063/1.4799779.

[47] E. P. W. E. C. Stoner, F. R. S., "A mechanism of magnetic hysteresis in heterogeneous alloys," *Philosophical Transactions of the Royal Society of London A: Mathematical, Physical and Engineering Sciences*, **240**(826), 599–642 (1948), doi:10.1098/rsta.1948.0007.

[48] C. Tannous and J. Gieraltowski, "The Stoner-Wohlfarth model of ferromagnetism," *European Journal of Physics*, **29**(3), 475 (2008), doi:10.1088/0143-0807/29/3/008.

[49] M. Urbaniak, "Magnetic Anisotropy," http://www.ifmpan.poznan.pl/~urbaniak/Wyklady2012/urbifmpan2012lect5_03.pdf, accessed: 2018-06-20.

[50] S. S. P. Parkin, "Spin-Polarized Current in Spin Valves and Magnetic Tunnel Junctions," *MRS Bulletin*, **31**(5), 389–394 (2006), doi:10. 1557/mrs2006. 99.

[51] R. Meservey and P. M. Tedrow, "Spin-polarized electron tunneling," *Physics Reports*, **238**(4), 173 – 243 (1994), doi:10.1016/0370-1573(94)90105-8.

[52] J. C. Slonczewski, "Conductance and exchange coupling of two ferromagnets separated by a tunneling barrier," *Phys. Rev. B*, **39**, 6995–7002 (1989), doi:10.1103/PhysRevB.39.6995.

[53] M. Julliere, "Tunneling between ferromagnetic films," *Physics Letters A*, **54**(3), 225 – 226 (1975), doi:10.1016/0375-9601(75)90174-7.

[54] T. Ishikawa, H.-x. Liu, T. Taira, K.-i. Matsuda, T. Uemura, and M. Yamamoto, "Influence of film composition in Co_2MnSi electrodes on tunnel magnetoresistance characteristics of Co_2MnSi/MgO/Co_2MnSi magnetic tunnel junctions," *Appl. Phys. Lett.*, **95**(23), 232512 (2009), doi:10.1063/1.3272926.

[55] P. Mavropoulos, M. Ležaić, and S. Blügel, "Half-metallic ferromagnets for magnetic tunnel junctions by ab initio calculations," *Phys. Rev. B*, **72**, 174428 (2005), doi:10.1103/PhysRevB.72.174428.

[56] C. H. Lambert, A. Rajanikanth, T. Hauet, S. Mangin, E. E. Fullerton, and S. Andrieu, "Quantifying perpendicular magnetic anisotropy at the Fe-MgO(001) interface," *Applied Physics Letters*, **102**(12), 122410 (2013), doi:10.1063/1.4798291.

[57] X. G. Zhang, W. H. Butler, and A. Bandyopadhyay, "Effects of the iron-oxide layer in Fe-FeO-MgO-Fe tunneling junctions," *Phys. Rev. B*, **68**, 092402 (2003), doi:10.1103/PhysRevB.68.092402.

[58] T. X. Wang, Y. Li, K. J. Lee, J. U. Cho, D. K. Kim, S. J. Noh, and Y. K. Kim, "Influence of interface state in Fe/MgO/Fe magnetic tunnel junction system: C modified interfaces – a first principle study," *Journal of Applied Physics*, **109**(8), 083714 (2011), doi:10.1063/1.3575337.

[59] F. Bonell, T. Hauet, S. Andrieu, F. Bertran, P. Le Fèvre, L. Calmels, A. Tejeda, F. Montaigne, B. Warot-Fonrose, B. Belhadji, A. Nicolaou, and A. Taleb-Ibrahimi, "Spin-Polarized Electron Tunneling in bcc FeCo/MgO/FeCo(001) Magnetic Tunnel Junctions," *Phys. Rev. Lett.*, **108**, 176602 (2012), doi:10.1103/PhysRevLett.108.176602.

[60] J. Jeong, Y. Ferrante, S. V. Faleev, M. G. Samant, C. Felser, and S. S. P. Parkin, "Termination layer compensated tunnelling magnetoresistance in ferrimagnetic Heusler compounds with high perpendicular magnetic anisotropy," *Nat. Commun.*, **7**, 10276 (2016), doi:10.1038/ncomms10276.

[61] S. Andrieu, A. Neggache, T. Hauet, T. Devolder, A. Hallal, M. Chshiev, A. M. Bataille, P. Le Fèvre, and F. Bertran, "Direct evidence for minority spin

gap in the Co_2MnSi Heusler compound," *Phys. Rev. B*, **93**(9), 094417 (2016), doi:10.1103/PhysRevB.93.094417.

[62] W. H. Butler, X. G. Zhang, T. C. Schulthess, and J. M. MacLaren, "Spin-dependent tunneling conductance of Fe/MgO/Fe sandwiches," *Phys. Rev. B*, **63**, 054416 (2001), doi:10.1103/PhysRevB.63.054416.

[63] A. Gangulee, J. A. Aboaf, and R. J. Kobliska, "Annealing behavior of amorphous ferromagnetic Co-Fe-B and Fe-B thin films," *Journal of Applied Physics*, **52**(4), 2928–2931 (1981), doi:10.1063/1.329029.

[64] J. Sinha, M. Gruber, M. Kodzuka, T. Ohkubo, S. Mitani, K. Hono, and M. Hayashi, "Influence of boron diffusion on the perpendicular magnetic anisotropy in Ta—CoFeB—MgO ultrathin films," *Journal of Applied Physics*, **117**(4), 043913 (2015), doi:10.1063/1.4906096.

[65] J. Hayakawa, S. Ikeda, Y. M. Lee, F. Matsukura, and H. Ohno, "Effect of high annealing temperature on giant tunnel magnetoresistance ratio of CoFeB/MgO/CoFeB magnetic tunnel junctions," *Applied Physics Letters*, **89**(23), 232510 (2006), doi:10.1063/1.2402904.

[66] S. Yuasa, Y. Suzuki, T. Katayama, and K. Ando, "Characterization of growth and crystallization processes in CoFeB/MgO/CoFeB magnetic tunnel junction structure by reflective high-energy electron diffraction," *Applied Physics Letters*, **87**(24), 242503 (2005), doi:10.1063/1.2140612.

[67] Everspin Technologies, "Spin-transfer Torque MRAM Technology," https://www.everspin.com/spin-transfer-torque-mram-technology, accessed: 2018-07-20.

[68] S. Mao, E. Linville, J. Nowak, Z. Zhang, S. Chen, B. Karr, P. Anderson, M. Ostrowski, T. Boonstra, H. Cho, O. Heinonen, M. Kief, S. Xue, J. Price, A. Shukh, N. Amin, P. Kolbo, P.-L. Lu, P. Steiner, Y. C. Feng, N.-H. Yeh, B. Swanson, and P. Ryan, "Tunneling magnetoresistive heads beyond 150 Gb/in^2," *IEEE Transactions on Magnetics*, **40**(1), 307–312 (2004), doi:10. 1109/TMAG. 2003.821167.

[69] Mouser Electronics, "Electronic Components," https://www.mouser.com/Electronic-Components/, accessed: 2018-07-20.

[70] R. L. Stamps, "Mechanisms for exchange bias," *Journal of Physics D: Applied Physics*, **33**(23), R247 (2000), doi:10.1088/0022-3727/33/23/201.

[71] M. D. Stiles and A. Zangwill, "Anatomy of spin-transfer torque," *Phys. Rev. B*, **66**, 014407 (2002), doi:10.1103/PhysRevB.66.014407.

[72] G. Yu, P. Upadhyaya, Y. Fan, J. G. Alzate, W. Jiang, K. L. Wong, S. Takei, S. A. Bender, L. T. Chang, Y. Jiang, M. Lang, J. Tang, Y. Wang, Y. Tserkovnyak, P. K. Amiri, and K. L. Wang, "Switching of perpendicular magnetization by spin-orbit torques in the absence of external magnetic fields," *Nat. Nanotechnol.*, **9**(7), 548–554 (2014), doi:10.1038/nnano.2014.94.

[73] Q. Ma, Y. Li, D. B. Gopman, Y. P. Kabanov, R. D. Shull, and C. L. Chien, "Switching a Perpendicular Ferromagnetic Layer by Competing Spin Currents," *Phys. Rev. Lett.*, **120**, 117703 (2018), doi:10.1103/PhysRevLett.120.117703.

[74] N. Tiercelin, Y. Dusch, A. Klimov, S. Giordano, V. Preobrazhensky, and P. Pernod, "Room temperature magnetoelectric memory cell using stress-mediated magnetoelastic switching in nanostructured multilayers," *Applied Physics Letters*, **99**(19), 192507 (2011), doi:10.1063/1.3660259.

[75] A. K. Biswas, S. Bandyopadhyay, and J. Atulasimha, "Energy-efficient magnetoelastic non-volatile memory," *Applied Physics Letters*, **104**(23), 232403 (2014), doi:10.1063/1.4882276.

[76] J. M. Hu, C. G. Duan, C. W. Nan, and L. Q. Chen, "Understanding and designing magnetoelectric heterostructures guided by computation: Progresses, remaining questions, and perspectives," *npj Comput. Mater.*, **3**(1), 1–20 (2017), doi:10.1038/s41524-017-0020-4.

[77] H. Weyl, "Gravitation and the electron," *Proceedings of the National Academy of Sciences*, **15**(4), 323–334 (1929), doi:10.1073/pnas.15.4.323.

[78] P. B. Pal, "Dirac, Majorana, and Weyl fermions," *American Journal of Physics*, **79**(5), 485–498 (2011), doi:10.1119/1.3549729.

[79] R. A. Battye and A. Moss, "Evidence for Massive Neutrinos from Cosmic Microwave Background and Lensing Observations," *Phys. Rev. Lett.*, **112**, 051303 (2014), doi:10.1103/PhysRevLett.112.051303.

[80] G. Xu, H. Weng, Z. Wang, X. Dai, and Z. Fang, "Chern Semimetal and the Quantized Anomalous Hall Effect in $HgCr_2Se_4$," *Phys. Rev. Lett.*, **107**, 186806 (2011), doi:10.1103/PhysRevLett.107.186806.

[81] X. G. Wen and Q. Niu, "Ground-state degeneracy of the fractional quantum Hall states in the presence of a random potential and on high-genus Riemann surfaces," *Phys. Rev. B*, **41**, 9377–9396 (1990), doi:10.1103/PhysRevB.41.9377.

[82] X. Chen, Z.-X. Liu, and X.-G. Wen, "Two-dimensional symmetry-protected topological orders and their protected gapless edge excitations," *Phys. Rev. B*, **84**, 235141 (2011), doi:10.1103/PhysRevB.84.235141.

[83] P. Roushan, J. Seo, C. V. Parker, Y. S. Hor, D. Hsieh, D. Qian, A. Richardella, M. Z. Hasan, R. J. Cava, and A. Yazdani, "Topological surface states protected from backscattering by chiral spin texture," *Nature*, **460**, 1106 (2009), doi:10.1038/nature08308.

[84] A. R. Mellnik, J. S. Lee, A. Richardella, J. L. Grab, P. J. Mintun, M. H. Fischer, A. Vaezi, A. Manchon, E. A. Kim, N. Samarth, and D. C. Ralph, "Spin-transfer torque generated by a topological insulator," *Nature*, **511**, 449 (2014), doi:10.1038/nature13534.

[85] D. Hsieh, Y. Xia, D. Qian, L. Wray, J. H. Dil, F. Meier, J. Osterwalder, L. Patthey, J. G. Checkelsky, N. P. Ong, A. V. Fedorov, H. Lin, A. Bansil, D. Grauer, Y. S. Hor, R. J. Cava, and M. Z. Hasan, "A tunable topological insulator in the spin helical Dirac transport regime," *Nature*, **460**, 1101 (2009), doi:10.1038/nature08234.

[86] C.-L. Zhang, S.-Y. Xu, I. Belopolski, Z. Yuan, Z. Lin, B. Tong, G. Bian, N. Alidoust, C.-C. Lee, S.-M. Huang, T.-R. Chang, G. Chang, C.-H. Hsu, H.-T. Jeng, M. Neupane, D. S. Sanchez, H. Zheng, J. Wang, H. Lin, C. Zhang, H.-Z. Lu, S.-Q. Shen, T. Neupert, M. Zahid Hasan, and S. Jia, "Signatures of the Adler-Bell-Jackiw chiral anomaly in a Weyl fermion semimetal," *Nat. Commun.*, **7**, 10735 (2016), doi:10.1038/ncomms10735.

[87] H.-J. Kim, K.-S. Kim, J. F. Wang, M. Sasaki, N. Satoh, A. Ohnishi, M. Kitaura, M. Yang, and L. Li, "Dirac versus Weyl Fermions in Topological Insulators: Adler-Bell-Jackiw Anomaly in Transport Phenomena," *Phys. Rev. Lett.*, **111**, 246603 (2013), doi:10.1103/PhysRevLett.111.246603.

[88] D. T. Son and B. Z. Spivak, "Chiral anomaly and classical negative magnetoresistance of Weyl metals," *Phys. Rev. B*, **88**, 104412 (2013), doi:10.1103/PhysRevB.88.104412.

[89] X. Wan, A. M. Turner, A. Vishwanath, and S. Y. Savrasov, "Topological semimetal and Fermi-arc surface states in the electronic structure of pyrochlore iridates," *Phys. Rev. B*, **83**, 205101 (2011), doi:10.1103/PhysRevB.83.205101.

[90] S.-Y. Xu, I. Belopolski, N. Alidoust, M. Neupane, G. Bian, C. Zhang, R. Sankar, G. Chang, Z. Yuan, C.-C. Lee, S.-M. Huang, H. Zheng, J. Ma, D. S. Sanchez, B. Wang, A. Bansil, F. Chou, P. P. Shibayev, H. Lin, S. Jia, and M. Z. Hasan, "Discovery of a Weyl fermion semimetal and topological Fermi arcs," *Science*, **349**(6248), 613–617 (2015), doi:10.1126/science.aaa9297.

[91] A. A. Burkov, "Chiral anomaly and transport in Weyl metals," *Journal of Physics: Condensed Matter*, **27**(11), 113201 (2015), doi:10.1088/0953-8984/27/11/113201.

[92] A. A. Burkov, "Negative longitudinal magnetoresistance in Dirac and Weyl metals," *Phys. Rev. B*, **91**, 245157 (2015), doi:10.1103/PhysRevB.91.245157.

[93] X. Huang, L. Zhao, Y. Long, P. Wang, D. Chen, Z. Yang, H. Liang, M. Xue, H. Weng, Z. Fang, X. Dai, and G. Chen, "Observation of the Chiral-Anomaly-Induced Negative Magnetoresistance in 3D Weyl Semimetal TaAs," *Phys. Rev. X*, **5**, 031023 (2015), doi:10.1103/PhysRevX.5.031023.

[94] R. D. dos Reis, M. O. Ajeesh, N. Kumar, F. Arnold, C. Shekhar, M. Naumann, M. Schmidt, M. Nicklas, and E. Hassinger, "On the search for the chiral anomaly in Weyl semimetals: the negative longitudinal magnetoresistance," *New Journal of Physics*, **18**(8), 085006 (2016), doi:10.1088/1367-2630/18/8/085006.

[95] F. Arnold, C. Shekhar, S.-C. Wu, Y. Sun, R. D. dos Reis, N. Kumar, M. Naumann, M. O. Ajeesh, M. Schmidt, A. G. Grushin, J. H. Bardarson, M. Baenitz, D. Sokolov, H. Borrmann, M. Nicklas, C. Felser, E. Hassinger, and B. Yan, "Negative magnetoresistance without well-defined chirality in the Weyl semimetal TaP," *Nat. Commun.*, **7**, 11615 (2016), doi:10.1038/ncomms11615.

[96] B. Q. Lv, H. M. Weng, B. B. Fu, X. P. Wang, H. Miao, J. Ma, P. Richard, X. C. Huang, L. X. Zhao, G. F. Chen, Z. Fang, X. Dai, T. Qian, and H. Ding, "Experimental Discovery of Weyl Semimetal TaAs," *Phys. Rev. X*, **5**, 031013 (2015), doi:10.1103/PhysRevX.5.031013.

[97] S. Borisenko, D. Evtushinsky, Q. Gibson, A. Yaresko, T. Kim, M. N. Ali, B. Buechner, M. Hoesch, and R. J. Cava, "Time-Reversal Symmetry Breaking Type-II Weyl State in $YbMnBi_2$," *ArXiv eprint 1507. 04847* https://arxiv.org/abs/1507.04847 (2015).

[98] N. Xu, H. M. Weng, B. Q. Lv, C. E. Matt, J. Park, F. Bisti, V. N. Strocov, D. Gawryluk, E. Pomjakushina, K. Conder, N. C. Plumb, M. Radovic, G. Autès, O. V. Yazyev, Z. Fang, X. Dai, T. Qian, J. Mesot, H. Ding, and M. Shi, "Observation of Weyl nodes and Fermi arcs in tantalum phosphide," *Nat. Commun.*, **7**, 11006 (2016), doi:10.1038/ncomms11006.

[99] T. Renner, *Quantities, Units and Symbols in Physical Chemistry*, The Royal Society of Chemistry (2007), ISBN 978-0-85404-433-7, doi:10. 1039/9781847557889.

[100] A. Lehnert, P. Buluschek, N. Weiss, J. Giesecke, M. Treier, S. Rusponi, and H. Brune, "High resolution in situ magneto-optic Kerr effect and scanning tunneling microscopy setup with all optical components in UHV," *Review of Scientific Instruments*, **80**(2), 023902 (2009), doi:10.1063/1.3077148.

[101] Z. Q. Qiu and S. D. Bader, "Surface magneto-optic Kerr effect," *Review of Scientific Instruments*, **71**(3), 1243–1255 (2000), doi:10.1063/1.1150496.

[102] C. S. Arnold, M. Dunlavy, and D. Venus, "Magnetic susceptibility measurements of ultrathin films using the surface magneto-optic Kerr effect: Optimization of the

signal-to-noise ratio," *Review of Scientific Instruments*, **68**(11), 4212–4216 (1997), doi:10.1063/1.1148368.

[103] D. A. Allwood, G. Xiong, M. D. Cooke, and R. P. Cowburn, "Magneto-optical Kerr effect analysis of magnetic nanostructures," *Journal of Physics D: Applied Physics*, **36**(18), 2175 (2003), doi:10.1088/0022-3727/36/18/001.

[104] J. M. Teixeira, R. Lusche, J. Ventura, R. Fermento, F. Carpinteiro, J. P. Araujo, J. B. Sousa, S. Cardoso, and P. P. Freitas, "Versatile, high sensitivity, and automatized angular dependent vectorial Kerr magnetometer for the analysis of nanostructured materials," *Review of Scientific Instruments*, **82**(4), 043902 (2011), doi:10.1063/1.3579497.

[105] A. Arora, S. Ghosh, and V. Sugunakar, "A mirror based polar magneto-optical Kerr effect spectroscopy arrangement," *Review of Scientific Instruments*, **82**(12), 123903 (2011), doi:10.1063/1.3669782.

[106] R. Mattheis and G. Quednau, "Determination of the anisotropy field strength in ultra-thin magnetic films using longitudinal MOKE and a rotating field: the ROTMOKE method," *Journal of Magnetism and Magnetic Materials*, **205**(2), 143 – 150 (1999), doi:10.1016/S0304-8853(99)00526-0.

[107] C. Kittel, "On the Theory of Ferromagnetic Resonance Absorption," *Phys. Rev.*, **73**, 155–161 (1948), doi:10.1103/PhysRev.73.155.

[108] A. V. Naumkin, A. Kraut-Vass, S. W. Gaarenstroom, and C. J. Powell, "NIST Standard Reference Database 20, Version 4. 1," `http://srdata.nist.gov/xps/Default.aspx` (2012).

[109] B. E. Warren, *X-ray diffraction*, Addison-Wesley Pub. Co., Reading, Mass. (1969), ISBN 978-0486663173.

[110] A. Monshi, M. R. Foroughi, and M. R. Monshi, "Modified Scherrer Equation to Estimate More Accurately Nano-Crystallite Size Using XRD," *World J. Nano Sci. Eng.*, **02**(03), 154–160 (2012), doi:10.4236/wjnse.2012.23020.

[111] P. A. Doyle and P. S. Turner, "Relativistic Hartree–Fock X-ray and electron scattering factors," *Acta Crystallographica Section A*, **24**(3), 390–397 (1968), doi:10.1107/S0567739468000756.

[112] P. F. Fewster, "X-ray analysis of thin films and multilayers," *Reports on Progress in Physics*, **59**(11), 1339 (1996), doi:10.1088/0034-4885/59/11/001.

[113] M. Imtiaz, U.-M. G. A., L. Wen, G. Renjie, A. Jarek, and F. Lorenzo, "X-Ray Reciprocal Space Mapping of MBE Grown HgCdTe on Alternative Substrates," *Crystal Research and Technology*, **52**(9), 1700167 (2017), doi:10.1002/crat.201700167.

[114] P. F. Fewster, "Reciprocal space mapping," *Critical Reviews in Solid State and Materials Sciences*, **22**(2), 69–110 (1997), doi:10.1080/10408439708241259.

[115] N. Nagaosa, J. Sinova, S. Onoda, A. H. MacDonald, and N. P. Ong, "Anomalous Hall effect," *Rev. Mod. Phys.*, **82**, 1539–1592 (2010), doi:10.1103/RevModPhys.82.1539.

[116] A. Damascelli, "Probing the Electronic Structure of Complex Systems by ARPES," *Physica Scripta*, **2004**(T109), 61 (2004), doi:10.1238/Physica.Topical.109a00061.

[117] Synchrotron SOLEIL, "Research," https://www.synchrotron-soleil.fr/en/research, accessed: 2018-06-28.

[118] Diamond Light Source, "I05 Beamline Layout," http://www.diamond.ac.uk/Instruments/Structures-and-Surfaces/I05/layout.html, accessed: 2018-06-28.

[119] Y. Chen, "ARPES at Oxford," http://www.arpes.org.uk/Research_ARPES.html, accessed: 2018-06-28.

[120] J. Kawasaki, *Epitaxial growth, surface, and electronic properties of unconventional semiconductors: RE-V/III-V nanocomposites and semiconducting Half Heusler alloys*, Thesis, Univ. of Calif. Santa Barbara, https://alexandria.ucsb.edu/lib/ark:/48907/f3x34vm4 (2014).

[121] B. A. N. F. Mott, "The scattering of fast electrons by atomic nuclei," *Proceedings of the Royal Society of London A: Mathematical, Physical and Engineering Sciences*, **124**(794), 425–442 (1929), doi:10.1098/rspa.1929.0127.

[122] D. H. Jakubassa-Amundsen and R. Barday, "The Sherman function in highly relativistic elastic electron-atom scattering," *Journal of Physics G: Nuclear and Particle Physics*, **39**(2), 025102 (2012), doi:10.1088/0954-3899/39/2/025102.

[123] H. Zama, Y. Ishii, H. Yamamoto, and T. Morishita, "Atomically Flat MgO Single-Crystal Surface Prepared by Oxygen Thermal Annealing," *Jpn. J. Appl. Phys.*, **40**(5A), L465 (2001), doi:10.1143/JJAP.40.L465.

[124] Q.-f. Zhan, S. Vandezande, C. Van Haesendonck, and K. Temst, "Manipulation of in-plane uniaxial anisotropy in Fe/MgO(001) films by ion sputtering," *Applied Physics Letters*, **91**(12), 122510 (2007), doi:10.1063/1.2789396.

[125] H. X. Yang, M. Chshiev, B. Dieny, J. H. Lee, A. Manchon, and K. H. Shin, "First-principles investigation of the very large perpendicular magnetic anisotropy at Fe|MgO and Co|MgO interfaces," *Phys. Rev. B*, **84**, 054401 (2011), doi:10.1103/PhysRevB.84.054401.

[126] S. Yang, H. K. Park, J. S. Kim, J. Y. Kim, and B. G. Park, "Magnetism of ultrathin Fe films on MgO(001)," *Journal of Applied Physics*, **110**(9), 093920 (2011), doi:10.1063/1.3662179.

[127] X. Kozina, S. Ouardi, B. Balke, G. Stryganyuk, G. H. Fecher, C. Felser, S. Ikeda, H. Ohno, and E. Ikenaga, "A nondestructive analysis of the B diffusion in Ta/CoFeB/MgO/CoFeB/Ta magnetic tunnel junctions by hard x-ray photoemission," *Applied Physics Letters*, **96**(7), 072105 (2010), doi:10.1063/1.3309702.

[128] H. Yamamoto, J. Hayakawa, K. Miura, K. Ito, H. Matsuoka, S. Ikeda, and H. Ohno, "Dependence of Magnetic Anisotropy in $Co_{20}Fe_{60}B_{20}$ Free Layers on Capping Layers in MgO-Based Magnetic Tunnel Junctions with In-Plane Easy Axis," *Applied Physics Express*, **5**(5), 053002 (2012), doi:10.1143/APEX.5.053002.

[129] J. Okabayashi, J. W. Koo, H. Sukegawa, S. Mitani, Y. Takagi, and T. Yokoyama, "Perpendicular magnetic anisotropy at the interface between ultrathin Fe film and MgO studied by angular-dependent x-ray magnetic circular dichroism," *Applied Physics Letters*, **105**(12), 122408 (2014), doi:10.1063/1.4896290.

[130] C. Martínez Boubeta, A. Cebollada, J. F. Calleja, C. Contreras, F. Peiró, and A. Cornet, "Magnetization reversal and magnetic anisotropies in epitaxial Fe/MgO and Fe/MgO/Fe heterostructures grown on Si(001)," *Journal of Applied Physics*, **93**(4), 2126–2134 (2003), doi:10.1063/1.1538317.

[131] J. Balogh, I. Dézsi, C. Fetzer, J. Korecki, A. Kozioł-Rachwał, E. Młyńczak, and A. Nakanishi, "Magnetic properties of the Fe-MgO interface studied by Mössbauer spectroscopy," *Phys. Rev. B*, **87**, 174415 (2013), doi:10.1103/PhysRevB.87.174415.

[132] Y.-s. Choi and K. Tsunekawa, "Significant reduction of coercivity without reduction of tunneling magnetoresistance ratio of CoFeB/MgO/CoFeB-based magnetic tunnel junction using sandwich-structured free layer," *Applied Physics Letters*, **91**(17), 172507 (2007), doi:10.1063/1.2801703.

[133] Q.-f. Zhan, S. Vandezande, K. Temst, and C. Van Haesendonck, "Magnetic anisotropy and reversal in epitaxial Fe/MgO(001) films," *Phys. Rev. B*, **80**, 094416 (2009), doi:10.1103/PhysRevB.80.094416.

[134] C. Martínez Boubeta, C. Clavero, J. M. García-Martín, G. Armelles, A. Cebollada, L. Balcells, J. L. Menéndez, F. Peiró, A. Cornet, and M. F. Toney, "Coverage effects on the magnetism of Fe/MgO(001) ultrathin films," *Phys. Rev. B*, **71**, 014407 (2005), doi:10.1103/PhysRevB.71.014407.

[135] P. K. J. Wong, Y. Fu, W. Zhang, Y. Zhai, Y. B. Xu, Z. C. Huang, Y. X. Xu, and H. R. Zhai, "Influence of Capping Layers on Magnetic Anisotropy in Fe/MgO/GaAs(100) Ultrathin Films," *IEEE Transactions on Magnetics*, **44**(11), 2907–2910 (2008), doi:10. 1109/TMAG. 2008.2002195.

[136] S. Sakshath, S. V. Bhat, P. S. Anil Kumar, D. Sander, and J. Kirschner, "Enhancement of uniaxial magnetic anisotropy in Fe thin films grown on GaAs(001) with an MgO underlayer," *Journal of Applied Physics*, **109**(7), 07C114 (2011), doi:10.1063/1.3556941.

[137] Y. Park, E. E. Fullerton, and S. D. Bader, "Growth-induced uniaxial in-plane magnetic anisotropy for ultrathin Fe deposited on MgO(001) by oblique-incidence molecular beam epitaxy," *Applied Physics Letters*, **66**(16), 2140–2142 (1995), doi:10.1063/1.113929.

[138] J. F. Anderson, M. Kuhn, U. Diebold, K. Shaw, P. Stoyanov, and D. Lind, "Surface structure and morphology of Mg-segregated epitaxial Fe_3O_4(001) thin films on MgO(001)," *Phys. Rev. B*, **56**, 9902–9909 (1997), doi:10.1103/PhysRevB.56.9902.

[139] X. Yuan, H. Wang, Y. Wu, X. Chen, G. Zeng, L. Leng, and C. Zhang, "A novel SnS_2/$MgFe_2O_4$/reduced graphene oxide flower-like photocatalyst: Solvothermal synthesis, characterization and improved visible-light photocatalytic activity," *Catalysis Communications*, **61**, 62 – 66 (2015), doi:10.1016/j.catcom.2014.12.003.

[140] S. R. Spurgeon, J. D. Sloppy, R. Tao, R. F. Klie, S. E. Lofland, J. K. Baldwin, A. Misra, and M. L. Taheri, "A study of the effect of iron island morphology and interface oxidation on the magnetic hysteresis of Fe-MgO (001) thin film composites," *Journal of Applied Physics*, **112**(1), 013905 (2012), doi:10.1063/1.4730630.

[141] A. Kozioł-Rachwał, W. Skowroński, T. Ślęzak, D. Wilgocka-Ślęzak, J. Przewoźnik, T. Stobiecki, Q. H. Qin, S. van Dijken, and J. Korecki, "Room-temperature perpendicular magnetic anisotropy of MgO/Fe/MgO ultrathin films," *Journal of Applied Physics*, **114**(22), 224307 (2013), doi:10.1063/1.4843675.

[142] S. Mizukami, A. Sakuma, A. Sugihara, T. Kubota, Y. Kondo, H. Tsuchiura, and T. Miyazaki, "Tetragonal $D0_{22}Mn_{3+x}Ge$ Epitaxial Films Grown on MgO(100) with a Large Perpendicular Magnetic Anisotropy," *Applied Physics Express*, **6**(12), 123002 (2013), doi:10.7567/APEX.6.123002.

[143] A. B. Gokhale and R. Abbaschian, "The Ge-Mn (Germanium-Manganese) system," *Journal of Phase Equilibria*, **11**(5), 460–468 (1990), doi:10. 1007/BF02898261.

[144] C. S. Barquist, I. H. Kwak, J. Bauer, T. Edmonds, A. Biswas, and Y. Lee, "Low temperature transport measurements on atomically smooth metallic and oxygen deficient strontium titanate," *Journal of Physics: Conference Series*, **568**(5), 052004 (2014), doi:10.1088/1742-6596/568/5/052004.

[145] D. Y. He, L. J. Qiao, A. A. Volinsky, Y. Bai, M. Wu, and W. Y. Chu, "Humidity effects on (001) $BaTiO_3$ single crystal surface water adsorption," *Applied Physics Letters*, **98**(6), 062905 (2011), doi:10.1063/1.3544586.

[146] J. W. Evans, P. A. Thiel, and M. C. Bartelt, "Morphological evolution during epitaxial thin film growth: Formation of 2D islands and 3D mounds," *Surface Science Reports*, **61**(1), 1 – 128 (2006), doi:10.1016/j.surfrep.2005.08.004.

[147] C. W. Snyder, B. G. Orr, D. Kessler, and L. M. Sander, "Effect of strain on surface morphology in highly strained InGaAs films," *Phys. Rev. Lett.*, **66**, 3032–3035 (1991), doi:10.1103/PhysRevLett.66.3032.

[148] J. Karel, F. Casoli, P. Lupo, L. Nasi, S. Fabbrici, L. Righi, F. Albertini, and C. Felser, "Evidence for in-plane tetragonal c-axis in Mn_xGa_{1-x} thin films using transmission electron microscopy," *Scripta Materialia*, **114**, 165 – 169 (2016), doi:10.1016/j.scriptamat.2015.11.019.

[149] The Materials Project, "Explore Materials," https://materialsproject.org, accessed: 2018-07-21.

[150] T. Hiratsuka, G. Kim, Y. Sakuraba, T. Kubota, K. Kodama, N. Inami, H. Naganuma, M. Oogane, T. Nakamura, K. Takanashi, and Y. Ando, "Fabrication of perpendicularly magnetized magnetic tunnel junctions with $L1_0$-CoPt / Co_2MnSi hybrid electrode," *J. Appl. Phys.*, **107**(9), 09C714 (2010), doi:10.1063/1.3358239.

[151] K. Borisov, G. Atcheson, G. D'Arcy, Y.-C. Lau, J. M. D. Coey, and K. Rode, "Exchange coupling of a perpendicular ferromagnet to a half-metallic compensated ferrimagnet via a thin hafnium interlayer," *Appl. Phys. Lett.*, **111**(10), 102403 (2017), doi:10.1063/1.5001172.

[152] M. Žic, K. Rode, N. Thiyagarajah, Y.-C. Lau, D. Betto, J. M. D. Coey, S. Sanvito, K. J. O'Shea, C. A. Ferguson, D. A. MacLaren, and T. Archer, "Designing a fully compensated half-metallic ferrimagnet," *Phys. Rev. B*, **93**, 140202 (2016), doi:10.1103/PhysRevB.93.140202.

[153] J. G. Azadani, K. Munira, J. Romero, J. Ma, C. Sivakumar, A. W. Ghosh, and W. H. Butler, "Anisotropy in layered half-metallic Heusler alloy superlattices," *J. Appl. Phys.*, **119**(4), 043904 (2016), doi:10.1063/1.4940878.

[154] H. T. Stokes and D. M. Hatch, "*FINDSYM*: program for identifying the space-group symmetry of a crystal," *J. Appl. Cryst.*, **38**(1), 237–238 (2005), doi:10.1107/S0021889804031528.

[155] J. W. Dong, L. C. Chen, C. J. Palmstrøm, R. D. James, and S. McKernan, "Molecular beam epitaxy growth of ferromagnetic single crystal (001) Ni_2MnGa on (001) GaAs," *Appl. Phys. Let.*, **75**(10), 1443–1445 (1999), doi:10.1063/1.125009.

[156] C. J. Palmstrøm, B. O. Fimland, T. Sands, K. C. Garrison, and R. A. Bartynski, "Epitaxial CoGa and textured CoAs contacts on $Ga_{1-x}Al_xAs$ fabricated by molecular-beam epitaxy," *J. Appl. Phys.*, **65**(12), 4753–4758 (1989), doi:10.1063/1.343228.

[157] H. Yamada and Y. Torii, "Low temperature heteroepitaxial film growth of Si on sapphire by reactive ion beam deposition," *J. Appl. Phys.*, **62**(6), 2298–2301 (1987), doi:10.1063/1.339488.

[158] T. Burkert, O. Eriksson, P. James, S. I. Simak, B. Johansson, and L. Nordström, "Calculation of uniaxial magnetic anisotropy energy of tetragonal and trigonal Fe, Co, and Ni," *Phys. Rev. B*, **69**, 104426 (2004), doi:10.1103/PhysRevB.69.104426.

[159] S. Fujii, S. Ishida, and S. Asano, "A half-metallic band structure and Fe_2MnZ (Z = Al, Si, P)," *Phys. Soc. Japan*, **64**(1), 185–191 (1995), doi:10.1143/JPSJ.64.185.

[160] M. Belkhouane, S. Amari, A. Yakoubi, A. Tadjer, S. Méçabih, G. Murtaza, S. Bin Omran, and R. Khenata, "First-principles study of the electronic and magnetic properties of Fe_2MnAl, Fe_2MnSi and $Fe_2MnSi_{0.5}Al_{0.5}$," *J. Magn. Magn. Mater.*, **377**(Supplement C), 211–214 (2015), doi:10.1016/j.jmmm.2014.10.094.

[161] S. M. Azar, B. A. Hamad, and J. M. Khalifeh, "Structural, electronic and magnetic properties of $Fe_{3-z}Mn_xZ$ (Z=Al, Ge, Sb) Heusler alloys," *J. Magn. Magn. Mater.*, **324**(10), 1776–1785 (2012), doi:10.1016/j.jmmm.2011.12.037.

[162] F. Dahmane, Y. Mogulkoc, B. Doumi, A. Tadjer, R. Khenata, S. B. Omran, D. P. Rai, G. Murtaza, and D. Varshney, "Structural, electronic and magnetic properties of Fe_2-based full Heusler alloys: A first principle study," *J. Magn. Magn. Mater.*, **407**(Supplement C), 167–174 (2016), doi:10.1016/j.jmmm.2016.01.074.

[163] K. Özdoğan, E. Şaşioğlu, B. Aktaş, and I. Galanakis, "Doping and disorder in the Co_2MnAl and Co_2MnGa half-metallic Heusler alloys," *Phys. Rev. B - Condens. Matter Mater. Phys.*, **74**, 172412 (2006), doi:10.1103/PhysRevB.74.172412.

[164] K. Özdoğan and I. Galanakis, "Effect of order on the half-metallic gap in Heusler compounds," *J. Appl. Phys.*, **110**(7), 076101 (2011), doi:10.1063/1.3642990.

[165] D. P. Rai, J. Hashemifar, M. Jamal, Lalmuanpuia, M. P. Ghimire, Sandeep, D. T. Khathing, P. K. Patra, B. Indrajit Sharma, Rosangliana, and R. K. Thapa, "Study of Co_2MnAl Heusler alloy as half metallic ferromagnet," *Indian J. Phys.*, **84**(6), 717–721 (2010), doi:10.1007/s12648-010-0077-0.

[166] Y. Sakuraba, K. Takanashi, Y. Kota, T. Kubota, M. Oogane, A. Sakuma, and Y. Ando, "Evidence of Fermi level control in a half-metallic Heusler compound Co_2MnSi by Al-doping: Comparison of measurements with first-principles calculations," *Phys. Rev. B*, **81**, 144422 (2010), doi:10.1103/PhysRevB.81.144422.

[167] W. Q. Li, J. X. Cao, J. W. Ding, and X. H. Yan, "Tuning Fermi level within half-metallic gap in Co-based Heusler alloys," *Eur. Phys. J. B*, **85**(7), 250 (2012), doi:10.1140/epjb/e2012-20881-0.

[168] A. Candan, G. Uğur, Z. Charifi, H. Baaziz, and M. R. Ellialtioğlu, "Electronic structure and vibrational properties in cobalt-based full-Heusler compounds: A first principle study of Co_2MnX (X = Si, Ge, Al, Ga)," *J. Alloys Compd.*, **560**, 215–222 (2013), doi:10.1016/j.jallcom.2013.01.102.

[169] J. C. Tung and G. Y. Guo, "High spin polarization of the anomalous hall current in co-based Heusler compounds," *New J. Phys.*, **15**(3), 033014 (2013), doi:10.1088/1367-2630/15/3/033014.

[170] Y. Miura, K. Abe, and M. Shirai, "Half-metallic behavior of Co_2MnSi/Co_2MnAl/MgO interface and its coherent tunneling conductance," *J. Phys. Conf. Ser.*, **200**(5), 052016 (2010), doi:10.1088/1742-6596/200/5/052016.

[171] Y. Feng, T. Zhou, X. Chen, H. Yuan, and H. Chen, "The effect of Mn content on magnetism and half-metallicity of off-stoichiometric Co_2MnAl," *J. Magn. Magn. Mater.*, **387**, 118–126 (2015), doi:10.1016/j.jmmm.2015.04.002.

[172] J. Barth, G. H. Fecher, B. Balke, T. Graf, A. Shkabko, A. Weidenkaff, P. Klaer, M. Kallmayer, H.-J. Elmers, H. Yoshikawa, S. Ueda, K. Kobayashi, and C. Felser, "Anomalous transport properties of the half-metallic ferromagnets Co_2TiSi, Co_2TiGe and Co_2TiSn," *Philosophical Transactions of the Royal Society of London A: Mathematical, Physical and Engineering Sciences*, **369**(1951), 3588–3601 (2011), doi:10.1098/rsta.2011.0183.

[173] L. Klein, J. S. Dodge, C. H. Ahn, J. W. Reiner, L. Mieville, T. H. Geballe, M. R. Beasley, and A. Kapitulnik, "Transport and magnetization in the badly metallic itinerant ferromagnet $SrRuO_3$," *Journal of Physics: Condensed Matter*, **8**(48), 10111 (1996), doi:10.1088/0953-8984/8/48/026.

[174] B. Raquet, M. Viret, E. Sondergard, O. Cespedes, and R. Mamy, "Electron-magnon scattering and magnetic resistivity in 3*d* ferromagnets," *Phys. Rev. B*, **66**, 024433 (2002), doi:10.1103/PhysRevB.66.024433.

[175] I. Mannari, "Electrical Resistance of Ferromagnetic Metals," *Progress of Theoretical Physics*, **22**(3), 335–343 (1959), doi:10.1143/PTP.22.335.

[176] C. L. Chien, J. Q. Xiao, and J. S. Jiang, "Giant negative magnetoresistance in granular ferromagnetic systems (invited)," *Journal of Applied Physics*, **73**(10), 5309–5314 (1993), doi:10.1063/1.353765.

[177] J. Q. Xiao, J. S. Jiang, and C. L. Chien, "Giant magnetoresistance in nonmultilayer magnetic systems," *Phys. Rev. Lett.*, **68**, 3749–3752 (1992), doi:10.1103/PhysRevLett.68.3749.

[178] N. Furukawa, "Unconventional One-Magnon Scattering Resistivity in Half-Metals," *Journal of the Physical Society of Japan*, **69**(7), 1954–1957 (2000), doi:10.1143/JPSJ.69.1954.

[179] P. A. Dowben and R. Skomski, "Are half-metallic ferromagnets half metals? (invited)," *Journal of Applied Physics*, **95**(11), 7453–7458 (2004), doi:10.1063/1.1682911.

[180] N. A. Sinitsyn, "Semiclassical theories of the anomalous Hall effect," *Journal of Physics: Condensed Matter*, **20**(2), 023201 (2008), doi:10.1088/0953-8984/20/02/023201.

[181] Y. Tian, L. Ye, and X. Jin, "Proper Scaling of the Anomalous Hall Effect," *Phys. Rev. Lett.*, **103**, 087206 (2009), doi:10.1103/PhysRevLett.103.087206.

[182] "University of Alabama Heusler Database," http://heusleralloys.mint.ua.edu, accessed: 2018-06-19.

[183] T. McGuire and R. Potter, "Anisotropic magnetoresistance in ferromagnetic 3d alloys," *IEEE Transactions on Magnetics*, **11**(4), 1018–1038 (1975), doi:10.1109/TMAG. 1975.1058782.

[184] M. Thompson, "Genplot RUMP," http://www.genplot.com, accessed: 2018-08-24.